AZIMUTHAL ANISOTROPY OF STRANGE AND MULTI-STRANGE HADRONS IN HEAVY-ION COLLISIONS AT RHIC

By

Vipul Bairathi

(PHYS11201304014)

National Institute of Science Education and Research

HBNI, Jatni 752050, India

A thesis submitted to the

Board of Studies in Physical Sciences

In partial fulfillment of requirements

for the Degree of
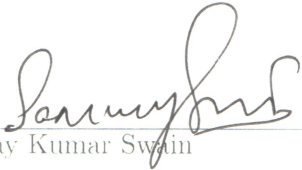
DOCTOR OF PHILOSOPHY
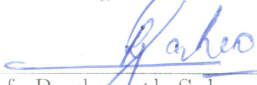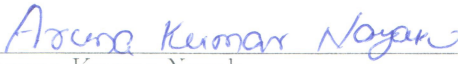
of

HOMI BHABHA NATIONAL INSTITUTE

August, 2019

Homi Bhabha National Institute

Recommendations of the Viva Voce Committee

As members of the Viva Voce Committee, we certify that we have read the dissertation prepared by **Vipul Bairathi** entitled **"Azimuthal anisotropy of strange and multi-strange hadrons in heavy-ion collisions at RHIC"** and recommend that it may be accepted as fulfilling the thesis requirement for the award of Degree of Doctor of Philosophy.

Chairman - Dr. Sanjay Kumar Swain   16/8/19

                  Date

Guide / Convener - Prof. Bedangadas Mohanty 16/8/2019

                  Date

External Examiner - Prof. Raghunath Sahoo 16.8.2019

                  Date

Member 1 - Dr. Prolay Kumar Mal   Aug 16, 2019

                  Date

Member 2 - Dr. Victor Roy   18.08.19

                  Date

External Member - Dr. Aruna Kumar Nayak 16/08/2019

                  Date

Final approval and acceptance of this thesis is contingent upon the candidate's submission of the final copies of the thesis to HBNI.

I hereby certify that I have read this thesis prepared under my direction and recommend that it may be accepted as fulfilling the thesis requirement.

Date: 16/8/2019

Place: NISER

Prof. Bedangadas Mohanty

STATEMENT BY AUTHOR

This dissertation has been submitted in partial fulfillment of requirements for an advanced degree at Homi Bhabha National Institute (HBNI) and is deposited in the Library to be made available to borrowers under rules of the HBNI.

Brief quotations from this dissertation are allowable without special permission, provided that accurate acknowledgement of source is made. Requests for permission for extended quotation from or reproduction of this manuscript in whole or in part may be granted by the Competent Authority of HBNI when in his or her judgement the proposed use of the material is in the interests of scholarship. In all other instances, however, permission must be obtained from the author.

Vipul Bairathi

DECLARATION

I, Vipul Bairathi, hereby declare that the investigation presented in the thesis has been carried out by me. The work is original and has not been submitted earlier as a whole or in part for a degree/diploma at this or any other Institution/University.

Vipul Bairathi

Dedicated
to
My Family and Friends

Acknowledgements

Summary

In this thesis work, the data collected with the STAR detector at RHIC for U+U collisions at $\sqrt{s_{NN}} = 193$ GeV per nucleon and Au+Au collisions at $\sqrt{s_{NN}} = 14.5$ GeV per nucleon are analyzed. The Uranium nucleus due to its deformed shape (pro-late) gives rise to various initial collision configurations in U+U collisions compared to more spherical Gold (Au) nucleus, hence measurements done in U+U collisions are important to understand collectivity and also chiral magnetic effect due to high magnetic field developed in relativistic heavy-ion collisions. A systematic measurement of transverse momentum (p_T) dependence of flow coefficients v_2, v_3 and v_4 of strange and multi-strange hadrons at mid-rapidity for different multiplicity classes in U+U collisions is presented using invariant mass technique. The magnitude of elliptic flow v_2 is found to be greater than that of the higher order flow coefficients v_3 and v_4. The shape and magnitude of differential $v_2(p_T)$ as a function of transverse momentum is similar to the published results in Au+Au collisions at $\sqrt{s_{NN}} = 200$ GeV, which shows the development of partonic collectivity of the medium created in U+U collisions at $\sqrt{s_{NN}} = 193$ GeV at RHIC. The v_2 values for peripheral collisions are higher than central collisions reflecting the effect of initial spatial anisotropy (eccentricity of overlap region) on final state momentum space azimuthal anisotropy. Higher order flow coefficients do not show centrality dependence, this is expected because the origins of higher order flow coefficients are event-by-event fluctuations in the initial density profile of participating nucleons rather than the initial overlap geometry. The observation of mass dependence of v_n coefficients at low p_T and particle type dependence at higher p_T leads to the number of constituent quark scaling of v_n coefficients. Further the measurements of azimuthal anisotropy of strange and multi-strange hadrons are compared with the heavy-ion collision model calculations. The AMPT model explains the results of strange and multi-strange v_n coefficients at low p_T and under-estimates the results at higher p_T. The hydrodynamics model also over-predicts the data, which shows the need of viscous corrections to the model.

This thesis work also includes systematic study of elliptic flow v_2 as a function of p_T, η and collision centrality in Au+Au collisions at $\sqrt{s_{NN}} = 14.5$ GeV. The inclusive charged hadrons v_2 results are obtained using several methods which are sensitive to different effects, these includes the event plane method and 2,4-particle cumulant method. The elliptic flow v_2 depends on the collision centrality and strongly correlated

with the initial co-ordinate space eccentricity. The increase of v_2 with beam energy is attributed to the change of baryon chemical potential from lower to higher energies and/or larger collectivity at higher collision energies. The results have been compared with the transport model calculations from AMPT and UrQMD to understand the particle production mechanism and partonic versus hadronic contribution to v_2 in Au+Au collisions. The UrQMD results are consistently lower than the data for the momentum range studied, which shows that only hadronic interactions are not sufficient to explain the experimental data. The AMPT-String melting with a parton-parton cross-section of 1.5 mb shows a good agreement with the data. This suggests the formation of partonic medium in Au+Au collisions at $\sqrt{s_{\mathrm{NN}}} = 14.5$ GeV. A larger parton cross-section of 10 mb over-estimates the data, which has been used to interpret hadronic versus partonic contribution to the v_2 because a larger parton cross-section means late start of hadron cascade. The ϕ-meson v_2 measurements are also done using event plane method at mid-rapidity in Au+Au collisions at $\sqrt{s_{\mathrm{NN}}} = 14.5$ GeV. A finite value of ϕ-meson v_2 at highest measured momentum bin in Au+Au collisions at $\sqrt{s_{\mathrm{NN}}} = 14.5$ GeV is observed. This indicates the formation of partonic phase of the medium at beam energies $\sqrt{s_{\mathrm{NN}}} > 14.5$ GeV in heavy-ion collisions.

In this thesis, a new method to select body-tip configuration from unbiased events in central U+U collisions using AMPT model is presented in context of experiments. A new method for binning the heavy-ion collisions events in terms of total spectator neutrons along with the centrality bins is also presented, which is found to be helpful to probe events with rare initial states which otherwise get masked when analysed by the centrality binning alone. The advantage of using total spectator neutrons to probe initial state is that it is an experimentally observable quantity. Also it is not required to know total spectator neutron number very precisely. The proposed new binning procedure can be use to analyze initial conditions with the current performance of ZDC detectors in heavy-ion collisions experiments to understand the QGP medium created in relativistic heavy-ion collisions more accurately.

List of publications and presentations

Publications as primary author:

1. "Selecting specific initial configurations using spectator neutrons in U + U collisions"
   Vipul Bairathi, Md. Rihan Haque, Bedangadas Mohanty
   Phys. Rev. C, **2015**, *91*, 054903.

2. "A review on ϕ-meson production in heavy-ion collision"
   Md. Nasim, Vipul Bairathi, Mukesh Kumar Sharma, Bedangadas Mohanty, Anju Bhasin
   Adv. High Energy Phys., **2015**, *2015*, 197930.

3. "Probing Pb + Pb collisions at $\sqrt{s_{\mathrm{NN}}} = 2760$ GeV with spectators"
   Vipul Bairathi, Sandeep Chatterjee, Md. Rihan Haque, Bedangadas Mohanty
   Phys. Lett. B, **2016**, *754*, 144-150.

4. "Centrality dependence of identified particle elliptic flow in relativistic heavy-ion collisions at $\sqrt{s_{\mathrm{NN}}} = 7.7$-$62.4$ GeV"
   L. Adamczyk *et al.* (STAR collaboration)
   Phys. Rev. C, **2016**, *93*, 014907.

5. "Bulk properties of the system formed in Au + Au collisions at $\sqrt{s_{\mathrm{NN}}} = 14.5$ GeV at STAR"
   (Submitted to Physical Review C)
   *arXiv:*1908.03585 [nucl-ex], **2019**.

Conference proceedings:

1. "Azimuthal anisotropy of ϕ-meson in U + U collisions at RHIC"
   Vipul Bairathi (for the STAR collaboration)
   Proceedings of the *DAE Symp. on Nucl. Phys.*, **2014**, *59*, 716-717.

2. "Selection of body-tip configuration in U + U collisions at $\sqrt{s_{\mathrm{NN}}} = 193$ GeV using spectator neutrons"
   Vipul Bairathi, Md. Rihan Haque, Bedangadas Mohanty
   Proceedings of the *DAE Symp. on Nucl. Phys.*, **2015**, *60*, 726-727.

3. "Azimuthal anisotropy of ϕ-meson in U + U and Au + Au collisions at RHIC"
   Vipul Bairathi (for the STAR collaboration)
   Proceedings of the *J. Phys. Conf. Ser.*, **2016**, *668*, 012039.

4. "Bulk properties of the system formed in Au + Au collisions at $\sqrt{s_{\mathrm{NN}}} = 14.5$ GeV using the STAR detector at RHIC"
   Vipul Bairathi (for the STAR collaboration)
   Proceedings of the *Nucl. Phys. A*, **2016**, *956*, 292-295.

5. "Probing heavy-ion collisions through initial state observables"
   Vipul Bairathi, Sandeep Chatterjee, Md. Rihan Haque, Bedangadas Mohanty
   Proceedings of the *DAE Symp. on Nucl. Phys.*, **2016**, *61*, 734-735.

6. "Azimuthal anisotropy of strange hadrons in U + U collisions at $\sqrt{s_{\mathrm{NN}}} = 193$ GeV"
   Vipul Bairathi (for the STAR collaboration)
   Proceedings of the *EPJ Web of Conf.*, **2018**, *171*, 13003.

Papers under review in STAR collaboration (as a primary author):

1. "Azimuthal anisotropy of strange and multi-strange hadrons in U + U collisions at $\sqrt{s_{\mathrm{NN}}} = 193$ GeV at RHIC"
   Intended to Physical Review C (under preparation in Physics Working Group)

STAR collaboration papers as an author:

1. "Beam energy dependence of directed flow of $\Lambda, \bar{\Lambda}, K^{\pm}, K_{\mathrm{s}}^{0}, \phi$ in Au + Au collisions"
   L. Adamczyk *et al.* (STAR collaboration)
   Phys. Rev. Lett., **2018**, *120*, 062301.

2. "Beam energy dependence of rapidity even dipolar flow in Au + Au collisions"
   L. Adamczyk *et al.* (STAR collaboration)
   Phys. Lett. B, **2018**, *784*, 26-32.

3. "Correlation measurements between flow harmonics in Au + Au collisions at RHIC"
   L. Adamczyk *et al.* (STAR collaboration)
   arXiv:1803.03876.

4. "Azimuthal anisotropy in Cu + Au collisions at $\sqrt{s_{\mathrm{NN}}} = 200$ GeV"
   L. Adamczyk *et al.* (STAR collaboration)
   Phys. Rev. C, **2018**, *98*, 014915.

5. "Collision energy dependence of moments of net-kaon multiplicity distributions at RHIC"
   L. Adamczyk *et al.* (STAR collaboration)
   Phys. Lett. B, **2018**, *785*, 551-560.

6. "Measurement of hyper triton lifetime in Au + Au collisions at the relativistic heavy-ion collider"
   L. Adamczyk *et al.* (STAR collaboration)
   Phys. Rev. C, **2018**, *97*, 054909.

7. "Bulk properties of the medium produced in relativistic heavy-ion collisions from beam energy scan program"
   L. Adamczyk *et al.* (STAR collaboration)
   Phys. Rev. C, **2017**, *96*, 044904.

8. "Measurement of D^0 azimuthal anisotropy at midrapidity in Au + Au collisions at $\sqrt{s_{\mathrm{NN}}} = 200$ GeV"
   L. Adamczyk *et al.* (STAR collaboration)
   Phys. Rev. Lett., **2017**, *118*, 212301.

9. "Energy dependence of J/ψ production in Au + Au collisions at $\sqrt{s_{\mathrm{NN}}} = 39$, 62.4 and 200 GeV"
   L. Adamczyk *et al.* (STAR collaboration)
   Phys. Lett. B, **2017**, *771*, 13-20.

10. "Direct virtual photon production in Au + Au collisions at $\sqrt{s_{\mathrm{NN}}} = 200$ GeV"
    L. Adamczyk *et al.* (STAR collaboration)
    Phys. Lett. B, **2017**, *770*, 451-458.

11. "Υ production in U + U collisions at $\sqrt{s_{\mathrm{NN}}} = 193$ GeV measured with the STAR experiment"
    L. Adamczyk *et al.* (STAR collaboration)
    Phys. Rev. C, **2016**, *94*, 064904.

12. "Centrality and transverse momentum dependence of elliptic flow of multi-strange hadrons and ϕ-meson in Au + Au collisions at $\sqrt{s_{\mathrm{NN}}} = 200$ GeV"
    L. Adamczyk *et al.* (STAR collaboration)
    Phys. Rev. Lett., **2016**, *116*, 062301.

Vipul Bairathi

Contents

4 Elliptic flow of ϕ-meson and inclusive charged hadrons in Au+Au

List of Figures

List of Tables

Chapter 1

Introduction

1.1 Quantum chromodynamics (QCD)

The theory of strong interactions is known as *Quantum chromodynamics* (QCD). It successfully describes the interactions among quarks and gluons [1,2]. The fundamental constituents of matter known today are leptons, quarks and gauge bosons (gluon (g), photon (γ), $W^{\pm}$ and Z^0 boson) [3, 4]. The standard model of particle physics predicts the existence of Higgs (H) boson which was discovered recently [5, 6]. The quarks and gluons carry color charge which generates the force field, just as the electric charge in electromagnetic field. Free quarks have never been observed experimentally. They are bound together inside hadrons by the strong interaction. Bound states of three quarks are known as *Baryons* (like proton or neutron), and combinations of a quark and an anti-quark are known as *Mesons* (like pion or kaon). Baryons and Mesons are collectively called *hadrons*. The massless gluon is the mediator of strong interaction. There are eight kinds of gluon which makes QCD very different from quantum electrodynamics (QED). The gluons can interact among themselves. This brings characteristic features in QCD: the confinement and asymptotic freedom [1,2].

1.1.1 Confinement and Asymptotic freedom

The strength of QCD is characterized by running coupling constant, α_S, given as [7]:

$$\alpha_S(Q^2) \approx \frac{12\pi}{(11C_A - 4n_f T_R)\ln(|Q^2|/\Lambda_{QCD}^2)}, \tag{1.1}$$

where Q^2 is the amount of momentum transfer, C_A is the color factor associated with gluon emission from gluon, n_f is the number of quark flavors, and T_R is the color factor for a gluon split to a $q\bar{q}$ pair. The Λ_{QCD} is known as energy scale parameter of QCD. The equation states that the strength of strong coupling constant becomes stronger at low Q^2 ($Q^2 \sim \Lambda_{QCD}$) or at large distances between the quarks, This is known as *Confinement*. At high Q^2 ($Q^2 \gg \Lambda_{QCD}$) or small distances, the coupling between the quarks become weak. As a result, QCD matter at very high temperatures behaves likes a gas of free quarks and gluons. This is known as *asymptotic freedom*. In this case, perturbative QCD (pQCD) calculations can be used. The value of α_S has been measured by many experiments at different scales and compared with pQCD predictions. The latest precise measurements come from hadronic Z^0 decay width [8]. The world average value of $\alpha_S = 0.1181 \pm 0.0011$ comes from the global fit to various calculations. Figure 1.1 shows the summary of measurements of $\alpha_S(Q^2)$ as a function of Q [7]. This shows the agreement of energy dependence of α_S with the QCD predictions of asymptotic freedom. The asymptotic freedom was discovered in the year 1973 by David Gross, Frank Wilczek, and David Politzer, for which they have received nobel prize in the year 2004.
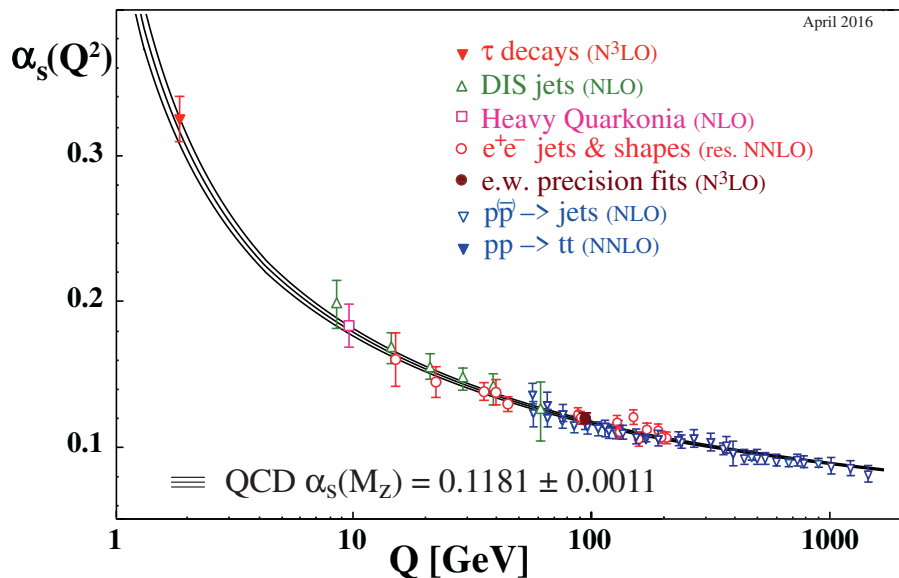
Figure 1.1: Summary of measurements of $\alpha_S(Q^2)$ as function of Q from various QCD calculations with different degree of perturbation theory. The figure is taken from Ref. [7]

1.2 Quark-Gluon Plasma (QGP)

Developments in high-energy physics predict a new state of matter with densities (ε) greater than 0.5 GeV/fm^3 ($\sim 10^{18}$ kg/m^3). Such densities are present in the early phases of the big-bang, the center of a neutron star and black-holes [9]. A neutron has a radius of about $0.5-1.0$ fm, and has a density of about 10^{18} kg/m^3, whereas the density of center of a neutron star is about $10^{19}-10^{20}$ kg/m^3 [10]. In the year 1974, T.D. Lee proposed that by having high nucleon density over a relatively large volume, it is possible to create such high density state of nuclear matter [11]. J. C. Collins and M. J. Perry in 1975 argued that the asymptotically free theory of strong interactions implies the existence of a highly dense state of matter [12]. Such dense

matter of free quarks and gluons is known as the *Quark-Gluon Plasma* (QGP) [13]. Experimentally QGP is defined as the local thermal equilibrated state of matter in which quarks and gluons are free to move in a volume much larger than the volume of a nucleon (hadron) [14].

1.3 The phases of QCD

A typical phase diagram of strongly interacting matter is shown in the Fig. 1.2. The QCD phase diagram is usually plotted as the temperature (T) versus the baryon chemical potential (μ_B). The baryon chemical potential (μ_B) is the energy that is absorbed or released due to change in the number of baryons. The baryon number (B) is a conserved quantity in QCD along with the electric charge (Q) and strangeness (S). In high energy heavy-ion collisions baryon chemical potential μ_B is relatively large compared to μ_Q and μ_S [15]. Different phases of the nuclear matter can be explored by varying the T and μ_B. The normal nuclear matter state is at T = 0 and $\mu_B \approx 938$ MeV. At high T and μ_B, the phase of de-confined quarks and gluons is expected to be present [13]. At low T and μ_B, the quarks and gluons are confined within hadrons. At low T and high μ_B, other interesting phases like color superconductivity occurs [16].

Experimentally, the phases of QCD can be explored by varying the beam energy of heavy-ion collisions. Both the temperature and the baryon chemical potential are a function of the center of mass energy ($\sqrt{s_{\mathrm{NN}}}$) [17]. The experimental programs at the Relativistic Heavy Ion Collider (RHIC) at BNL, the Large Hardon Collider (LHC) at CERN and future Facility for Anti-proton and Ion Research (FAIR) at GSI and Nuclotron based Ion Collider (NICA) at JINR aim at exploring the phase diagram of QCD.
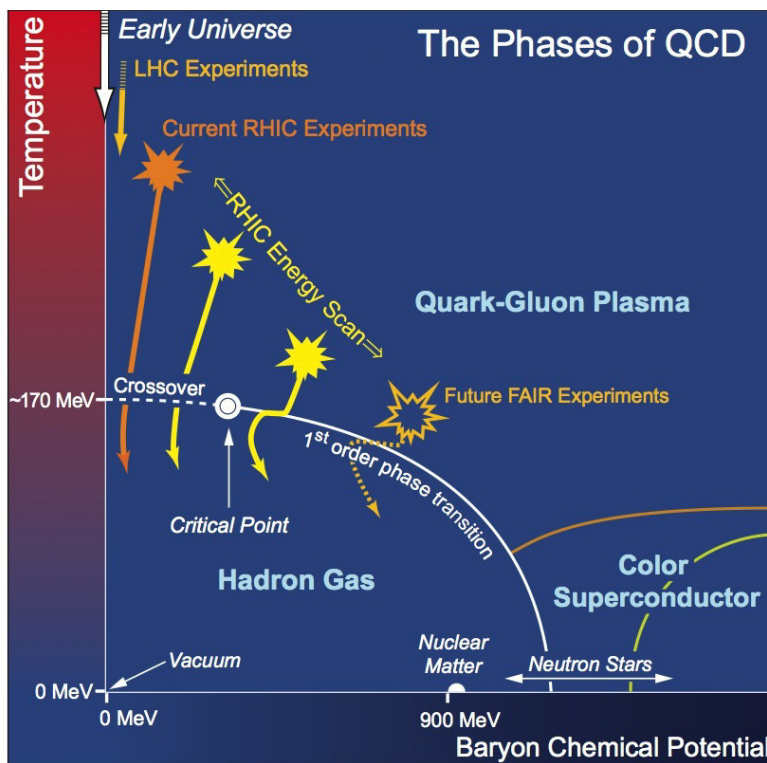
Figure 1.2: Schematic diagram of the phases of QCD [18] plotted as the temperature (T) versus the baryon chemical potential (μ_B). The solid lines show the phase boundaries for various phases. The dotted curve marks crossover transition between hadronic and QGP phases. The solid circle depicts the possible location of QCD critical point [19].

Theoretically, the phases of QCD are explored through numerical simulations on a space-time lattice in non-pertubative QCD regime. This is known as *lattice QCD* (lQCD). The formulation of lattice QCD is first provided by the K. Wilson in 1974 [20]. The first numerical simulation of lattice QCD is performed by M. Creutz in 1980 [21]. The lQCD calculations can be classified in the following cases: (i) In the zero-temperature limit, it shows good agreement with the experimentally measured mass of hadrons and it also predicts breaking of chiral symmetry [22]. (ii) In the finite-temperature limit, it predicts a phase transition from hadronic phase to QGP phase of the nuclear matter at a critical temperature (T_c) of (154±8) MeV [23]. There is a sharp increase in energy density around T_c which indicates increase in the number

of degrees of freedom of the system. This shows a transition to the phase where the quarks and gluons are relevant degrees of freedom. Figure 1.3 shows the lattice calculations for energy density (ε/T^4) as a function of the temperature (T/T_c). The nature of the QCD phase transition depends on the values of the quark masses m_q and the number of flavors (N_f). LQCD calculations at finite-temperature $(T > 0)$ and $\mu_B = 0$ suggest a cross-over above T_c [24], while at large μ_B several model calculations show the transition to be the first order phase transition [25]. It also predicts a point where the first order phase transition ends, known as critical point [26].
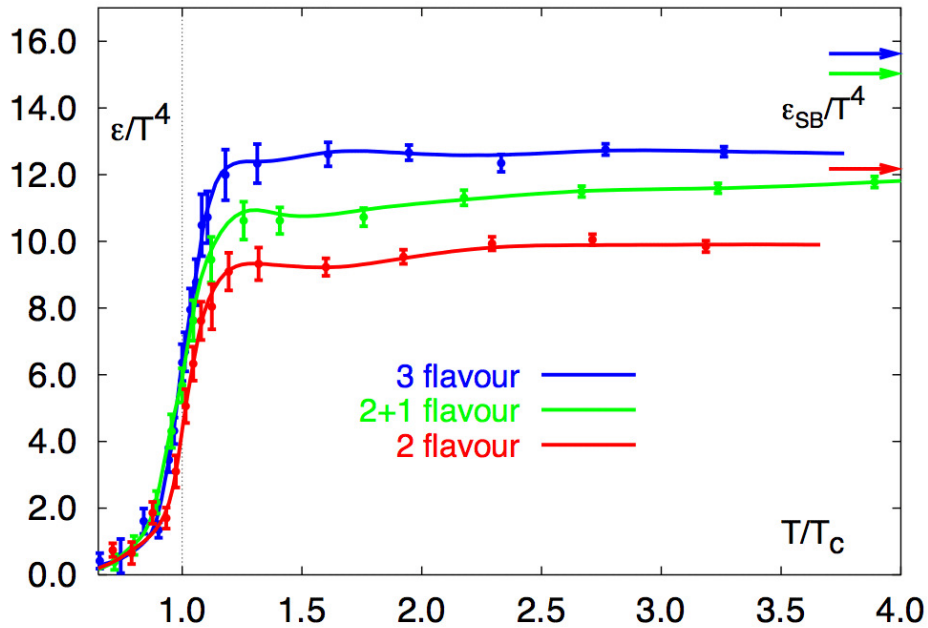
Figure 1.3: Lattice QCD results of energy density (ε) normalized by T^4 as a function of the temperature normalized to the critical temperature (T/T_c) for phase transition. The arrow indicates the Stefan-Boltzmann ideal gas limits (ε_{SB}/T^4). The figure is taken from Ref. [23]

1.4 Relativistic Heavy-Ion Collisions

The main aim of heavy-ion collisions at relativistic energies is to create de-confined state of quarks and gluons and study its properties in extreme temperature and energy density. This new form of matter is believed to have existed in the Universe a few microseconds after the Big-Bang. It is possible to create the new state of matter in the laboratory by colliding heavy-ions at ultra-relativistic energies (sometimes called 'little bang'). The study of relativistic heavy-ion collisions started at the Bevalac, Lawrence Berkeley National Laboratory in the 1970s. The first heavy-ion collision at moderate energy of about 1-2 A GeV/c was done at Bevalac. The success of these experiments to study excited nuclear matter gave birth to the heavy-ion collision programmes at Brookhaven National Laboratory (BNL) and the European Organization for Nuclear Research (CERN). We will discuss about the different experimental facilities in the next chapter. For now, we will discuss about the collision geometry, space-time evolution and kinematic variables of the heavy-ion collisions.

1.4.1 Geometry of heavy-ion collision

Figure 1.4 shows a schematic picture of collision of two symmetric heavy-ions. In the center of mass frame both the projectile and the target nuclei are Lorentz contracted along the beam direction (generally taken as 'z-axis'). The perpendicular distance between the centers of the two colliding nucleus is known as *impact parameter* (b). It characterizes the degree of overlap between the two colliding nuclei. The nucleons inside the nuclei taking part in the collision are called participant nucleons and rest of the nucleons which do not take part are called spectator nucleons. A central collision is defined as having large number of participating nucleons or small impact parameter, whereas a peripheral collision is defined as low number of participating nucleons or

large impact parameter. The impact parameter cannot be measured directly in heavy-ion experiments, therefore particle multiplicity (number of charged particle produced) is used to characterize the geometry of the heavy-ion collisions (referred as 'collision centrality'). The details of centrality determination using charged particle multiplicity is discussed in Chapter 3.
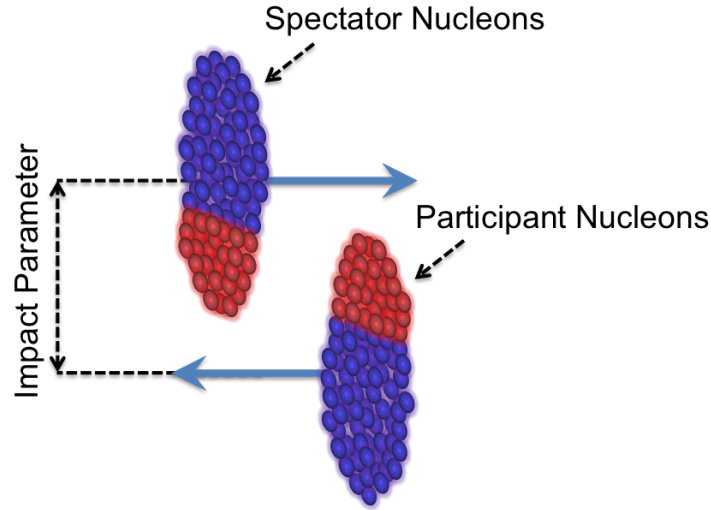
Figure 1.4: A schematic picture of the geometry of relativistic heavy-ion collision.

1.4.2 Space-Time evolution

In relativistic heavy-ion collisions, two Lorentz contracted nuclei moving towards each other with velocity nearly equal to the velocity of light (c). They appear as two thin disks in the center of mass frame along the beam direction because of the relativistic speeds. Figure 1.5 shows a simplified picture of the space-time evolution of a heavy-ion collision. The two nuclei collide at the proper time $\tau = 0$ (i.e. t = 0, z = 0). The proper time define as: $\tau = \sqrt{t^2 - z^2}$. The region $\tau < 0$ (space like) is inaccessible for the physical particles, as it needs velocity $v > c$. The line t = z (light like) is for massless particles traveling with c and the region $\tau > 0$ (time like) is accessible for physical particles. Particle production occurs only in the time like region.
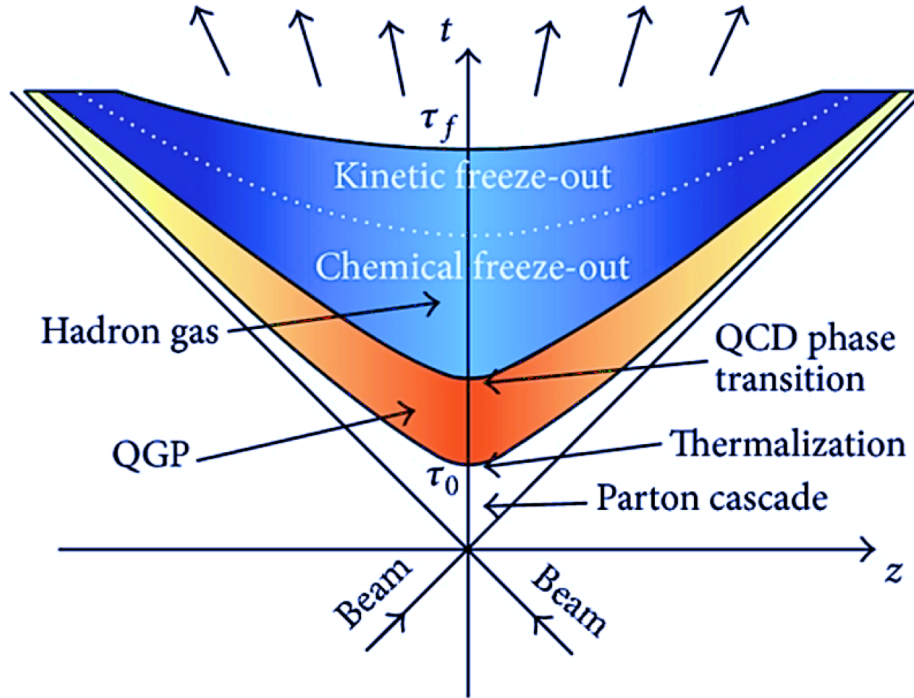
Figure 1.5: A space-time diagram for the evolution of relativistic heavy-ion collision [27].

A nucleus-nucleus collision goes through various stages in the evolution as shown in the Fig. 1.5. We can broadly classify it in different stages depending upon the proper time τ.

- **Initial stage** $(\tau < 0)$: Before the collision, the quarks and gluons (partons) distributions inside the two nuclei can be described by their structure functions. The two nuclei then collide at $\tau = 0$.

- **Partonic stage** $(0 < \tau < \tau_0)$: After the collision, a large amount of initial kinetic energy is deposited in the overlap region of the two colliding nuclei. The initial kinetic energy produces a highly excited state of matter which is often called as *fireball*. If the deposited initial kinetic energy and temperature is large enough, then the de-confined state of quarks and gluons (QGP) will be

formed. The formation of parton and scattering between partons are described by several theoretical models such as color glass condensate (CGC) [28], color-string model [29] and pQCD based models [30].

- **QGP stage $(\tau_0 < \tau < \tau_f)$:** The frequent interactions among the constituents of the fireball lead to the local thermal equilibrium at τ_0. In local thermal equilibrium the system undergoes collective expansion due to the pressure gradient. In this state, the relativistic hydrodynamics can be used to describe the dynamics of the system. As the system expands and cools below the transition temperature T_c, de-confined quarks and gluons will start to convert into hadrons. This process is called *hadronization*. If the transition is first order then there will be a mixed phase of QGP and hadronic resonance gas.

- **Freeze-out stage $(\tau > \tau_f)$:** The system continues to expand and the inelastic collisions among hadrons will cease at some stage. This stage is known as *chemical freeze-out* and it is characterized by the temperature T_{ch}. The relative number of hadron species will remain same at chemical freeze-out. The hadron gas further expands and reaches a temperature T_{fo}, where the mean free path between hadrons become larger than system size and thus the elastic collisions also cease. This stage is known as thermal freeze-out or *kinetic freeze-out*.

After the kinetic freeze-out, the particles move freely towards the detectors, where we can measure their energy-momentum for the analysis of the data to make physics conclusions.

1.5   Kinematic variables in heavy-ion collisions

In relativistic heavy-ion collisions it is convenient to use kinematic variables which are invariant or take simple form under the Lorentz transformation from one frame to another frame of reference. In this section, we briefly discuss such kinematic variables used in heavy-ion collision experiments.
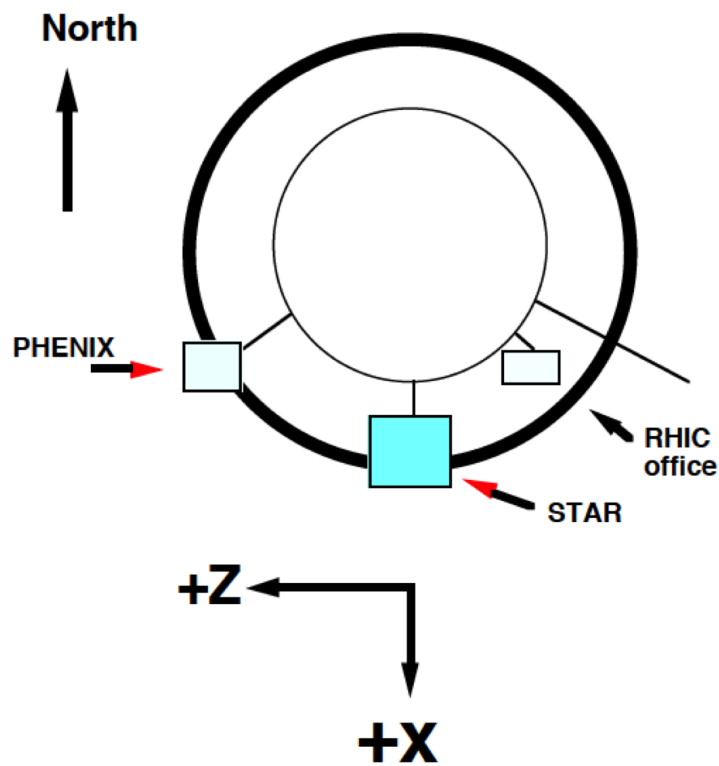
Figure 1.6: Schematic diagram of the coordinate system at RHIC.

In this thesis the analysis is done using the data from the STAR detector at the RHIC. The coordinate system at RHIC is chosen such that the z-axis is parallel to the beam direction. The STAR detector at RHIC is situated at 6'o clock direction as shown in the Fig. 1.6. The +z-axis points in the west direction and -z-axis in the east direction. The +x-axis taken towards the south and -x-axis in the north

direction. The positive and negative y-axis is taken as upwards and downwards, respectively. The position of the nominal interaction point (IP) is (x,y,z) = (0,0,0) coordinate (taken as centre of the STAR detector). The beams are focused such that the collisions between the heavy-ions take place around the IP. Although, the collisions do not always exactly happen at this point. Thus the collision point is reconstructed during the experiment, which is known as *primary vertex.*

1.5.1 Natural units

In high energy heavy-ion collisions, all the quantities are usually expressed in natural units i.e. $\hbar = c = k_B = 1$. All the basic SI units are then converted into natural units using the conversion, $\hbar c = 0.1975$ GeV fm. In natural units, length and time are expressed in GeV^{-1} and mass in GeV. The advantage of using natural units is that it can simplify the expression used in the calculation of experimental variables.

1.5.2 Center-of-mass energy

In a two body collision process, one can define a quantity, which is the square of sum of four momentum of the two incoming particles. This quantity is Lorentz invariant Mandelstam variable 's' defined as:

$$
\begin{aligned}
s &= (p_1 + p_2)^2 \\
&= (E_1 + E_2)^2 - (\vec{p_1} + \vec{p_2})^2 \\
&= (E_1 + E_2)^2 \\
\sqrt{s} &= E_1 + E_2.
\end{aligned}
\tag{1.2}
$$

Where p_1 and p_2 are the four-momenta of the colliding particles. E_1, E_2 and $\vec{p_1}$, $\vec{p_2}$ are the energy and momentum vector of the particles, respectively. In center of mass frame $\vec{p_1} = -\vec{p_2}$ and also if the mass of two colliding particles are same then $E_1 = E_2 = E$. Therefore, the center of mass energy $\sqrt{s} = E_1 + E_2 = 2E$. High energy heavy-ion collider such as RHIC accelerates gold nuclei at 100 GeV/nucleon, for which we can estimate the total center of mass energy (for a head-on collision b=0) as, 2×100 GeV $\times$ 197 nucleons $= 39.4$ TeV. This shows that the high energy heavy-ion collisions involve large amount of energy in a small volume.

1.5.3   Transverse momentum

The total momentum (p) has three components p_x, p_y and p_z. It is defined as:

$$
\begin{aligned}
p &= \sqrt{\left(p_x^2 + p_y^2 + p_z^2\right)} \\
&= \sqrt{\left(p_T^2 + p_z^2\right)} \\
p_T &= \sqrt{\left(p_x^2 + p_y^2\right)},
\end{aligned}
\tag{1.3}
$$

here p_T is known as *transverse momentum*. This is also a Lorentz invariant quantity.

1.5.4   Rapidity

In relativistic energy, we use a more appropriate variable instead of longitudinal momentum (p_z). This variable is called *rapidity*, defined as:

$$
\begin{aligned}
y &= \frac{1}{2} \ln \left(\frac{E + p_z}{E - p_z} \right) \\
&= \frac{1}{2} \ln \left(\frac{1 + p_z/E}{1 - p_z/E} \right) \\
&= \frac{1}{2} \ln \left(\frac{1 + \beta}{1 - \beta} \right),
\end{aligned}
\tag{1.4}
$$

here β is called longitudinal velocity along the z-axis direction. The rapidity variable has an advantage of being additive under a Lorentz boost. In non-relativistic limits, $p \ll m$, rapidity is equivalent to the velocity,

$$y = \frac{1}{2} \left[\ln \left(1 + \beta \right) - \ln \left(1 - \beta \right) \right] \approx \beta.$$

1.5.5 Pseudo-rapidity

In relativistic heavy-ion collisions, depending on the type of detectors used, mass of the particles cannot be measured directly in a experiment. Therefore, energy (E) of a particle cannot be measured simultaneously with the momentum (p). Hence experimentalists often use another variable known as *pseudo-rapidity*. The pseudo-rapidity (η) of a particle is defined as:

$$
\begin{aligned}
\eta &= \frac{1}{2} \ln \left(\frac{p + p_z}{p - p_z} \right) & (1.5) \\
&= \frac{1}{2} \ln \left(\frac{p + p \cos \theta}{p - p \cos \theta} \right) \\
&= -\ln \tan(\theta/2), & (1.6)
\end{aligned}
$$

where $\theta = \tan^{-1}(p_T/p_z)$, is the angle of a particle emitted with respect to the beam axis. The pseudo-rapidity variable is a Lorentz invariant quantity. Looking at the definition of η in Eq. 1.6, we can see that it only depends on the angle (θ). Thus it is convenient to use η, when details of the particle like mass, energy etc. are not known. In relativistic limits, $p \gg m$ (E $\approx$ p), pseudo-rapidity is equivalent to the rapidity,

$$\eta = \frac{1}{2} \ln \left(\frac{p + p_z}{p - p_z} \right) \approx \frac{1}{2} \ln \left(\frac{E + p_z}{E - p_z} \right) \approx y.$$

1.5.6 Azimuthal angle

In relativistic heavy-ion collisions, the most suitable coordinate system to measure particles is (p_T, ϕ, η). The azimuthal angle (ϕ) of a particle emitted in the laboratory frame is defined as,

$$\phi = \tan^{-1}\left(\frac{p_y}{p_x}\right).\tag{1.7}$$

It is the angle between the momentum vector and x-axis in the transverse plane (x-y plane) of the emitted particle.

1.5.7 Particle multiplicity

An event, in heavy-ion collisions, is the collision between two nuclei. In an event, number of particles produced is known as the *multiplicity*. Since most of the detectors used in particle tracking or identification only measure charged particles, therefore the multiplicity generally refers to the charged particle multiplicity. Details of measurement of particle multiplicity and calculation of centrality using charged particle multiplicity is given in the chapter 3.

1.5.8 Invariant differential yield

The Lorentz invariant differential yield is, $Ed^3\sigma/dp^3$. This quantity is also called invariant cross-section. In experiments, the invariant cross-section is measured using the expression,

$$E\frac{d^3\sigma}{dp^3} = \frac{1}{L_{int}}E\frac{d^3N}{dp^3},\tag{1.8}$$

where σ is the cross-section, E and L_{int} are the energy and integrated luminosity of the beam, respectively. The invariant differential yield can be decomposed in terms

of experimental quantities as,

$$
\begin{aligned}
E\frac{d^3N}{dp^3} &= E\frac{d^3N}{dp_xdp_ydp_z} \\
&= E\frac{d^3N}{p_Tdp_Td\phi dp_z} \\
&= \frac{d^3N}{p_Tdp_Td\phi dy} \\
E\frac{d^3N}{dp^3} &= \frac{d^2N}{2\pi p_Tdp_Tdy},
\end{aligned}
\tag{1.9}
$$

where we used the relations, $dp_xdp_y = p_Tdp_Td\phi$ and $dy = dp_z/E$.

1.6 Experimental probes and signatures of QGP

Relativistic heavy-ion collisions provide the unique opportunity to probe highly excited dense nuclear matter. The motivation for such studies at heavy-ion collision experiments is the observation of new form of matter, called the Quark-Gluon Plasma. However, unlike the ordinary electromagnetic plasma, there are no direct observables for the detection of the QGP. This is because it has a very short lifetime ($\sim$ few fm/c) [31]. Due to the well known property of strong interactions, color confinement, the initial state of de-confined matter turns into a final state of hadrons. In experiments, we can only detect these hadrons. Therefore a careful analysis of the observed final state is required for the evidence of formation of QGP. In this section, we briefly discuss some of the experimental probes and signatures of the formation of QGP.

1.6.1 Jet quenching

Scattering of highly energetic particles (partons in nucleons or nuclei) with large momentum transfer is called the hard scattering process. This hard scattering results in the production of high momentum quarks or gluons, which fragments into a number of highly collimated hadrons. These are known as *Jets*. The motivation for the study of jets is that hard scattering occurs in the early stage of the collisions well before the dense quark matter is expected to form. The jets will sense the complete space-time evolution of the collision and thus probe the later formed hot and dense matter. The
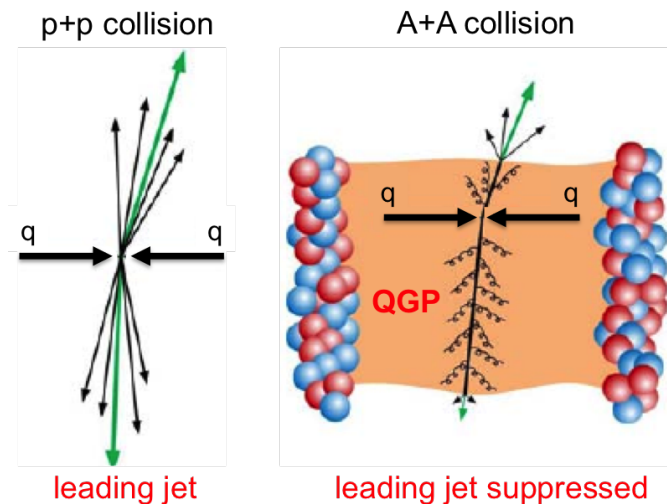
Figure 1.7: Illustration of jets formation in p+p and A+A collisions.

majority of hard processes are the two-body scatterings, which means two jets will be produced back to back (180° away from each other in azimuth) as shown in the Fig. 1.7. In high energy nucleus-nucleus collisions (e.g. Au+Au), jets can be produced near the edge of the created QGP medium. Then the one jet will be emitted away from the medium but other will have to traverse through the medium. Partons in the jet interacting with the QGP medium may lose its energy significantly before the formation of hadrons. This phenomena is known as *jet quenching*.

17

Jet quenching can be measured in heavy-ion collision experiments using the correlation between the two sufficiently high momentum hadrons. A high momentum particle is used as a trigger particle. The azimuthal distribution of particles relative to this trigger particle is measured. This type of correlation is called the di-hadron correlation. An example of this di-hadron correlation is shown in the Fig. 1.8. There is a near side peak at $\Delta\phi = 0$ from the jet. The blue points show the data from central Au+Au collisions, the red points are from the d+Au collisions and the black line is from p+p collisions. The away side peak from the other partner jet is at $\Delta\phi = \pi$ as observed for p+p and d+Au collisions. However, the away side peak is strikingly, and strongly suppressed in case of central Au+Au collisions, which is the effect of jet quenching in the highly dense medium. The observation of jet quenching in central Au+Au collisions at the RHIC has provided a clear signature for the formation of strongly interacting dense matter.
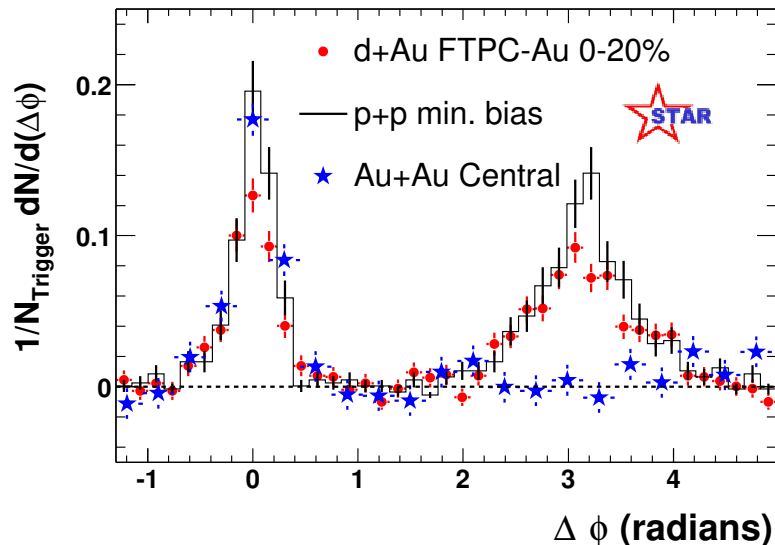
Figure 1.8: Di-hadron azimuthal correlations at high p_T for p+p, d+Au and central Au+Au collisions from STAR collaboration [14, 32].

The observable characterizing the jet suppression in A+A collisions with respect to p+p collisions is the *nuclear modification factor* (R_{AA}), defined as,

$$R_{AA} = \frac{dN_{AA}/d\eta d^2 p_T}{\langle N_{coll} \rangle dN_{pp}/d\eta d^2 p_T}. \tag{1.10}$$

Here, $\langle N_{coll} \rangle$ is the number of binary collisions, a theoretical parameter that depends on the centrality of the collisions and usually estimated using the Glauber model calculation [33]. N_{AA} and N_{pp} are the yields in A+A and p+p collisions, respectively. The R_{AA} in Eq. 1.10 represents the ratio of yields produced in A+A collisions to the p+p collisions. If the nucleus-nucleus collision is just a superposition of proton-proton collision scale with number of binary collisions, then the value of R_{AA} should be equal to the unity (i.e. $R_{AA} = 1$). A lower value of $R_{AA} < 1$ suggests the formation of highly dense and opaque medium in heavy-ion collisions.
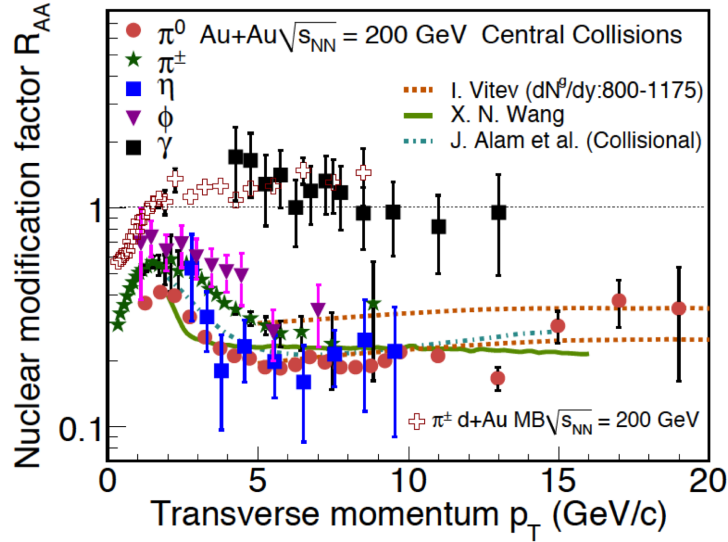
Figure 1.9: Nuclear modification factor (R_{AA}) for various mesons and photons from RHIC experiments for central Au+Au collisions at $\sqrt{s_{NN}} = 200$ GeV at mid-rapidity. R_{dAu} is also shown for charged pions for $\sqrt{s_{NN}} = 200$ GeV. The lines are theoretical calcuations. The figure is taken from Ref. [18]

Figure 1.9 displays the nuclear modification factor of various mesons and direct photons produced in Au+Au collisions at $\sqrt{s_{\mathrm{NN}}} = 200$ GeV from RHIC. A strong suppression $R_{AA} \sim 0.2$ of high-p_T mesons is observed in central Au+Au collisions. The suppression is similar for different mesons and stays nearly flat up to $p_T = 20$ GeV/c. This suppression has been attributed to energy loss of high-p_T partons and indicates the formation of dense matter in A+A collisions. The direct photons measured do not interact with the medium created via strong interactions. The direct photons have $R_{AA} \approx 1$, which is considered as a proof that the strong suppression is not an effect of initial state but is caused by the interaction of final state high momentum partons with the medium. The $R_{AA} \sim 1$ for charged pions at high-p_T in d+Au collisions at $\sqrt{s_{\mathrm{NN}}} = 200$ GeV, where the QGP medium is not expected to be form. This further consolidates the evidence for the formation of highly dense medium created in heavy-ion collisions.

1.6.2 Strangeness enhancement

Enhanced production of strange quarks in hot and dense matter created in heavy-ion collisions relative to p+p collisions is known as the *strangeness enhancement*. The enhancement of strange hadron production in relativistic heavy-ion collisions is one of the interesting signatures for the formation of QGP. This strangeness enhancement was proposed by J. Rafelski and B. Muller more than 35 years ago [34]. In nucleus-nucleus collisions, no valance strange quarks $(s, \bar{s})$ are present in the initial colliding system. If a QGP system is created in nucleus-nucleus collisions then the s and $\bar{s}$ quarks can be produced in the QGP or hadronic phase. In the QGP phase thermal s and $\bar{s}$ quarks can be produced through the gluon-gluon interactions process $g + g \rightarrow s + \bar{s}$ and quark-quark interactions process $q + \bar{q} \rightarrow s + \bar{s}$ [35]. In the hadronic phase, the hadron consist of strange particles can be formed via various reactions:

$\pi + \pi \rightarrow K + K$, $N + N \rightarrow N + \Lambda + K$ etc. The s and $\bar{s}$ quarks can coalesce to form ϕ-mesons. Production of ϕ-mesons by this process is not subjected to the OZI (Okubo-Zweig-Izuka) suppression rule [36]. Alternate ideas of the canonical suppression of strangeness in the small systems (i.e. p+p collisions) can also lead to the enhancement of strange particles [37]. The ϕ-meson ($s\bar{s}$) has zero net strangeness. This will rule out the canonical suppression scenario. Therefore, the enhancement of ϕ-meson production in heavy-ion collisions relative to p+p collisions clearly indicates the formation of a QGP medium.
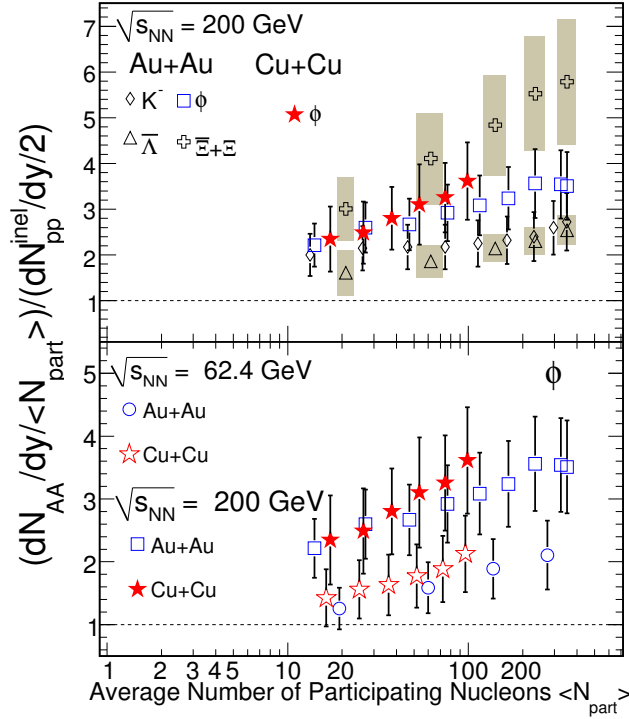
Figure 1.10: The ratio of yields of K^-, ϕ, $\bar{\Lambda}$, $\Xi + \bar{\Xi}$ normalized to $\langle N_{\text{part}} \rangle$ in nucleus-nucleus (Au+Au, Cu+Cu) collisions to corresponding yields in p+p collisions as a function of $\langle N_{\text{part}} \rangle$ at $\sqrt{s_{\text{NN}}} = 62.4$ and 200 GeV. The figure is taken from Ref. [38]

A comparison of experimental data for the yield of strange particles like $K^{\pm}$, Λ, Ξ, Ω with ϕ-meson will provide test for the strangeness enhancement. The upper panel of the Fig. 1.10 shows the ratio of yields of strange particles normalized to

$\langle N_{\mathrm{part}} \rangle$ in nucleus-nucleus collisions relative to the p+p collisions at $\sqrt{s_{\mathrm{NN}}} = 200$ GeV from RHIC. The results show the enhancement of strange particle production in nucleus-nucleus collisions relative to p+p collisions. Furthermore, the observed enhancement of ϕ-meson clearly indicates the formation of a dense partonic medium in heavy-ion collisions. Lower panel of the Fig. 1.10 shows the energy dependence of observed enhancement in ϕ-meson production, which is related to the density of medium created in heavy-ion collisions.

1.6.3 Bulk observables

The multiplicity, hadron yields, momentum spectra, correlation of hadrons emerging from heavy-ion collisions, especially in the low-p_T, where most of the hadrons are produced, reflect the properties of the bulk matter produced in relativistic heavy-ion collisions. In this section, we discuss about: (i) hadron yields at chemical freeze-out and transverse momentum spectra of different particle species averaged over the azimuthal angle at kinetic freeze-out at mid-rapidity , (ii) their azimuthal anisotropy with respect to the reaction plane. The measured particle spectra provide detailed information about the hot and dense matter at kinetic freeze-out. The transverse momentum distribution of different particles has two components, a random and a collective component. The random component is related to the temperature of the system at kinetic freeze-out. The collective component arises from the pressure gradients generated due to the interactions among the constituents of matter. This is called collective flow, which is sensitive to the strength of interactions and equation of state of the dense matter.

1.6.3.1 Hadron yield

The point in space-time at which the inelastic scatterings among particles stop and chemical abundances become fixed is referred to the chemical freeze-out. This takes place before the kinetic freeze-out, therefore more direct information about earlier stages can be obtained from the integrated yields of different hadron species.
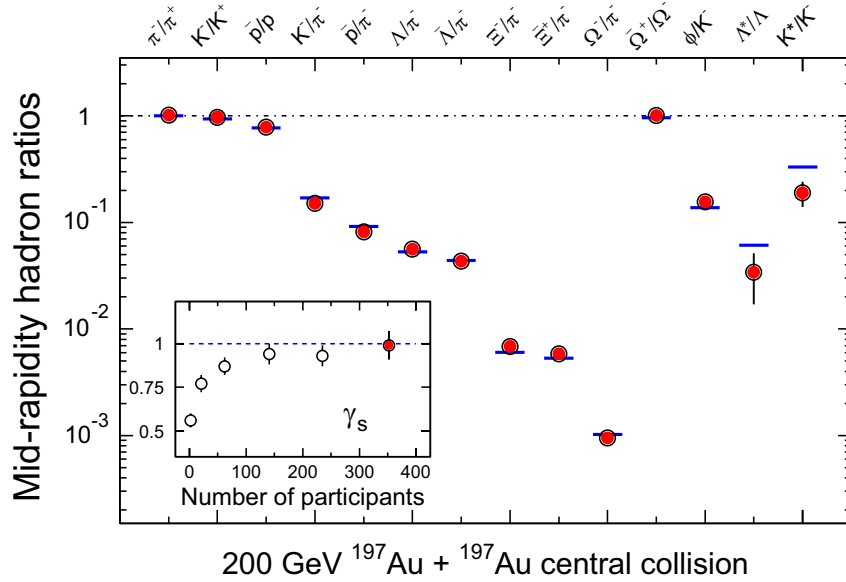
Figure 1.11: The ratios of p_T-integrated yields for different hadron species at mid-rapidity measured in STAR experiment at RHIC for central Au+Au collisions at $\sqrt{s_{NN}} = 200$ GeV. The results from statistical and thermal model fits to the measured yield ratios are represented by the horizontal bars. γ_s as a function of centrality is also shown in the inset, including the value (leftmost point) from fits to yield ratios measured by STAR for p+p collisions at 200 GeV. The figure is taken from Ref. [14]

Figure 1.11 shows the measurements of p_T-integrated hadron yield ratios for different particle species in central Au+Au collisions at $\sqrt{s_{NN}} = 200$ GeV from STAR experiment. Comparison of the results from statistical thermal model are shown by the horizontal lines [39]. These model usually assumes thermodynamic equilibrium. The model parameters are the chemical freeze-out temperature (T_{ch}), the baryon

chemical potential (μ_B) and the strangeness suppression factor (γ_S) [39]. The values of parameters obtained from fits are $T_{ch} = 163 \pm 4$ MeV, $\mu_B = 24 \pm 4$ MeV and $\gamma_s = 0.99 \pm 0.07$. Excellent agreement is observed between the data and the model for these ratios, which include stable and long-lived hadrons (like π, K, p), through multi-strange baryons (Λ, Ξ and Ω). Although significant deviations observed for the short lived resonance yields such as $\Lambda^\star$ and $K^\star$, which is possibly due to hadronic rescattering after the chemical freeze-out. The strangeness suppression factor (γ_s) as a function of centrality is shown in the inset of Fig. 1.11. It reflects the deviation from the chemical equilibrium. The value of γ_s is close to unity for central Au+Au collisions, which suggests that the chemical equilibrium has been reached in central Au+Au collisions at $\sqrt{s_{\mathrm{NN}}} = 200$ GeV.

The characteristics of the bulk matter at kinetic freeze-out can be obtained by the measurements of transverse momentum distribution of various hadron species. The measured hadron spectra is fitted by hydrodynamics motivated fits to characterize the transverse dynamics of the system [40]. The model parameters extracted from fits are kinetic freeze-out temperature (T_{fo}) for random motion and transverse radial flow velocity ($\langle \beta_T \rangle$) for collective motion.

Centrality dependence for these parameters are shown in the Fig. 1.12 for different hadron species in Au+Au collisions at $\sqrt{s_{\mathrm{NN}}} = 200$ GeV from STAR experiment. As the events become more and more central, the value of $\langle \beta_T \rangle$ increases, while the value of T_{fo} decrease for π, K and p. This suggests that the bulk of the system freeze-out at relatively lower temperature and develops a more rapid expansion for more central collisions. Although ϕ and Ω freeze-out at higher temperature and has smaller radial flow velocity compare to π, K and p in the most central collisions. This may indicate less sensitivity of ϕ and Ω to the late stage hadronic interactions after
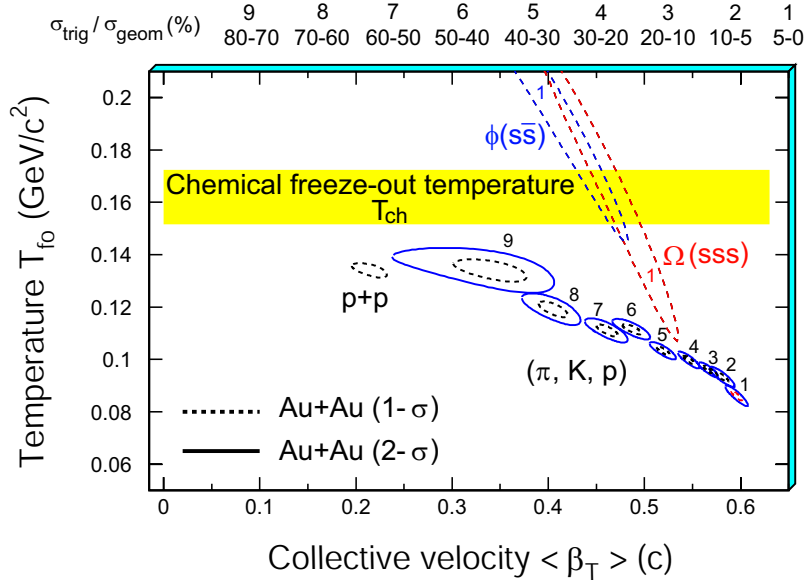
Figure 1.12: The χ^2 contours plot for the kinetic freeze-out temperature (T_{fo}) and the transverse radial flow velocity ($\langle \beta_T \rangle$), extracted from thermal+radial flow fits for the produced hadrons π, K and p and multi-strange hadrons ϕ and Ω. The numerical labels on the top of the plot indicate nine centrality bins from top 5% most central to 70-80% for Au+Au collisions at $\sqrt{s_{NN}} = 200$ GeV [15]. The results for ϕ and Ω are shown only for the most central Au+Au collisions. The dashed and solid curves represent 1σ and 2σ contours, respectively.

the chemical freeze-out [41]. Thus the multi-strange hadrons are more sensitive to the collective behavior during the early stages of the evolution of system created in heavy-ion collisions.

1.6.4 Collective phenomena

Collective phenomena refers to a common behavior shown by a group of entities, like particles moving with a common velocity in a system. Collectivity in heavy-ion collisions is a result of multi-particle correlations among the particles on the basis of their interactions. An important aim of studying the collective phenomena is to understand the macroscopic behavior of a system. In relativistic heavy-ion collisions, the initial energy density has spatial gradients due to the geometry and the position of

constituent nucleons of the colliding nuclei. Interactions among the constituents of the medium produced in relativistic heavy-ion collisions convert these spatial gradients into pressure gradients, which result in collective flow of the matter.

In non-central nucleus-nucleus collisions, the initial overlap region of the two colliding nuclei is spatially anisotropic in the transverse plane. As shown in the left panel of Fig. 1.13, the initial spatial anisotropy for Au+Au collisions at an impact parameter b = 7 fm [42]. The initial anisotropy can be characterized by the spatial eccentricity defined as:

$$\varepsilon_x = \frac{\langle y^2 - x^2 \rangle}{\langle y^2 + x^2 \rangle},$$
(1.11)

where $\langle \ \rangle$ denotes the average weighted by the energy density.

As the system expands, the spatial anisotropy will be converted into momentum anisotropy because of the pressure gradient generated due to the frequent interactions among the constituents of the medium as depicted in the right panel of Fig. 1.13. In the expansion process, the initial space anisotropy will wash out and it becomes more spherical, which means that the anisotropy only exists during the early stages of the collisions. Therefore, the azimuthal anisotropy is sensitive to the dynamics of early stages in heavy-ion collisions. Thus azimuthal anisotropy is a unique observable which can provide direct information about the very early stages of collisions where the QGP medium is formed.

1.6.4.1 Azimuthal anisotropy

In non-central nucleus-nucleus collisions, azimuthal angle (ϕ) distribution of produced particles in momentum space is anisotropic with respect to the reaction plane. This is known as *azimuthal anisotropy.* The reaction plane is the plane containing the impact parameter vector and the beam direction (z-axis). The angle between the
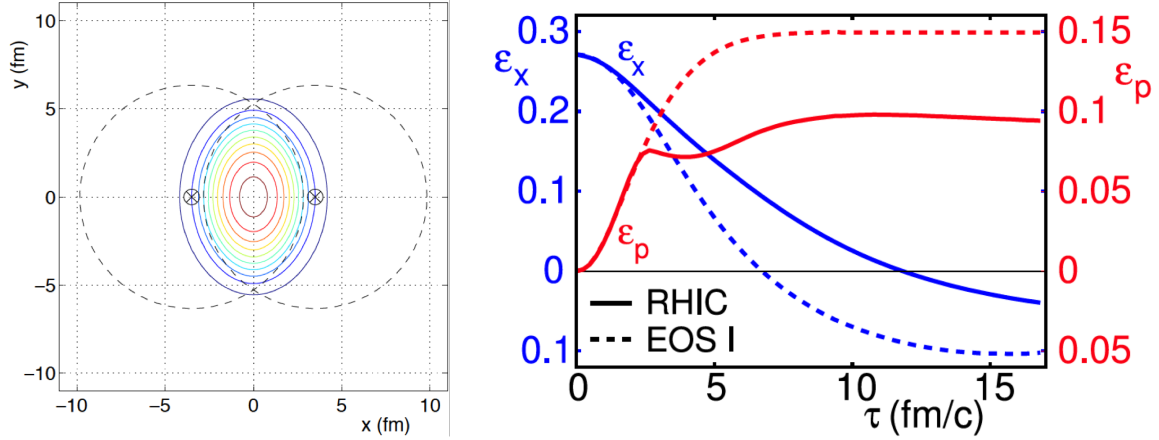
Figure 1.13: Left panel: Contours plot for density of nucleus-nucleus collisions in the transverse plane for Au+Au collision at impact parameter b = 7 fm [42]. Right panel: Conversion of initial spatial eccentricity ε_x into momentum space eccentricity ε_p with time [43].

reaction plane and the x-axis is known as *reaction plane angle*. The azimuthal angle distribution of particles produced in heavy-ion collisions can be expanded in terms of a Fourier series [44, 45].

$$E\frac{d^3N}{dp^3} = \frac{d^2N}{2\pi p_T dp_T dy}\left(1 + \sum_{n=1}^{\infty} 2v_n \cos\left[n(\phi - \Psi_r)\right]\right), \qquad (1.12)$$

where ϕ is the azimuthal angle of a particle and Ψ_r is the reaction plane angle of an event. p_T and y are transverse momentum and rapidity of a particle, respectively as defined earlier.

The coefficients v_n are known as *Fourier coefficients* for the nth order flow harmonics. They can be measured as:

$$v_n = \langle\langle\cos\left[n(\phi - \Psi_r)\right]\rangle\rangle. \qquad (1.13)$$

The angle brackets mean a double average over all particles in all events. The first order flow coefficient v_1 is called *directed flow*. The second order flow coefficient is
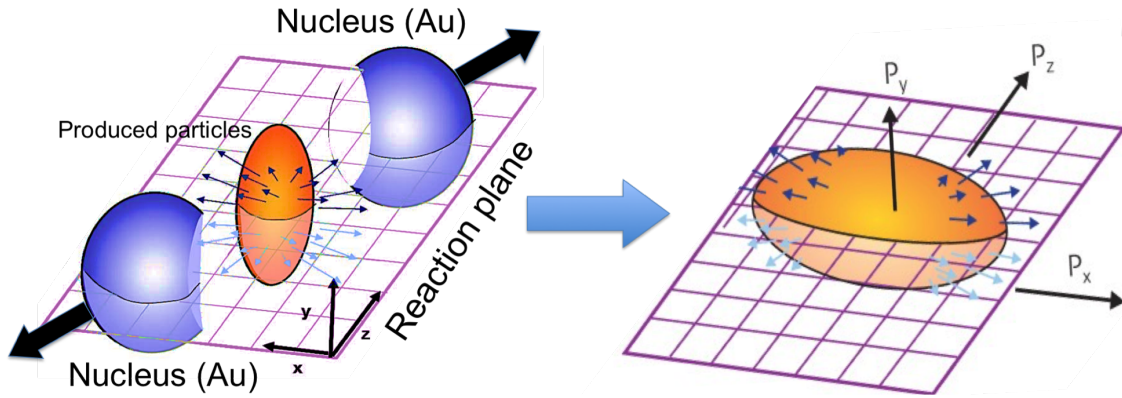
Figure 1.14: Schematic diagram of non-central nucleus-nucleus collision and subsequent conversion of initial spatial anisotropy of overlap region into momentum space anisotropy with respect to the reaction plane [46].

called *elliptic flow* v_2, which characterizes the elliptical shape of the overlap region. The third and forth order coefficients are generally called *triangular* v_3 and *quadrangular flow* v_4 and so on. The higher order flow harmonics v_n $(n > 2)$ arise due to the Event-by-Event fluctuations in the geometry of collision. A schematic diagram of the elliptic and triangular shape of collision geometry is depicted in the Fig. 1.15.
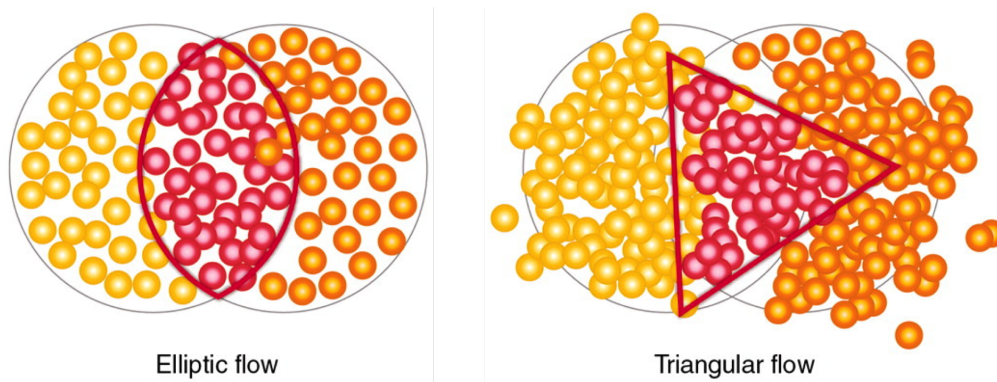
Figure 1.15: Schematic diagram of the shape of overlap region in heavy-ion collisions [47].

Elliptic flow v_2 is extensively studied at RHIC. One of the most important results at RHIC is the observation of large elliptic flow, which lead to the discovery

of formation of the strongly interacting QGP medium in relativistic heavy-ion collisions [48, 49].
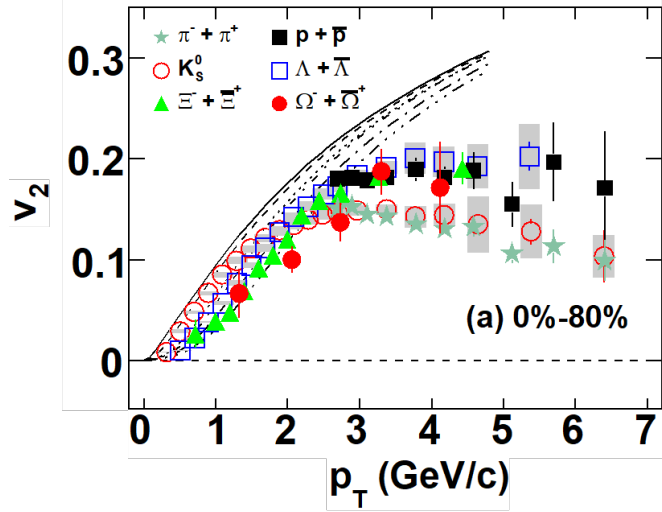
Figure 1.16: Elliptic flow v_2 as a function of p_T for identified hadrons $\pi^+ + \pi^-$, $p + \bar{p}$, K_s^0, $\Lambda + \bar{\Lambda}$, $\Xi + \bar{\Xi}$ and $\Omega + \bar{\Omega}$ in minimum bias Au+Au collisions at $\sqrt{s_{NN}} = 200$ GeV from STAR experiment at RHIC. Results from ideal hydrodynamic calculations are also shown by the lines [50]. The lines from top to bottom represent $v_2(p_T)$ for π, K, p, Λ, Ξ and Ω. The figure is from Ref. [51].

Figure 1.16 shows v_2 as a function of p_T for light quark carrying hadrons ($\pi^+ + \pi^-$, $p + \bar{p}$), strange hadrons (K_s^0, $\Lambda + \bar{\Lambda}$) and multi-strange hadrons ($\Xi + \bar{\Xi}$, $\Omega + \bar{\Omega}$) at mid-rapidity in minimum bias Au+Au collisions at $\sqrt{s_{NN}} = 200$ GeV from STAR experiment at RHIC [51]. For low p_T-region (< 2 GeV/c), the lighter hadrons have larger v_2 than heavier hadrons. This is known as mass-ordering of v_2. Such a mass-ordering is expected from the ideal hydrodynamic calculations [50]. For comparison, the results from ideal hydrodynamic model calculations are also shown by the lines. At intermediate p_T-region ($2 < p_T < 5$ GeVc), v_2 of all identified hadrons separated into two groups, baryons and mesons. Such baryon-meson difference in v_2 is consistent with the quark coalescence models [52], which suggests existence of a de-confined state of quarks and gluons. The multi-strange hadrons have small hadronic cross-section and early freeze-out time, therefore their elliptic flow should be developed in

the partonic phase of the medium. The measured sizeable v_2 for these multi-strange hadrons indicates that the partonic collectivity is indeed developed in the early stages of the collisions at RHIC [53].
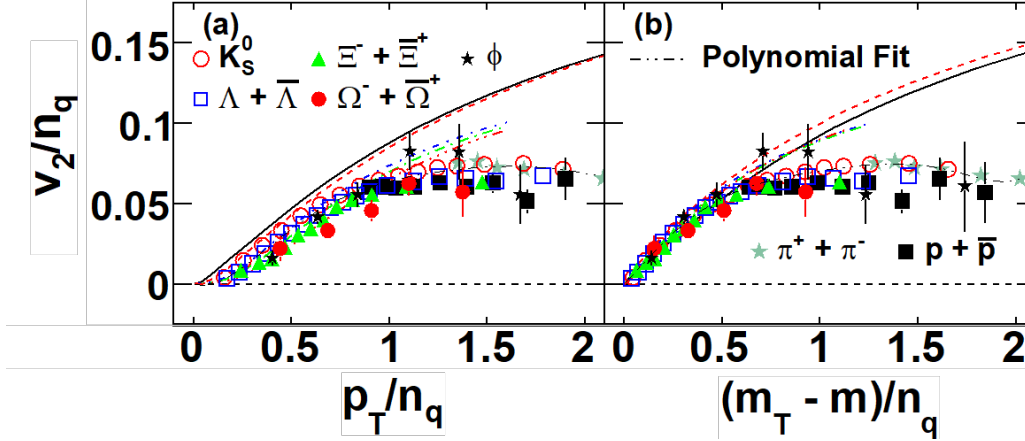
Figure 1.17: Number of constituent quark scaled v_2 (v_2/n_q) as function of p_T/n_q (left panel) and $(m_T - m)/n_q$ (right panel) for identified hadrons in minimum bias Au+Au collisions at $\sqrt{s_{NN}} = 200$ GeV from STAR experiment at RHIC. The figure is from Ref. [51].

It has been observed that when elliptic flow v_2 of identified hadrons is divided by the number of constituent quarks n_q ($= 2$ for mesons and 3 for baryons) and plotted versus $(m_T - m)/n_q$, it follows a universal curve. This scaling is known as *number of constituent quark (NCQ) scaling*. Figure 1.17 shows v_2 scaled by n_q as a function of p_T/n_q (left panel) and $(m_T - m)/n_q$ (right panel) for identified hadrons at mid-rapidity in minimum bias Au+Au collisions at $\sqrt{s_{NN}} = 200$ GeV from STAR [51]. The choice of variable $(m_T - m)/n_q$, where m is rest mass of a particle, is to remove the particle mass dependence from v_2 at low p_T. The observed scaling can be explained by the quark recombination and coalescence models [52]. These models assume that the flow is developed at quarks level before the hadronization and flow of hadrons is a result of recombination of their constituent quarks. Therefore, this NCQ scaling of elliptic flow suggests the formation of partonic medium, where quarks and gluons are the effective degrees of freedom in Au+Au collisions at 200 GeV.

1.7 Thesis motivation

In this thesis, we present measurements of elliptic flow v_2 and higher order harmonics v_3, v_4 for strange and multi-strange hadrons using experimental data of U+U collisions at center of mass energy $\sqrt{s_{\mathrm{NN}}} = 193$ GeV from STAR experiment at RHIC. We also present inclusive charged hadrons elliptic flow v_2 in Au+Au collisions data at $\sqrt{s_{\mathrm{NN}}}$ = 14.5 GeV from RHIC beam energy scan program phase-I. Study of initial state in heavy-ion collisions using the data of different simulation models of high energy heavy-ion collisions is also presented. Motivations and aims for these studies are as follows:

1.7.1 Strange and multi-strange hadrons v_n measurements in U+U collisions

Identified hadrons v_n has been extensively studied in Au+Au and Cu+Cu collisions at top RHIC energy [54,55]. Most interesting result from the previous studies is the observation of large elliptic flow, which indicates the formation of QGP medium in these collisions. In comparison to the Gold (^{197}Au) nucleus, Uranium (^{238}U) nucleus has higher mass number and it has a deformed shape. Monte Carlo simulations based studies suggest that the maximum transverse particle density achieved in U+U collisions can be increased 6-35% compared to Au+Au collisions [56–58]. Furthermore, due to the deformed shape various initial collision configurations can be possible in U+U collisions. They depend on the angles of the two incoming Uranium nuclei relative to the reaction plane. Therefore, study of azimuthal anisotropy in these interesting initial conditions will help in test the properties of the medium created in relativistic heavy-ion collisions. The data on v_n of identified hadrons in U+U colli-

sions will also provide information to test various models with different initial state effects in heavy-ion collisions.

Multi-strange hadrons such as ϕ and Ω because of their large mass and small hadronic interactions cross-section, are less sensitive to the later stage hadronic re-scattering in the medium. They are considered as clean probes for the partonic phase of the medium. In this thesis, we present the measurements of centrality and transverse momentum dependence of v_2, v_3 and v_4 coefficients for K_s^0, ϕ, $\Lambda + \bar{\Lambda}$, $\Xi + \bar{\Xi}$ and $\Omega + \bar{\Omega}$ at mid-rapidity in U+U collisions at $\sqrt{s_{NN}} = 193$ GeV at RHIC. We have also discussed partonic collectivity by testing the validity of NCQ scaling of v_n coefficients in U+U collisions. A systematic study of transverse momentum and centrality dependence of strange and multi-strange v_n is presented in chapter 3.

1.7.2 Inclusive charged hadrons and ϕ-meson v_2 measurements in Au+Au collisions

Study of elliptic flow v_2 as function of several variables like center of mass energy, centrality of collision, transverse momentum and pseudo-rapidity is found to be important as it is sensitive to the equation of state (EOS), thermalization, initial conditions and transport coefficients of the medium created in relativistic heavy-ion collisions. Inclusive charged hadrons and identified hadrons v_2 measurements have been studied previously at RHIC energies [59, 60]. A beam-energy scan program (BES) has been started at RHIC in the year 2010-11 to study the QCD phase diagram. The BES program allows to study elliptic flow at different center of mass energies from $\sqrt{s_{NN}}$ = 7.7 - 200 GeV. These energies correspond to the baryon chemical potential μ_B from 20 to 400 MeV. A non-monotonic behavior of v_2 as function of beam energy and centrality would indicate the softest point of the EOS in heavy-ion collisions [61].

In this thesis, we present inclusive charged hadrons v_2 as a function of transverse momentum (p_T), pseudo-rapidity (η) using various methods in Au+Au collisions at $\sqrt{s_{NN}} = 14.5$ GeV. This new data of BES phase-I program is taken in the year 2014. The energy $\sqrt{s_{NN}} = 14.5$ GeV lies between the 11.5 and 19.6 GeV, where hadronic and partonic interactions dominate, respectively [60]. Therefore, it is very important to measure v_2 at $\sqrt{s_{NN}} = 14.5$ GeV energy in comparison with the previous results. A systematic measurement of inclusive charged hadrons v_2 at mid-rapidity in Au+Au collisions at $\sqrt{s_{NN}} = 14.5$ GeV is presented in chapter 4.

Furthermore, the ϕ-meson is the lightest bound state of s and $\bar{s}$ quarks. Its interaction cross-section with other non-strange hadrons is small. The total cross section $\sigma(\phi N)$ estimated from ϕ-meson photo production on the proton is about $10-12$ mb [62]. Also it freezes out early compared to the light hadrons [14]. The lifetime of ϕ-meson decay is about 42 fm/c. Because of the longer lifetime, its decay daughters will re-scatter less in the later hadronic phase. Therefore, study of ϕ-meson v_2 can be used to probe the dynamics of the early stages in heavy-ion collisions. A systematic measurement of ϕ-meson v_2 at mid-rapidity in Au+Au collisions at $\sqrt{s_{NN}} = 14.5$ GeV is presented in chapter 4.

1.7.3 Study of initial states in heavy-ion collisions

Due to the deformed shape, U+U collisions have unique initial collision configurations. The elliptic flow v_2 is found to be strongly correlated with these configurations of the initial overlap region [63]. In central heavy-ion collisions the initial overlap region for spherical nuclei like Au or Pb is circular. However, in case of U+U collisions the initial overlap region can have different configuration depending on the orientation of two colliding Uranium nuclei with respect to the reaction plane. It is possible to study events which has much lower ellipticity but sufficient magnetic field for

disentanglement of chiral magnetic effect (CME) [64] from its dominant background anisotropic flow. Therefore, U+U collisions may provide a unique opportunity of study effects to these exotic initial conditions on final state observables in relativistic heavy-ion collisions.

It has not been experimentally possible so far to unambiguously select specific configurations in U+U collisions. In this thesis, we propose a new method to select specific collision configuration called Body-Tip from unbiased events in U+U collisions. We have shown that using the asymmetry in spectator neutron number in the two opposite directions, it is possible to separate the body-tip events from all possible random configurations in deformed Uranium nuclei. We present the method of selecting the body-tip events using simulation data of U+U collisions at $\sqrt{s_{\mathrm{NN}}} = 193$ GeV from AMPT model in chapter 5.

A precise knowledge of initial states is required in order to correctly describe the dynamics and evolution of the strongly interacting matter created in relativistic heavy-ion collisions. There is geometric as well as quantum event by event fluctuations in the initial states of heavy-ion collisions. The standard technique to characterize initial states of heavy-ion collisions in terms of the centrality obtained from the final state particle multiplicity averages out the various initial configurations. Thus restricts the study to only a limited range of initial conditions. In this thesis, we propose an additional binning using total spectator neutrons in an event along with the standard centrality binning. This may provide us control to probe events with rare initial conditions and give opportunity to carry out precise comparisons between theory and experiment. In chapter 6, we present the method of additional binning using total spectator neutrons in symmetric heavy-ion collisions. We have used the simulation data of Pb+Pb collisions at $\sqrt{s_{\mathrm{NN}}} = 2.76$ TeV from AMPT and HIJING models for this study.

Bibliography

[1] "Ultraviolet Behavior of Non-Abelian Gauge Theories", David J. Gross and Frank Wilczek, *Phys. Rev. Lett.*, **1973**, *30*, 1343;

"Asymptotically Free Gauge Theories. I", David J. Gross and Frank Wilczek, *Phys. Rev. D*, **1973**, *8*, 3633.

[2] "Reliable Perturbative Results for Strong Interactions?", H. D. Politzer, *Phys. Rev. Lett.*, **1973**, *30*, 1346.

[3] David Griffiths, *Introduction to elementary particles,* Wiley-VCH, 1st edition (1986).

[4] "Partial Symmetries of Weak Interactions", S. L. Glashow, *Nucl. Phys.*, **1961**, *22*, 579-588;

"Unified Field Theory in a Nutshell—Elicit Dreams of a Final Theory Series", A. Salam and J. C. Ward, *Phys. Lett.*, **1964**, *13*, 168-171;

"A Model of Leptons", S. Weinberg, *Phys. Rev. Lett.*, **1967**, *19*, 1264.

[5] "Broken symmetries, massless particles and gauge fields", P. W. Higgs, *Phys. Lett.* **1964**, *12*, 132-133;

"Broken Symmetries and the Masses of Gauge Bosons", P. W. Higgs, *Phys. Rev. Lett.*, **1964**, *13*, 508;

"Broken Symmetry and the Mass of Gauge Vector Mesons", F. Englert and R. Brout, *Phys. Rev. Lett.*, **1964**, *13*, 321.

[6] "Observation of a new particle in the search for the Standard Model Higgs boson with the ATLAS detector at the LHC", G. Aad *et al.* (ATLAS Collaboration), *Phys. Lett. B*, **2012**, *716*, 1-29;

"Observation of a new boson at a mass of 125 GeV with the CMS experiment at the LHC", W. Adam *et al.* (CMS Collaboration), *Phys. Lett. B*, **2012**, *716*, 30-61.

[7] "Review of Particle Physics", M. Tanabashi *et al.* (Particle Data Group), *Phys. Rev. D*, **2018**, *98*, 030001.

[8] "Order α_s^4 QCD Corrections to Z and τ Decays", P. A. Baikov, K. G. Chetyrkin, J. H. Kuhn, *Phys. Rev. Lett.*, **2008**, *101*, 012002.

[9] Stuart, L. Shapiro and, Saul A. Teukolsky, *Black Holes, White Dwarfs and Neutron Stars: The Physics of Compact Objects,* Willey-VCH (1983).

[10] J. Kapusta, B. Muller and J. Rafelski, *Quark-Gluon Plasma: Theoretical foundations,* Elsevier Science, 1st edition (2003).

[11] "Vacuum stability and vacuum excitation in a spin-0 field theory", T. D. Lee, G. C. Wick, *Phys. Rev. D*, **1974**, *9*, 2291.

[12] "Superdense Matter: Neutrons or Asymptotically Free Quarks?", J. C. Collins, M. J. Perry, *Phys. Rev. Lett.*, **1975**, *34*, 1353.

[13] "Quantum chromodynamics and the theory of superdense matter", E. V. Shuryak, *Phys. Rep.*, **1980**, *61*, 71-158;

"The physics of the quark-gluon plasma", L. D. McLerran, *Rev. Mod. Phys.*, **1986**, *58*, 1021.

[14] "Experimental and Theoretical Challenges in the Search for the Quark Gluon Plasma: The STAR Collaboration's Critical Assessment of the Evidence from RHIC Collisions", J. Adams *et al.* (STAR Collaboration), *Nucl. Phys. A*, **2005**, *757*, 102-183;

[15] "Systematic measurements of identified particle spectra in pp, d+Au, and Au+Au collisions at the STAR detector", B. I. Abelev *et al.* (STAR Collaboration), *Phys. Rev. C*, **2009**, *79*, 034909.

[16] "Color superconductivity in dense quark matter", M. G. Alford *et al.*, *Rev. Mod. Phys.*, **2008**, *80*, 1455.

[17] "The quest for the quark–gluon plasma", P. B. Munzinger and J. Stachel, *Nature*, **2007**, *448*, 302-309.

[18] "Exploring the quantum chromodynamics landscape with high-energy nuclear collisions", B. Mohanty, *New Journal of Physics*, **2011**, *13*, 065031.

[19] "On the critical end point of QCD", R. V. Gavai, S. Gupta, *Phys. Rev. D*, **2005**, *71*, 114014.

[20] "Confinement of quarks", K. G. Wison, *Phys. Rev. D*, **1974**, *10*, 2445.

[21] "Monte Carlo study of quantized SU(2) gauge theory", M. Creutz, *Phys. Rev. D*, **1980**, *21*, 2308.

[22] "Ab Initio Determination of Light Hadron Masses", S. Durr *et al.*, *Science*, **2008**, *322*, 1224-1227.

[23] "Lattice results on QCD thermodynamics", F. Karsch, *Nucl. Phys. A*, **2002**, *698*, 199-208.

[24] "Remarks on the chiral phase transition in chromodynamics", R. Pisarski and F. Wilczek, *Phys. Rev. D*, **1984**, *29*, 338;

"On the existence of a phase transition for QCD with three light quarks", F. R. Brown *et al.*, *Phys. Rev. Lett.*, **1990**, *65*, 2491;

"APPLICATION OF THE RENORMALIZATION GROUP TO A SECOND-ORDER QCD PHASE TRANSITION", F. Wilczek, *Int. J. Mod. Phys. A*, **1992**, *7*, 3911-3925;

"The order of the quantum chromodynamics transition predicted by the standard model of particle physics", Y. Aoki *et al.*, *Nature*,**2006**, *443*, 675-678.

[25] "The Condensed Matter Physics of QCD", K. Rajagopal and F. Wilczek, *At The Frontier of Particle Physics*, **2001**, 2061-2151.

[26] "QCD Phase Diagram and the Critical Point", M. Stephanov, *Prog. Theor. Phys. Suppl.*, **2004**, *153*, 139-156;

"Critical point of QCD at finite T and μ, lattice results for physical quark masses", Z. Fodor and S. Katz, *JHEP*, **2004**, *04*, 50;

"QCD at finite chemical potential with six time slices", R. Gavai and S. Gupta, *Phys. Rev. D*, **2008**, *78*, 114503.

[27] "Highly relativistic nucleus-nucleus collisions: The central rapidity region", J. D. Bjorken, *Phys. Rev. D*, **1983**, *27*, 140.

[28] "The Color glass condensate and small x physics: Four lectures", L. McLerran, *Lect. Notes Phys.*, **2002**, *583*, 291-334.

[29] "Dynamical evolution of the quark-gluon plasma and phenomenology", T. Matsui, *Nucl. Phys. A*, **1987**, *461*, 27-48.

[30] "A pQCD-based approach to parton production and equilibration in high-energy nuclear collisions", X. N. Wang, *Phys. Rep.*, **1997**, *280*, 287-371.

[31] "The maximum lifetime of the quark-gluon plasma", D. H. Rischke, M. Gyulassy, *Nucl. Phys. A*, **1996**, *597*, 701-726.

[32] "Evidence from d+Au Measurements for Final-State Suppression of High-p_T Hadrons in Au+Au Collisions at RHIC", J. Adams *et al.* (STAR Collaboration), *Phys. Rev. Lett.*, **2003**, *91*, 072304.

[33] "Glauber Modeling in High Energy Nuclear Collisions", M. L. Miller *et al.*, *Ann. Rev. Nucl. Part. Sci.*, **2007**, *57*, 205-243.

[34] "Strangeness Production in the Quark-Gluon Plasma", J. Rafelski and B. Muller, *Phys. Rev. Lett.*, **1982**, *48*, 1066.

[35] "Strangeness in relativistic heavy ion collisions", P. Koch, B. Muller and J. Rafelski, *Phys. Rep.*, **1986**, *142*, 167-262;

"ϕ-Meson Production as a Probe of the Quark-Gluon Plasma", A. Shor, *Phys. Rev. Lett.*, **1985**, *54*, 1122.

[36] "ϕ-meson and unitary symmetry model", S. Okubo, *Phys. Lett.*, **1963**, *5*, 165-168;

"Systematics and Phenomenology of Boson Mass Levels. III", J. Iizuka, K. Okada and O. Shito, *Prog. Theor. Phys.*, **1966**, *35*, 1061-1073.

[37] "Hadronic ratios as a function of baryon number", J. Cleymans and A. Muronga, *Phys. Lett. B*, **1997**, *388*, 5-9;

"Exact baryon, strangeness, and charge conservation in hadronic gas models", J. Cleymans, M. Marais and E. Suhonen, *Phys. Rev. C*, **1997**, *56*, 2747.

[38] "Energy and system size dependence of ϕ meson production in Cu+Cu and Au+Au collisions", B. Abelev (STAR Collaboration), *Phys. Lett. B*, **2009**, *673*, 183-191.

[39] "Thermal and hadrochemical equilibration in nucleus-nucleus collisions at the SPS", P. Braun-Munzinger *et al.*, *Phys. Lett. B*, **1996**, *365*, 1-6;

K. Huang. *Statistical Mechanics,* John Wiley and Sons, 2nd edition, 1987;

"PARTICLE PRODUCTION IN HEAVY ION COLLISIONS", P. Braun-Munzinger, K. Redlich, J. Stachel, *Quark–Gluon Plasma 3*, **2004**, 491-599.

[40] "Thermal phenomenology of hadrons from 200A GeV S+S collisions", E. Schnedermann, J. Sollfrank, and U. Heinz, *Phys. Rev. C*, **1993**, *48*, 2462.

[41] "Hadronic freeze-out following a first order hadronization phase transition in ultrarelativistic heavy-ion collisions", S. A. Bass *et al.*, *Phys. Rev. C*, **1999**, *60*, 021902;

"Probing collision dynamics at RHIC", O. Barannikova *et al.*, *arXiv*:nucl-ex/0403014 (2004);

"Multistrange Baryon Production in Au-Au Collisions at $\sqrt{s_{NN}} = 130$ GeV", J. Adams *et al.* (STAR Collaboration), *Phys. Rev. Lett.* **2004**, *92*, 182301.

[42] "Hydrodynamic description of ultrarelativistic heavy-ion collisions", P. F. Kolb and U. Heinz, *arXiv*:nucl-th/0305084 (2003).

[43] "Emission angle dependent HBT at RHIC and beyond", P. F. Kolb and U. Heinz, *Nucl. Phys. A*, **2003**, *715*, 653c-656c.

[44] "Flow Study in Relativistic Nuclear Collisions by Fourier Expansion of Azimuthal Particle Distributions", S. Voloshin and Y. Zhang, *Z. Phys. C*, **1996**, *70*, 665-672.

[45] "Methods for analyzing anisotropic flow in relativistic nuclear collisions", A. Poskanzer and S. Voloshin, *Phys. Rev. C*, **1998**, *58*, 1671.

[46] "The strongly coupled quark-gluon plasma created at RHIC", U. Heinz, *J. Phys. A*, **2009**, *42*, 214003;

[47] "The Exploration of Hot Nuclear Matter", B. V. Jacak, B. Muller, *Science*, **2012**, *337*, 310-314.

[48] "Quark–gluon plasma and color glass condensate at RHIC? The perspective from the BRAHMS experiment", I. Arsene *et al.* (BRAHMS Collaboration), *Nucl. Phys. A*, **2005**, *757*, 1-27;

"The PHOBOS perspective on discoveries at RHIC", B. Back *et al.* (PHOBOS Collaboration), *Nucl. Phys. A*, **2005**, *757*, 28-101;

"Experimental and theoretical challenges in the search for the quark–gluon plasma: The STAR Collaboration's critical assessment of the evidence from RHIC collisions", J. Adams *et al.* (STAR Collaboration), *Nucl. Phys. A*, **2005**, *757*, 102-183;

"Formation of dense partonic matter in relativistic nucleus–nucleus collisions at RHIC: Experimental evaluation by the PHENIX Collaboration", K. Adcox *et al.* (PHENIX Collaboration), *Nucl. Phys. A*, **2005**, *757*, 184-283.

[49] "New forms of QCD matter discovered at RHIC", M. Gyulassy and L. McLerran, *Nucl. Phys. A*, **2005**, *750*, 30-63.

[50] "Hydrodynamic Models for Heavy Ion Collisions", P. Huovinen and P. Ruuskanen, *Ann. Rev. Nucl. Part. Sci.*, **2006**, *56*, 163-206.

[51] "Centrality dependence of charged hadron and strange hadron elliptic flow from $\sqrt{s_{NN}} = 200$ GeV Au+Au collisions", B. Abelev *et al.* (STAR Collaboration), *Phys. Rev. C*, **2008**, *77*, 54901.

[52] "Elliptic Flow at Large Transverse Momenta from Quark Coalescence", D. Molnar and S. Voloshin, *Phys. Rev. Lett.*, **2003**, *91*, 092301;

"Hadron production in heavy ion collisions: Fragmentation and recombination from a dense parton phase", R. Fries *et al.*, *Phys. Rev. C*, **2003**, *68*, 044902;

"Parton Coalescence and the Antiproton/Pion Anomaly at RHIC", V. Greco, C. M. Ko and P. Levai, *Phys. Rev. Lett.*, **2003**, *90*, 202302.

[53] "Multistrange Baryon Production in Au-Au Collisions at $\sqrt{s_{NN}} = 130$ GeV", J. Adams *et al.* (STAR Collaboration), *Phys. Rev. Lett.*, **2004**, *92*, 182301.

"Multistrange Baryon Elliptic Flow in Au+Au Collisions at $\sqrt{s_{NN}} = 200$ GeV", J. Adams *et al.* (STAR Collaboration), *Phys. Rev. Lett.*, **2005**, *95*, 122301.

[54] "Centrality dependence of charged hadron and strange hadron elliptic flow from $\sqrt{s_{NN}} = 200$ GeV Au+Au collisions", B. Abelev *et al.* (STAR Collaboration), *Phys. Rev. C*, **2008**, *77*, 054901;

"Centrality and Transverse Momentum Dependence of Elliptic Flow of Multistrange Hadrons and ϕ Meson in Au+Au Collisions at $\sqrt{s_{NN}} = 200$ GeV", L. Adamczyk *et al.* (STAR Collaboration), *Phys. Rev. Lett.*, **2016**, *116*, 062301.

[55] "Charged and strange hadron elliptic flow in Cu+Cu collisions at $\sqrt{s_{NN}} = 62.4$ and 200 GeV", B. Abelev *et al.* (STAR Collaboration), *Phys. Rev. C*, **2010**, *81*, 044902.

[56] "Anisotropic Flow and Jet Quenching in Ultrarelativistic U+U Collisions", U. Heniz and A. Kuhlman, *Phys. Rev. Lett.*, **2005**, *94*, 132301;

"Multiplicity distribution and source deformation in full-overlap U+U collisions", A. Kuhlman and U. Heniz, *Phys. Rev. C*, **2005**, *72*, 037901.

[57] "Elliptic flow in U+U collisions at $\sqrt{s_{\mathrm{NN}}} = 200$ GeV and in Pb+Pb collisions at $\sqrt{s_{\mathrm{NN}}} = 2.76$ TeV: Prediction from a hybrid approach", T. Hirano, P. Huovinen and Y. Nara, *Phys. Rev. C*, **2011**, *83*, 021902(R).

[58] "Selection of special orientations in relativistic collisions of deformed heavy nuclei", C. Nepali, G. Fai and D. Keane, *Phys. Rev. C*, **2007**, *76*, 051902(R);

"Advantage of U+U over Au+Au collisions at constant beam energy", C. Nepali, G. Fai and D. Keane, *Phys. Rev. C*, **2006**, *73*, 034911.

[59] "Inclusive charged hadron elliptic flow in Au+Au collisions at $\sqrt{s_{\mathrm{NN}}} = 7.7-39$ GeV", L. Adamczyk *et al.* (STAR Collaboration), *Phys. Rev. C*, **2012**, *86*, 054908.

[60] "Elliptic flow of identified hadrons in Au+Au collisions at $\sqrt{s_{\mathrm{NN}}} = 7.7-62.4$ GeV", L. Adamczyk *et al.* (STAR Collaboration), *Phys. Rev. C*, **2013**, *88*, 014902;

"Observation of an Energy-Dependent Difference in Elliptic Flow between Particles and Antiparticles in Relativistic Heavy Ion Collisions", L. Adamczyk *et al.* (STAR Collaboration), *Phys. Rev. Lett.*, **2013**, *110*, 142301;

"Centrality dependence of identified particle elliptic flow in relativistic heavy ion collisions at $\sqrt{s_{\mathrm{NN}}} = 7.7-62.4$ GeV", L. Adamczyk *et al.* (STAR Collaboration), *Phys. Rev. C*, **2016**, *93*, 014907.

[61] "Highly Sensitive Centrality Dependence of Elliptic Flow: A Novel Signature of the Phase Transition in QCD", H. Sorge, *Phys. Rev. Lett.*, **1999**, *82*, 2048.

[62] "ϕ-meson photoproduction from nuclei", A. Sibirtsev *et al.*, *Eur. Phys. J. A*, **2006**, *29*, 209-220.

[63] "Multiplicity, average transverse momentum, and azimuthal anisotropy in U+U collisions at $\sqrt{s_{\mathrm{NN}}} = 200$ GeV using a multiphase transport model", Md. R. Haque, Z. W. Lin and B. Mohanty, *Phys. Rev. C*, **2012**, *85*, 034905.

[64] "Parity violation in hot QCD: why it can happen, and how to look for it", D. Kharzeev, *Phys. Lett. B*, **2006**, *633*, 260-264;

"Charge separation induced by P-odd bubbles in QCD matter", D. Kharzeev and A. Zhitnitsky, *Nucl. Phys. A*, **2007**, *797*, 67-79;

"The effects of topological charge change in heavy ion collisions: "Event by event P and CP violation"", D. Kharzeev *et al.*, *Nucl. Phys. A*, **2008**, *803*, 227-253.

Chapter 2

Experimental System at RHIC

2.1 Introduction

This chapter briefly describes the experimental system used for this analysis. The main focus is on the detectors which were primarily used to record the data on which the analysis and physics results of this thesis are based.

Theoretical work on the exploration of hot and dense matter initiated the idea of heavy-ion collisions at relativistic energies. The possibility of formation and study of a new state of matter, the QGP motivated experiments with higher beam energies of heavy-ions. In the year 2000, RHIC at BNL became the first collider experiment in the world, capable of colliding heavy-ions at relativistic energies. The top energy at RHIC is 100 GeV per nucleon for Au beams and 250 GeV for proton beams. It can also accelerate various nuclei such as deuteron, helium, copper, gold and uranium at center of mass energies ranging from $\sqrt{s_{NN}} = 7.7$-200 GeV. It can also provide data for the spin-polarized protons up to $\sqrt{s_{NN}} = 500$ GeV [1, 2].

2.2   Relativistic Heavy-Ion Collider Complex
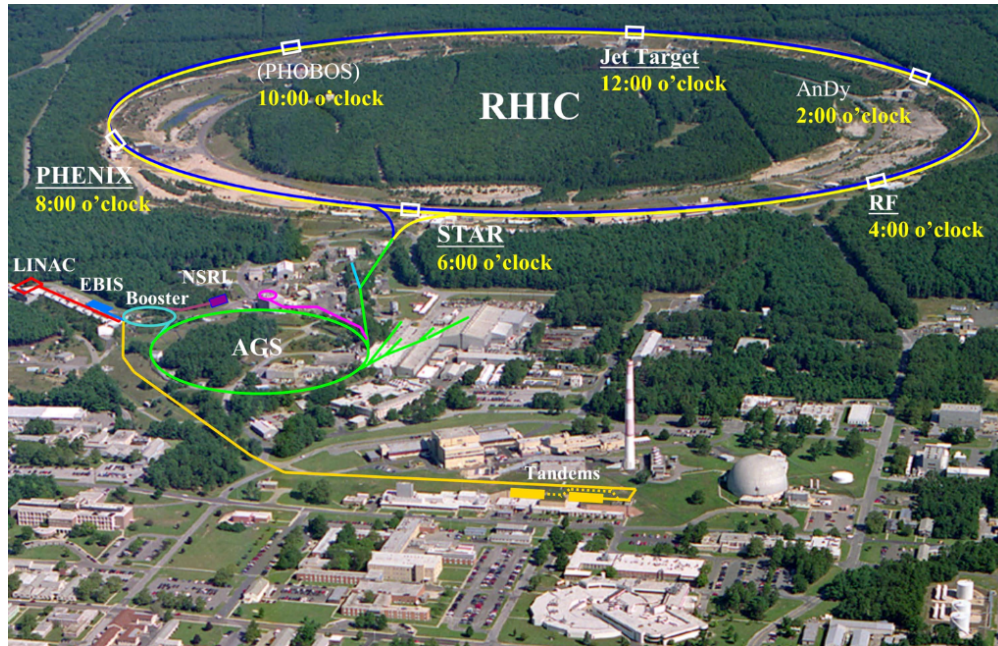
Figure 2.1: Aerial view of the RHIC accelerator complex at Brookhaven National Laboratory, Upton, New York [3].

Figure 2.1 shows a layout of RHIC facility. A brief description of the collider described in Ref. [4] is as follows. The collider consists of two superconducting rings of about 3.834 km circumference. The rings intersect each other at six different locations. The six crossing points are arranged as on a clock. The two major experiments are PHENIX [5] and STAR [6], of which PHENIX is no longer running and two minor experiments PHOBOS [7] and BRAHMS [8] have also completed data taking. The LINAC is the injector for polarized protons into the three accelerators chain (Booster/AGS/RHIC). For heavy-ion collision, negatively charged gold ions from the pulsed sputter ion source at the Tandem Van de Graaff (100 μA, 700 μs) are passed through a carbon stripping foil to partially strip off their electrons. Then the ions are accelerated to an energy of 1 MeV per nucleon by the second stage of the Tandem [9].

After further stripping at the exit of the Tandem, beam of Au ions with +32 charge state are transferred to the Booster Synchrotron. In the year 2012, the Tandem Van De Graaff accelerators were replaced with the Electron Beam Ion Source (EBIS) along with two small linear accelerators. They can be more easily operated and maintained, and have the ability to accelerate more ion species, such as Uranium. The booster provides more energy to the ions by radio frequency electromagnetic waves and accelerates to 95 MeV per nucleon. Ions are stripped off electrons again to reach the charge state of Au^{+77} at the exit from the booster. The Au^{+77} ions are injected into a larger synchrotron, with four-time the radius of the booster, known as the Alternating Gradient Synchrotron (AGS) via the Booster-to-AGS line.

Au ions, in the 24 bunches are injected into the AGS for the acceleration up to a energy of 10.8 GeV per nucleon. Inside the AGS, the Au ions are de-bunched and re-bunched and finally four bunches are ejected. At the exit from the AGS, Au ions are fully stripped off electrons to the charge of state of +79 and transferred to RHIC through the AGS-to-RHIC Beam Transfer Line. A total of up to 111 bunches are injected into each collider ring in bunch-to-bucket fashion. A switching magnet directs the ion bunches to one of two rings of RHIC. The ring in which ions travel in a clockwise direction is named "Blue Ring" and in anti-clockwise direction is named "Yellow Ring". These independent rings have their sets of superconducting magnets which bend and focus the ions [10]. Acceleration and storage of beam bunches at RHIC is done using two Radio Frequency (RF) cavities. One of which operates at 28 MHz and the other at 197 MHz frequency. The ion beams are accelerated to the desired collision energy (100 GeV per nucleon for Au+Au collisions) inside the RHIC rings and stored for collisions and subsequent data taking. The two beams collide at interaction points (IPs), till the luminosity drops below a certain level, then the beams are removed from the rings (dumped).

Table 2.1: RHIC design and achieved performance parameters at top RHIC energy [11].

Mode	Energy (GeV/u)	Year	No. of bunches	Ions/bunch (10^9)	L_{peak} $(cm^{-2}s^{-1})$	L_{avg} $(cm^{-2}s^{-1})$
			Design values			
Au + Au	200	2000	56	1.0	9×10^{26}	2×10^{26}
p + p	500	2000	56	100	5×10^{30}	4×10^{30}
			Achieved values			
U + U	193	2012	111	0.3	8.8×10^{26}	5.6×10^{26}
Au + Au	200	2017	111	2.0	155×10^{26}	87×10^{26}
p + p	500	2017	111	110	13×10^{30}	10×10^{30}

The RHIC performance design parameters along with the achieved values are listed in the table 2.1. The top RHIC energy is 100 GeV/u for $^{197}_{79}$Au ions. The number depends on the charge over mass ratio of the ions. Therefore, the top energy of proton beams is 250 GeV/u and 96.5 GeV/u for heavier ion beams $(^{238}_{92}$U$)$. The interaction rate $R = L \times \sigma$, between the two colliding beams depend on Luminosity (L) and cross section (σ). If there are n bunches in each beam with number of particles per bunch in two beams are N_A and N_B, revolving in the collider at a frequency f, then the luminosity is given by [12],

$$L \;=\; f \times \frac{n N_A N_B}{A}. \tag{2.1}$$

Where A is cross-sectional area of overlap between the two colliding beams. The designed value of average luminosity was 2×10^{26} cm^{-2}s^{-1}. The luminosity is substantially increased through stochastic electron cooling.

There are six interaction points along the RHIC ring. Four of these have been occupied by heavy-ion experiments:

- Broad RAnge Hadron Magnetic Spectrometer (BRAHMS), located at 2 o'clock

position.

- Solenoidal Tracker At RHIC (STAR), located at 6 o′clock position.

- Pioneering High Energy Nuclear Interaction eXperiment (PHENIX), located at 8 o′clock position.

- PHOBOS (named after a moon of Mars), located at 10 o′clock position.

BRAMHS and PHOBOS detector completed their datataking in June 2005 and 2006, respectively. PHENIX detector completed its data taking in June 2016. Currently only STAR detector is in operational mode.

2.3 The STAR experiment at RHIC

STAR (Solenoidal Tracker At RHIC) detector is one of the two large experiments at RHIC. It is specialized in tracking thousands of particles produced by each heavy-ion collision. It is optimized for measurements of hadrons at mid-rapidity with full azimuthal angle coverage so that individual event can be characterized. These capabilities of STAR detector is used to search for the signatures of the QGP.

A layout of STAR detector system is displayed in the Fig. 2.2. All the results presented in this thesis are based on the data collected using the STAR detector. STAR consists of several types of detector subsystems. These detector work together for taking data and subsequent physics analysis to draw conclusion about the collision. Most of the detectors of STAR experiment are inside a large solenoidal magnet [13]. The STAR magnet can be maintained at the magnitude of 0.25 Tesla (half field mode) and 0.5 Tesla (full field mode). The magnetic field direction is parallel to the z direction, which bends the trajectories of charged particles allowing measurement of the corresponding momenta. The beam pipe is made up of Beryllium material [14].

The Time Projection Chamber (TPC) [15] is the heart of the STAR detector system, which provides the charged particle tracking and particle identification at mid-rapidity ($|\eta| < 1.8$) with full azimuthal coverage ($\Delta\phi = 2\pi$) in x-y plane. Outside the TPC is the barrel Time-of-Flight (TOF) [16] detector to extend the particle identification ability of STAR detector. The TOF detector, fully installed in 2010, is within rapidity region of $|\eta| < 0.9$ with 2π azimuthal angle coverage.
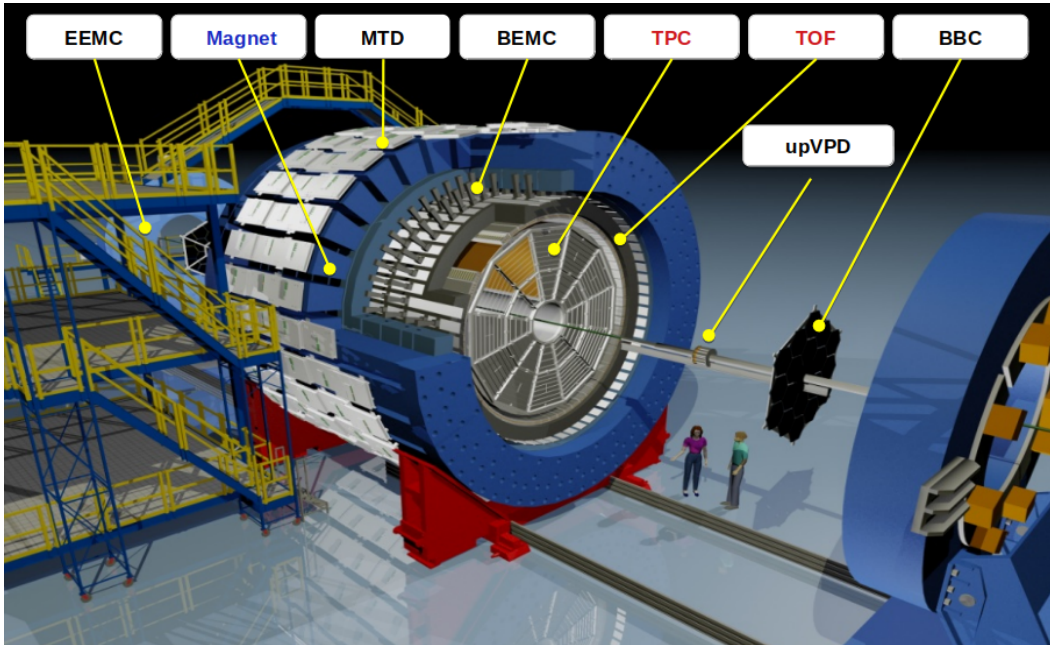
Figure 2.2: A three dimensional layout of STAR detector system. Figure is taken from [17].

The STAR calorimeter system consists of a Barrel Electromagnetic Calorimeter (BEMC) and Barrel Shower Maximum Detector (BSMD) [18], which covers $|\eta| < 1$ and an Endcap Electromagnetic Calorimeter (EEMC) [19] at west side, covering rapidity region of $1 \leq \eta \leq 2$. Both the calorimeter detectors have full azimuthal coverage. Within the acceptance, they add capabilities to measure high p_T photons, electrons, and electromagnetically decaying hadrons (π^0, η) to the STAR detector system. They also enhance the triggering process of STAR for high-p_T particles and jets. The STAR detector system also includes the Beam-Beam Counters (BBC) [20],

the two Zero Degree Calorimeters (ZDC) [21], the two Vertex Position Detectors (VPD) [22] for the purpose of event triggering and beam monitoring. The BBC is a pair of scintillator annuli located on both east and west side at a distance of 3.75 meters from the center of STAR system. The BBC trigger defines a minimum bias trigger for the event. A pair of ZDC very close ($\theta \leq 2$ mrad) to the beam pipe located 18 meters from the center of the STAR. The RHIC ZDCs are hadron calorimeters, used to measure total energy of spectator neutrons emitted along the beam directions. The two VPDs are part of a TOF system located on both sides at 5.6 meters from the center of STAR. These very fast detectors serve as trigger detectors. They also provide the start time of collision for the calculation of time of flight for particle identification.

The work presented in this thesis is mainly based on the TPC, TOF and Trigger detectors. The details of these detector sub-systems are discussed in the following sub-sections. We also propose in this thesis a method of using spectator neutron measurements in the ZDCs to select certain collision configurations in U+U collisions.

2.3.1 Time Projection Chamber (TPC)

At RHIC, a large number of charged particles are produced in each collision. A central Au+Au collision at $\sqrt{s_{\mathrm{NN}}} = 200$ GeV produces close to 1000 primary particles along with their secondary particles per unit of pseudo-rapidity. These primary and secondary particles are tracked and identified by the TPC detector at STAR. It records the tracks of charged particles, measures their momenta, and identifies the particles through measurement of their ionization energy loss (dE/dx) [15]. It can identify charged particles of momentum from 100 MeV/c to greater than 1 GeV/c. It can also measure their momenta from 100 MeV/c to 30 GeV/c.

2.3.1.1 Design of TPC

TPC is a gas detector system [15]. Figure 2.3 shows the schematic diagram of the TPC. It is a cylinder of length 4.2 m and 4 m external diameter. The TPC consists of a thin conductive Central Membrane (CM), two concentric field-cages and two end caps. The central membrane is made of 70 μm thick carbon coated kapton located at center of TPC in the xy plane. It divides the TPC cylinder into two equal parts, east and west end of the TPC as shown in the Fig. 2.3. The CM is maintained at -28 kV potential with respect to the ground and acts as cathode.
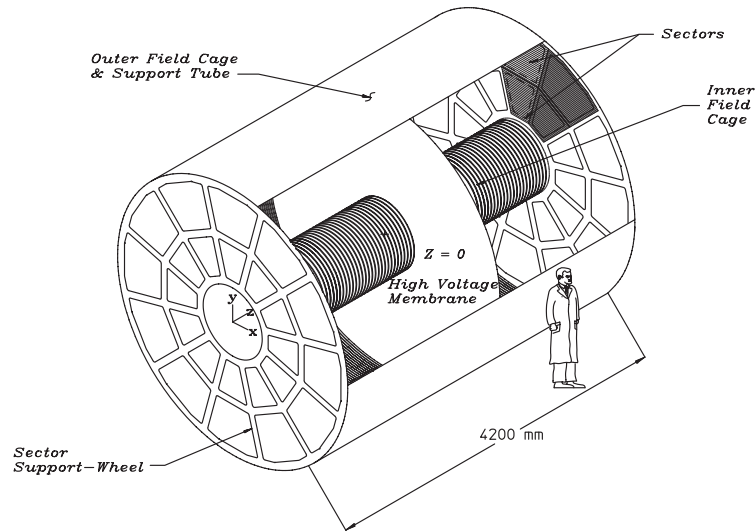
Figure 2.3: The technical layout of the TPC detector at STAR [15].

The field cage cylinders prevent gas contamination from the outside air. It also provides nearly perfect electric field for electrons to drift, which avoids the distortions of the recorded tracks from multiple Coulomb scattering. A uniform electric field of ~135 V/cm, along the $\pm z$ direction is maintained between the CM, concentric field-cage rings, and the readout end caps. The end caps providing the readout system are at ground potential and act as anodes.

The readout system is based on Multi-Wire Proportional Chambers (MWPC). The 12 readout pads or modules on each readout plane are arranged in a circle as on a clock. Each sector is divided into inner and outer sub-sectors. Inner sectors contain small pads arranged in 13 widely spaced pad rows to maximize the position and track resolution for high particle density close to the interaction region. Outer sectors are densely packed in 32 pad rows to optimize the dE/dx in a region of lower particle density. A track in TPC can have maximum 45 hits if it crosses all the 45 pad rows. A full sector of TPC is shown in the Fig. 2.4. The TPC is filled with a mixture of Argon
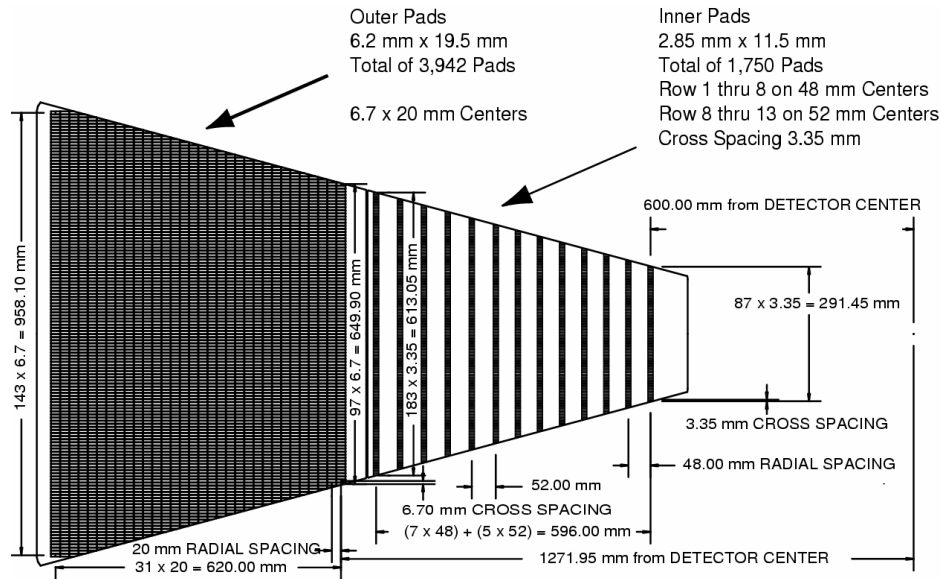
Figure 2.4: The layout one TPC sector in anode plane. the inner sub-sector on the right and outer sub-sector on the left are also shown with their respective padrows [15].

(Ar) and Methane (CH$_4$) gas in the ratio 90:10 (P10 gas) and regulated at 2 mbar above the atmospheric pressure. The P10 gas has fast drift velocity which peaks at a low electric field. Operating on the peak of velocity makes the drift velocity stable and insensitive to small variations in temperature and pressure. Design of the detector becomes simpler because of lower field strengths which require lower voltages. The drift velocity of electron through P10 gas is $\sim$5.5 cm/μs at 130 V/cm drift field [15].

2.3.1.2 Track reconstruction

The tracks of primary particles are reconstructed by identifying the 3D-space coordinates (x, y, z). A charged particle ionizes the gas atoms and molecules along its path when passing through the TPC gas volume. The electrons from ionization drift towards the anode due to the strong electric field from the central membrane. The uniform magnetic field of the STAR magnet constrains the path of electrons in a straight line. The x, y positions of a ionization cluster are determined by the charged measured on adjacent pads along the single pad row. The z-position is determined by the time of drift measured from the point of origin to the anodes on the endcaps times the average drift velocity.

After getting positions of the cluster, a tracking algorithm is used to reconstruct the tracks. This algorithm first associates space points to form tracks and then fit the points to get the information like momentum of the particle. Each track in the track model is a helix to first order, but second order effects can also be present because of energy loss in the gas and multiple Coulomb scattering. The track information from the TPC together with the additional tracking information from the other inner detectors are then used to refit by the Kalman Fit Method [23]. The primary collision vertex is determined by extrapolating the reconstructed tracks back to the origin. The global average is the primary vertex position. If a reconstructed global track has a distance of closet approach (DCA) to the primary vertex less than 3 cm, then the track is refitted with primary vertex position as an additional space point. These tracks are known as primary tracks. The track reconstruction efficiency depends on the acceptance of the detector, track multiplicity, particle type and track quality cuts.

2.3.1.3 Particle identification

Charge particles traversing through the TPC gas volume loose their energy due to interactions. This ionization energy loss (dE/dx) can be used to identifiy charge particles in the TPC. The dE/dx of particle is extracted from a maximum of 45 pad rows. However, the length over which energy loss is measured is too short and due to large ionization fluctuations, the most probable dE/dx value is used instead of average dE/dx. This is done by removing 30% clusters having largest signal and calculating truncated mean of the 70% of the clusters. This is known as truncated mean method for most probable dE/dx value. The ionization energy loss depends on the mass of the charge particles, specially in the low momentum, although becomes less mass-dependent as its velocity increases. The dE/dx can be well described by the Bichsel functions [24], which is an improved version of the Bethe-Bloch formula [25].
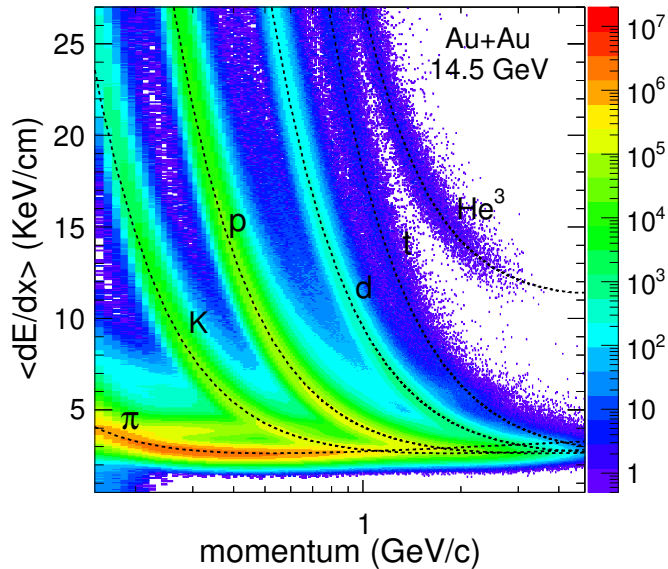
Figure 2.5: The energy loss as a function of momentum for charged particles in the TPC from Au+Au collisions at STAR.

Figure 2.5 shows the dE/dx for charge particles as a function of momentum in the TPC. The bands represent measured energy loss for the Au+Au collision data

from the STAR TPC. The solid black lines represent the theoretical predictions from Bichsel functions for various charge particles. The TPC dE/dx resolution is about $6-9\%$. Pions and kaons can be separated up to a transverse momentum of about 0.75 GeV/c, while protons can be identified up to 1.1 GeV/c using the TPC detector at STAR. Details of analysis technique for particle identification is explained in chapter 3.

2.3.2 Time of Flight Detector (TOF)

A Time-of-Flight (TOF) [16] system at STAR experiment is added to extend the particle identification capabilities at high transverse momentum (>1.0 GeV/c). The TOF system is consists of two detector sub-systems. One is VPD (the "start" detector) and the other is TOF tray (the "stop" detector). It covers a pseudo-rapidity region of $|\eta| < 0.9$ and full azimuthal coverage ($\Delta\phi = 2\pi$). Figure 2.6 shows the TOF system at STAR.
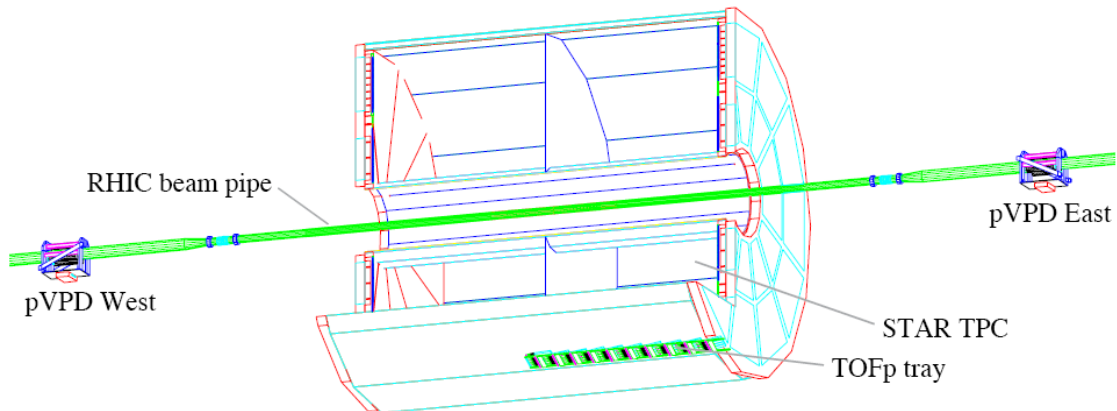
Figure 2.6: A cut view of TOF detector system showing positions of VPDs and TOF trays relative to the STAR TPC and RHIC beam pipe [22].

The TOF detector consists of 120 highly segmented trays surrounding the TPC, 60 on east side and 60 on west side of the interaction point ($z = 0$). Each tray covers

6 degree in azimuth direction around the TPC. The dimension of each individual tray is 2.4 m long, 21.3 cm wide and 8.5 cm deep. There are 32 Multi-gap Resistive Plate Chamber (MRPC) modules in each tray, placed along beam (z) direction. Each module has dimensions 94 mm × 212 mm × 12 mm and the active area of 61 mm × 200 mm. The MRPC is basically a stack of resistive plates arranged in parallel. The intermediate plates create a series of gas gaps. Electrodes are applied to the outer surfaces of the two outer plates. A strong electric field is generated in each sub-gap by applying a high voltage across these external electrode. A charged particle going through the chamber generates avalanches in the gas gaps. Since plates are resistive they are transparent to signal induced by avalanches, thus a signal induced in the pickup pad is the sum of signals from all the gas gaps. The electrodes are made of graphite tape with a surface resistivity of 400 kΩ/square which covers the entire active area. The outer and inner glass plates are 1.8 and 0.55 mm thick, respectively. They are kept parallel by using 220 μm diameter nylon fishing-line. The signal is read out with a 1 × 6 array of copper pickup pads, each pad with an area of 63 mm × 31.5 mm, and the distance between pads is 3 mm. The pickup pad layers are separated from the outer electrodes by 0.35 mm of Mylar.

The charged particles produced in heavy-ion collisions can be identified directly by the time of flight from TOF system along with their corresponding momentum (p) from the TPC detector. The VPDs provide the common start time of the event. The stop time is provided by the TOF trays. The difference between these two is the time of flight (Δt). The total time resolution of TOF is about 100 ps. Now using the measured time of flight from TOF, and path length of the track (s) from TPC, velocity (β) of the particle can be calculated. Then using the corresponding momentum (p) and the velocity, mass of the particle can also be calculated using Eq. 2.2.

$$\beta = \frac{s}{c\Delta t}$$

$$\gamma = \frac{1}{\sqrt{1-\beta^2}}$$

$$m = \frac{p}{\gamma\beta c}, \tag{2.2}$$

where s is the path length of the track and c is the velocity of light. Figure 2.7 shows the $1/\beta$ and m^2 as a function of momentum in Au+Au collisions at mid-rapidity for few particle species. Using the information from TOF, π, K and p can be separated in the momentum range $\sim$0.3 GeV/c to 1.7 GeV/c and K, p for $\sim$0.3 GeV/c to 3.0 GeV/c.
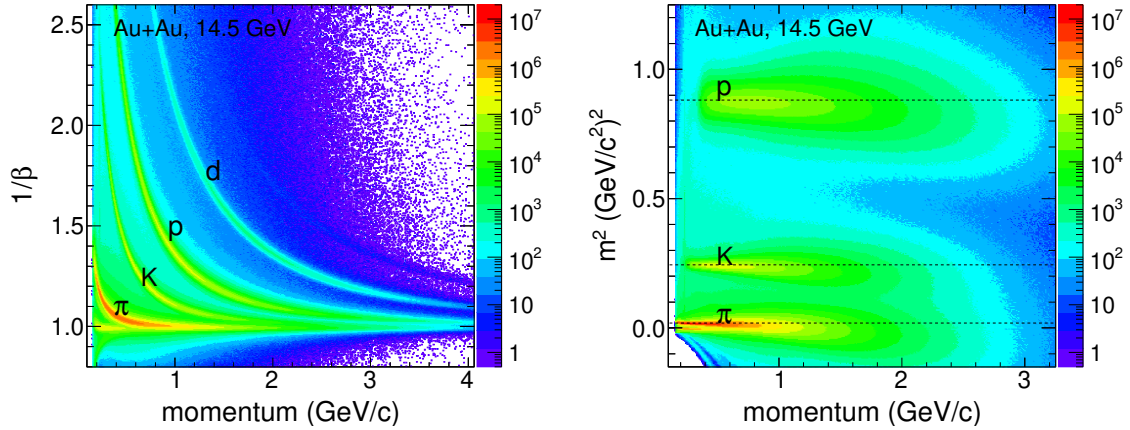
Figure 2.7: $1/\beta$ (left panel) and m^2 (right panel) as a function of momentum in Au+Au collisions at $\sqrt{s_{\mathrm{NN}}} = 14.5$ GeV.

2.3.3 Trigger system

The colliding beams at RHIC are in form of bunches with the bunch crossing rate of 9.37 MHz. The STAR trigger is a multi-level pipelined system that examines every

bunch crossing (every 107 ns) at STAR [26]. The trigger system analyzes data from fast trigger detectors and decide whether to accept a event for recording or not. When an event of interest is detected the trigger initiates the STAR data acquisition system (DAQ) for storing [27] .

Currently, there are three types of detectors used by the STAR trigger system. First type is the vertex detectors used to locate the primary vertex position, measure multiplicity of the collision, for event plane and polarization of the colliding beams. This set consists of ZDC [21], BBC [20] and VPD [22] detectors. The second is the mid-rapidity detectors used to measure collision centrality, select rare jets and dimuons events. This set includes TOF [16], EMCs [19] and MTD [28] detectors. Final type is the forward rapidity detectors used to select high rapidity electromagnetic particles and scattered protons. This set includes Forward Meson Spectrometer (FMS) [29] and Roman Pot Detector (RPD) [30]. The pseudo-rapidity coverage of all these detectors are shown in the table 2.2.

Table 2.2: Pseudo-rapidity (η) coverage of the STAR Trigger detectors [26].

Vertex detectors	Mid-rapidity detectors	Forward rapidity detectors
BBC: $2.2 < |\eta| < 5.0$	MTD: $|\eta| < 0.5$	FMS: $2.5 < |\eta| < 4.0$
VPD: $4.25 < |\eta| < 5.1$	TOF: $|\eta| < 0.9$	RPD: $7.0 < |\eta| < 9.0$
ZDC: $|\eta| > 6.0$	BEMC: $|\eta| < 1.0$	
	EEMC: $1.07 < |\eta| < 2.0$	

Vertex detectors

A pair of ZDCs are located on either side of the interaction point at STAR [21]. These are placed at ± 18 m from the center ($z = 0$) of the STAR detector and at zero degrees ($\theta \leq 2$ mrad) with respect to the beam direction (z-axis). The ZDCs are hadronic calorimeters designed to measure energy, and thus multiplicity of spectator

neutrons. As all the other charged particles are deflected by the dipole magnets from the zero degree region. A coincidence between the two ZDCs indicates minimum-biased event of a heavy-ion collision at STAR. The ZDCs are also very useful in locating interaction vertices by using the time delay between the coincidences. A shower maximum detector was installed between the first and second modules of each existing STAR ZDC to study the spatial distribution of the neutron hits on the transverse plane of the ZDCs. The addition of ZDC-SMD to the STAR experiment enhances its capability in different areas of physics such as anisotropic flow, ultra-peripheral collisions, study of initial conditions and spin physics [31].

The two BBC modules are mounted on the East and West pole-tips of the STAR magnet [20]. It covers full azimuth using hexagonal geometry. The BBC are designed to provide minimum bias trigger for proton-proton collisions. A coincidence of signals is required between two BBC for a minimum-bias event. BBC coincidences are also used to reject beam gas events. Measurement of the difference in arrival times of discriminator signals from each module is used to get information of the primary vertex position. In addition, BBC are also useful to reconstruct the first order event plane for flow analysis [32].

A pair of high resolution Vertex Position Detectors (VPD) [22] is used to handle much higher multiplicity produced in heavy-ion collisions. Each module consists of 19 lead converters plus plastic scintillators with photomultiplier (PMT) cells. The cell size is much smaller than the BBC tiles and Each VPD is approximately 5.7 m from the interaction point. A coincidence signal in the east and west VPD detectors defines trigger for the minimum-bias (MB) event. Measuring the difference in the mean arrival times of photons from π^0 decays gives information of the z component of the primary vertex.

Mid-rapidity detectors

The STAR EMC detectors are electromagentic calroimeters, comprise of a barrel (BEMC) [18] and an Endcap (EEMC) [19] calroimeter. They are used to trigger on and study rare and high p_T processes such as jets, direct photons, and heavy quarks. The MTD are MRPC technology based detector mounted on the iron outside the STAR magnet. Therefore, MTD is used to measure muons tracks. The measured hit time from MTD is compared with VPD hit time to determine muon produced at the primary vertex.

Forward rapidity detectors

Forward Pion detector (FPD) installed in 2003, is upgraded in Forward Meson Spectrometer (FMS) in 2008. It consists of 1264 lead-glass Cherenkov detectors. It measures photons and electrons produced at high-rapidity. The FMS is fast detector used for the triggering purpose. The Roman Pot Detector (RPD) consists of 4 modules located near the ZDCs along the beamline. Each module contains 4 silicon detectors and a scintillator, used for the triggering. Combinations of hits in RPD detectors are used to trigger elastic and diffractive proton interactions at STAR [30].

A preshower Photon Multiplicity Detector (PMD) was installed in the year 2002 to enhance the phase space coverage of the STAR experiment at RHIC [33]. Athough the detector is not used in the physics analysis results presented in this thesis, but I am mentioning it briefly here because it was the Indian detector group's contribution to the STAR experiment. The PMD detector covers the forward region within the η range of 2.3−3.5 with full azimuthal coverage and p_T as low as ∼25 MeV. The PMD detector was located at 550 cm from the primary vertex outside the STAR magnet [33]. The detector consists of an array of honeycomb proportional counters. A honeycomb of 24×24 hexagonal cells forms a unit module [34].

The PMD detector was designed to measure photon multiplicity in the forward region where particle density is high. It allows event-by-event measurement of photon multiplicity and the spatial distribution of photons. Using the measurements of spatial distribution and multiplicity of photons event-by-event, the PMD detector was used: (a) to determine the event plane angle for the study of azimuthal anisotropy [35], (b) observables like multiplicity and pseudo-rapidity distributions for the study of QGP phase transition [36] and (c) signals of chiral symmetry restoration e.g. disoriented chiral condensates (DCC) [37].

2.4   Detectors used for the analysis of data

We have used data from several detector systems of the STAR experiment for the analysis presented in this thesis. We have used vertex position detectors (VPDs), zero degree calorimeters (ZDCs) and beam-beam counters (BBCs) to select minimum bias events from all the collected data. TPC detector is used to get total charged particle multiplicity to determine the centrality of an event. Momentum and identification of individual tracks from the events are done using the TPC detector. For identification of high momentum tracks TOF detector is used along with the TPC. BBC and TPC detectors are used to calculate event plane angle for flow measurements. We also used the concept of ZDC measuring neutrons to select initial configuration in deformed U+U collisions.

Bibliography

[1] "Prospects for Spin Physics at RHIC", G. Bunce *et al.*, *Ann. Rev. Nucl. Part. Sci.*, **2000**, *50*, 525-575;

"QCD spin physics: Status and prospects for relativistic heavy-ion collider", W. Vogelsang, *Pramana*, **2004**, *63*, 1251-1267.

[2] "Spin Physics at RHIC", L. C. Bland, *AIP Conf. Proc.*, **2003**, *675*, 98-111;

"Spin Physics at RHIC - a Theoretical Overview", M. Stratmann, *arXiv*:0211317.

[3] RHIC Accelerator complex, `https://www.bnl.gov/rhic/complex.asp`.

[4] "RHIC project overview", M.Harrison, T.Ludlam, S.Ozaki, *Nucl. Inst. Meth. A*, **2003**, *499*, 235-244.

[5] "PHENIX detector overview", K. Adcox *et al.* (PHENIX Collaboration), *Nucl. Inst. Meth. A*, **2003**, *499*, 469-479.

[6] "STAR detector overview", K. Ackermann *et al.* (STAR Collaboration), *Nucl. Inst. Meth. A*, **2003**, *499*, 624-632.

[7] "The PHOBOS detector at RHIC", B. B. Back *et al.* (PHOBOS Collaboration), *Nucl. Inst. Meth. A*, **2003**, *499*, 603-623.

[8] "The BRAHMS experiment at RHIC", M. Adamczyk *et al.* (BRAHMS Collaboration), *Nucl. Inst. Meth. A*, **2003**, *499*, 437-468.

[9] "Injecting RHIC from the Brookhaven Tandem Van De Graaff", J. Benjamin *et al.*, *IEEE Particle Accelerator Conference (PAC99)*, **1999**, *4*, 2277-2279.

[10] "The RHIC magnet system", M. Anerella *et al.*, *Nucl. Inst. Meth. A*, **2003**, *499*, 280-315.

[11] `http://www.agsrhichome.bnl.gov/RHIC/Runs/`.

[12] R. Fernow, *Introduction to Experimental Particle Physics* (Cambridge University Press, Cambridge, 1986).

[13] "The STAR detector magnet subsystem", F. Bergsma *et al.*, *Nucl. Inst. Meth. A*, **2003**, *499*, 633-639.

[14] "Integration and conventional systems at STAR", H. S. Matis *et al.*,*Nucl. Inst. Meth. A*, **2003**, *499*, 802-813.

[15] "The STAR time projection chamber: a unique tool for studying high multiplicity events at RHIC", M. Anderson *et al.*, *Nucl. Inst. Meth. A*, **2003**, *499*, 659-678.

[16] "A single Time-of-Flight tray based on multigap resistive plate chambers for the STAR experiment at RHIC", B. Bonner *et al.*, *Nucl. Inst. Meth. A*, **2003**, *508*, 181-184.

[17] 3D picture of STAR detector by Alex Schmah (STAR Collaboration) and Maria.

[18] "The STAR Barrel Electromagnetic Calorimeter", M. Beddo *et al.*, *Nucl. Inst. Meth. A*, **2003**, *499*, 725-739.

[19] "The STAR endcap electromagnetic calorimeter", C. E. Allgower *et al.*, *Nucl. Inst. Meth. A*, **2003**, *499*, 740-750.

[20] "Local Polarimetry for Proton Beams with the Star Beam Beam Counters", J. Kiryluk, *Trieste/Maine SPIN 2004*, **2004**, *718-721*; *arXiv*:hep-ex/0501072;

"Spin Physics with STAR at RHIC", J. Kiryluk, *Beijing ICHEP 2004*, **2004**, *1*, 604-608.

[21] "The RHIC Zero Degree Calorimeter", C. Adler *et al.*, *Nucl. Inst. Meth. A*, **2001**, *470*, 488-499.

[22] "The TOFp/pVPD time-of-flight system for STAR", W. J. Llope *et al.*, *Nucl. Inst. Meth. A*, **2004**, *522*, 252-273.

"The STAR Vertex Position Detector", W. J. Llope *et al.*, *Nucl. Inst. Meth. A*, **2014**, *759*, 23-28.

[23] "Track Fitting in the STAR Detector using the Kalman Filter Method", D. Liko, *STAR Internal Note*, **1994**, *SN0087*.

[24] "A method to improve tracking and particle identification in TPCs and silicon detectors", H. Bichsel, *Nucl. Inst. Meth. A*, **2006**, *562*, 154-197.

[25] "Review of Particle Physics", W. M. Yao *et al.*, *J. Phys. G: Nucl. Part. Phys.*, **2006**, *33*, 1.

[26] "The STAR trigger", F. S. Beiser *et al.*, *Nucl. Inst. Meth. A*, **2003**, *499*, 766-777;

"The evolution of the STAR Trigger System", E. G. Judd *et al.*, *Nucl. Inst. Meth. A*, **2018**, *902*, 228-237.

[27] "The STAR experiment's data acquisition system", A. Ljubicic *et al.*, *IEEE Trans. Nucl. Sci.*, **2000**, *47*, 99-102;

"An overview of the STAR DAQ system", J. M. Landgraf *et al.*, *Nucl. Inst. Meth. A*, **2003**, *499*, 762-765.

[28] "Perspectives of a mid-rapidity dimuon program at the RHIC: a novel and compact muon telescope detector", L. Ruan *et al.*, *J. Phys. G: Nucl. Part. Phys.*, **2009**, *36*, 095001.

[29] "Future of low-x forward physics at RHIC", L. C. Bland *et al.*, *Eur. Phys. J. C*, **2005**, *43*, 427-435;

"STAR Calorimetry", W. W. Jacobs (for the STAR Collaboration), *J. Phys. Conf. Ser.*, **2009**, *160*, 012008.

[30] "The PP2PP experiment at RHIC: silicon detectors installed in Roman Pots for forward proton detection close to the beam", S. Bultmann, *et al.*, *Nucl. Inst. Meth. A*, **2004**, *535*, 415-420.

[31] "System-Size Independence of Directed Flow Measured at the BNL Relativistic Heavy-Ion Collider", B. I. Abelev *et al.* (STAR Collaboration), *Phys. Rev. Lett.*, **2008**, *101*, 252301;

"STAR ZDC-SMD proposal", *STAR Note*, **2003**, *SN0448*.

[32] "Inclusive charged hadron elliptic flow in Au+Au collisions at $\sqrt{s_{\mathrm{NN}}} = 7.7-39$ GeV", L. Adamczyk *et al.* (STAR Collaboration), *Phys. Rev. C*, **2012**, *86*, 054908.

[33] "The STAR Photon Multiplicity Detector", M. M. Aggarwal *et al.*, *Nucl. Inst. Meth. A*, **2003**, *499*, 751-761.

[34] "A honeycomb proportional counter for photon multiplicity measurement in the ALICE experiment", M. M. Aggarwal *et al.*, *Nucl. Inst. Meth. A*, **2002**, *488*, 131-143.

[35] "Determination of azimuthal anisotropy of neutral pions from the measured anisotropy of photons in ultra-relativistic nuclear collisions", R. Raniwala, S. Raniwala, Y. P. Viyogi, *Phys. Lett. B*, **2000**, *489*, 9-14;

"Azimuthal anisotropy of photon and charged particle emissionin ^{208}Pb + ^{208}Pb collisions at 158.A GeV/c", M. M. Aggarwal *et al.* (WA98 Collaboration), *Eur. Phys. J C*, **2005**, *41*, 287-296;

"Elliptic flow of inclusive photons in Au–Au and Cu–Cu collisions at $\sqrt{s_{NN}} = $ 200 GeV", R. Raniwala (STAR collaboration), *J. Phys. G*, **2008**, *35*, 10.

[36] "Multiplicity and Pseudorapidity Distributions of Photons in Au+Au Collisions at $\sqrt{s_{NN}} = 62.4$ GeV", J. Adams *et al.* (STAR Collaboration), *Phys. Rev. Lett.*, **2005**, *95*, 062301;

"Multiplicity and pseudorapidity distributions of charged particles and photons at forward pseudorapidity in Au+Au collisions at $\sqrt{s_{NN}} = 62.4$ GeV", J. Adams *et al.* (STAR Collaboration), *Phys. Rev. C*, **2006**, *73*, 034906;

"Center of mass energy and system-size dependence of photon production at forward rapidity at RHIC", B. I. Abelev *et al.* (STAR Collaboration), *Nucl. Phys. A*, **2010**, *832*, 134-147.

[37] "Disoriented chiral condensate: Theory and experiment", B. Mohanty, J. Serreau, *Phys. Rept.*, **2005**, *414*, 263-358.

Chapter 3

Azimuthal anisotropy of strange and multi-strange hadrons in U+U collisions at RHIC

3.1 Introduction

The aim of relativistic heavy-ion collisions is to study the properties of QGP [1–4]. One of the main observable sensitive to the properties of QGP is the azimuthal anisotropy of particles produced in the transverse plane to the beam direction [5]. Azimuthal anisotropies, also known as anisotropic flow, arise from the asymmetries in the initial geometry of the heavy-ion collisions [6–10]. The anisotropic flow depends on the QGP properties such as equation of state, speed of sound in the medium and the value of shear viscosity to entropy density ratio (η/s) [11, 12].

In non-central nucleus-nucleus collisions, the initial overlap region between the two colliding nuclei is spatially anisotropic. This initial spatial anisotropy is converted into an anisotropy in momentum space through frequent interactions among par-

tons and at later stages among the produced particles. The magnitude of azimuthal anisotropy is quantified by the flow coefficients (v_n) in the Fourier decomposition of the particle azimuthal angle distribution with respect to the reaction plane angle. The second order flow coefficient v_2, called elliptic flow, studied at RHIC and LHC shows that the medium produced in heavy-ion collision is strongly-coupled quark-gluon plasma with a small value of η/s, very close to the lower limit ($1/4\pi$) from the AdS/CFT [13].

Additionally, fluctuations in the initial density profile of nucleons participating in the collision generate higher order flow harmonics such v_3, v_4 etc [14]. These higher order flow coefficients are more sensitive to η/s than elliptic flow [15] and also sensitive to the non-linear hydrodynamic response of the medium [16]. Higher order flow coefficients can provide constraints to initial conditions and η/s value for hydrodynamical calculations [17]. This can be done by studying the flow coefficients as a function of transverse momentum and collision centrality for different particle species in heavy-ion collisions.

Azimuthal anisotropy of identified particles plays important role when studying the properties of the QGP. Particles produced in heavy-ion collisions are affected by the late-stage interactions during hadronic phase. The resonances having short lifetime of the order of 10^{-23} sec decay in the hadronic phase. This can alter the information about the initial QGP phase carried by the flow coefficients, which leads to the deviation in the mass ordering of $v_n(p_T)$ at low p_T [18]. The "pure" strange hadrons such as ϕ-meson ($s\bar{s}$) and Ω (sss) have large mass and small hadronic interactions cross-section and, are less sensitive to the later stage hadronic re-scattering in the medium [19–21]. They are considered a sensitive probe for the QGP phase.

In this chapter, we present systematic measurements of v_2, v_3 and v_4 of K_s^0, ϕ, $\Lambda + \bar{\Lambda}$, $\Xi + \bar{\Xi}$ and $\Omega + \bar{\Omega}$ at mid-rapidity in U+U collisions at $\sqrt{s_{NN}} = 193$ GeV.

The results are presented as a function transverse momentum for different centrality classes. We have also discussed partonic collectivity by testing the validity of NCQ scaling of v_n coefficients in U+U collisions.

3.2 Dataset, Event and Track selection

The results presented in this chapter are obtained from the data collected by the STAR experiment at RHIC in the year 2012 for U+U collisions at $\sqrt{s_{\mathrm{NN}}} = 193$ GeV. The data-set consists of information about each Uranium (^{238}U) on Uranium (^{238}U) collision, known as events. The events are stored in so-called mircoDST files for the physics analysis. The associated trigger information and the signals recorded in various detector sub-systems along with track information like momentum vectors of the produced particles in each event are also stored in these files.

3.2.1 Data-set and Trigger

During data-taking, events are recorded in the files. There are a total of 783 runs ($13116051 - 13136015$) in U+U data-set. A total of 19 bad runs are rejected from the analysis based on the quality assurance (QA) checks of the data [22]. The QA checks are done run-by-run by monitoring the mean interaction rates, the mean transverse momentum, the mean vertex position, and the mean multiplicity of the events. A list of bad run removed from the analysis is given below.

- 13117026
- 13117027
- 13117028
- 13117029
- 13117030

- 13117031
- 13117032
- 13117033
- 13117034
- 13117035

- 13117036
- 13118009
- 13118034
- 13118035
- 13119016

- 13119017
- 13129047
- 13129048
- 13132047

Minimum-bias trigger is used to select good events for the analysis. A minimum-bias trigger requires a coincidence between the east and west ZDC and/or between the east and west VPD. The data-set is protected against pile-up events. A pile-up event is the event in which particles from more than one collision are recorded. It was required that atleast two tracks from the primary vertex were matched to the cells of the TOF detector to eliminate pile-up events.

Table 3.1: Data-set and trigger information for Run 12 U+U collisions at $\sqrt{s_{NN}} = 193$ GeV.

System/Energy	Production Id	Trigger Ids	Events
U+U, 193 GeV	P12id	400005, 400025, 400035	∼270 Million

3.2.2 Event selection

Events analyzed in this analysis were required to have a primary vertex position along the longitudinal direction (V_z) within ±30 cm from the center of the TPC detector. An additional cut on the radial direction of the primary vertex ($V_r = \sqrt{V_x^2 + V_y^2}$) is required to be less than 2.0 cm from the center of the beam pipe to minimize effects of beam and beam-pipe interactions. To reduce pile-up events, difference in the V_z from TPC and VPD, less than 3.0 cm is also required. After applying all event cuts, a total of ∼270 million good events are selected for the analysis. A list of event cuts used is given in the table 3.2 below.

Table 3.2: Event selection cuts for U+U collisions at $\sqrt{s_{NN}} = 193$ GeV.

System/Energy	V_z (cm)	V_r (cm)	VPD V_z - TPC V_z (cm)
U+U, 193 GeV	$|V_z| < 30$	$V_r < 2.0$	$|vpdV_z - V_z| < 3.0$

Figure 3.1 shows the distributions of V_z and V_r before and after applying the event selection cuts in U+U collisions at $\sqrt{s_{\mathrm{NN}}} = 193$ GeV.
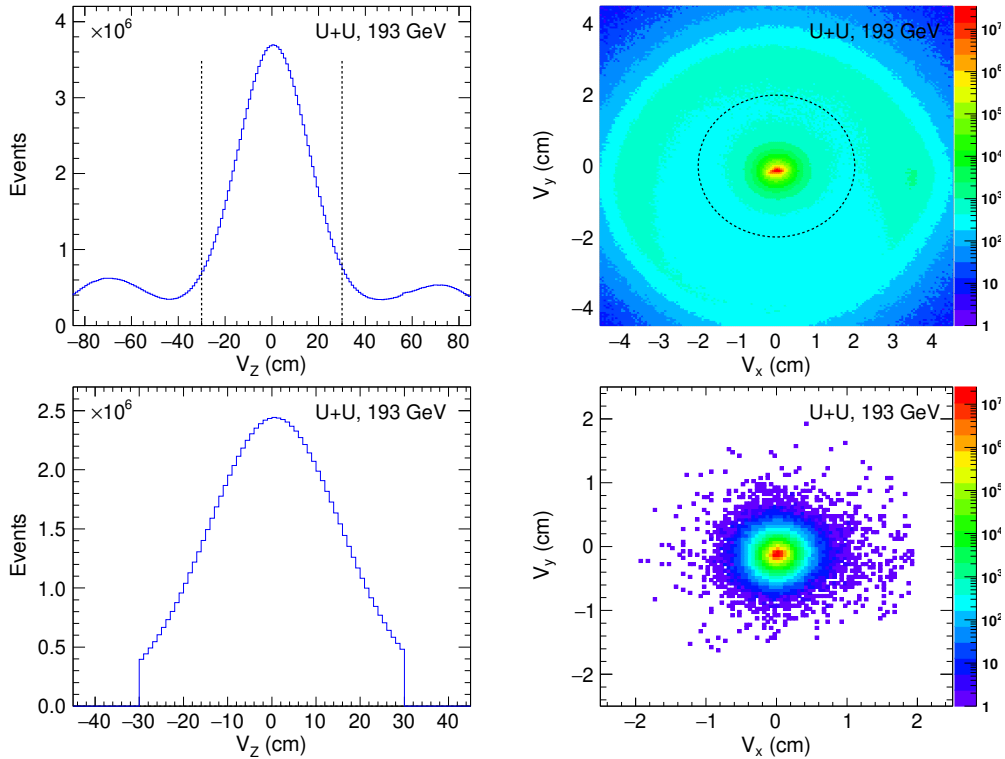
Figure 3.1: Distribution of z-component of primary vertex (left panels) and V_r (right panels) before and after the event selection cuts in U+U collisions at $\sqrt{s_{\mathrm{NN}}} = 193$ GeV.

3.2.3   Centrality selection

Overlap between the two colliding nuclei is termed as centrality of an event, which depends on the impact parameter. Impact parameter (b) is the perpendicular distance between the centers of two colliding nuclei. Events with low impact parameter values are called central events. High impact parameter values corresponds to the peripheral events. In central events, large number of particles are produced therefore multiplicity of the events is high, while in peripheral events multiplicity is low. The impact parameter cannot be measured experimentally. Therefore, centrality of the events

are determined by an experimental observable, reference multiplicity (N_{ch}). The reference multiplicity is defined as the number of primary charged tracks from the TPC detector with number of hit fit points greater than and equal to 15, pseudo-rapidity range of $|\eta| < 0.5$, distance of closet approach (DCA) to the primary vertex less than 3 cm and $|V_z| < 30$ cm. The measured N_{ch} is compared with the multiplicity from two-component Monte Carlo (MC) Glauber Model [23]. Figure 3.2 shows the measured uncorrected multiplicity distribution for charged particles from the TPC (open circles) and for those obtained from MC Glauber model (blue dashed line).
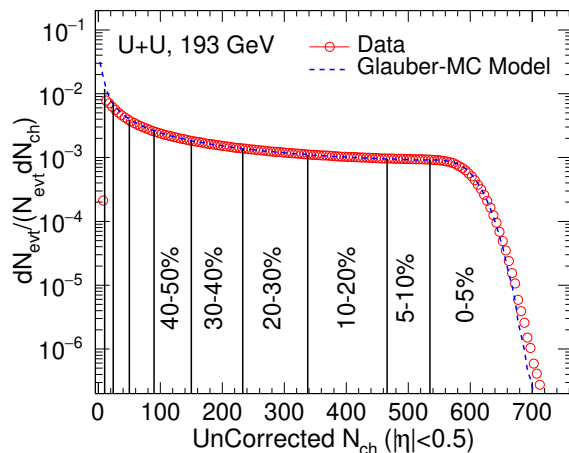
Figure 3.2: Uncorrected charged particle multiplicity distribution (open circles) measured from the TPC detector within $|\eta| < 0.5$ in U+U collisions at $\sqrt{s_{NN}} = 193$ GeV. The blue dashed line represents the multiplicity distribution from Monte Carlo Glauber model [23]. The vertical lines represent the centrality selection criteria used in the analysis. Statistical error bars are within the marker size.

The multiplicity distribution in two-component model [24] is given by the equation,

$$\frac{dN_{ch}}{d\eta} = n_{pp}[(1-x)\frac{N_{part}}{2} + xN_{coll}], \qquad (3.1)$$

where N_{part} is the number of participant nucleons and N_{coll} is the number of binary nucleon-nucleon collisions in the Glauber Monte-Carlo simulations [23]. The fitting parameter n_{pp} is the average multiplicity per unit pseudo-rapidity ($dN_{ch}/d\eta$)

in minimum-bias $p + p$ collisions and x is the fraction of produced charged particles from the hard component. The x value is set at 0.13 ± 0.02 based on the linear interpolation of the PHOBOS results at $\sqrt{s_{NN}} = 19.6$ and 200 GeV [25]. The inelastic nucleon-nucleon cross-section $\sigma_{NN}^{\text{inel}}$ is extracted from fitting the results of available NN data for total and elastic $p+p$ cross-sections from the Particle Data Group [26]. A summary of fitting and input parameters of two-component model for U+U collisions at $\sqrt{s_{NN}} = 193$ GeV is shown in the Table 3.3.

Table 3.3: Summary of fitting and input parameters of two-component model for U+U collisions at $\sqrt{s_{NN}} = 193$ GeV.

$\sqrt{s_{NN}}$ (GeV)	n_{pp}	x	$\sigma_{NN}^{\text{inel}}$ (mb)
193	2.43 $\pm$0.05	0.13 $\pm$ 0.02	41.2 $\pm$ 1.0

The event-by-event variation in the multiplicity has been taken into account by convoluting the Negative Binomial Distribution (NBD) for a given N_{part} and N_{coll}. The NBD distribution in multiplicity n has two parameters, n_{pp} and k, and is defined as,

$$P_{\text{NBD}}(n_{\text{pp}}, k; n) = \frac{\Gamma(n + k)}{\Gamma(n + 1)\Gamma(k)} \frac{(n_{\text{pp}}/k)^n}{(n_{\text{pp}}/k + 1)^{n+k}}, \tag{3.2}$$

where, Γ is the Gamma function. The values $k = 2.0$ and $n_{\text{pp}} = 2.43$ are obtained by fitting the measured multiplicities with those from the simulations. The fitting is performed for $N_{ch} > 50$ in order to avoid the trigger inefficiency in peripheral collisions. The centrality classes are defined by calculating the fraction of the total cross-section obtained from the simulated multiplicity. The centrality selection criteria used in this analysis for U+U collisions at $\sqrt{s_{NN}} = 193$ GeV are listed in the appendix given at the end of the chapter [27].

3.2.4 Track selection

In this analysis both primary and global tracks are used. In order to identify the charge particles and to ensure the quality of data several track quality cuts are applied to the reconstructed tracks from the TPC detector. Short tracks were eliminated from the analysis by requiring that all tracks have atleast 15 hit fit points in the TPC. The effect of track-splitting by the tracking algorithm is minimized by the number of fit points are more than half the number of total possible hit points for a track. Pile-up tracks are identified during the data production and flagged with an ID greater than 1000. All tracks with the flag between 0 to 1000 are selected for the analysis. To ensure that the tracks comes from the primary vertex, a requirement is placed on the DCA between the track and the event vertex. All tracks within the pseudo-rapidity range of $|\eta| < 1.0$ are selected. A list of the track cuts applied on individual tracks are shown in the Table 3.4.

Table 3.4: Track selection cuts for U+U collisions at $\sqrt{s_{\mathrm{NN}}} = 193$ GeV.

Track parameter	value
Number of fit points	nHitsFit > 15
nHitsFit/nHitsPoss	Ratio ≥ 0.52
Transverse Momentum	$0.15 < p_T < 10$ (GeV/c)
Pseudorapidity	$|\eta| < 1.0$

3.3 Particle identification

In this section, we discuss identification methods of charged particles using the TPC and TOF detectors.

3.3.1 Particle identification using TPC

A characteristic plot of measured ionization energy loss (dE/dx) from TPC is shown in the upper panel of Fig. 3.3. In the figure, the color bands represent the dE/dx of charged particles from TPC as a function of momentum within $|\eta| < 1$ for U+U collisions at $\sqrt{s_{\mathrm{NN}}} = 193$ GeV. The dashed lines correspond to the theoretical values of specific energy loss obtained from Bichsel functions [28]. The Bichsel function is a good approximation for the prediction of dE/dx for the STAR TPC.

To identify individual charged particle, we define a variable normalized energy loss ($n\sigma$),

$$n\sigma = \ln\left[\frac{(dE/dx)_{Exp.}}{(dE/dx)_{Bichsel}}\right]/R, \tag{3.3}$$

where the quantity R is the dE/dx resolution of the TPC detector for individual hadrons. For a minimum ionizing particle that produces a single track with the maximum possible number of TPC pad rows (45), the dE/dx resolution is found to be about 6-8% [29]. A cut of $|n\sigma| < 2$ along with other basic track selection cuts has been applied to identify pions, kaons and protons.

3.3.2 Particle identification using TOF

The Time-of-Flight (TOF) detector measures the flight time (Δt) of the tracks in full azimuthal coverage and pseudo-rapidity range of $|\eta| < 0.9$ [30]. The flight time is the time taken by a track to traverse the distance L from the primary vertex to the TOF detector. Velocity (β) of the track can be calculated using the time of flight information. Using the velocity and corresponding momentum (p) from the TPC, mass (m) of the particle can be calculated as,

$$m^2 = p^2 \left(\frac{1}{\beta^2} - 1 \right). \tag{3.4}$$

TOF detector is able to enhance the particle identification of the tracks with high momentum (> 1.0 GeV/c) where the dE/dx bands of different particles starts to merge. A representative plot of m^2 as a function of particle momentum is shown in the lower panel of Fig. 3.3 for U+U collisions at $\sqrt{s_{\text{NN}}} = 193$ GeV. The different color bands corresponds to the square of mass of different particles. Dashed lines corresponds to the m^2 values for different particles from PDG [31].
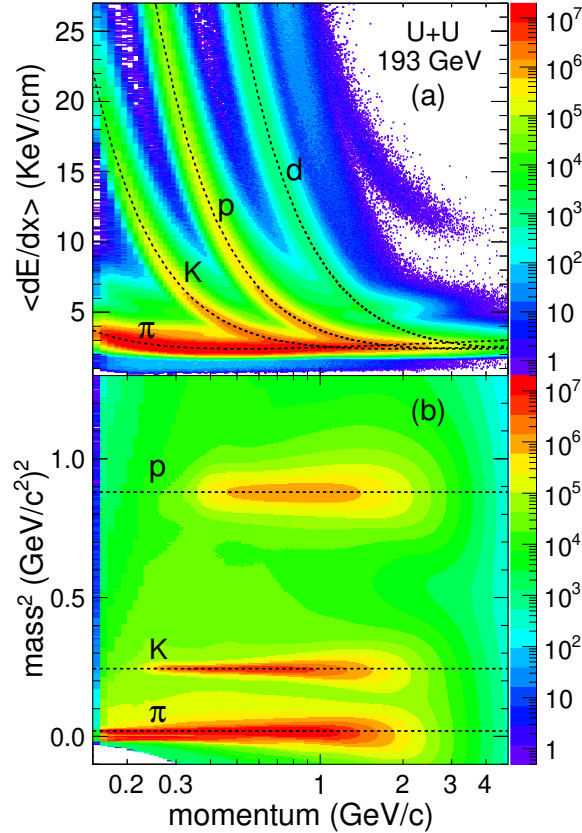
Figure 3.3: (a) The energy loss (dE/dx) distribution of charged particles from TPC as a function of momentum within $|\eta| < 1.0$ for U+U collisions at $\sqrt{s_{\text{NN}}} = 193$ GeV. The dashed lines corresponds the expected mean value of dE/dx for the corresponding particle from Bichsel function [28]. (b) m^2 as a function of momentum in U+U collisions at $\sqrt{s_{\text{NN}}} = 193$ GeV. The dashed lines represent the m^2 values from PDG for the corresponding particle.

3.4 Reconstruction of strange and multi-strange hadrons

In this section, we discuss the methods for reconstructing strange and multi-strange hadrons K_s^0, ϕ, $\Lambda + \bar{\Lambda}$, $\Xi + \bar{\Xi}$ and $\Omega + \bar{\Omega}$ at mid-rapidity ($|y| < 1.0$) in U+U collisions at $\sqrt{s_{NN}} = 193$ GeV. A summary of their properties of decays are listed in the Table 3.5 [31].

Table 3.5: A summary of properties of K_s^0, ϕ, $\Lambda + \bar{\Lambda}$, $\Xi + \bar{\Xi}$ and $\Omega + \bar{\Omega}$.

Particle	Decay channel (for this analysis)	Branching Ratio (%)	Decay length (cm)	Mass (MeV/c^2)
ϕ	$K^+ + K^-$	48.90±0.50	(Strong decay)	1019.461±0.016
K_s^0	$\pi^+ + \pi^-$	69.20±0.05	2.684±0.001	497.611±0.013
$\Lambda(\bar{\Lambda})$	$p + \pi^-$ $(\bar{p} + \pi^+)$	63.90±0.50	7.890±0.060	1115.683±0.006
$\Xi(\bar{\Xi})$	$\Lambda + \pi^-$ $(\bar{\Lambda} + \pi^+)$	99.89±0.04	4.910±0.040	1321.710±0.070
$\Omega(\bar{\Omega})$	$\Lambda + K^-$ $(\bar{\Lambda} + K^+)$	67.80±0.70	2.461±0.033	1672.450±0.290

3.4.1 ϕ reconstruction

ϕ-meson is reconstructed using invariant mass technique through it's hadronic decay channel: $\phi \to K^+ K^-$ (branching ratio = 48.9 ± 0.5%) [32]. Decay daughter kaon tracks are identified using both the TPC and TOF detector. Kaon m^2 information is used whenever a TOF matched track is available, otherwise TPC dE/dx information is used to identify kaon tracks. The track selection cuts for the ϕ-meson reconstruction in U+U collisions at $\sqrt{s_{NN}} = 193$ GeV is listed in the Table 3.6.

Table 3.6: Track selection cuts for ϕ-meson reconstruction.

Number of fit points in TPC	nHitsFit > 15
nHitsFit/nHitsPoss	Ratio ≥ 0.52
DCA to primary vertex	$|\text{DCA}| < 3.0$ cm
Transverse momentum	$p_T \geq 0.15$ (GeV/c)
Pseudo-rapidity	$|\eta| < 1.0$
$n\sigma_{K^\pm}\ dE/dx$	$|n\sigma| \leq 2.0$
$m^2_{K^\pm}$ from TOF	$0.16 \leq m^2 \leq 0.36\ (GeV/c^2)^2$

3.4.2 K^0_s and Λ reconstruction

The weakly decaying neutral strange particles K^0_s ($d\bar{s}$) and $\Lambda(\bar{\Lambda})$ (uds), are reconstructed using invariant mass technique and their weak-decay (V0) topology (two oppositely charged daughters at a secondary vertex) [33]. Decay daughter tracks were identified using the ionization energy loss (dE/dx) in TPC and information of mass square (m^2) from TOF. The basic cuts for track selection using TPC and TOF are listed in the Table 3.7.

Table 3.7: Track selection cuts for K^0_s and $\Lambda(\bar{\Lambda})$ reconstruction.

Number of fit points in TPC	nHitsFit > 15
nHitsFit/nHitsPoss	Ratio ≥ 0.52
Transverse momentum	$p_T \geq 0.15$ (GeV/c)
Pseudo-rapidity	$|\eta| < 1.0$
$n\sigma\ dE/dx$ of p and π	$|n\sigma| \leq 3.0$
m^2 for protons	$0.5 \leq m^2 \leq 1.5\ (GeV/c^2)^2$
m^2 for pions	$(0.017\text{-}0.013 \times \text{p}) \leq m^2 \leq 0.05\ (GeV/c^2)^2$
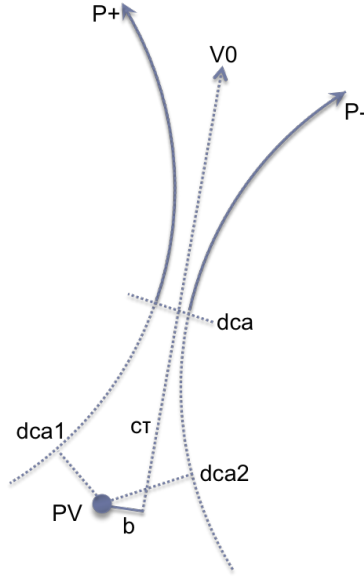
Figure 3.4: Schematic diagram of V0 decay topology.

After applying basic cuts for the selection of daughter tracks, V0 topology cuts are used to reconstruct the K_s^0 and $\Lambda(\bar{\Lambda})$. A schematic diagram of V0 topology of weak-decay is shown in Fig. 3.4. The positive and negative charged decay daughter tracks are denoted by P^+ and P^-, respectively. PV denotes the primary vertex, and DCA denotes distance of closest approach. $Dca1$ and $Dca2$ are the DCA of the two daughters from the primary vertex. These $Dca1$ and $Dca2$ should not be very close to primary vertex if they are daughters of K_s^0 or $\Lambda(\bar{\Lambda})$ (the typical values of decay length are given in Table 3.5). The parameter b is the DCA from the primary vertex to the direction of V0 momentum. The decay length is shown by parameter $c\tau$. The coordinates of the positive and negative tracks are combined at the mid-point of the DCA between the two daughter tracks to form the parent particle decay vertex. If the reconstructed decay vertex passes the selection criteria listed in the Table 3.8,

then the invariant mass of the parent particle is calculated as follows:

$$m_{inv} = \sqrt{\left(\sqrt{p_1^2 + m_1^2} + \sqrt{p_2^2 + m_2^2}\right)^2 - (\vec{p_1} + \vec{p_2})^2}, \tag{3.5}$$

where $\vec{p_1}, \vec{p_2}$ are the momentum vectors and m_1, m_2 are the rest masses of daughter particles.

Table 3.8: V0 topological cuts for K_s^0 and $\Lambda(\bar{\Lambda})$.

V0 cuts	K_s^0		$\Lambda(\bar{\Lambda})$	
	$p_T < 2.0$	$p_T \geq 2.0$	$p_T < 2.0$	$p_T \geq 2.0$
	(GeV/c)		(GeV/c)	
DCA V0 to PV (cm)	≤ 0.7	≤ 0.8	≤ 0.7	≤ 0.7
DCA Daughters (cm)	≤ 0.7	≤ 0.8	≤ 0.7	≤ 0.7
DCA Protons to PV (cm)	–	–	≥ 0.5	≥ 0.25
DCA Pions to PV (cm)	≥ 1.5	≥ 0.35	≥ 1.0	≥ 1.0
Decay Length (cm)	≥ 4.5	≥ 7.0	≥ 4.5	≥ 4.5

3.4.3 Ξ and Ω reconstruction

The multi-strange particles $\Xi^-(\bar{\Xi}^+)$ (dss) and $\Omega^-(\bar{\Omega}^+)$ (sss) decay into a charged decay daughter and a neutral V0 particle (Λ), which in turn decays into two charged particles [34, 35]. These multi-strange baryons can be reconstructed by calculating decay kinematics of the three charged decay daughters. A schematic diagram of decay topology of Ξ^- decay is shown in Fig. 3.5. Decay daughter tracks were identified by the ionization energy loss (dE/dx) in TPC and information of mass square (m^2) from TOF. The basic cuts for track selection using TPC and TOF are same as listed in the Table 3.7. The process of reconstruction of multi-strange baryons involves finding of two secondary decay vertex as shown in Fig. 3.5. The reconstruction is done in

two steps, first finding a decay vertex of neutral V0 candidate using decay kinematics. After finding suitable V0 candidate, the next step is to find a matching charged meson from Ξ or Ω decay. The topological cuts for Ξ or Ω reconstruction are listed in the Table 3.9.
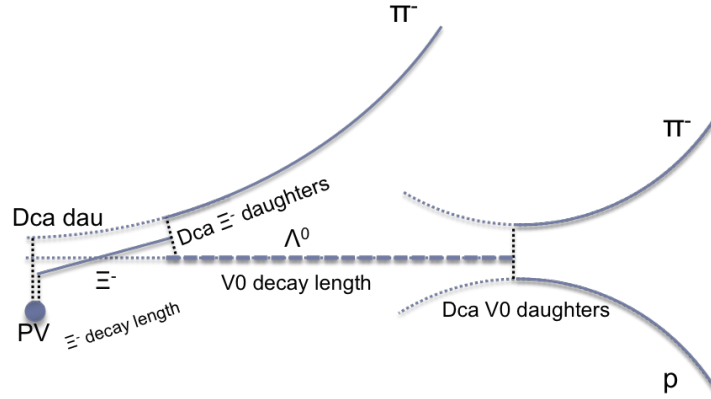
Figure 3.5: Schematic diagram of decay topology of Ξ^-. The charged decay daughters are represented by solid lines and neutral Λ track by bold dashed line.

Table 3.9: Topological cuts for Ξ and Ω.

topology cuts	Ξ	topology cuts	Ω
DCA Ξ to PV	≤ 0.5 cm	DCA Ω to PV	≤ 0.4 cm
DCA daughters of Ξ	≤ 0.8 cm	DCA daughters of Ω	≤ 0.7 cm
DCA bachelor (π) to PV	≥ 2.0 cm	DCA bachelor (K) to PV	≥ 1.0 cm
DCA V0 (Λ) to PV	≥ 0.7 cm	DCA V0 (Λ) to PV	≥ 0.4 cm
DCA daughters of Λ	≤ 0.8 cm	DCA daughters of Λ	≤ 0.7 cm
DCA π from Λ to PV	≥ 2.0 cm	DCA π from Λ to PV	≥ 2.0 cm
DCA p from Λ to PV	≥ 0.6 cm	DCA p from Λ to PV	≥ 0.6 cm
Decay length Ξ	≥ 4.0 cm	Decay length Ω	≥ 3.0 cm
Decay length Λ	≥ 5.0 cm	Decay length Λ	≥ 5.0 cm
Mass width of Λ	≤ 6 MeV	Mass width of Λ	≤ 6 MeV

3.5 Combinatorial background estimation

3.5.1 Mixed event background

The combinatorial background from uncorrelated pair of particles is estimated using the mixed-event technique for ϕ-meson. The fact that there are no correlations between the charged tracks from one event to another event and under appropriate condition of mixing of similar kind of event, the mixed event technique reproduces the shape of the background well.

Events are divided into nine bins of centrality, ten bins of z-vertex (V_z) and five bins of event plane angle (ψ), which makes a total of 450 event classes. For each event class, five events are mixed and then combinatorial background is reconstructed using invariant mass of uncorrelated pair of particles. Event mixing always results in a large number of reconstructed mixed events, and thus results in a larger number of reconstructed background candidates than in the real event sample. The mixed event background is normalized using iterative method. The background distribution was scaled by the ratio of the integral of the signal to the integral of the background distribution in a fixed invariant mass region including the ϕ mass peak ($0.99 < m_{inv} < 1.05$ GeV/c^2). The background distribution was then subtracted from the signal distribution and the remaining signal was fitted with a Breit-Wigner function plus a straight line. The signal integral was then set to be the integral in the mass range minus the integral of the Breit-Wigner function, the ratio was recalculated and the background re-scaled. Four iterations were needed to stabilize the final scaling factor. This procedure is illustrated in the Fig. 3.6 for ϕ-meson.

The upper left panel of the Fig. 3.6 shows the signal + background invariant mass distribution in red, and the mixed event background is the grey shaded area. The
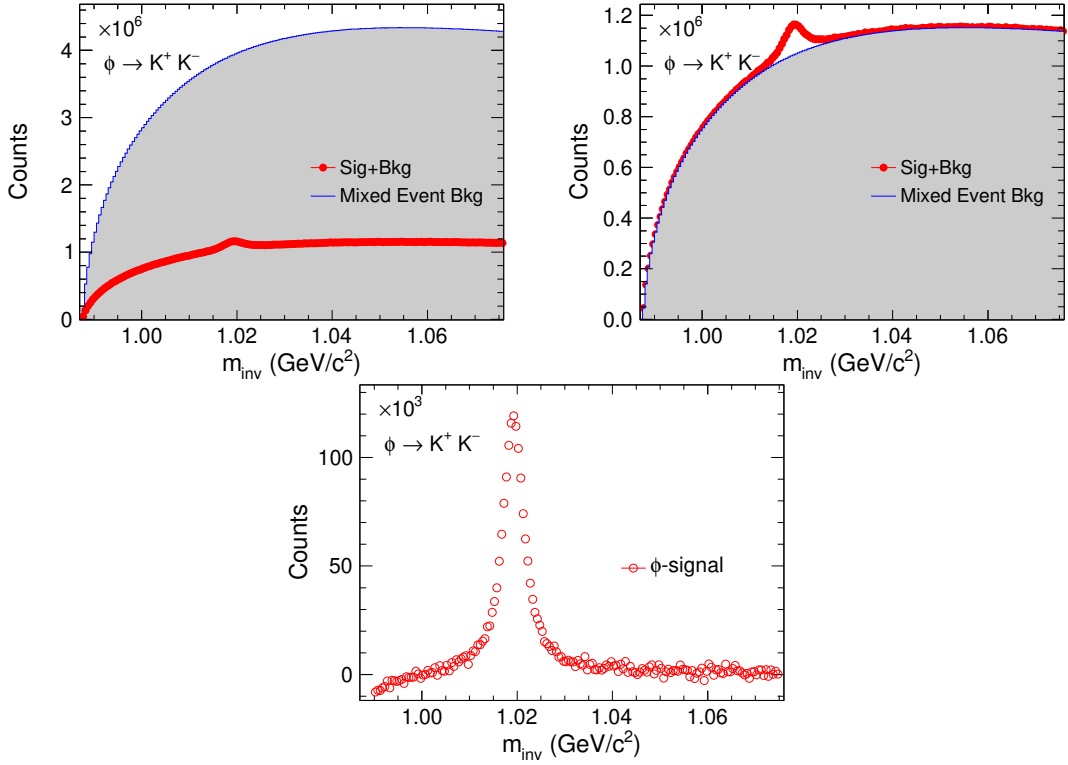
Figure 3.6: llustration of mixed event background estimation for ϕ-meson in U+U collisions at $\sqrt{s_{\mathrm{NN}}} = 193$ GeV for 0-80% centrality. Upper left panel shows the signal+background and the mixed event background. Upper right panel shows the same after the background is normalized and Bottom panel represents the invariant mass peak for ϕ after background subtraction.

upper right panel shows the same after the normalization of mixed event background, and in the bottom panel, the normalized background has been subtracted from the signal+background distribution.

3.5.2 Like-sign background

The combinatorial background for K_s^0 and $\Lambda(\bar{\Lambda})$ is constructed using like-sign method. In this method, invariant mass of same sign particles from a event is calculated to reproduce background shape. The same sign particles are not correlated with K_s^0 and Λ decays. For the case of K_s^0, like-sign background is constructed using $\pi^+\pi^+$ and $\pi^-\pi^-$ pair. Figure 3.7 shows the signal+background and combinatorial

background using like-sign method and K_s^0 signal after subtraction of background from signal+background. For the case of $\Lambda(\bar{\Lambda})$, like-sign background is constructed using $p\pi^+$ and $\bar{p}\pi^-$ pair. Figure 3.8 shows the signal+background and combinatorial background using like-sign method and Λ-signal after the subtraction of background from signal+background.
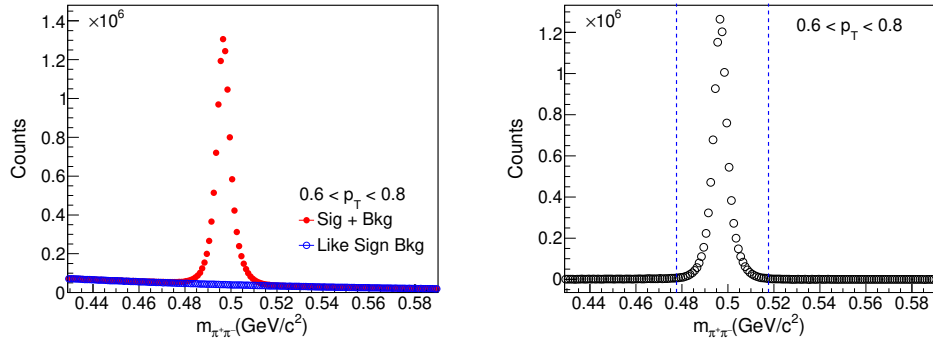
Figure 3.7: Illustration of like-sign background estimation for K_s^0 in U+U collisions at $\sqrt{s_{\mathrm{NN}}} = 193$ GeV for 0-80% centrality for a p_T range of $0.6 < p_T < 0.8$ (GeV/c). Left panel shows the signal+background (red marker) and like-sign background (blue marker). Right panel represents the invariant mass peak for K_s^0 after background subtraction.
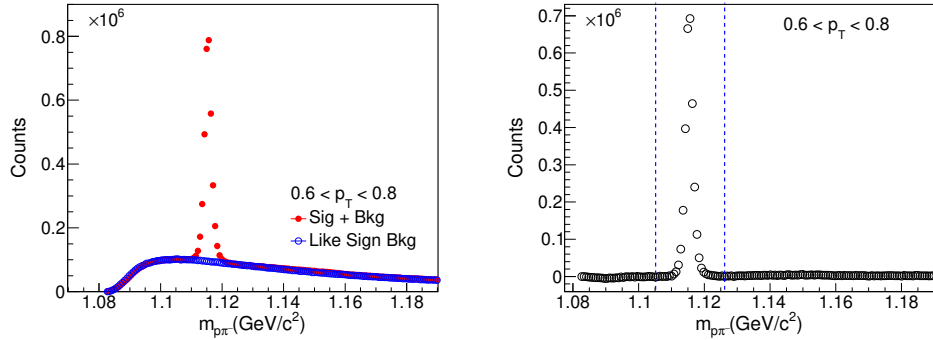
Figure 3.8: Illustration of like-sign background estimation for $\Lambda(\bar{\Lambda})$ in U+U collisions at $\sqrt{s_{\mathrm{NN}}} = 193$ GeV for 0-80% centrality for a p_T range of $0.6 < p_T < 0.8$ (GeV/c). Left panel shows the signal+background (red marker) and like-sign background (blue marker). Right panel represents the invariant mass peak for $\Lambda(\bar{\Lambda})$ after background subtraction.

3.5.3 Rotational background

For Ξ and Ω, the combinatorial background is constructed using rotational background method. In the rotational background method, one of the daughter track is rotated by $180°$ in the transverse plane, and the resulting tracks are used to reconstruct the background. This rotation breaks the correlation between the two decay daughters and therefore the calculated invariant mass does not have signal but reproduces the shape of the combinatorial background. In this analysis, momentum vector of Λ is rotated by $180°$. Figure 3.9 shows the signal+background and combinatorial background using rotational method in the left panel and Ξ-signal after subtraction of background from signal+background in the right panel. Figure 3.10 left panel shows the signal+background and combinatorial background using rotational method and Ω-signal after the subtraction of background from signal+background. The residual bump at lower invariant mass in Fig. 3.10 is due to the fake Ξ candidates being reconstructed because of fake Λ candidates. These fake Λ candidates are constructed due to the mis-identification of one of the decay daughters (π,p). But this residual correlation does not affect the signal peak.
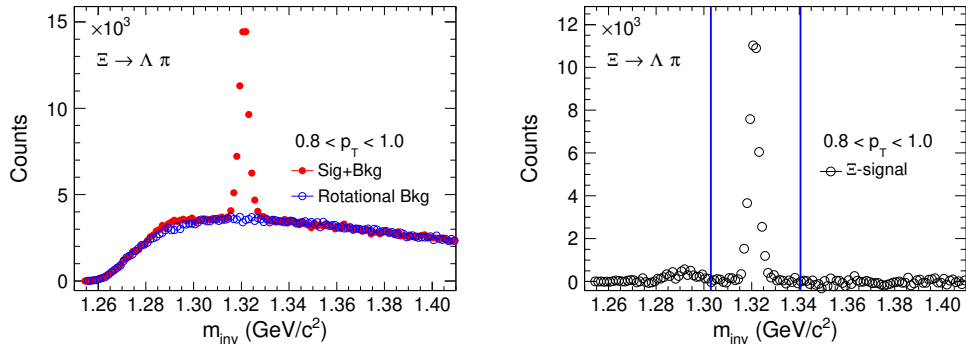
Figure 3.9: Illustration of rotational background estimation for Ξ in U+U collisions at $\sqrt{s_{\mathrm{NN}}} = 193$ GeV for 0-80% centrality for a p_T range of $0.8 < p_T < 1.0$ (GeV/c). Left panel shows the signal+background (red marker) and rotational background (blue marker). Right panel represents the invariant mass peak for Ξ after background subtraction.

Figure 3.10: Illustration of rotational background estimation for Ω in U+U collisions at $\sqrt{s_{\mathrm{NN}}} = 193$ GeV for 0-80% centrality for a p_T range of $1.5 < p_T < 2.0$ (GeV/c). Left panel shows the signal+background (red marker) and rotational background (blue marker). Right panel represents the invariant mass peak for Ω after background subtraction.

3.6 Flow analysis method

The azimuthal distribution of produced particles $dN/d\phi$ is a periodic function with 2π principal period. We know that any periodic function can be expanded into a Fourier series. Therefore, the Fourier expansion of the azimuthal distribution $dN/d\phi$ is [7],

$$
\begin{aligned}
\frac{dN}{d\phi} &= \frac{x_0}{2\pi} + \frac{1}{\pi} \sum_{n=1}^{\infty} \left(x_n \cos(n\phi) + y_n \sin(n\phi) \right) \\
&= \frac{x_0}{2\pi} \left(1 + 2 \sum_{n=1}^{\infty} \left(\frac{x_n}{x_0} \cos(n\phi) + \frac{y_n}{y_0} \sin(n\phi) \right) \right),
\end{aligned}
\tag{3.6}
$$

where the coefficients of Fourier expansion are,

$$
\begin{aligned}
a_0 &= \frac{1}{2\pi} \int_0^{2\pi} \frac{dN}{d\phi} d\phi &= \frac{x_0}{2\pi} \\
a_n &= \frac{1}{\pi} \int_0^{2\pi} \frac{dN}{d\phi} \cos(n\phi) d\phi &= \frac{x_n}{\pi} \\
b_n &= \frac{1}{\pi} \int_0^{2\pi} \frac{dN}{d\phi} \sin(n\phi) d\phi &= \frac{y_n}{\pi}.
\end{aligned}
\tag{3.7}
$$

As there are finite number of particles in each event, the Fourier coefficients x_n and y_n can be expressed as (from Eq. 3.7):

$$x_n = \int_0^{2\pi} \frac{dN}{d\phi} \cos(n\phi)d\phi = \sum_{i=1}^{N} w_i \cos(n\phi_i) \equiv Q_x, \qquad (3.8)$$

$$y_n = \int_0^{2\pi} \frac{dN}{d\phi} \sin(n\phi)d\phi = \sum_{i=1}^{N} w_i \sin(n\phi_i) \equiv Q_y, \qquad (3.9)$$

where N is number of particles used to calculate the event plane angle. ϕ_i is the azimuthal angle of the ith particle and w_i are the weights, which can be p_T, ϕ etc. The weights are used to maximize the event plane resolution by maximizing the flow contributions to the flow vector. The vector $\mathbf{Q}$ (Q_x, Q_y) is known as flow vector. Now from Eq. 3.8 and 3.9, the reaction plane angle (ψ_R) can be defined as,

$$\psi_R = \frac{Q_y}{Q_x} = \frac{1}{n} \tan^{-1}\left(\frac{y_n}{x_n}\right), \quad 0 \leq \psi_R \leq \frac{2\pi}{n}. \qquad (3.10)$$

If azimuthal angle (ϕ) of a produced particle is measured with respect to the true reaction plane (ψ_R). Then $dN/d\phi$ in Eq. 3.6 becomes an even function and the integration terms containing sine would be zero. Then we can re-write Eq. 3.6 as,

$$\frac{dN}{d\phi} = \frac{x_0}{2\pi}(1 + 2\sum_{n=1}^{\infty} \frac{x_n}{x_0} \cos(n\,[\phi - \psi_R])). \qquad (3.11)$$

We can now define two variables,

$$v_n^{obs} = \frac{x_n}{x_0} \qquad (3.12)$$

$$\psi_n = \frac{1}{n} \tan^{-1}\left(\frac{y_n}{x_n}\right), \quad 0 \leq \psi_n \leq \frac{2\pi}{n} \qquad (3.13)$$

then Eq. 3.11 becomes,

$$\frac{dN}{d\phi} = \frac{x_0}{2\pi}\left(1 + 2\sum_{n=1}^{\infty} v_n^{obs} \cos(n\,[\phi - \psi_n])\right), \tag{3.14}$$

where v_n^{obs} is the magnitude of flow coefficients. ψ_n is the nth-order event plane angle, which is an estimate of true reaction plane angle (ψ_R). It is reconstructed for each event using azimuthal angle of the produced particles itself. Determination of the event plane angle is described in the following sub-sections. The event plane angle in general not always coincides with the true reaction plane in the experiments (because of the finite multiplicity N). If the error in the measurement of reaction plane is denoted by $\Delta\psi_R$, then $\psi_n = \psi_R + \Delta\psi_R$. We can obtain the relation between the observed flow coefficients v_n^{obs} and true flow coefficients v_n by averaging over all events ($\langle\rangle$):

$$
\begin{aligned}
v_n^{obs} &= \langle\cos(n[\phi - \psi_n])\rangle \\
&= \langle\cos(n[\phi - \psi_n + \psi_R - \psi_R])\rangle \\
&= \langle\cos(n[\phi - \psi_R] - n[\psi_n - \psi_R])\rangle \\
&= \langle\cos(n[\phi - \psi_R] - n[\Delta\psi_R])\rangle \\
&= \langle\cos(n[\phi - \psi_R]).\cos(n\Delta\psi_R)\rangle + \langle\sin(n[\phi - \psi_R]).\sin(n[\Delta\psi_R])\rangle \\
&= \langle\cos(n[\phi - \psi_R]).\cos(n\Delta\psi_R)\rangle \\
&= v_n \langle\cos(n\Delta\psi_R)\rangle. \tag{3.15}
\end{aligned}
$$

Here, to arrive at Eq. 3.15, we have assumed that the $\phi - \psi_R$ and $\Delta\psi_R$ are statistically independent and the average sine term vanishes because of their reflection symmetry. These assumption are valid for the system with large multiplicity.

3.6.1 Determination of event plane

Reaction plane is defined as the plane formed by the beam axis (z-axis) and the impact parameter vector (perpendicular distance between the center of colliding nuclei). The angle between x-axis and the reaction plane is called the reaction plane angle (ψ_R). Experimentally, the impact parameter cannot be measured directly. Therefore it is not possible to find reaction plane angle for a collision in an experiment. The estimated reaction plane is determined from the produced particles, known as event plane. The nth-order event plane angle ψ_n is calculated using [8],

$$\psi_n = \frac{1}{n} \tan^{-1} \left(\frac{Q_{ny}}{Q_{nx}} \right) \tag{3.16}$$

$$Q_n \cos(n\psi_n) \;=\; Q_{nx} = \sum_{i=1}^{N} w_i \cos(n\phi_i). \tag{3.17}$$

$$Q_n \sin(n\psi_n) \;=\; Q_{ny} = \sum_{i=1}^{N} w_i \sin(n\phi_i). \tag{3.18}$$

Where Q_n are the nth-order event flow vectors, w_i are the weight and N is the total number of particles in a event used for flow vector calculation. The imperfect azimuthal symmetry of the TPC (affected by imperfections such as sector boundaries, non-uniform efficiency, temporarily dead channels, etc.) makes the reconstructed event plane distribution non-uniform (not-flat), and could bias flow measurements if not corrected for this effect. To correct this non-uniformity, three methods are widely used, namely phi weighting, re-centering and shifting. Figure 3.11 shows raw event plane angle distribution for various order.
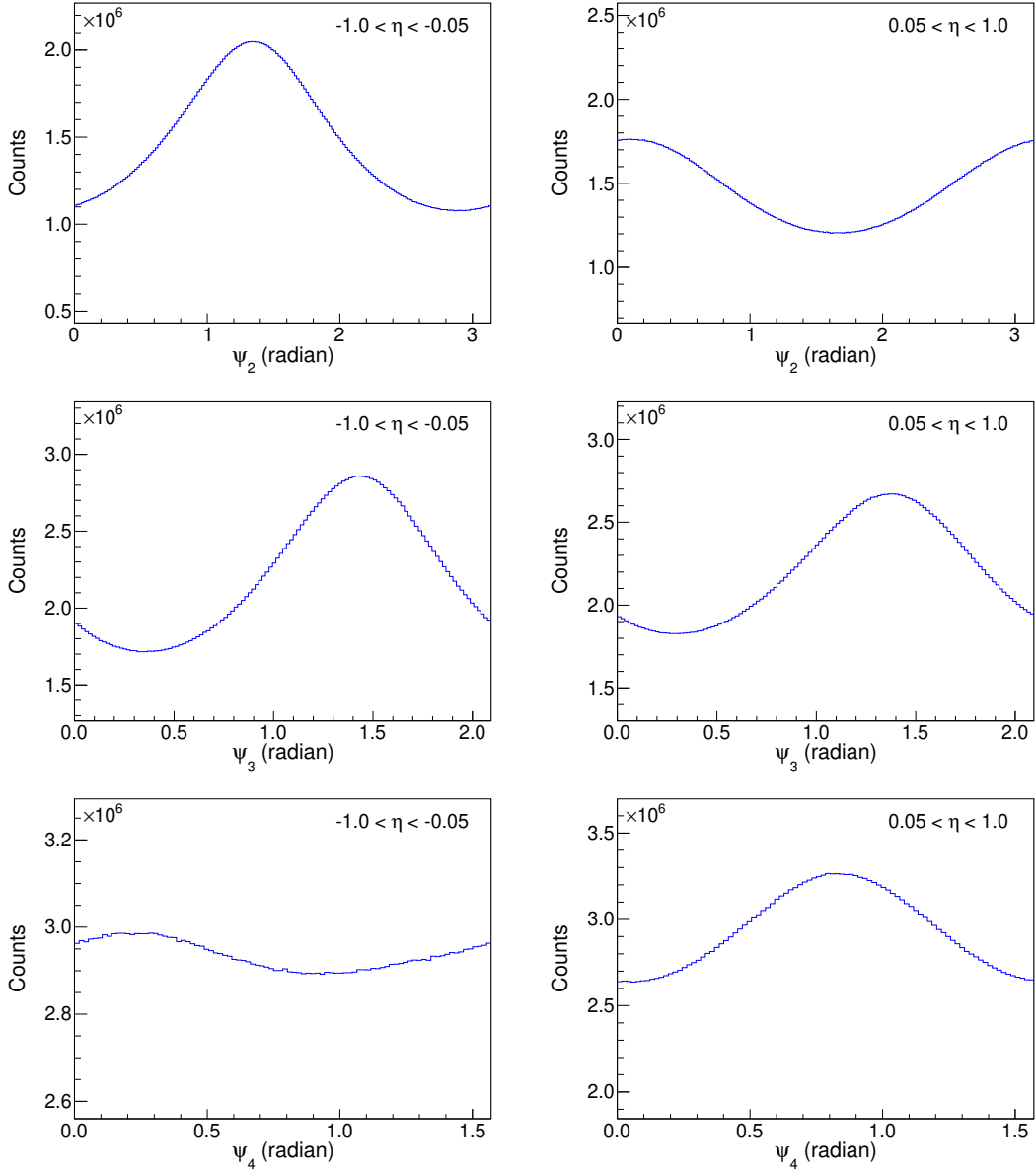
Figure 3.11: Uncorrected (Raw) event plane angle distributions for east (-1.0 < η < -0.05) and west (0.05 < η < 1.0) in U+U collisions at $\sqrt{s_{NN}}$ = 193 GeV.

In order to minimize the contribution to the event plane determination from effects and phenomena which are not necessarily correlated with the event plane, called non-flow effects, for example jets, only particles with $p_T < 2$ GeV/c were used in the calculation. A list of track cuts for calculation of the event plane angle are shown in Table 3.10.

Table 3.10: Track selection cuts for event plane angle.

Number of fit points in TPC	nHitsFit > 15
nHitsFit/nHitsPoss	Ratio ≥ 0.52
DCA to primary vertex	$|DCA| < 2.0$ cm
Transverse momentum	$0.15 < p_T < 2.0$ (GeV/c)
Pseudo-rapidity	$|\eta| < 1.0$
Pseudo-rapidity gap	$\Delta\eta = 0.1$

3.6.2 Detector acceptance corrections

The event plane angle is random in the laboratory frame. Its distribution should be uniform for a perfect detector. However, in the experiments, finite detector acceptance can lead to anisotropic particle distributions in the laboratory frame. Therefore it is necessary to ensure that the event plane angle distribution over all events is isotropic (i.e. flat with respect to azimuthal angle ϕ). In this section, we discussed about the phi-weight, re-center and shift correction needed to correct non-uniformity in the event plane angle distribution due to detector acceptance.

3.6.2.1 ϕ-weight correction

The weight factor used for the event plane angle correction is $w_i = p_{Ti} \times w_\phi$ [8]. The ϕ-weight factor, w_ϕ, is necessary to correct for the detector acceptance effects which can lead to anisotropic particle distributions in the laboratory frame, which are not due to anisotropic flow. This is done by finding the azimuthal distribution of all particles used in the event plane determination over many events and taking the inverse (per ϕ bin) as the correction factor w_ϕ. Figure 3.12 shows the raw distributions of ϕ-weight for a centrality bin. The corrections are performed for the positive and negative η regions and for positive and negative V_z regions separately in U+U collisions at $\sqrt{s_{NN}}$

= 193 GeV for 9 different centrality classes.
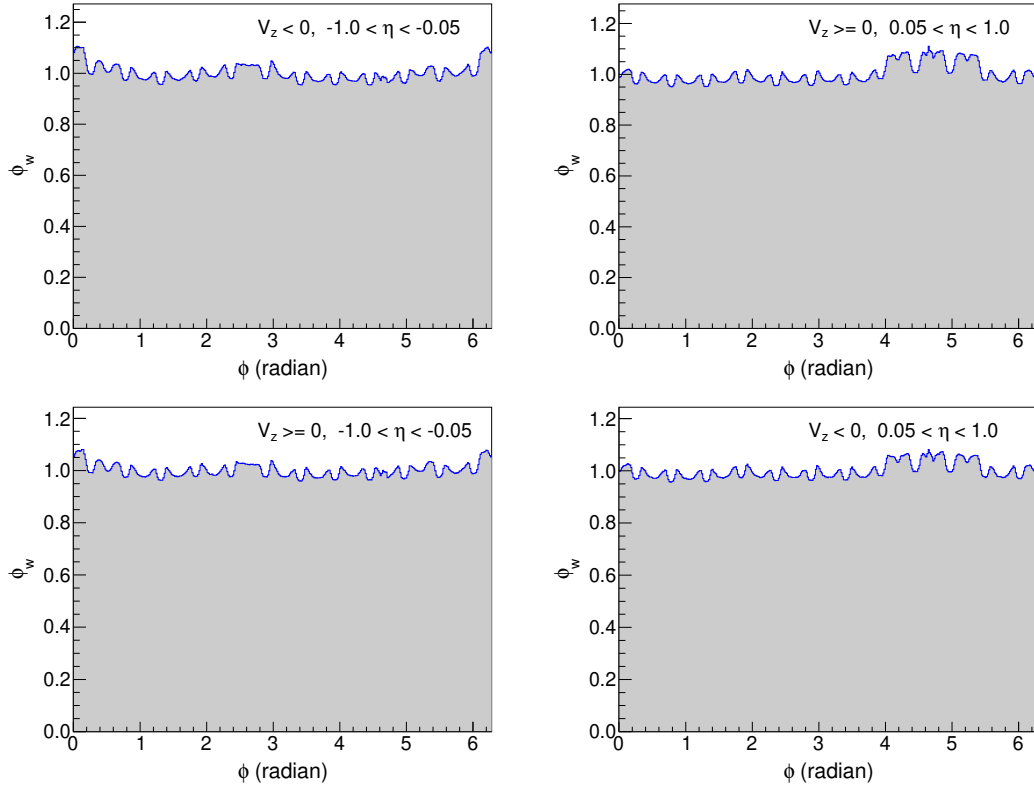
Figure 3.12: ϕ-weight distributions of charged particles used in determination of the event plane, for negative (left panels) and positive (right panels) pseudo-rapidity (η) in U+U collisions at $\sqrt{s_{\mathrm{NN}}} = 193$ GeV.

The ϕ-weight method has few disadvantages. This method will not work if the azimuthal distribution of the particles is either zero for some *phi*-range or very low in phase-space. This situation can occur because of the few dead sectors in the TPC during collection of data. This method also does not take into account the multiplicity fluctuations around the mean value. Therefore other methods are necessary for the correction of event plane angle distribution.

3.6.2.2 Recenter correction

The second method for the correction of event plane angle is known as re-centering [36]. In recenter correction method, average flow vector $< Q_{nx} >$ and $< Q_{ny} >$ are cal-

culated run-by-run for different centrality classes as correction factors. Then the correction factors are applied event-by-event to correct the flow vector as:

$$
\begin{aligned}
Q_{nxi} &= w_i \cos(n\phi_i) - <Q_{nx}>, \\
Q_{nyi} &= w_i \sin(n\phi_i) - <Q_{ny}> .
\end{aligned}
\tag{3.19}
$$

The disadvantage of this method is that it does not eliminate the higher order harmonics from the distribution of lower order event plane angle. To eliminate contributions of higher harmonics, the event plane angle has been further corrected by the event-by-event shift correction method.

3.6.2.3 Shift correction

In the shift correction method [8], a correction term $\Delta\psi$ is calculated from the re-center corrected event plane distribution. The event plane angle distribution can be expanded in a Fourier series as follows:

$$
\frac{dN}{d\psi} = \frac{a_0}{2} + \sum_n (a_n \cos n\psi + b_n \sin n\psi),
\tag{3.20}
$$

where a_n and b_n are given by,

$$
\begin{aligned}
a_n &= \frac{1}{\pi} \int_{-\pi}^{\pi} \frac{dN}{d\psi} \cos n\psi d\psi, \quad n = 0, 1, 2.... \\
b_n &= \frac{1}{\pi} \int_{-\pi}^{\pi} \frac{dN}{d\psi} \sin n\psi d\psi, \quad n = 1, 2, 3....
\end{aligned}
$$

Then the corrected event plane angle ψ' can be written as,

$$
\psi' = \psi + \Delta\psi
\tag{3.21}
$$

94

where $\Delta\psi$ is the correction term and can be written in the form,

$$\Delta\psi = \sum_n (A_n \cos n\psi + B_n \sin n\psi). \tag{3.22}$$

By imposing the condition of a flat event plane angle distribution on Eq. 3.21, which require the nth Fourier harmonic to be vanish, it is found that

$$\frac{dN}{d\psi'} = \frac{N}{2\pi} = \frac{a_0}{2}. \tag{3.23}$$

We can write Eq. 3.21 as,

$$\psi' = \psi + \sum_n (A_n \cos n\psi + B_n \sin n\psi), \tag{3.24}$$

using Eq. 3.24,

$$\frac{dN}{d\psi} = \frac{dN}{d\psi'}\frac{d\psi'}{d\psi}$$
$$\frac{dN}{d\psi} = \frac{a_0}{2}\left[1 + \sum_n (-nA_n \sin n\psi + nB_n \cos n\psi)\right]. \tag{3.25}$$

Comparing the above with Eq. 3.20, we can get the coefficients A_n and B_n. We can write the Fourier series coefficients a_n and b_n in terms of average as $<\cos n\psi>$ and $<\sin n\psi>$. Then the corrected event plane distribution becomes,

$$\psi' = \psi + \sum_n \frac{2}{n}(-\langle\sin n\psi\rangle \cos n\psi + \langle\cos n\psi\rangle \sin n\psi). \tag{3.26}$$

Here, the angular brackets denote the average over a large number of events. To get a reasonably flat event plane distribution, it is necessary to repeat the calculation of the correction term multiple times. In this analysis, we use up to the 20th harmonic

to flatten the event plane angle distribution. The equation for the shift correction for n^{th} harmonic event plane angle used is,

$$\Delta\psi_n = \frac{1}{n}\sum_{i=1}^{i_{max}}\frac{2}{i}[-\langle\sin(in\psi_n)\rangle\cos(in\psi_n) + \langle\cos(in\psi_n)\rangle\sin(in\psi_n)]. \qquad (3.27)$$

Figure 3.13 shows uncorrected, recenter corrected and recenter + shift corrected event plane angle distributions for $n = 2, 3, 4$ harmonic in U+U collisions at $\sqrt{s_{\mathrm{NN}}}$ = 193 GeV. The final corrected distributions are fitting with a polynomial function,

$$f(x) = p_0[1 + p_1\cos(nx) + p_2\sin(nx)]. \qquad (3.28)$$

The fit parameter p_1 and p_2 are consistent with zero indicating that the event plane angle distributions are flat. Now the event plane is flat, measurement of flow coefficients v_n will not be affected by the biases due to the detector acceptance.

3.6.3 Event plane resolution correction

The estimated event plane angle ψ_n depends on the flow magnitude and the multiplicity of the particles used in the determination of the event plane. The estimated event plane may not always coincide with the true reaction plane. Therefore one has to calculate event plane resolution (R) for this difference. Then the observed v_n^{obs} should be corrected as [8],

$$v_n = \frac{v_n^{obs}}{R} = \frac{v_n^{obs}}{\langle\cos n(\psi_n - \psi_R)\rangle}. \qquad (3.29)$$

Here ψ_R is true reaction plane, which is unknown. Therefore, event plane resolution is calculated by the correlation of two independent sub-events, namely A and B.
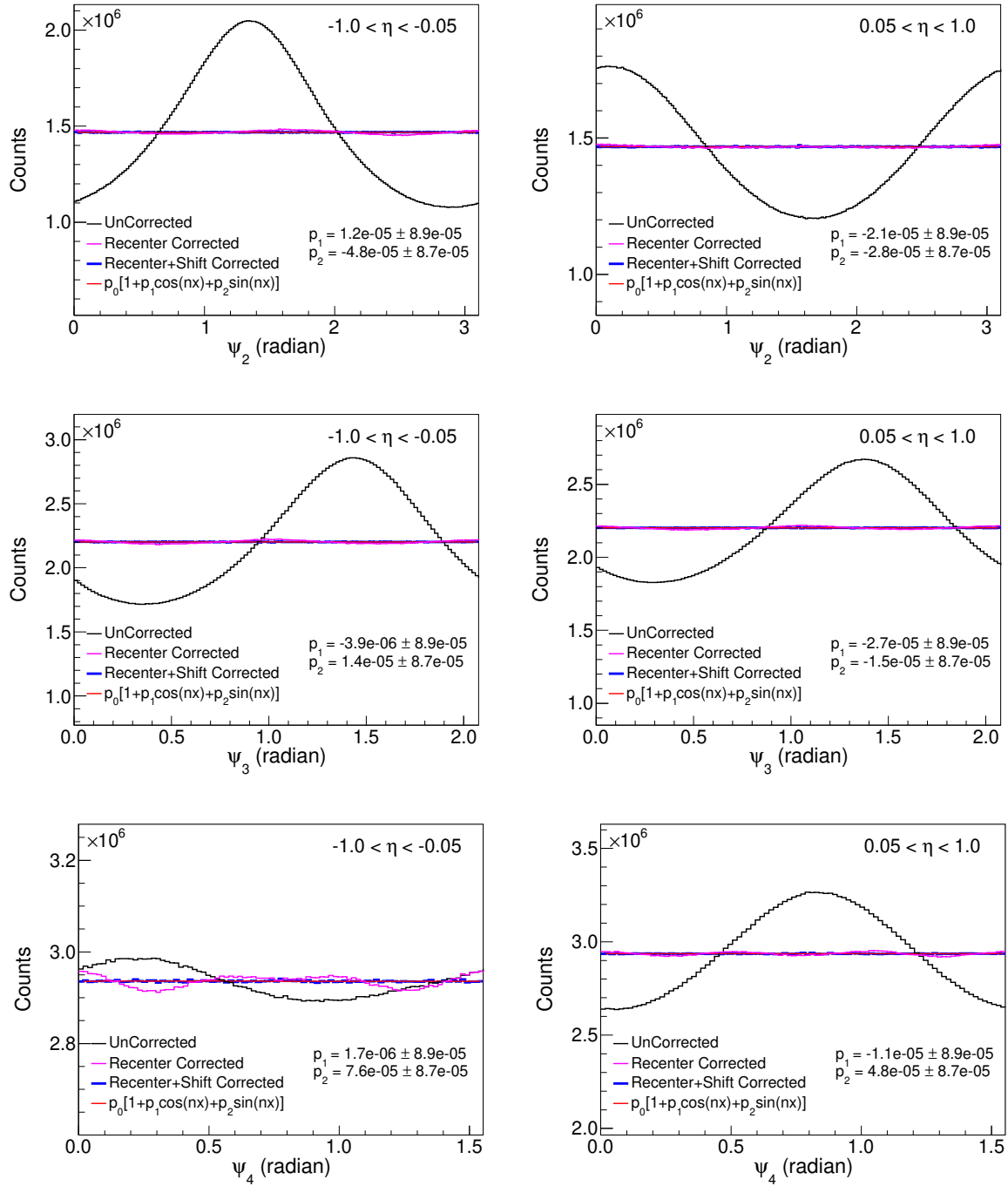
Figure 3.13: Distributions of event plane angle corrected with phi-weight, re-center and shift method, for negative (left panels) and positive (right panels) pseudo-rapidity (η) in U+U collisions at $\sqrt{s_{\mathrm{NN}}} = 193$ GeV. The solid red lines represent fit to the corrected event plane angles.

The two sub-events are constructed by dividing the TPC acceptance into two similar multiplicity groups. These sub-event groups are based on the pseudo-rapidity regions $(-1.0 < \eta < -0.05)$ and $(0.05 < \eta < 1.0)$, with a η-gap of 0.1 between the two sub-events. If the two sub-events have approximately same multiplicity, hence their resolution are similar, then the event plane resolution can be estimated as,

$$R_{sub} = \langle \cos n(\psi_n - \psi_R) \rangle \approx \sqrt{\langle \cos n(\psi_n^A - \psi_n^B) \rangle}. \qquad (3.30)$$
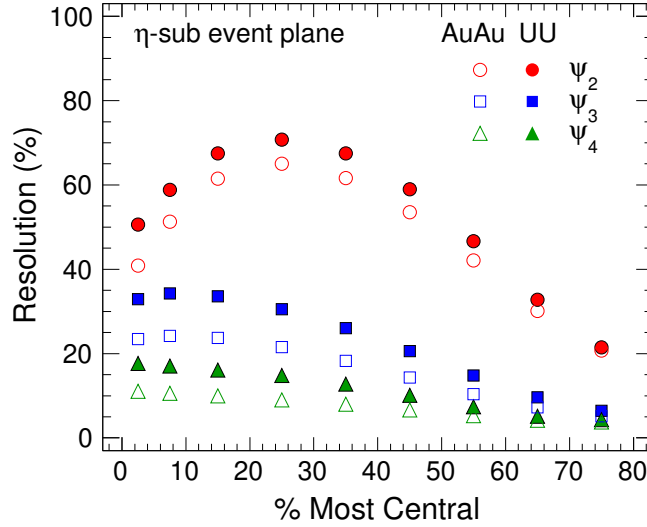
Figure 3.14: Event plane resolution as a function of centrality for ψ_2, ψ_3 and ψ_4 in U+U collisions at $\sqrt{s_{\mathrm{NN}}} = 193$ GeV compared with Au+Au collisions at $\sqrt{s_{\mathrm{NN}}} = 200$ GeV.

In this analysis, the event plane resolution is calculated for 9 different centrality classes (0-5%, 5-10%, 10-20%, 20-30%, 30-40%, 40-50%, 50-60%, 60-70%, 70-80%). The event plane resolution varies with the centrality. Since the resolution depends on the number of particles used for the event plane reconstruction, therefore it increases from peripheral to central collisions. It also depends on the strength of the anisotropic flow of the events itself, therefore the resolution decreases for more central collisions where anisotropic flow is small. Because of these two competing effects the resultant resolution first increases from peripheral to mid-central collision and then decreases

again. Figure 3.14 shows the η-sub event plane resolution as a function of centrality for ψ_2, ψ_3 and ψ_4 in U+U collisions at $\sqrt{s_{\text{NN}}} = 193$ GeV. A comparison with the event plane resoultion for Au+Au collisions at $\sqrt{s_{\text{NN}}} = 200$ GeV is also shown. It shows the event plane resolution is more in U+U collisions compared to Au+Au collisions. This is expected because of higher multiplicity density in U+U collisions compared to Au+Au collisions [37].

The values of TPC event plane resolution from η-sub events for U+U collisions at $\sqrt{s_{\text{NN}}} = 193$ GeV are shown in the Table 3.11. Statistical errors on the resolution are less than 4% for all the orders in all centrality classes.

Table 3.11: n^{th}-order event plane resolution for η-sub event method in U+U collisions at $\sqrt{s_{\text{NN}}} = 193$ GeV.

Centrality	Resolution(ψ_2)	Resolution(ψ_3)	Resolution(ψ_4)
0-5%	0.506 ± 0.0002	0.329 ± 0.0003	0.177 ± 0.0005
5-10%	0.588 ± 0.0001	0.342 ± 0.0002	0.171 ± 0.0005
10-20%	0.674 ± 0.0001	0.336 ± 0.0002	0.161 ± 0.0004
20-30%	0.707 ± 0.0001	0.305 ± 0.0002	0.148 ± 0.0004
30-40%	0.675 ± 0.0001	0.260 ± 0.0002	0.127 ± 0.0005
40-50%	0.590 ± 0.0001	0.206 ± 0.0003	0.101 ± 0.0006
50-60%	0.466 ± 0.0001	0.148 ± 0.0004	0.074 ± 0.0008
60-70%	0.328 ± 0.0002	0.096 ± 0.0006	0.052 ± 0.0012
70-80%	0.215 ± 0.0003	0.065 ± 0.0011	0.043 ± 0.0016

In case of wide centrality classes (e.g. 0-10%, 10-40% and 40-80%), the combined resolution is calculated as the average of the resolutions weighted by the raw-yield. A summary of the raw-yield weighted average resolution correction factors for the wide centrality bins are shown in Table 3.13 in the Appendix at the end of this chapter.

3.6.4 v_n extraction methods

3.6.4.1 $\phi - \psi_n$ binning method

The $\phi-\psi_n$ binning method is used for the extraction of flow coefficients v_n of identified particles. In this method raw yield (number of particles) of the chosen particle is measured in the bins of angle $(\phi - \psi_n)$, where ϕ is the azimuthal angle of the particle in the lab-frame and ψ_n is the nth-order event plane angle. The measured distribution $dN/d(\phi - \psi_n)$ is fitted with the functional form of Fourier function to extract v_n.

For particles like ϕ, K_s^0, Λ, Ξ and Ω, where the signal consists of a mass peak sitting above a large combinatorial background as discussed in section 3.5, it is therefore necessary to remove the background from the signal to extract of raw yield of the particle. Raw yields extraction is done by two methods, function fit (for resonance like ϕ-meson) and bin-counting (for weak decay particles K_s^0, Λ, Ξ and Ω).

An illustration of the raw-yield extraction using function fit for ϕ-meson is shown in the Fig. 3.15. The ϕ-meson signal after subtraction of mixed event background is fitted with a Breit-Wigner plus a 2nd order polynomial function for residual background shown by the red line. The invariant mass range chosen for fitting is $0.995 < m_{inv} < 1.075$ (GeV/c^2). The ϕ-meson yield is calculated by integrating the Breit-Wigner function only. This procedure is repeated for various p_T ranges and five $\phi-\psi_n$ bins extend over $[0, \pi/n]$ in each p_T bin.

Raw-yields for weak-decay particles, K_s^0, Λ, Ξ and Ω are extracted using bin-counting. In bin-counting method, histogram bin content are added in a defined invariant mass range. An invariant mass range of $\pm$ 20 MeV is taken for K_s^0 and $\Lambda(\bar{\Lambda})$ around their mass values. For $\Xi(\bar{\Xi})$ and $\Omega(\bar{\Omega})$ bin counting is done in the invariant mass range of ± 10 MeV around their mass values from PDG. The same procedure is followed for all p_T bins and each $\phi - \psi_n$ bin within a p_T bin for all centrality classes

in U+U collisions at $\sqrt{s_{\mathrm{NN}}} = 193$ GeV. Figure 3.16 shows the raw-yield extraction using bin-counting method.
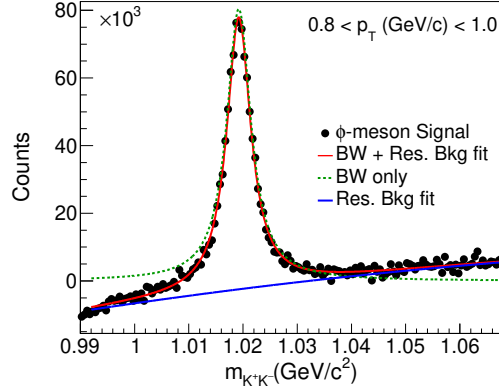
Figure 3.15: ϕ-meson invariant mass distribution for $0.8 < p_T < 1.0$ (GeV/c) for 0-80% centrality in U+U collisions at $\sqrt{s_{\mathrm{NN}}} = 193$ GeV. The distribution is fitted with a Breit-Wigner plus 2nd order polynomial function to extract raw-yield.
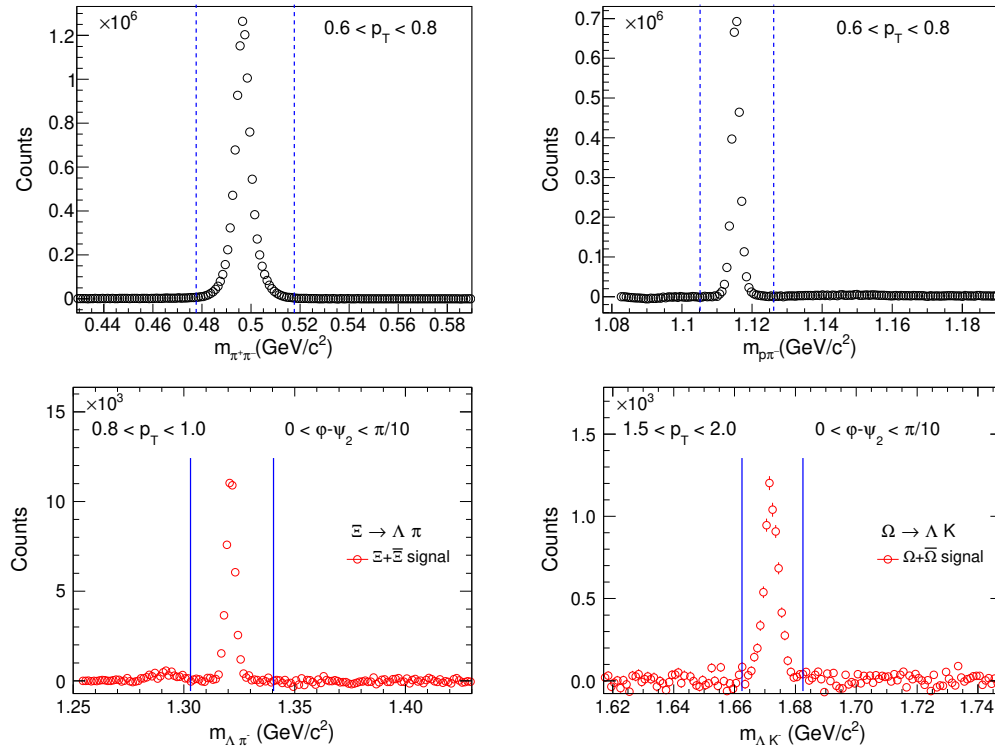
Figure 3.16: Invariant mass distributions for K_s^0, Λ, Ξ and Ω in a fix p_T (GeV/c) bin for 0-80% centrality in U+U collisions at $\sqrt{s_{\mathrm{NN}}} = 193$ GeV. The blue vertical lines represent the invariant mass range taken for bin-counting to extract raw-yield.

The raw yields extracted as a function of $\phi - \psi_n$ in a given p_T bin for particles ϕ, K_s^0, Λ, Ξ and Ω in mid-rapidity for minimum-bias (0-80%) U+U collisions at $\sqrt{s_{NN}}$ = 193 GeV are shown in the Fig. 3.17. The obtain raw yields are fitted with the function,

$$\frac{dN}{d(\phi - \psi_n)} = A\left(1 + 2v_n^{obs}\cos n(\phi - \psi_n)\right), \qquad (3.31)$$

where A and v_n^{obs} are the fit parameters. The measured v_n^{obs} values obtained from fit are divided by the appropriate event plane resolution to get final v_n values. The p_T dependence of the flow coefficients is studied by repeating the above procedure for fixed ranges in p_T for various centrality classes in U+U collisions at $\sqrt{s_{NN}}$ = 193 GeV.
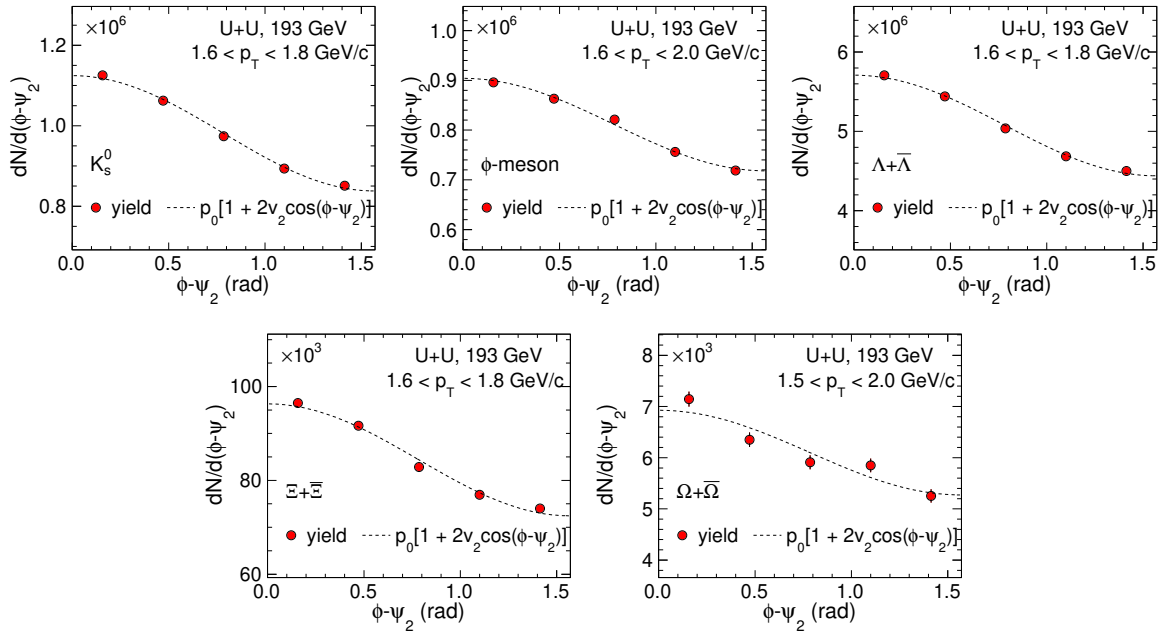
Figure 3.17: $\phi - \psi_n$ ($n = 2$) distributions for K_s^0, ϕ, Λ, Ξ and Ω in mid-rapidity for 0-80% centrality in U+U collisions at $\sqrt{s_{NN}}$ = 193 GeV. The black dashed curves represent the fits to the raw-yield as mentioned in Eq. 3.31 to extract v_n coefficients. Error bars shown are the statistical uncertainties.

3.6.4.2 Invariant mass method

Invariant mass method [38] for the extraction of v_n coefficients is used for the particles which decay into two daughter particles like K^0_s, ϕ, Λ, Ξ and Ω. In this method v_n of a reconstructed particle is calculated as a function of its invariant mass (m_{inv}) using equation $v_n^{S+B} = \langle \cos[n(\phi - \psi_n)] \rangle$. The measured v_n^{S+B} can be decomposed in the following functional form,

$$v_n^{S+B}(m_{inv}) = v_n^S \frac{S}{S+B}(m_{inv}) + v_n^B(m_{inv}) \left[1 - \frac{S}{S+B}(m_{inv}) \right], \qquad (3.32)$$

where v_n^S, v_n^B and v_n^{S+B} are the flow coefficients (v_n) of the signal, background and total particle, respectively. The term $\frac{S}{S+B}$ is the ratio of yield of signal (S) and total (S+B), which is a function of invariant mass. $v_n^B(m_{inv})$ is parameterized as a 3rd order polynomial function. v_n^S is a fit parameter. The measured v_n^{S+B} distribution is fitted with the Eq. 3.32 as shown in Fig. 3.18. The v_n parameter obtained from the fit are then corrected for the corresponding event plane resolution.
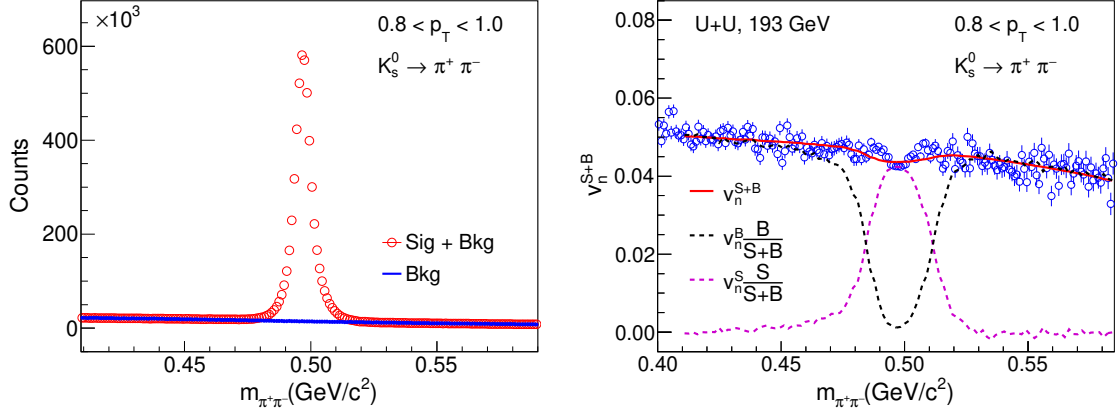
Figure 3.18: An illustration of invariant mass method for v_n measurements. Signal+Background and Background (left panel) and measured v_n^{S+B} distributions (right panel) for K^0_s at mid-rapidity for $0.8 < p_T < 1.0$ GeV/c in minimum bias U+U collisions at $\sqrt{s_{NN}} = 193$ GeV. The curves represent the fits to the v_n^{S+B} distribution as mentioned in Eq. 3.32 to extract v_n coefficients.

In this thesis, we have used $\phi - \psi_n$ binning method as default for the measurements of flow coefficients v_n. Results from the invariant mass method are consistent with the $\phi - \psi_n$ binning method within statistical uncertainties. The difference between the two method is taken into account as systematic uncertainty. We will discuss about systematic uncertainties in the next section.

3.7 Systematic uncertainties

Point-by-point systematic uncertainties on v_n coefficients are studied by varying parameters used for the event selection, track selection, particle identification, V0 topology and combinatorial background. Most of the parameters are varied $\sim 20\%$ from their reference values. For all systematic checks, the parameters are changed one at a time. For each variation, root mean square deviation (RMS) from default value is calculated using,

$$RMS = \sqrt{\frac{1}{n}\sum_{i=1}^{n}(y_i - y_{def})^2} \tag{3.33}$$

where n = the total number of variations used for the systematic study.

Lists of cuts varied for event selection, track selection, V0 topology for the study of systematic uncertainties are presented in the Appendix at the end of this chapter. An average of $\sim 10\%$ systematic uncertainty on v_2, $\sim 15\%$ on v_3 and $\sim 25\%$ on v_4 is found for strange and multi-strange hadrons in U+U collisions at $\sqrt{s_{\mathrm{NN}}} = 193$ GeV.

3.8 Results and Discussion

In this section, we present the systematic measurements of flow coefficients v_n as a function of transverse momentum (p_T) from U+U collisions at $\sqrt{s_{\mathrm{NN}}} = 193$ GeV for minimum bias (0-80%) and centrality classes 0-10%, 10-40% and 40-80%. The results are presented for strange and multi-strange hadrons K_s^0, ϕ, $\Lambda(\bar{\Lambda})$, $\Xi(\bar{\Xi})$ and $\Omega(\bar{\Omega})$ at mid-rapidity ($|y| < 1$).

3.8.1 Transverse momentum dependence of $v_n(p_T)$

Figure 3.19 shows the p_T dependence of v_n coefficients for K_s^0, ϕ, $\Lambda + \bar{\Lambda}$, $\Xi + \bar{\Xi}$ and $\Omega + \bar{\Omega}$ in minimum bias (0-80%) U+U collisions at $\sqrt{s_{\mathrm{NN}}} = 193$ GeV. The results are compared with the published elliptic flow (v_2) in Au+Au collisions at $\sqrt{s_{\mathrm{NN}}} = 200$ GeV. The data for the results of Au+Au collisions are taken from the Ref. [39, 40]. The two analyses are done under similar conditions, therefore direct comparison with the new results from U+U collisions data is possible. The results from U+U collisions are represented by the solid markers. Statistical errors are shown by the vertical lines. Systematic uncertainties are represented by the color bands. Open markers show the results from Au+Au collisions.

The v_n (n = 2,3,4) coefficients are measured upto $p_T \sim 5$ GeV/c for K_s^0, ϕ and $\Lambda + \bar{\Lambda}$ and upto $p_T \sim 4$ GeV/c for $\Xi + \bar{\Xi}$ and $\Omega + \bar{\Omega}$. Elliptic flow v_2 increases with p_T and then saturates at higher p_T. This p_T dependence of v_2 in U+U collisions is consistent with the corresponding results from Au+Au collisions. A similar p_T dependence for higher harmonics v_3 and v_4 is also observed in U+U collisions. The magnitude of $v_2 > v_3 > v_4$ in minimum bias U+U collisions at $\sqrt{s_{\mathrm{NN}}} = 193$ GeV.
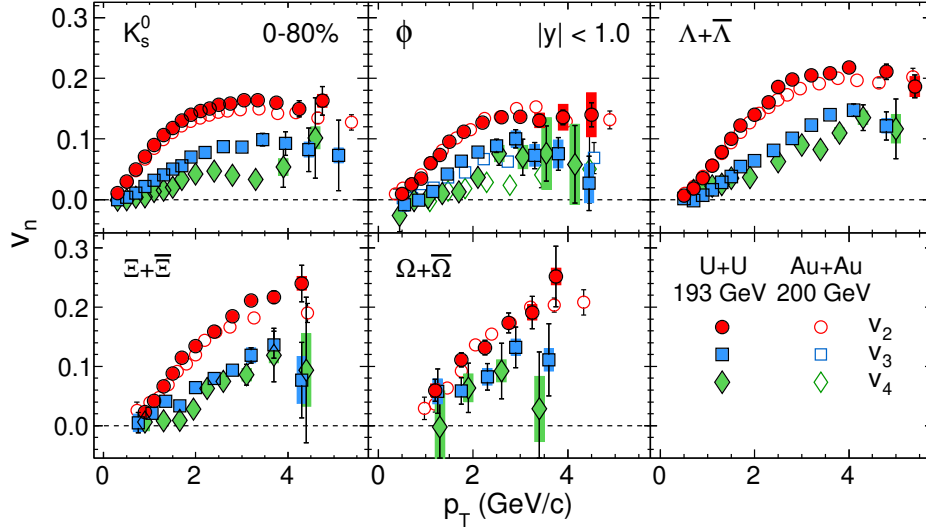
Figure 3.19: Flow coefficients v_n as a function of transverse momentum for K_s^0, ϕ, $\Lambda + \bar{\Lambda}$, $\Xi + \bar{\Xi}$ and $\Omega + \bar{\Omega}$ at mid-rapidity ($|y| < 1.0$) in minimum bias (0-80%) U+U collisions at $\sqrt{s_{NN}} = 193$ GeV. Statistical errors are shown by the vertical lines. Systematic uncertainties are represented by the bands. Open symbol shows results from Au+Au collisions at $\sqrt{s_{NN}}$ = 200 GeV [39, 40]. These results are STAR Preliminary.

3.8.2 Centrality dependence of $v_n(p_T)$

Figure 3.20 shows the $v_n(p_T)$ for strange and multi-strange hadrons at mid-rapidity, measured in U+U collisions at $\sqrt{s_{NN}} = 193$ GeV for three centrality classes: central (0-10%), mid-central (10-40%) and peripheral (40-80%). The results from U+U collisions are represented by the solid markers. Statistical errors are shown by the vertical lines. Systematic uncertainties are represented by the color bands. The results are compared with the published elliptic flow (v_2) in Au+Au collisions at $\sqrt{s_{NN}} = 200$ GeV [39, 40].

A clear centrality dependence is observed for v_2 in U+U collisions similar to Au+Au collisions. The v_2 values are higher in peripheral collisions than central collisions, which reflects the effect of the initial spatial anisotropy (higher eccentricity) on final momentum space azimuthal anisotropy. Higher order flow coefficients does not show a centrality dependence because they are generated due to the event-by-event fluctuations in the initial density profile of participating nucleons.
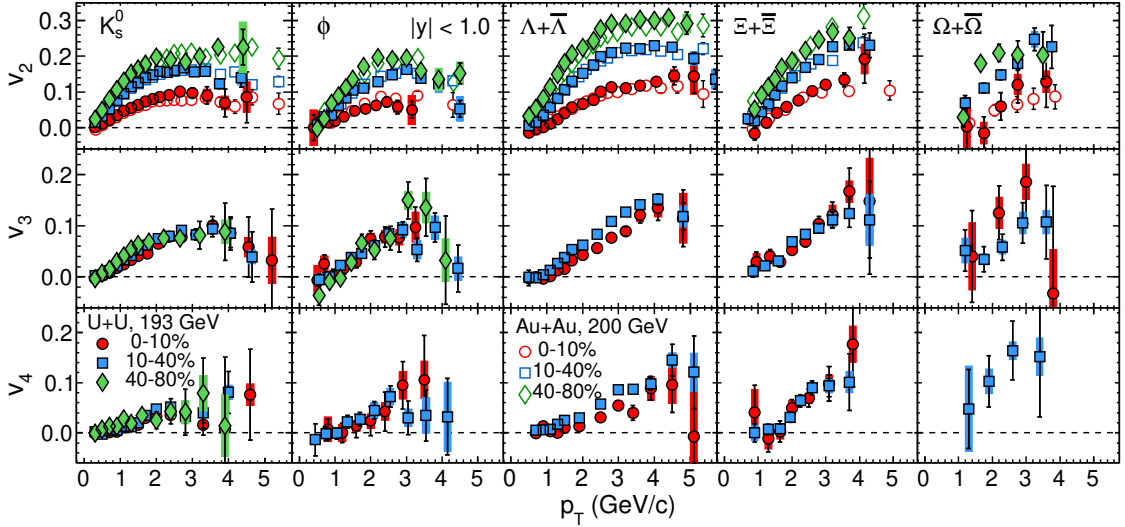
Figure 3.20: Flow coefficients v_n as a function of transverse momentum for K_s^0, ϕ, $\Lambda + \bar{\Lambda}$, $\Xi + \bar{\Xi}$ and $\Omega + \bar{\Omega}$ at mid-rapidity ($|y| < 1.0$) in U+U collisions at $\sqrt{s_{NN}} = 193$ GeV for centrality 0-10%, 10-40% and 40-80%. Statistical errors are shown by the vertical lines. Systematic uncertainties are represented by the bands. Open symbol shows the corresponding results from Au+Au collisions at $\sqrt{s_{NN}} = 200$ GeV. These results are STAR Preliminary.

3.8.3 Particle mass dependence of $v_n(p_T)$

Figure 3.21 shows the $v_n(p_T)$ for various particle species K_s^0, ϕ, $\Lambda + \bar{\Lambda}$, $\Xi + \bar{\Xi}$ and $\Omega + \bar{\Omega}$ at mid-rapidity, measured in minimum bias (0-80%) U+U collisions at $\sqrt{s_{NN}} = 193$ GeV. Statistical errors are shown by the vertical lines. Systematic uncertainties are represented by the bands.

Mass-ordering of strange and multi-strange hadron $v_2(p_T)$ is observed at low p_T (< 2 GeV/c) for the studied particles . For low p_T, lighter mass particles have higher v_2 than the heavier particles. This observed mass ordering of $v_2(p_T)$ is consistent with the predictions of hydrodynamic model of heavy-ion collisions [41]. A particle type (meson/baryon) dependence is observed beyond p_T (> 2 GeV/c), where all particles are grouped according to hadron type. v_2 of baryons (Λ, Ξ and Ω) is higher than the mesons (K_s^0 and ϕ). Higher order flow coefficients v_3 and v_4 seems to follow the same

trend as v_2 but it is difficult to conclude due to statistical fluctuations.
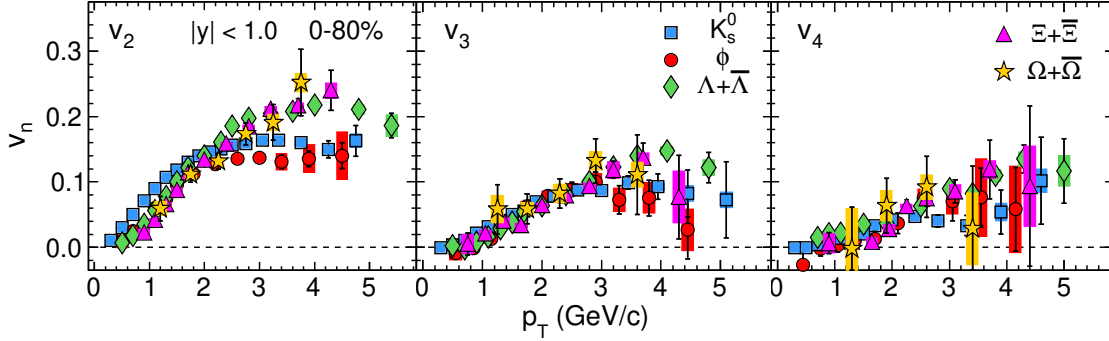
Figure 3.21: Flow coefficients v_2, v_3 and v_4 as a function of transverse momentum for K_s^0, ϕ, $\Lambda + \bar{\Lambda}$, $\Xi + \bar{\Xi}$ and $\Omega + \bar{\Omega}$ at mid-rapidity ($|y| < 1.0$) in U+U collisions at $\sqrt{s_{NN}} = 193$ GeV for centrality 0-80%. Statistical errors are shown by the vertical lines. Systematic uncertainties are represented by the bands. These results are STAR Preliminary.

3.8.4   Number of Constituent Quarks (NCQ) scaling

Quark coalescence [42] and recombination models [43] for heavy-ion collisions predict that if particles are made up of quarks then the elliptic flow $v_2(p_T)$ of the particles will scale with their number of constituent quarks. Such scaling indicates that the collective flow has been developed at the partonic phase of the medium created in heavy-ion collisions. Thus, NCQ scaling is considered as a evidence for partonic degrees of freedom. Previous measurements in Au+Au collisions at top RHIC energy show that the identified hadron elliptic flow scales with the number of consistuent quarks [44].

The large statistics data collected by the STAR detector in the year 2012 will allow us to test the NCQ scaling of v_2 and higher harmonics v_3 and v_4 in U+U collisions. Figure 3.22 shows the v_n divided by the powers of number of constituent quarks ($n_q^{n/2}$) as function of transverse kinetic energy $(m_T - m_0)/n_q^{n/2}$ for various particle species studied at mid-rapidity in U+U collisions at $\sqrt{s_{NN}} = 193$ GeV. Here n is the order of flow coefficients and m_0 is rest mass of the corresponding particle. Transverse mass

m_T is defined as $m_T = \sqrt{p_T^2 + m_0^2}$. The variable transverse kinetic energy is chosen in order to remove particle mass dependence from the flow coefficients. For v_2 (n = 2) the scale factor $n_q^{n/2}$ reduces to the usual $n_q^{2/2} = n_q$. We observed NCQ scaling of $v_2(p_T)$ for identified hadrons at mid-rapidity in U+U collisions at $\sqrt{s_{\mathrm{NN}}} = 193$ GeV for minimum bias (0-80%) and other centrality classes within statistical uncertainties.

Although, the NCQ scaling works fairly well at RHIC [44], but there are hints from the deviation of the universal NCQ scaling presented in the recently published work [40,45,46]. A modified scaling has been suggested for higher order flow harmonics v_n (n > 2). For v_3 and v_4 the scale factor $n_q^{n/2}$ will be modified than the usual n_q. Approximate NCQ scaling for v_3 and v_4 is observed in U+U collisions at $\sqrt{s_{\mathrm{NN}}}$ = 193 GeV within statistical and systematic uncertainties.
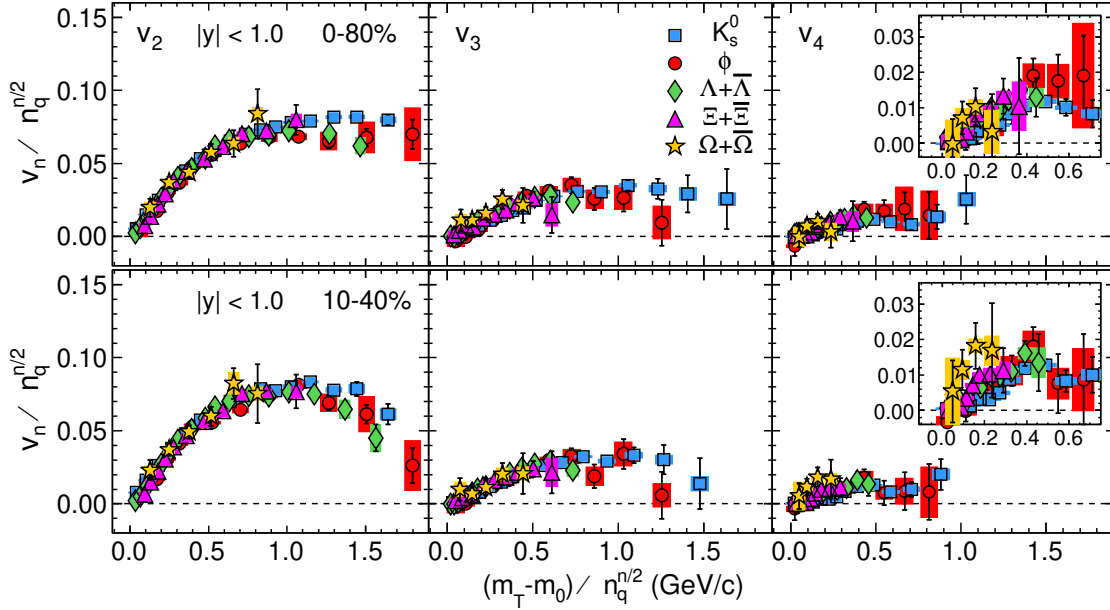
Figure 3.22: Flow coefficients v_n divided by the powers of the number of constituent quarks $(n_q^{n/2})$ as a function of $(m_T - m_0)/n_q^{n/2}$ at mid-rapidity ($|y| < 1.0$) in U+U collisions at $\sqrt{s_{\mathrm{NN}}} = 193$ GeV. Statistical errors are shown by the vertical lines. Systematic uncertainties are represented by the bands. These results are STAR Preliminary.

3.8.5 Comparison with $\pi^\pm$, $K^\pm$, $p(\bar{p})$

Figure 3.23 shows v_2 as function of p_T for K_s^0, ϕ and $\Lambda + \bar{\Lambda}$ at mid-rapidity in U+U collisions at $\sqrt{s_{NN}} = 193$ GeV for centrality 0-10%, 10-40% and 40-80%. The results are compared with the v_2 of light hadrons $\pi^\pm$, $K^\pm$ and $p(\bar{p})$. Statistical errors are shown by the vertical lines and systematic uncertainties by the color bands.

We observed a mass-ordered hierarchy of v_2 at low p_T (< 2 GeV/c) in U+U collisions at $\sqrt{s_{NN}} = 193$ GeV. The lighter mass particles have more v_2 than the heavier particles. For $p_T > 2$ GeV/c, we observed a particle type dependence (meson/baryon) within statistical uncertainties. The v_2 values form two different groups for baryons and mesons. The baryon group has higher flow than the meson group.
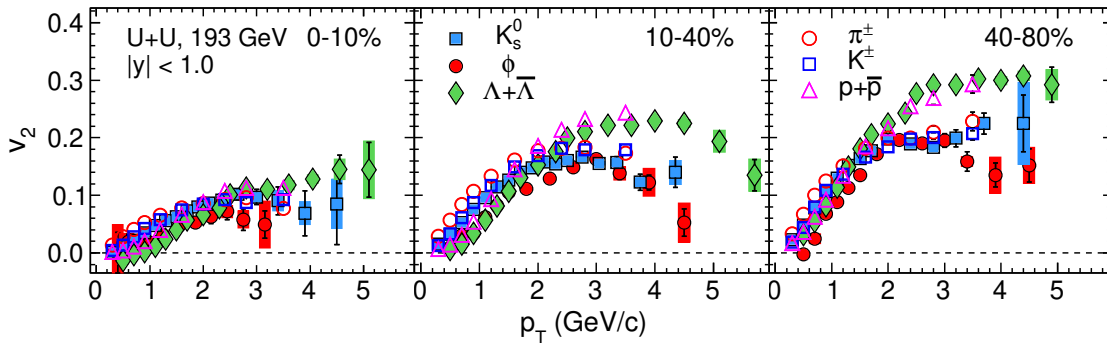
Figure 3.23: Elliptic flow v_2 as a function of p_T for $\pi^\pm$, $K^\pm$, $p(\bar{p})$, K_s^0, ϕ, and $\Lambda + \bar{\Lambda}$ at mid-rapidity ($|y| < 1.0$) in U+U collisions at $\sqrt{s_{NN}} = 193$ GeV for centrality classes 0-10%, 10-40% and 40-80%. Statistical errors are shown by the vertical lines. Systematic uncertainties are represented by the bands. These results are STAR Preliminary.

3.8.6 Model comparisons

Measurement of azimuthal anisotropy at RHIC has been compared with hydrodynamical calculations [47]. Hydrodynamical model calculations predict that v_2 as a function of p_T follows mass ordering. In addition to the hydrodynamical model, other models with dynamical evolution of the system, such as AMPT, which is based on

transport theory, are also able to describe some of the main features of measurements of azimuthal anisotropy [48, 49]. In this section, we have compared results of strange and multi-strange v_n in U+U collisions at $\sqrt{s_{\mathrm{NN}}} = 193$ GeV with these two theoretical model calculations.

A Multi Phase Transport (AMPT) model, is a hybrid transport model. It consists of four main stages: the initial conditions, partonic interactions, conversion from the partonic to the hadronic matter, and the hadronic interactions. AMPT model uses the same initial conditions as in HIJING [50]. Interactions among partons are modelled by Zhang's parton cascade [51], which calculates two-body parton-parton scatterings using cross sections from pQCD with screening masses. In the default AMPT model, partons are recombined with their parent strings and when they stop interacting, the resulting strings fragment into hadrons according to the Lund string fragmentation model [52]. In case of AMPT string melting scenario, the strings are melted into soft partons and a quark coalescence model is used to combine partons into hadrons. The evolution dynamics of the hadronic matter is described by A Relativistic Transport (ART) model [53].

The AMPT model is modified for the deformaed shape (prolate) of Uranium nucleus [37]. Various possible initial configuration of collisions like tip-tip, body-body, side-side and body-tip are implemented in the model. The initial parameter settings for the model follow the recommendation in the cited Ref. [49].

Figure 3.24 shows the comparison of v_n results from AMPT model in default and string melting scenario for strange and multi-strange hadrons at mid-rapidity in minimum bias (0-80%) U+U collisions at $\sqrt{s_{\mathrm{NN}}} = 193$ GeV. We observed that the AMPT model with string melting describe the mass-ordering of v_n coefficients at low p_T (< 2 GeV/c) and particle type dependence at $p_T > 2$ GeV/c. In contrast to data, the default AMPT model doesn't show particle type dependence of v_n coefficients.
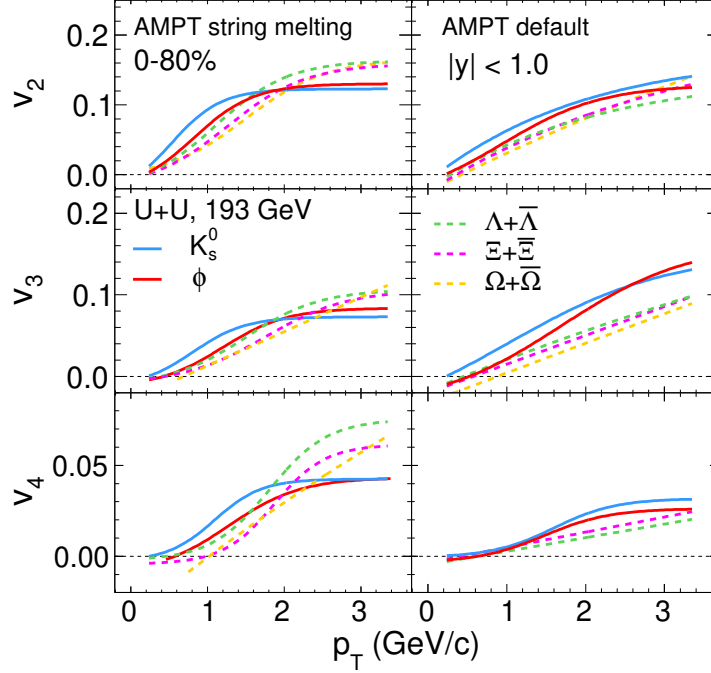
Figure 3.24: Comparison of flow coefficients $v_n(p_T)$ at mid-rapidity ($|y| < 1.0$) for U+U collisions at $\sqrt{s_{\mathrm{NN}}} = 193$ GeV for centrality 0-80% in AMPT default and string melting version. The solid lines and dashed lines represent the v_n values for mesons (K_s^0, ϕ) and baryons (Λ, Ξ and Ω), respectively.

Figure 3.25 shows the comparison of v_n as function of p_T between data and model calculations in U+U collisions at $\sqrt{s_{\mathrm{NN}}} = 193$ GeV for centrality classes 0-80% and 10-40%. AMPT string melting (SM) model (version v2.25t7d) with a parton-parton interaction cross-section of 3 mb is used for the calculations. The hyrdo-model results are from ideal-hydrodynamics model with LQCD equation of state [54]. We observed that AMPT model with 3 mb parton cross-section explain data at low p_T ($< 2\,\mathrm{GeV}/c$) in U+U collisions for all the particles studied. The hydro model results over-predicts the data, which shows the need of viscous corrections to the model.
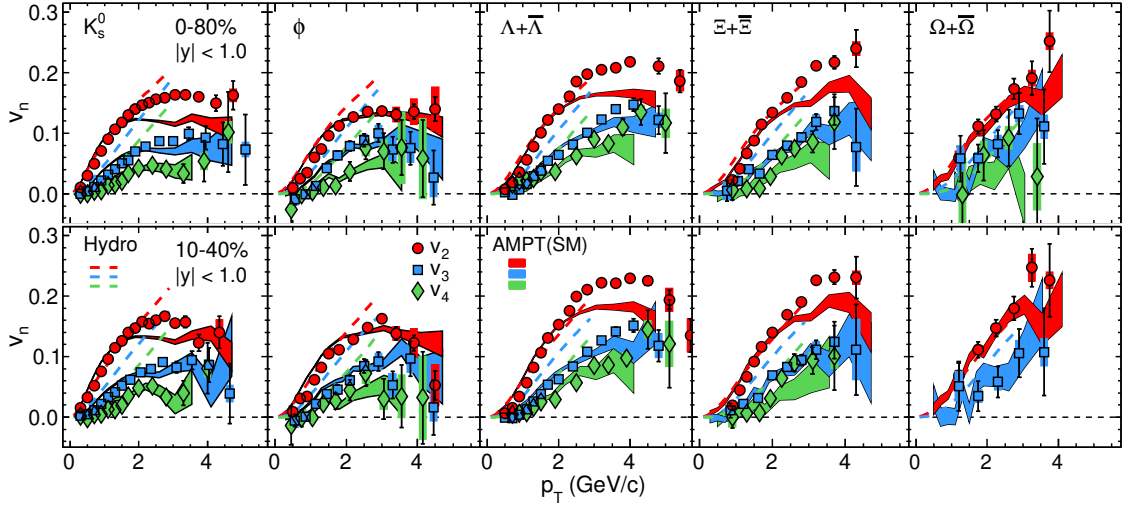
Figure 3.25: Comparison of flow coefficients $v_n(p_T)$ at mid-rapidity in U+U collisions at $\sqrt{s_{NN}} = 193$ GeV for centrality classes 0-80% and 10-40% with AMPT(SM) and hydrodynamic models. Markers represent the results from U+U collisions data. AMPT model calculations are shown by the bands and dashed lines represent the corresponding results from hydro-model. These results are STAR Preliminary.

3.8.7 Ratios of $v_n(p_T)$

Figure 3.26 shows the ratios of v_n as function of p_T at mid-rapidity in minimum bias U+U collisions at $\sqrt{s_{NN}} = 193$ GeV. The ratios calculated are of two types: (a) v_3/v_2 and (b) $v_4/(2v_2^2)$. For comparison, the ratios from AMPT(SM) and ideal-hydrodynamic model are also shown. Markers represent the results from U+U collisions data. AMPT model and hydro-model calculations are shown by the bands and black lines, respectively. Statistical error bars are shown by the vertical lines.

The ratio v_3/v_2 increases at low p_T (< 2.0 GeV/c), which shows that the relative strength of v_3 increases with the transverse momentum compared to v_2. This observation suggests that v_3 is more sensitive to viscosity than v_2 as predicted by the viscous hydrodynamics models [9, 55, 56]. We have also observed the ratio v_3/v_2 for $p_T > 2.0$ GeV/c becomes flat and does not depends on the mass of the particles. This mass independence of the ratio v_3/v_2 is also predicted by the viscous hydrodynamics

for fast particles (i.e high p_T particles) [57].

The ratio $v_4/(2v_2^2)$ shows a weak p_T dependence and its value approaches to 1.0 for $p_T > 2.0$ GeV/c. The values of the ratio $v_4/(2v_2^2)$ larger than 0.5 indicate deviations from ideal fluid behavior predicted by the hydrodynamical models [10, 57, 58]. The ratio $v_4/(2v_2^2)$ for identified hadrons is related to the $v_4/(2v_2^2)$ of quarks in simple coalescence models for heavy-ion collisions [59]. The large $v_4/(2v_2^2)$ ratio might also be an indication of large quark v_4 values. Results from ideal hydro-dynamical model showing the similar trend, but over-estimates the values of v_n ratios. AMPT(SM) model results agree well with the data within statistical uncertainties.
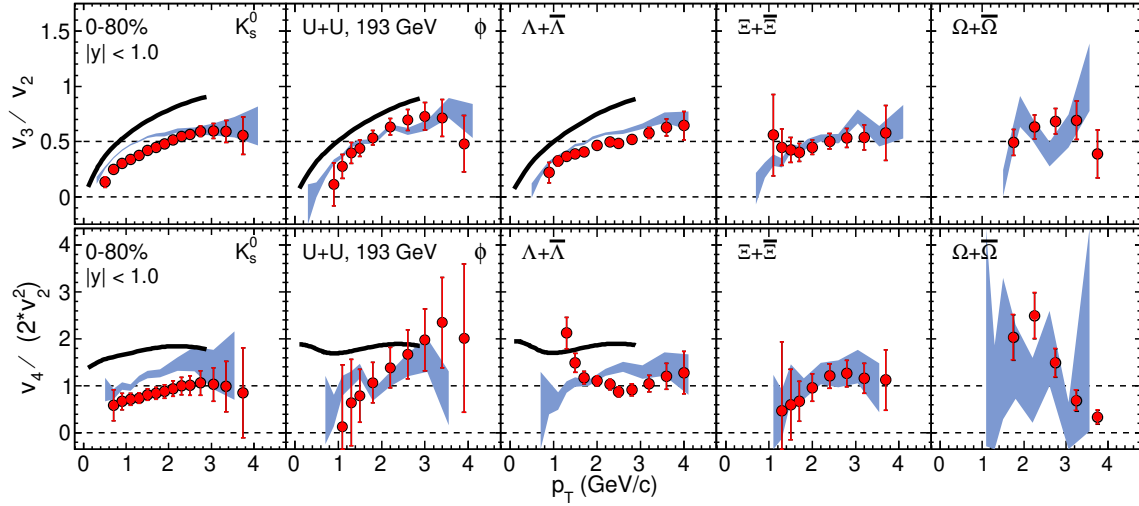
Figure 3.26: Ratios of $v_n(p_T)$ at mid-rapidity ($|y| < 1.0$) in minimum bias U+U collisions at $\sqrt{s_{NN}} = 193$ GeV compared with results from the AMPT(SM) and ideal-hydrodynamic models. Markers represent the results from data. AMPT model calculations are shown by the bands and black solid lines represent the corresponding results from the hydro-model. These results are STAR Preliminary.

3.9 Summary

In this chapter, we have presented the measurements of transverse momentum (p_T) and centrality dependence of various order of azimuthal anisotropy v_n (n = 2,3,4) for K_s^0, ϕ, $\Lambda + \bar{\Lambda}$, $\Xi + \bar{\Xi}$ and $\Omega + \bar{\Omega}$ at mid-rapidity in U+U collisions at $\sqrt{s_{NN}} = 193$ GeV data collected by the STAR detector at RHIC in the year 2012. The results are compared with the published results from Au+Au collisions at 200 GeV. A detail comparison of the results with AMPT and ideal-hydrodynamic model are done in U+U collisions at $\sqrt{s_{NN}} = 193$ GeV.

We found that the magnitude of flow coefficients $v_2 > v_3 > v_4$ in minimum bias U+U collisions. A strong centrality dependence is observed for elliptic flow v_2 of K_s^0, ϕ, $\Lambda + \bar{\Lambda}$, $\Xi + \bar{\Xi}$ and $\Omega + \bar{\Omega}$ in U+U collisions at $\sqrt{s_{NN}} = 193$ GeV. Higher order flow coefficients v_3 and v_4 does not show centrality dependence. Particle mass dependence of v_2 is observed for $p_T < 2.0$ GeV/c. Particle type (baryon/mesons) dependence is observed for $p_T > 2.0$ GeV/c. v_3 and v_4 seems to follow the same dependence although statistical uncertainties are large to conclude the same. NCQ scaling for v_2 and modified NCQ scaling for v_3 and v_4 is observed in minimum bias (0-80%) and 10-40% centrality classes, which indicates partonic collectivity in U+U collisions similar to the Au+Au collisions at $\sqrt{s_{NN}} = 200$ GeV. AMPT model explains the data at low p_T, while ideal hydrodynamics model over-predicts the data in U+U collisions at $\sqrt{s_{NN}} = 193$ GeV.

Bibliography

[1] *Review of Properties of Quark - Gluon Plasma and Ultra-relativistic Nuclear Collisions* - Larry D. McLerran, *FERMILAB-CONF-86-134-T*, **1986**.

[2] "Physics and Signatures of the Quark - Gluon Plasma", B. Muller, *Rept. Prog. Phys.*, **1995**, *58*, 611-636.

[3] "THE SEARCH FOR THE QUARK-GLUON PLASMA", J. W. Harris, B. Muller, *Ann. Rev. Nucl. Part. Sci.*, **1996**, *46*, 71-107.

[4] "What RHIC Experiments and Theory tell us about Properties of Quark-Gluon Plasma ?", E. Shuryak, *Nucl. Phys. A*, **2005**, *750*, 64-83.

[5] "Flow at the SPS and RHIC as a Quark-Gluon Plasma Signature", D. Teaney, J. Lauret, and E. Shuryak, *Phys. Rev. Lett.*, **2001**, *86*, 4783.

[6] "Anisotropy as a signature of transverse collective flow", J. Y. Ollitrault, *Phys. Rev. D*, **1992**, *46*, 229.

[7] "Flow Study in Relativistic Nuclear Collisions by Fourier Expansion of Azimuthal Particle Distributions", S. Voloshin, Y. Zhang, *Z. Phys. C*, **1996**, *70*, 665-672.

[8] "Methods for analyzing anisotropic flow in relativistic nuclear collisions", A. Poskanzer, S. Voloshin, *Phys. Rev. C*, **1998**, *58*, 1671;

"Collective phenomena in non-central nuclear collisions", S. Voloshin, A. Poskanzer and R. Snellings, *arXiv*:0809.2949[nucl-ex], **2008**.

[9] "Collision-geometry fluctuations and triangular flow in heavy-ion collisions", B. Alver and G. Roland, *Phys. Rev. C*, **2010**, *81*, 054905.

[10] "Momentum spectra, anisotropic flow, and ideal fluids", N. Borghini and J. Y. Ollitrault, *Phys. Lett. B*, **2006**, *642*, 227-231.

[11] "Highly Sensitive Centrality Dependence of Elliptic Flow: A Novel Signature of the Phase Transition in QCD", H. Sorge, *Phys. Rev. Lett.*, **1999**, *82*, 2048.

[12] "Collective Flow and Viscosity in Relativistic Heavy-Ion Collisions", U. Heinz and R. Snellings, *Ann. Rev. Nucl. Part. Sci.*, **2013**, *63*, 123-151.

[13] "Viscosity in Strongly Interacting Quantum Field Theories from Black Hole Physics", P. Kovtun, D. Son, and A. Starinets, *Phys. Rev. Lett.*, **2005**, *94*, 111601.

[14] "Collision-geometry fluctuations and triangular flow in heavy-ion collisions", B. Alver and G. Roland, *Phys. Rev. C*, **2010**, *81*, 054905.

[15] "Translation of collision geometry fluctuations into momentum anisotropies in relativistic heavy-ion collisions", G. Y. Qin *et al.*, *Phys. Rev. C*, **2010**, *82*, 064903; "Triangularity and dipole asymmetry in relativistic heavy ion collisions", D. Teaney and L. Yan, *Phys. Rev. C*, **2011**, *83*, 064904.

[16] "Nonlinearities in the harmonic spectrum of heavy ion collisions with ideal and viscous hydrodynamics", D. Teaney and L. Yan, *Phys. Rev. C*, **2012**, *86*, 044908; "v_4, v_5, v_6, v_7:Nonlinear hydrodynamic response versus LHC data", L. Yan, J. Y. Ollitrault, *Phys. Lett. B*, **2015**, *744*, 82-87;

"Linear and non-linear flow mode in Pb–Pb collisions at $\sqrt{s_{\text{NN}}} = 2.76$ TeV", S. Acharya *et al.*, *Phys. Lett. B*, **2017**, *773*, 68-80.

[17] "Initial fluctuation effect on harmonic flows in high-energy heavy-ion collisions", L. X. Han *et al.*, *Phys. Rev. C*, **2011**, *84*, 064907.

[18] "Effects of hadronic rescattering on multistrange hadrons in high-energy nuclear collisions", S. Takeuchi *et al.*, *Phys. Rev. C*, **2015**, *92*, 044907.

[19] "Measurements of ϕ meson production in relativistic heavy-ion collisions at the BNL Relativistic Heavy Ion Collider (RHIC)", B. Abelev *et al.* (STAR Collaboration), *Phys. Rev. C*, **2009**, *79*, 064903.

[20] "ϕ-Meson Production as a Probe of the Quark-Gluon Plasma", A. Shor, *Phys. Rev. Lett.*, **1985**, *54*, 1122;

"Collision rates for ρ-, ω- and ϕ-mesons at nonzero temperature", K. Haglin, *Nucl. Phys. A*, **1995**, *584*, 719-736;

"Collision broadening of the ϕ meson in baryon rich hadronic matter", W. Smith and K. Haglin, *Phys. Rev. C*, **1998**, *57*, 1449.

[21] "Probe of the QCD phase diagram with ϕ-mesons in high-energy nuclear collisions", B. Mohanty, N. Xu, *J. Phys. G*, **2009**, *36*, 064022.

[22] H. Masui, `https://www.star.bnl.gov/protected/bulkcorr/hmasui/2013/Centrality_UU_193GeVhmasui_centrality_UU_200GeV_bulkcorr_Mar20_2013.pdf`.

[23] "Glauber Modeling in High-Energy Nuclear Collisions", M. Miller *et al.*, *Annu. Rev. Nucl. Part. Sci.*, **2007**, *57*, 205-243.

[24] "Hadron production in nuclear collisions at RHIC and high-density QCD", D. Kharzeev and M. Nardi, *Phys. Lett. B*, **2001**, *507*, 121-128.

[25] "Collision geometry scaling of Au+Au pseudorapidity density from $\sqrt{s_{\mathrm{NN}}} = 19.6$ to 200 GeV", B. Back *et al.*, *Phys. Rev. C*, **2004**, *70*, 021902(R).

[26] "Review of Particle Physics", J. Beringer *et al.* (Particle Data Group), *Phys. Rev. D*, **2012**, *86*, 010001.

[27] "Azimuthal Anisotropy in U+U and Au+Au Collisions at RHIC", L. Adamczyk *et al.* (STAR Collaboration), *Phys. Rev. Lett.*, **2015**, *115*, 222301;

"Υ production in U + U collisions at $\sqrt{s_{\mathrm{NN}}} = 193$ GeV measured with the STAR experiment", L. Adamczyk *et al.* (STAR Collaboration), *Phys. Rev. C*, **2016**, *94*, 064904;

https://drupal.star.bnl.gov/STAR/blog/yezhenyu/nbinary-and-npart-uu-collisions-zhenyu.

[28] "A method to improve tracking and particle identification in TPCs and silicon detectors", H. Bichsel, *Nucl. Inst. Meth. A*, **2006**, *562*, 154-197.

[29] "The STAR Time Projection Chamber: A Unique Tool for Studying High Multiplicity Events at RHIC", M. Anderson *et al.*, *Nucl. Inst. Meth. A*, **2003**, *499*, 659-678.

[30] "The large-area time-of-flight upgrade for STAR", W. J. Llope, *Nucl. Inst. Meth. B*, **2005**, *241*, 306-310.

[31] "Review of Particle Physics", M. Tanabashi *et al.* (Particle Data Group), *Phys. Rev. D*, **2018**, *98*, 030001.

[32] "ϕ meson production in Au+Au and p+p collisions at $\sqrt{s_{\mathrm{NN}}} = 200$ GeV", J. Adams *et al.* (STAR Collaboration), *Phys. Lett. B*, **2005**, *612*, 181.

[33] "Measurements of identified particles at intermediate transverse momentum in the STAR experiment from Au+Au collisions at $\sqrt{s_{\mathrm{NN}}}$=200 GeV", J. Adams *et al.* (STAR Collaboration), *arXiv*:nucl-ex/0601042v1(2006).

[34] "Multistrange Baryon Production in Au-Au Collisions at $\sqrt{s_{\mathrm{NN}}} = 130$ GeV", J. Adams *et al.* (STAR Collaboration), *Phys. Rev. Lett.*, **2004**, *92*, 182301.

[35] "Multistrange Baryon Elliptic Flow in Au+Au Collisions at $\sqrt{s_{\mathrm{NN}}} = 200$ GeV", J. Adams *et al.* (STAR Collaboration), *Phys. Rev. Lett.*, **2005**, *95*, 122301.

[36] "Collective motion in nucleus-nucleus collisions at 800 MeV/nucleon", P. Danielewicz *et al.*, *Phys. Rev. C*, **1998**, *38*, 120;

"Energy and charged particle flow in 10.8 GeV/c Au+Au collisions", J. Barrette *et al.*, *Phys. Rev. Lett.*, **1997**, *55*, 1420;

"Proton and pion production relative to the reaction plane in Au + Au collisions at 11A GeV/c", J. Barrette *et al.*, *Phys. Rev. C*, **1997**, *56*, 3254.

[37] "Predictions of Elliptic flow and nuclear modification factor from 200 GeV U+U collisions at RHIC", H. Masui, B. Mohanty and N. Xu, *Phys. Lett. B*, **2009**, *679*, 440-444;

"Multiplicity, average transverse momentum, and azimuthal anisotropy in U+U collisions at $\sqrt{s_{\mathrm{NN}}} = 200$ GeV using a multiphase transport model", Md. R. Haque, Z. W. Lin and B. Mohanty, *Phys. Rev. C*, **2012**, *85*, 034905.

[38] "Azimuthally sensitive correlations in nucleus-nucleus collisions", N. Borghini and J. Ollitrault, *Phys. Rev. C*, **2004**, *70*, 064905.

[39] "Centrality dependence of charged hadron and strange hadron elliptic flow from $\sqrt{s_{\mathrm{NN}}} = 200$ GeV Au+Au collisions", B. Abelev *et al.* (STAR Collaboration), *Phys. Rev. C*, **2008**, *77*, 054901.

[40] "Centrality and Transverse Momentum Dependence of Elliptic Flow of Multi-strange Hadrons and ϕ Meson in Au+Au Collisions at $\sqrt{s_{\mathrm{NN}}} = 200$ GeV", L. Adamczyk *et al.* (STAR Collaboration), *Phys. Rev. Lett.*, **2016**, *116*, 062301.

[41] "Emission angle dependent HBT at RHIC and beyond", P. F. Kolb, U. Heinz, *Nucl. Phys. A*, **2003**, *715*, 653-656.

[42] "Elliptic Flow at Large Transverse Momenta from Quark Coalescence", D. Molnar and S. Voloshin, *Phys. Rev. Lett.*, **2003**, *91*, 092301.

[43] "Scaling distributions of quarks, mesons, and proton for all p_T, energy, and centrality", R. C. Hwa and C. B. Yang, *Phys. Rev. C*, **2003**, *67*, 064902.

"Hadronization in Heavy-Ion Collisions: Recombination and Fragmentation of Partons", R. Fries *et al.*, *Phys. Rev. Lett.*, **2003**, *90*, 202303.

[44] "Partonic Flow and ϕ-Meson Production in Au+Au Collisions at $\sqrt{s_{\mathrm{NN}}} = 200$ GeV", B. Abelev *et al.* (STAR Collaboration), *Phys. Rev. Lett.*, **2007**, *99*, 112301.

[45] "Deviation from quark number scaling of the anisotropy parameter v_2 of pions, kaons, and protons in Au+Au collisions at $\sqrt{s_{\mathrm{NN}}} = 200$ GeV", A. Adare *et al.* (PHENIX Collaboration), *Phys. Rev. C*, **2012**, *85*, 064914.

[46] "Elliptic flow of identified hadrons in Pb-Pb collisions at $\sqrt{s_{\mathrm{NN}}} = 2.76$ TeV", B. Abelev *et al.* (ALICE Collaboration), *JHEP*, **2015**, *06*, 190.

[47] "Centrality dependence of charged hadron and strange hadron elliptic flow from $\sqrt{s_{\mathrm{NN}}} = 200$ GeV Au+Au collisions", B. Abelev *et al.* (STAR Collaboration), *Phys. Rev. C*, **2008**, *77*, 54901.

[48] "Multiphase transport model for relativistic nuclear collisions", B. Zhang *et al.*, *Phys. Rev. C*, **2000**, *61*, 067901;

"Multiphase transport model for relativistic heavy ion collisions", Z. W. Lin *et al.*, *Phys. Rev. C*, **2005**, *72*, 064901.

[49] "Charged particle rapidity distributions at relativistic energies", Z. W. Lin *et al.*, *Phys. Rev. C*, **2001**, *64*, 011902;

"Triangular flow in heavy ion collisions in a multiphase transport model", J. Xu, C. M. Ko, *Phys. Rev. C*, **2011**, *84*, 014903.

[50] "hijing: A Monte Carlo model for multiple jet production in pp, pA, and AA collisions", X. N. Wang and M. Gyulassy, *Phys. Rev. D*, **1991**, *44*, 3501.

[51] "ZPC 1.0.1: a parton cascade for ultrarelativistic heavy ion collisions", B. Zhang, *Comput. Phys. Commun.*, **1998**, *109*, 193-206.

[52] "Parton fragmentation and string dynamics", B. Andersson *et al.*, *Phys. Rep.*, **1983**, *97*, 31-145.

[53] "Formation of superdense hadronic matter in high energy heavy-ion collisions", B. A. Li and C. M. Ko, *Phys. Rev. C*, **1995**, *52*, 2037;

[54] V. Roy *et al.*, *private communication*, **2018**;

"Anisotropic transverse flow and the quark-hadron phase transition", P. F. Kolb, J. Sollfrank, and U. Heinz, *Phys. Rev. C*, **2000**, *62*, 054909;

"Transverse flow and hadrochemistry in Au+Au collisions at $\sqrt{s_{\mathrm{NN}}} = 200$ GeV", P. F. Kolb and R. Rapp, *Phys. Rev. C*, **2003**, *67*, 044903;

"Hydrodynamic description of ultrarelativistic heavy-ion collisions", P. F. Kolb and U. Heinz, *arXiv*:nucl-th/0305084, **2003**.

[55] "Triangular flow in hydrodynamics and transport theory", B. Alver *et al.*, *Phys. Rev. C*, **2010**, *82*, 034913.

[56] "Third harmonic flow of charged particles in Au+Au collisions at $\sqrt{s_{\mathrm{NN}}} = 200$ GeV", L. Adamczyk *et al.* (STAR Collaboration), *Phys. Rev. C*, **2013**, *88*, 014904.

[57] "Dissipative corrections to particle spectra and anisotropic flow from a saddle-point approximation to kinetic freeze out", C. Lang, N. Borghini, *Eur. Phys. J. C*, **2014**, *74*, 2955.

[58] "Constraining the viscous freeze-out distribution function with data obtained at the BNL Relativistic Heavy Ion Collider (RHIC)", M. Luzum, J. Y. Ollitrault, *Phys. Rev. C*, **2010**, *82*, 014906.

[59] "Momentum anisotropies in the quark coalescence model", P. Kolb *et al.*, *Phys. Rev. C*, **2004**, *69*, 051901;

"Partonic effects on higher-order anisotropic flows in relativistic heavy-ion collisions", L. W. Chen, C. M. Ko, Z. W. Lin, *Phys. Rev. C*, **2004**, *69*, 031901.

3.10 Appendix

3.10.1 Centrality selection from reference multiplicity

Table 3.12: Centrality selection criteria, N_{part} and N_{coll} information for U+U collisions at $\sqrt{s_{\mathrm{NN}}}$ = 193 GeV [27].

Centrality (%)	RefMult	$\langle N_{part} \rangle$	$\langle N_{coll} \rangle$	No. of events
0-5	> 535	414.87	1281.26	17.64 M
5-10	> 466	355.42	1010.97	17.67 M
10-20	> 338	277.52	714.081	35.73 M
20-30	> 233	195.66	435.854	35.17 M
30-40	> 150	133.08	253.489	35.51 M
40-50	> 90	86.17	137.384	34.78 M
50-60	> 50	52.63	69.3415	33.34 M
60-70	> 24	29.38	31.8468	33.16 M
70-80	> 10	14.66	13.1883	27.06 M

3.10.2 Event plane resolution in wide centrality bins

Table 3.13: Summary of the averaged resolution for wide centrality for various particles studied in U+U collisions at $\sqrt{s_{\mathrm{NN}}}$ = 193 GeV.

Particle	ψ_n	Average resolution ($< R >$)			
		0-80%	0-10%	10-40%	40-80%
K_s^0	2	0.619	0.548	0.686	0.499
K_s^0	3	0.289	0.336	0.307	0.167
K_s^0	4	0.143	0.174	0.148	0.083
ϕ	2	0.600	0.544	0.685	0.468
ϕ	3	0.266	0.336	0.304	0.151
ϕ	4	0.132	0.174	0.147	0.078
Λ	2	0.622	0.548	0.686	0.504
Λ	3	0.292	0.336	0.307	0.169
Λ	4	0.144	0.174	0.148	0.084
Ξ	2	0.617	0.544	0.685	0.511
Ξ	3	0.302	0.335	0.310	0.171
Ξ	4	0.150	0.174	0.150	0.085
Ω	2	0.610	0.541	0.684	0.520
Ω	3	0.312	0.335	0.313	0.176
Ω	4	0.156	0.174	0.151	0.087

3.10.3 Parameter variations for systematic uncertainty

3.10.3.1 Event selection

Table 3.14: Summary of variations of event selection cuts for systematic uncertainties.

Parameter	default	var1	var2
$|V_z|$ (cm)	< 30	< 25	< 20
$|\Delta\eta|$	0.1	0.05	0.15

3.10.3.2 Track selection

Table 3.15: Summary of variations of event selection cuts for systematic uncertainties.

Parameter	default	var1	var2	var3
nHitsFit TPC	≥ 15	≥ 18	≥ 21	≥ 24
$|DCA|$(cm)	≤ 3.0	≤ 2.5	≤ 2.0	≤ 1.5
nσ	≤ 2.0	≤ 3.0	≤ 2.5	≥ 1.5

3.10.3.3 V0 topology selection

Table 3.16: Summary of V0 topology cuts for systematic uncertainties for K_s^0 in U+U collisions at $\sqrt{s_{NN}} = 193$ GeV.

Parameter	Default (cm)		Minimum (cm)		Maximum (cm)	
p_T (GeV/c) $\rightarrow$	$p_T < 2.0$	$p_T \geq 2.0$	$p_T < 2.0$	$p_T \geq 2.0$	$p_T < 2.0$	$p_T \geq 2.0$
DCA V0 to PV	≤ 0.7	≤ 0.8	≤ 0.56	≤ 0.64	≤ 0.84	≤ 0.96
DCA Daughters	≤ 0.7	≤ 0.8	≤ 0.56	≤ 0.64	≤ 0.84	≤ 0.96
DCA Pions to PV	≥ 1.5	≥ 0.35	≥ 1.2	≥ 0.28	≥ 1.8	≥ 0.42
Decay Length	≥ 4.5	≥ 7.0	≥ 3.6	≥ 5.6	≥ 5.4	≥ 8.4

Table 3.17: Summary of V0 topology cuts for systematic uncertainties for $\Lambda(\bar{\Lambda})$ in U+U collisions at $\sqrt{s_{\mathrm{NN}}} = 193$ GeV.

Parameter	Default (cm)		Minimum (cm)		Maximum (cm)	
p_T **(GeV/c)** $\rightarrow$	$p_T < 2.0$	$p_T \geq 2.0$	$p_T < 2.0$	$p_T \geq 2.0$	$p_T < 2.0$	$p_T \geq 2.0$
DCA V0 to PV	≤ 0.7	≤ 0.7	≤ 0.56	≤ 0.56	≤ 0.84	≤ 0.84
DCA Daughters	≤ 0.7	≤ 0.7	≤ 0.56	≤ 0.56	≤ 0.84	≤ 0.84
DCA Protons to PV	≥ 0.5	≥ 0.25	≥ 0.3	≥ 0.2	≥ 0.4	≥ 0.3
DCA Pions to PV	≥ 1.0	≥ 1.0	≥ 0.8	≥ 0.8	≥ 1.2	≥ 1.2
Decay Length	≥ 4.5	≥ 4.5	≥ 3.6	≥ 3.6	≥ 5.4	≥ 5.4

Table 3.18: Summary of V0 topology cuts for systematic uncertainties for $\Xi(\bar{\Xi})$ in U+U collisions at $\sqrt{s_{\mathrm{NN}}} = 193$ GeV.

Parameter	Default (cm)	Minimum (cm)	Maximum (cm)
DCA Ξ to PV	≤ 0.5	≤ 0.4	≤ 0.6
DCA Daughters Ξ	≤ 0.8	≤ 0.6	≤ 1.0
DCA π from Ξ	≥ 2.0	≥ 1.5	≥ 2.5
DCA Λ from Ξ	≥ 0.7	≥ 0.56	≥ 0.84
Decay Length Ξ	≥ 4.0	≥ 3.0	≥ 5.0
Mass width Λ (MeV)	≤ 6	≥ 4	≥ 5

Table 3.19: Summary of V0 topology cuts for systematic uncertainties for $\Omega(\bar{\Omega})$ in U+U collisions at $\sqrt{s_{\mathrm{NN}}} = 193$ GeV.

Parameter	Default (cm)	Minimum (cm)	Maximum (cm)
DCA Ω to PV	≤ 0.4	≤ 0.3	≤ 0.5
DCA Daughters Ω	≤ 0.7	≤ 0.56	≤ 0.84
DCA K from Ω	≥ 1.0	≥ 0.75	≥ 1.25
DCA Λ from Ω	≥ 0.4	≥ 0.3	≥ 0.5
Decay Length Ω	≥ 3.0	≥ 2.0	≥ 4.0
Mass width Λ (MeV)	≤ 6	≥ 4	≥ 5

3.10.4 Raw yield extraction for ϕ-meson (0-80%)

p_T range is in GeV/c and $\phi - \psi_n$ range is in radian for all the legends mentioned in the figures.

For low p_T:
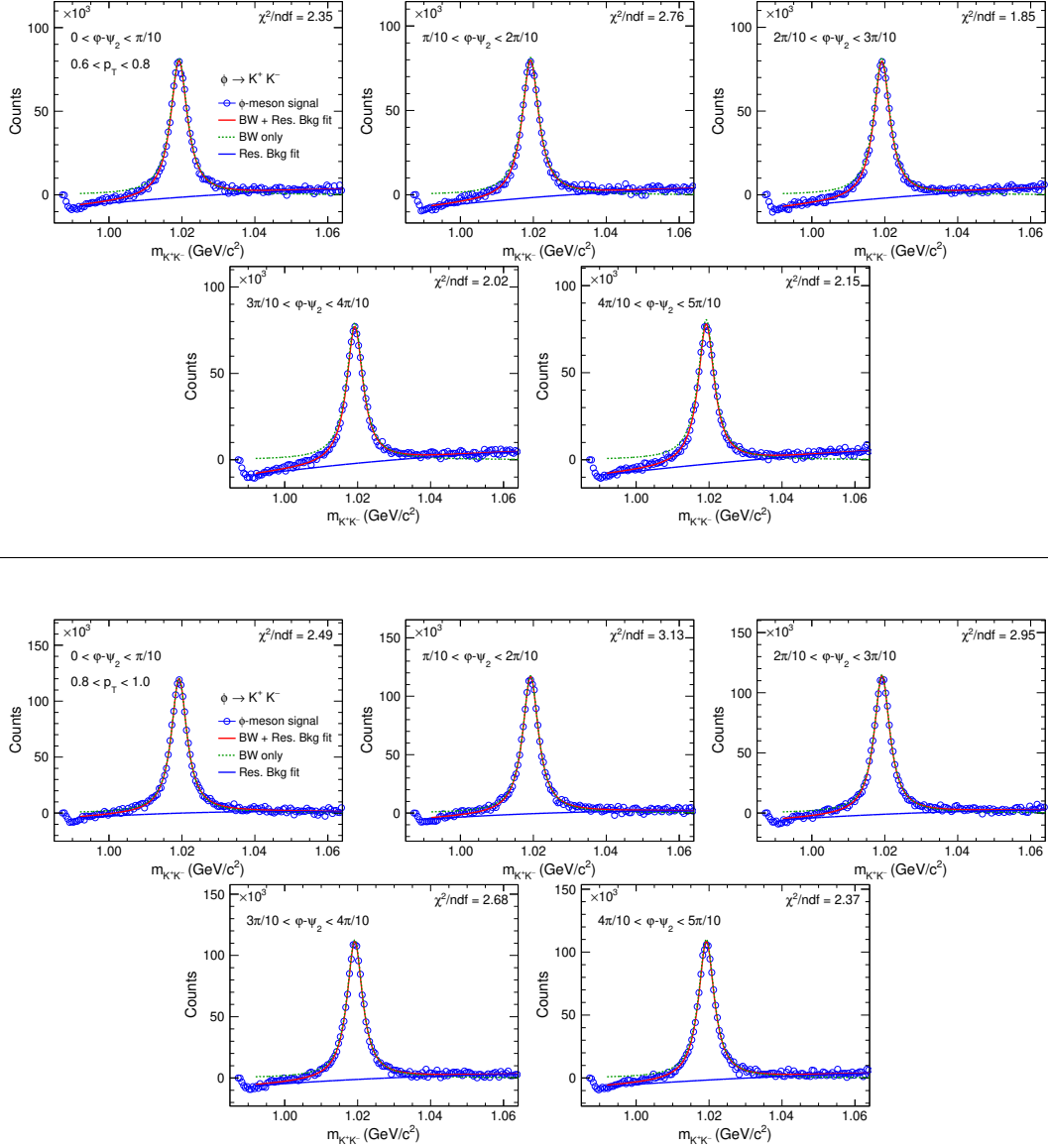
For mid p_T:
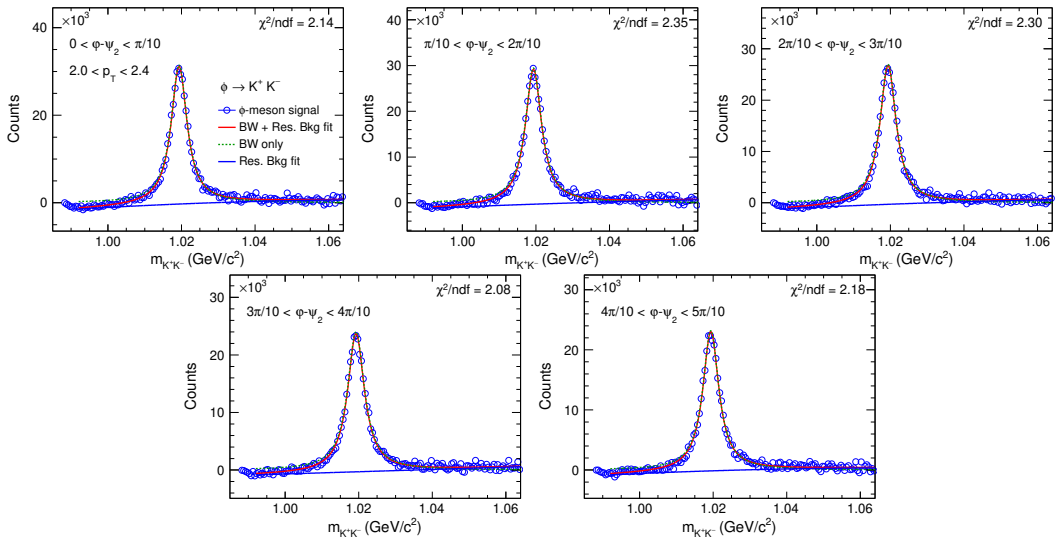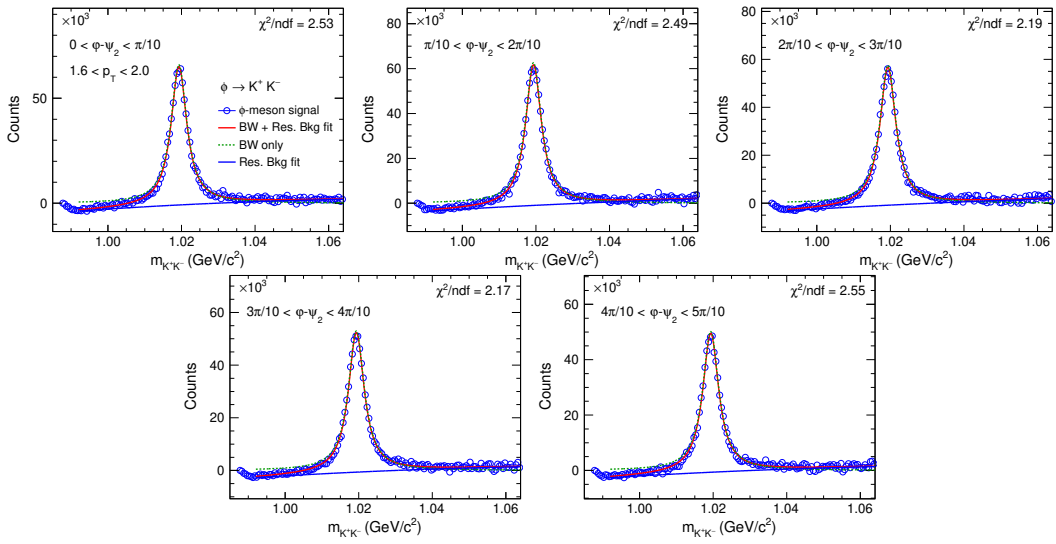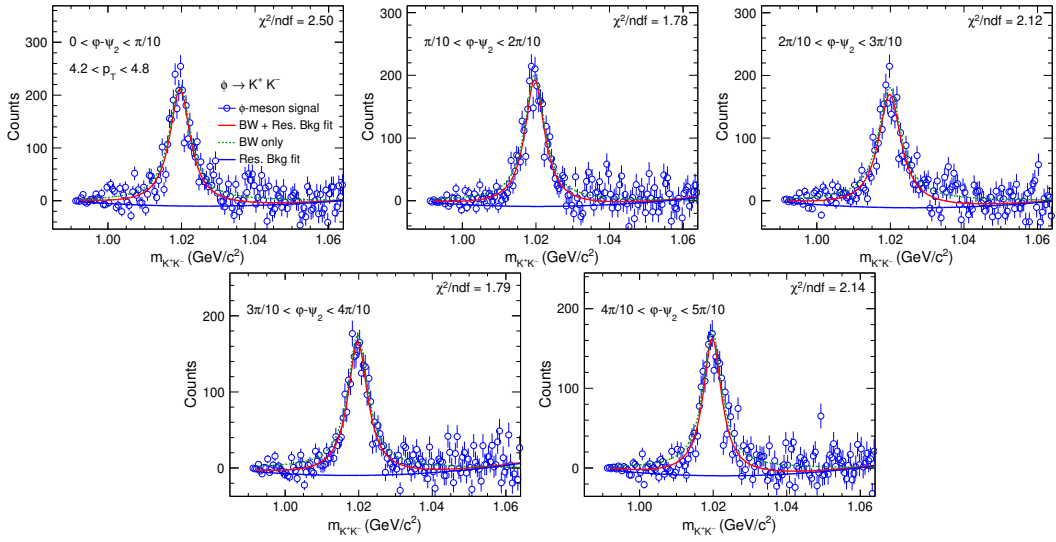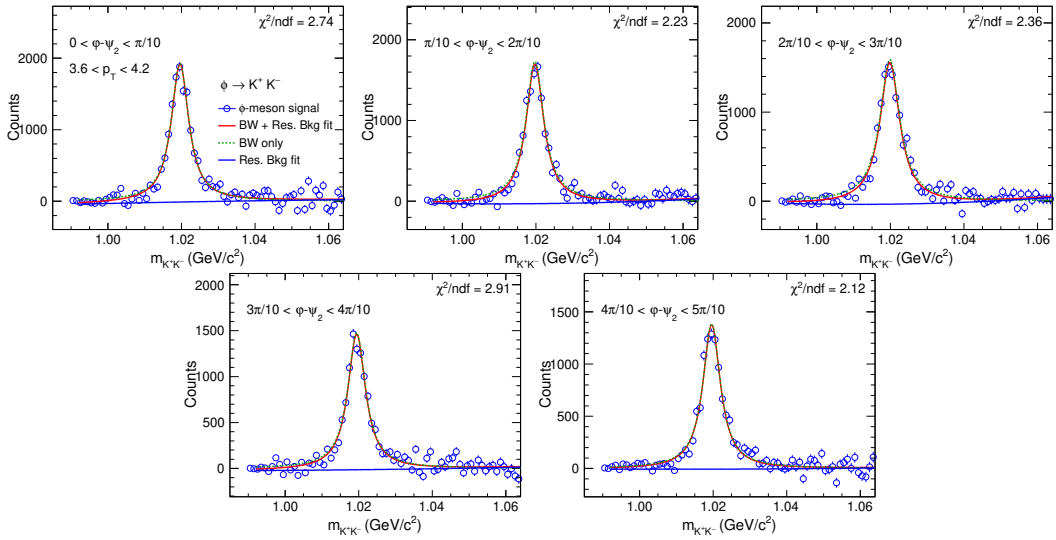
For high p_T:

3.10.5 Raw yield extraction for K_s^0 (0-80%)

For low p_T:
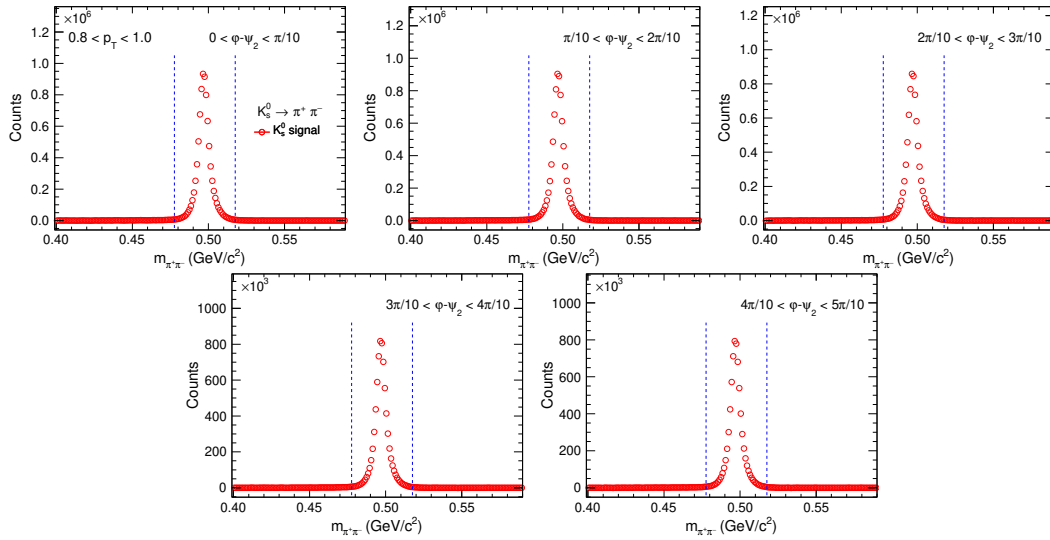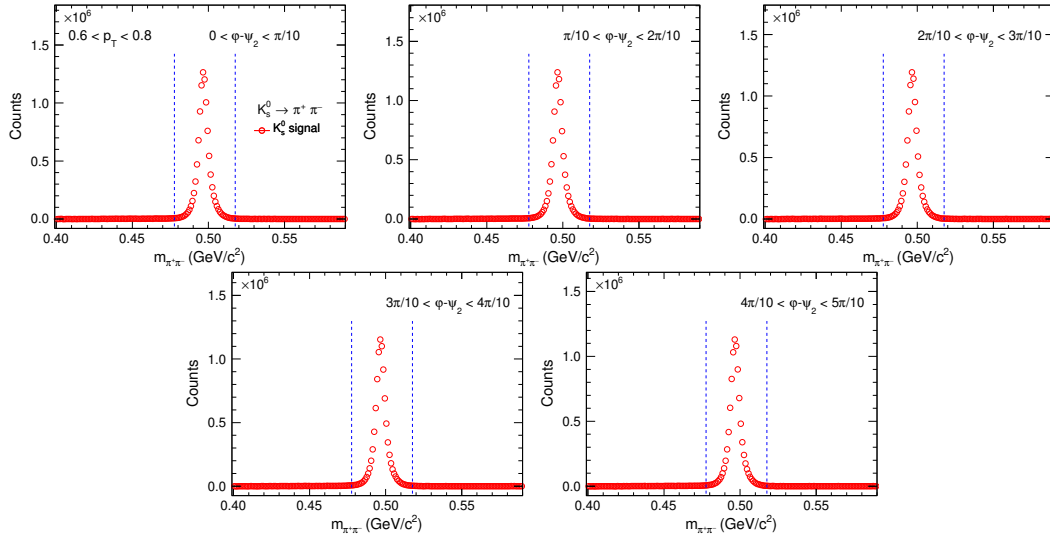
For mid p_T:
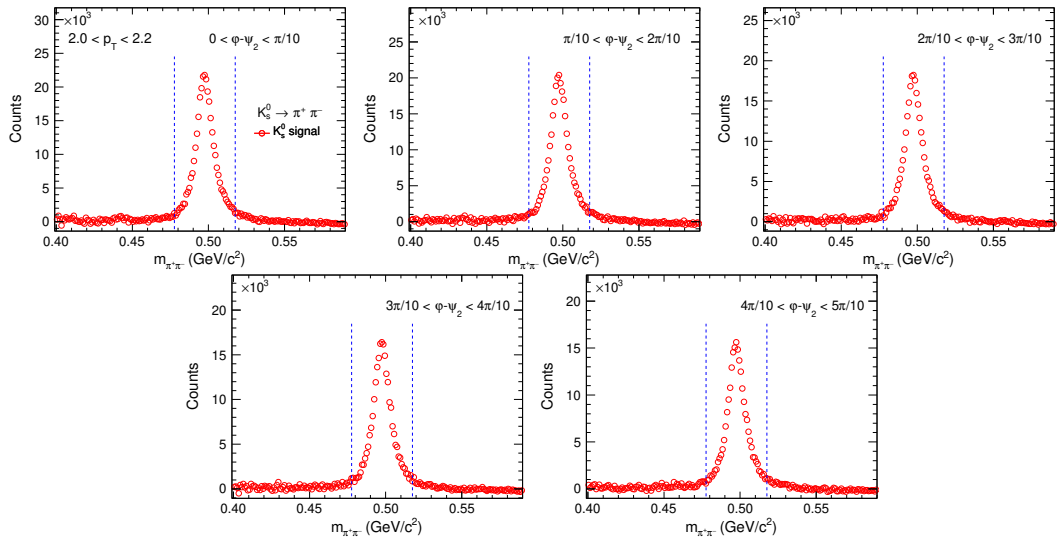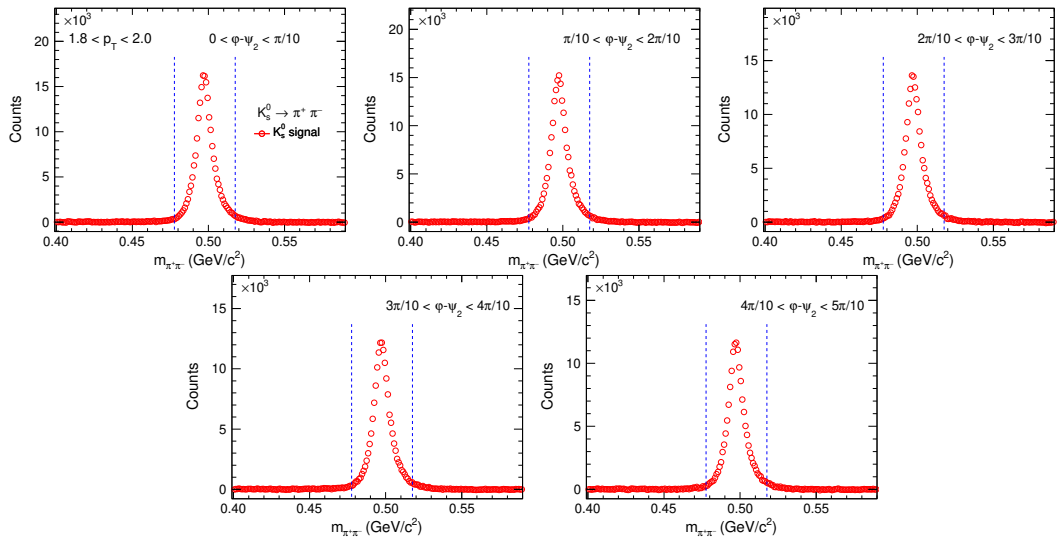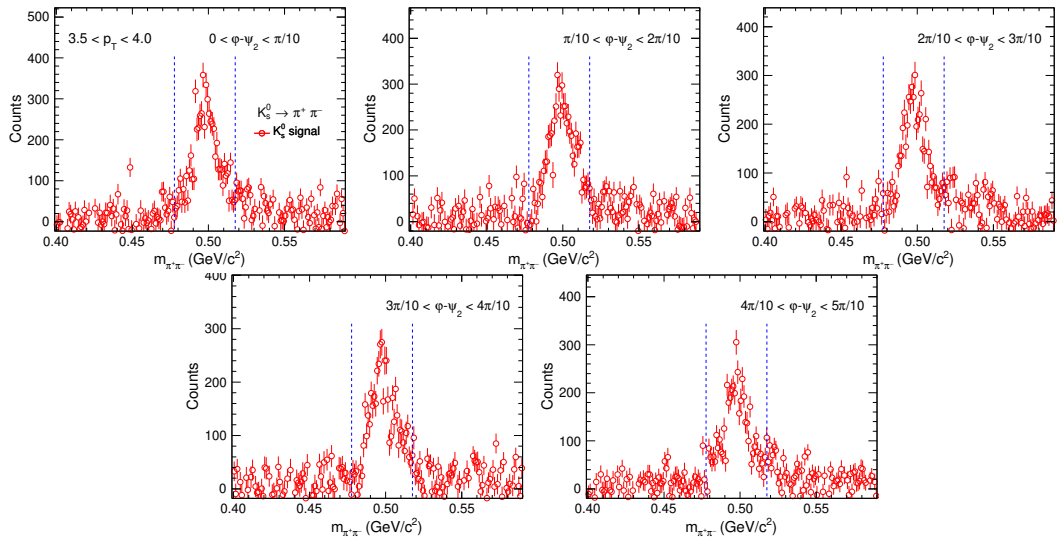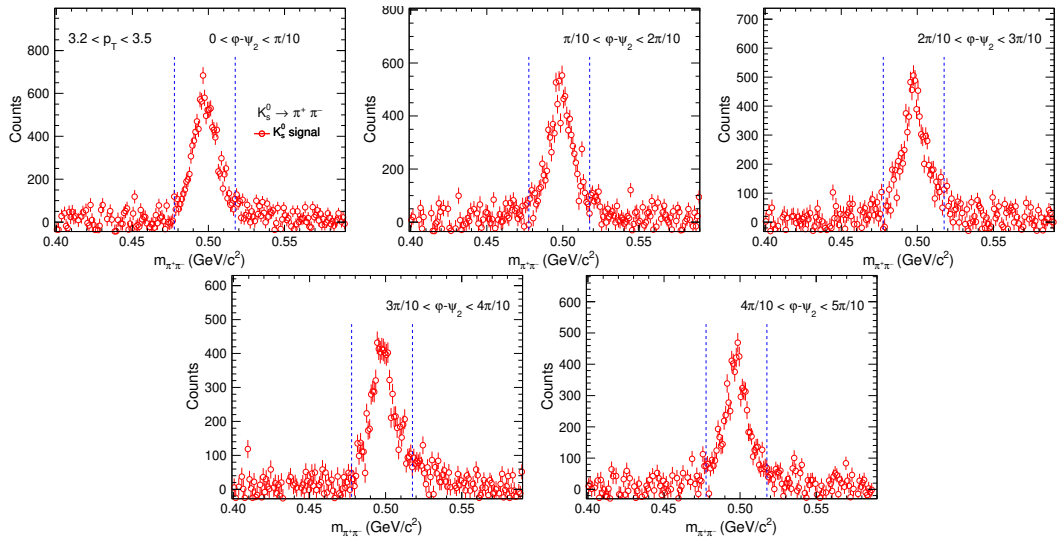
For high p_T:

3.10.6 Raw yield extraction for $\Lambda + \bar{\Lambda}$ (0-80%)

For low p_T:

For mid p_T:

For high p_T:

135
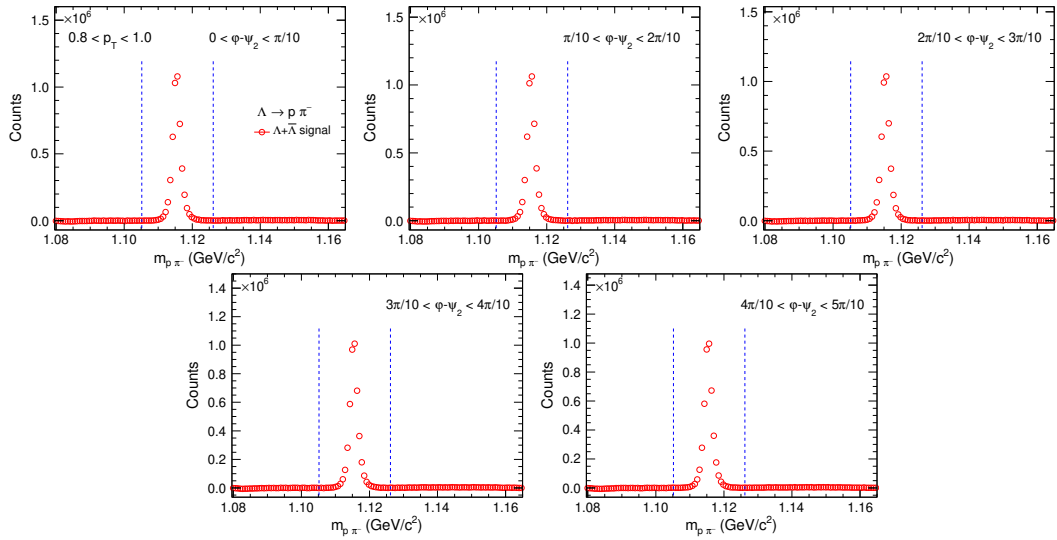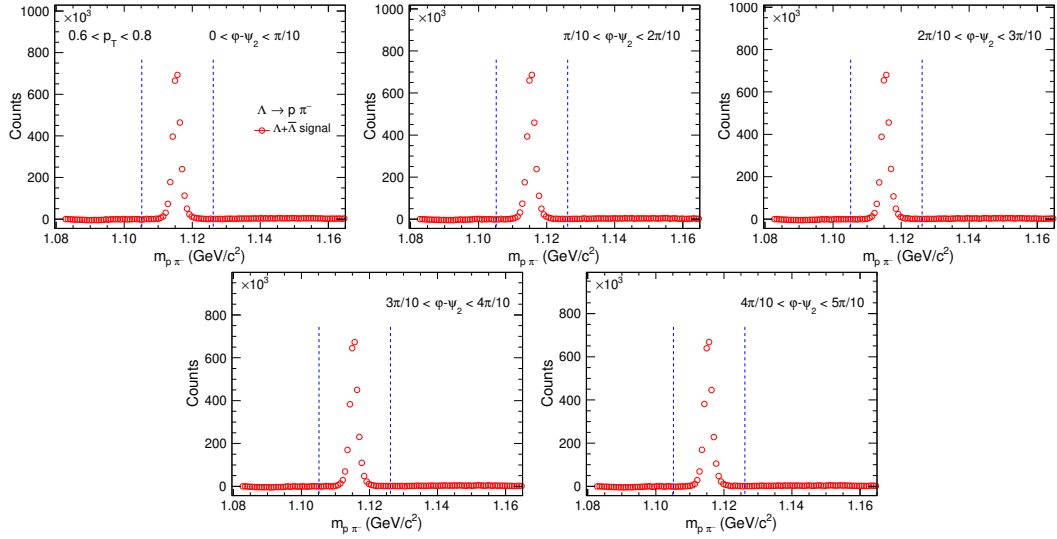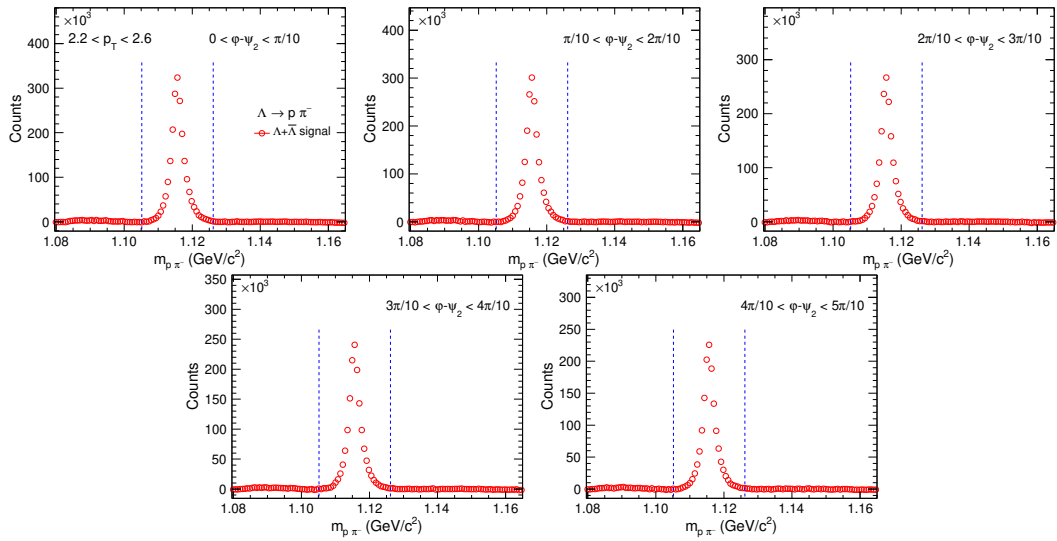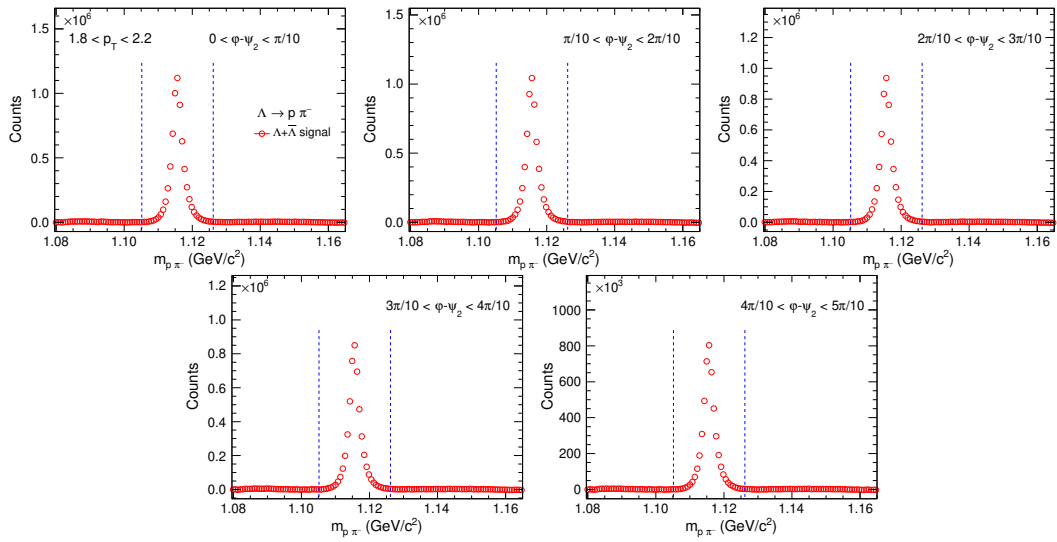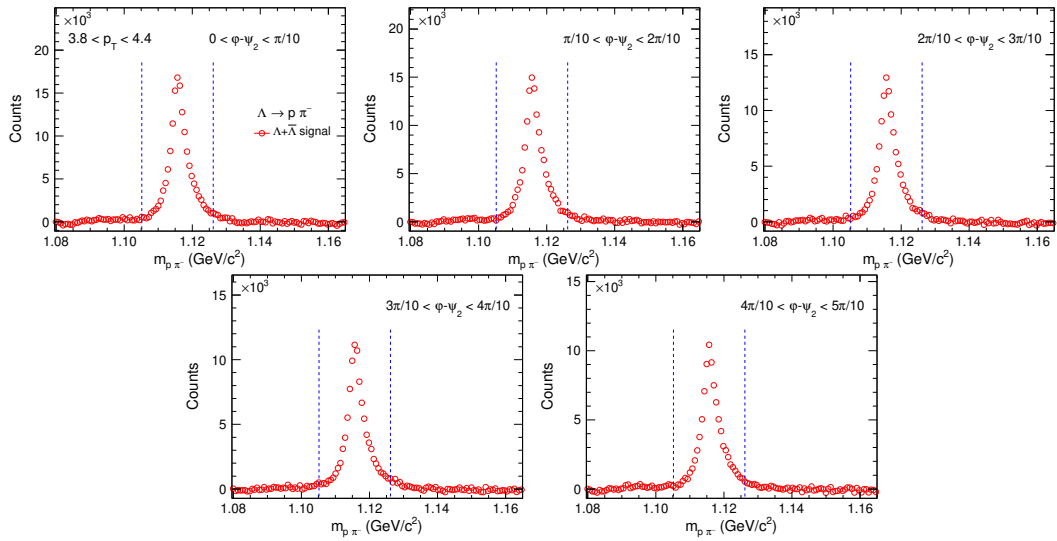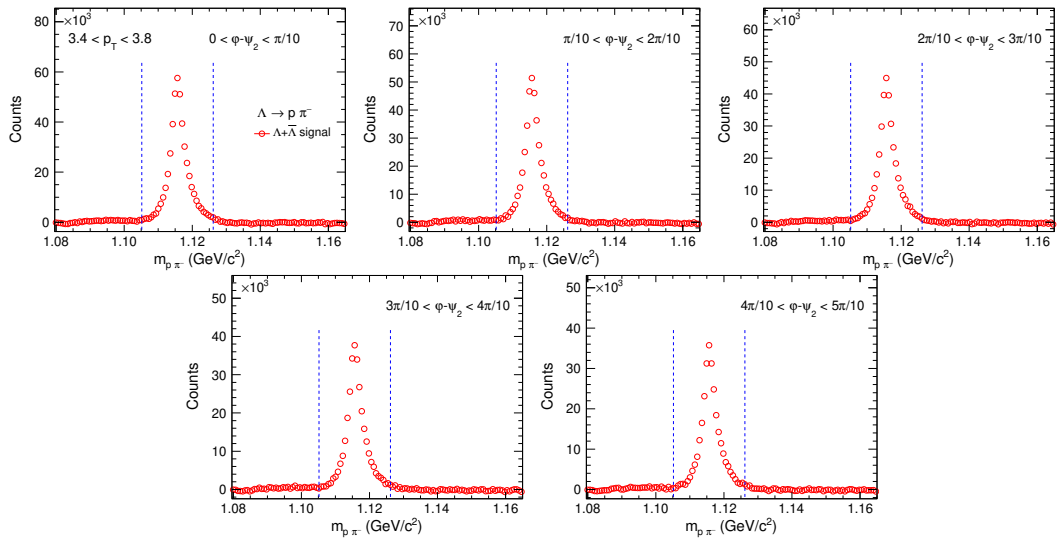
3.10.7 Raw yield extraction for $\Xi + \bar{\Xi}$ (0-80%)

For low p_T:

For mid p_T:

For high p_T:

138
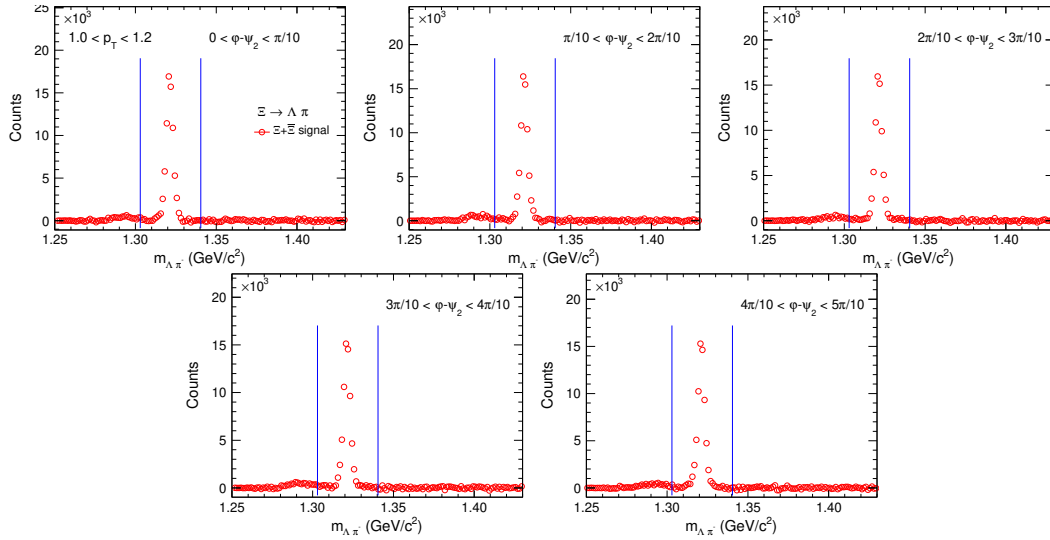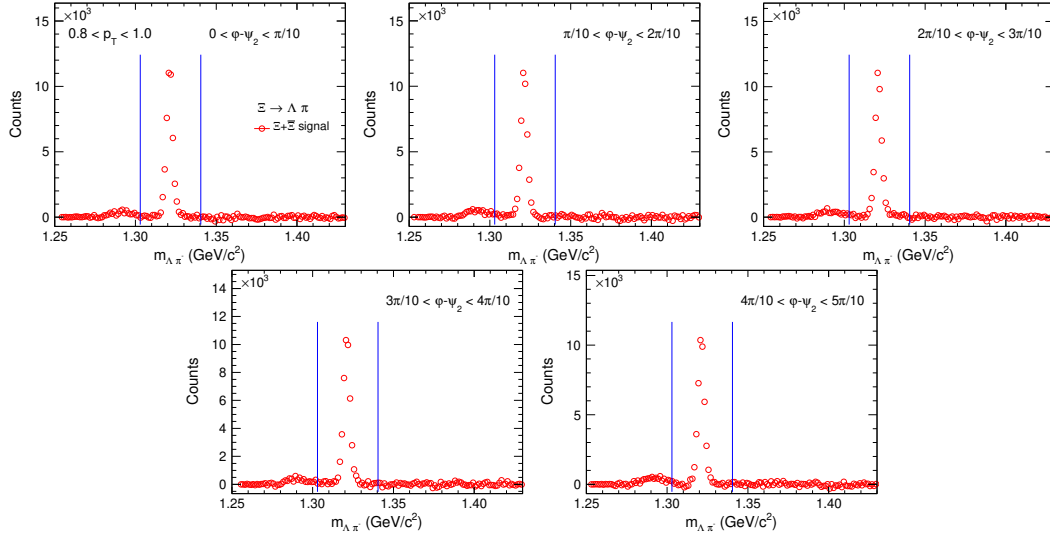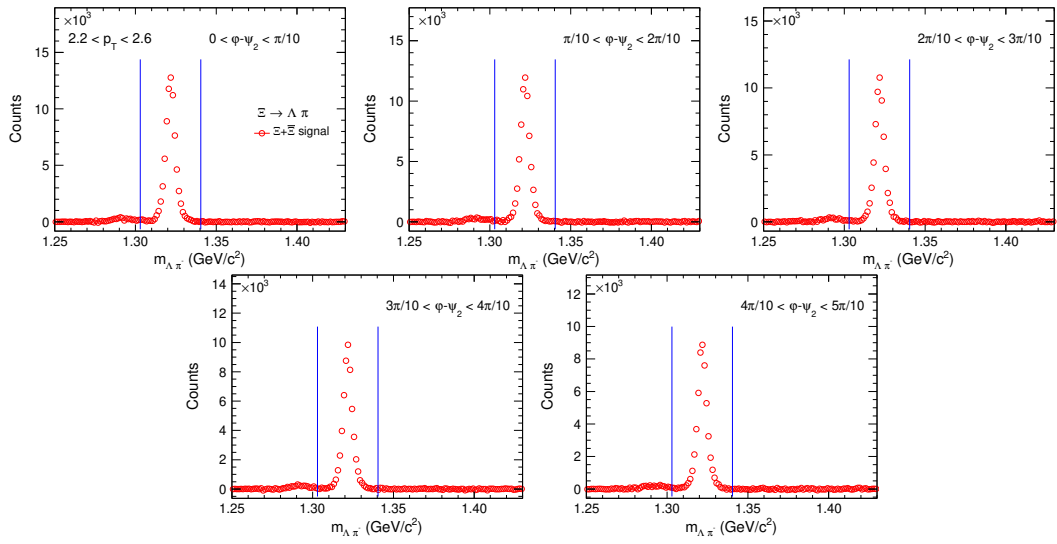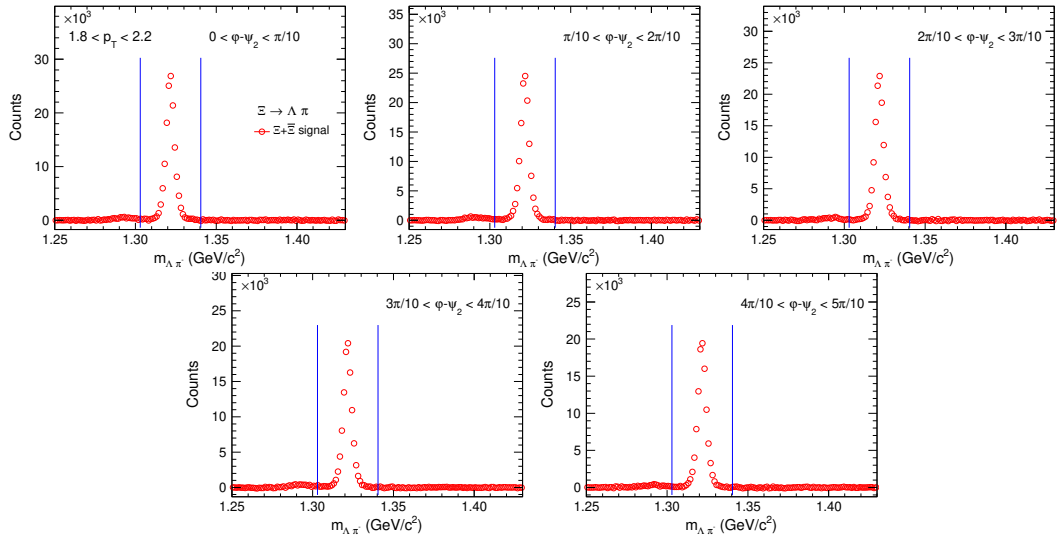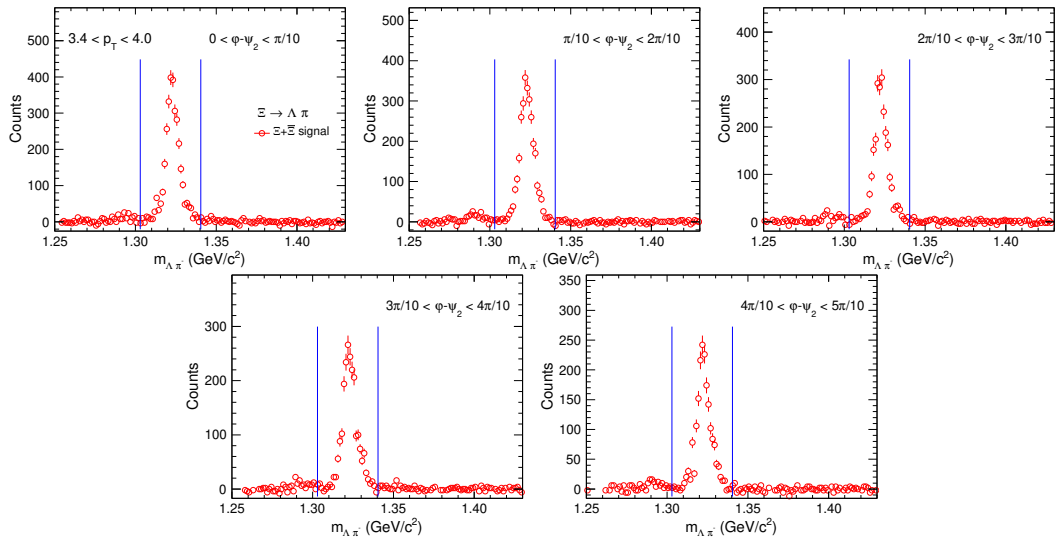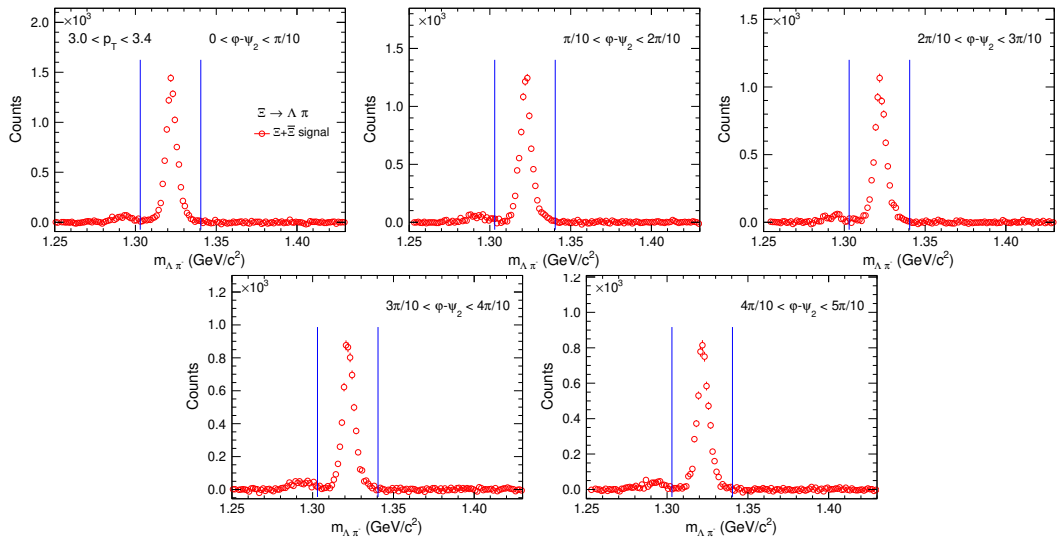
3.10.8 Raw yield extraction for $\Omega + \bar{\Omega}$ (0-80%)

For low p_T:
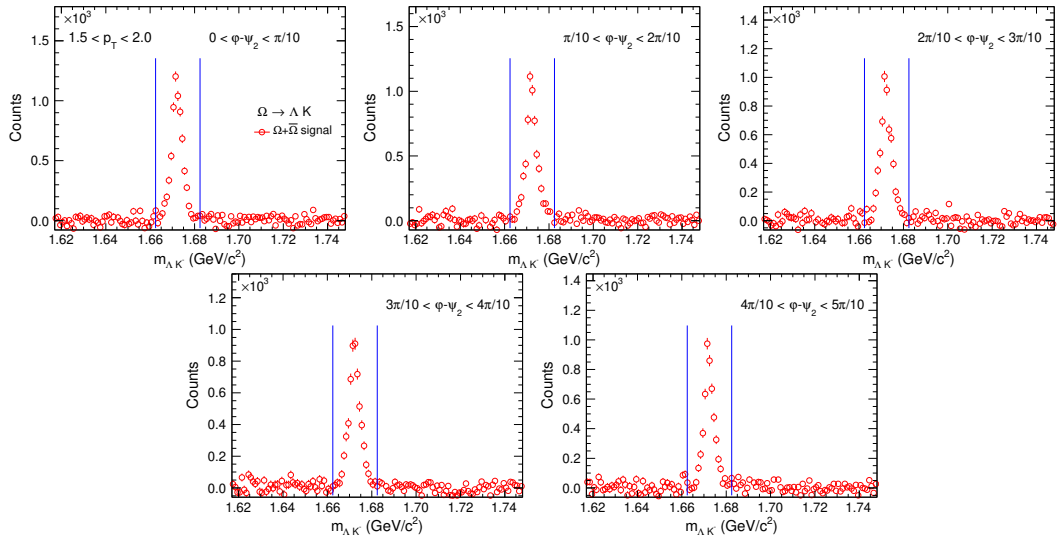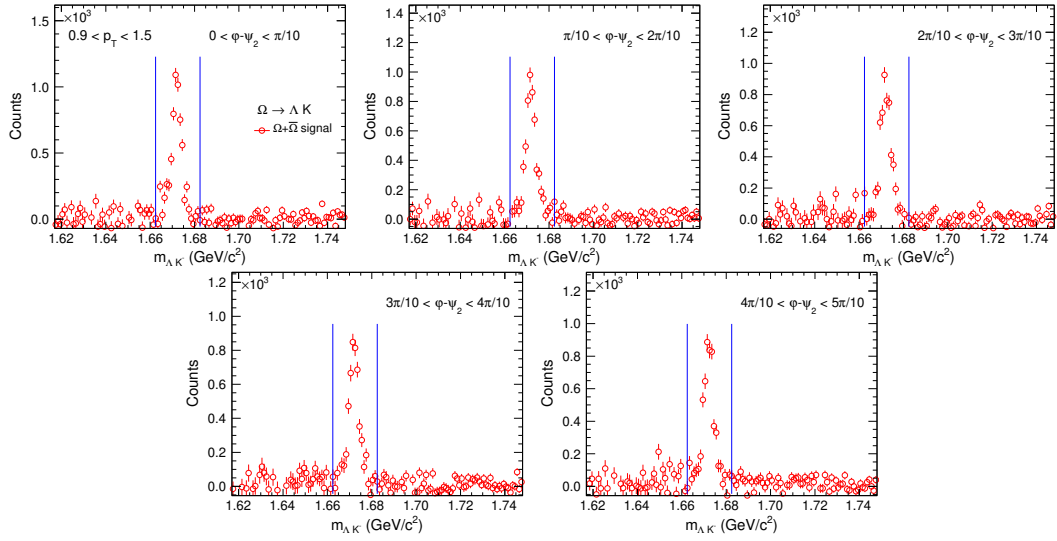
For mid p_T:
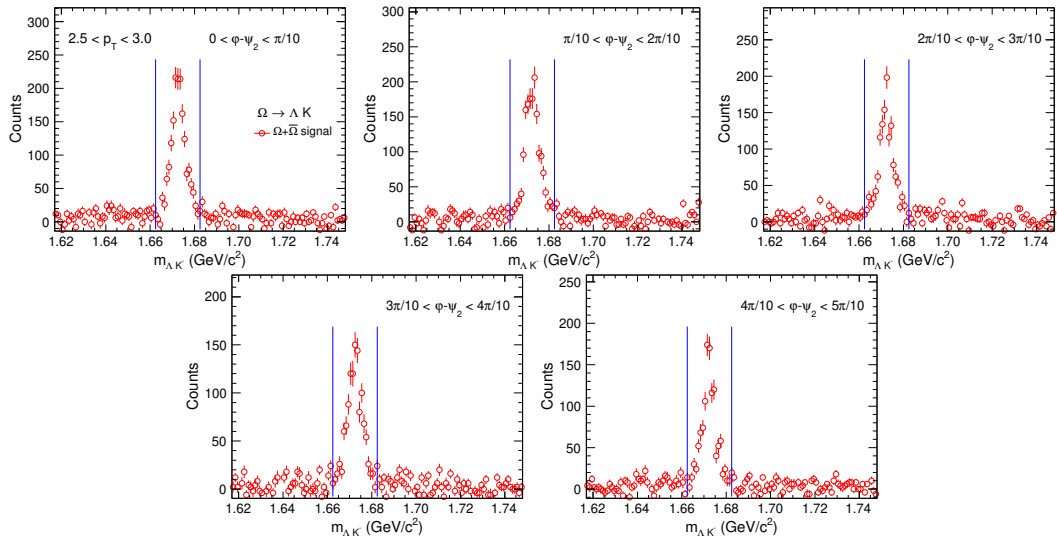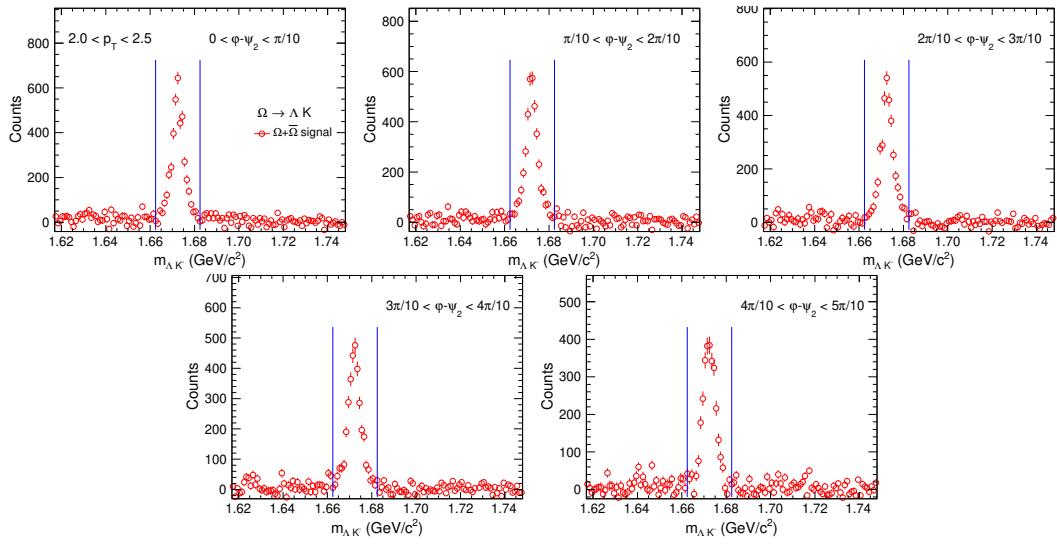
For high p_T:
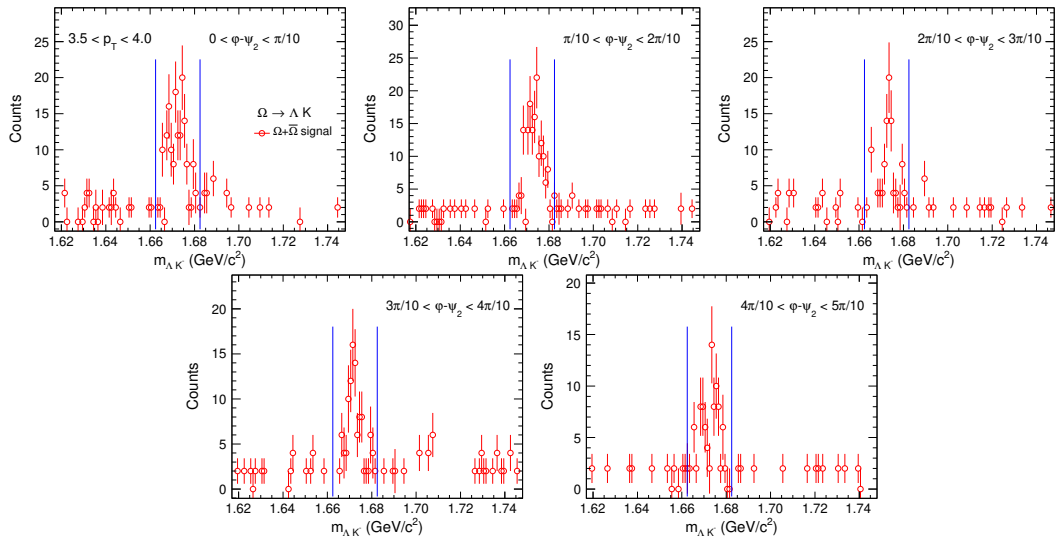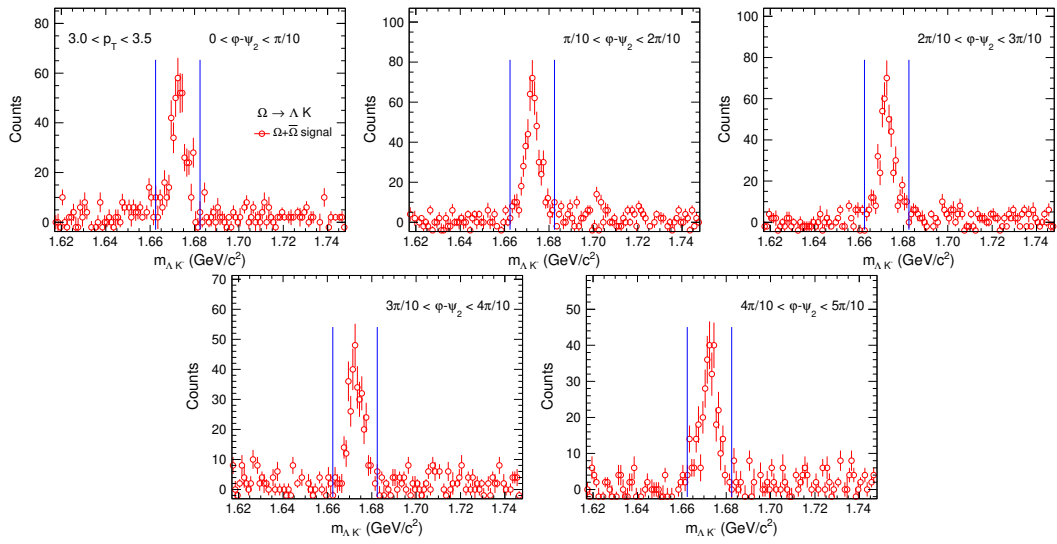
3.10.9 Yield vs. $\phi - \psi_n$ distribution for v_n extraction (0-80%)

143
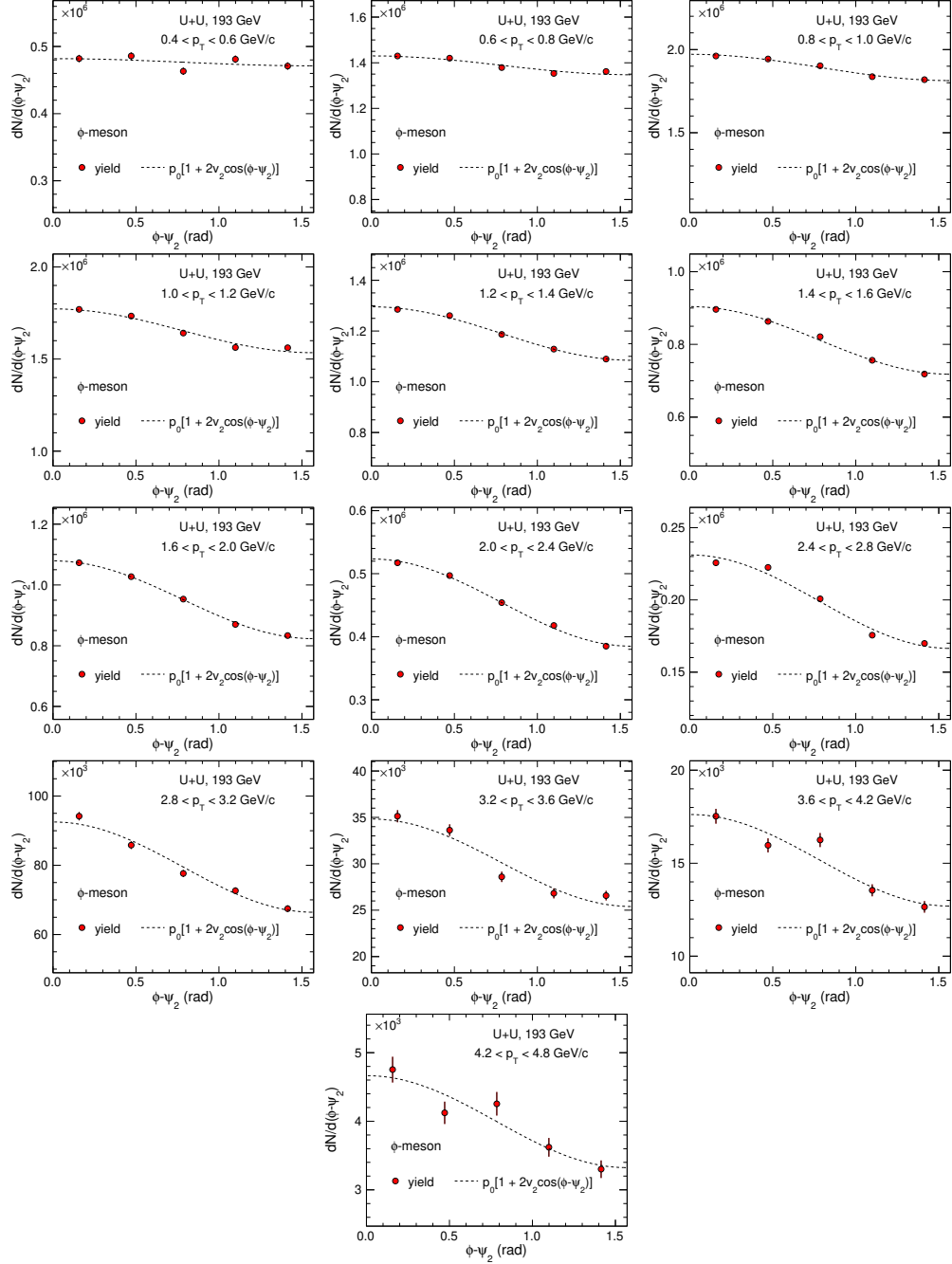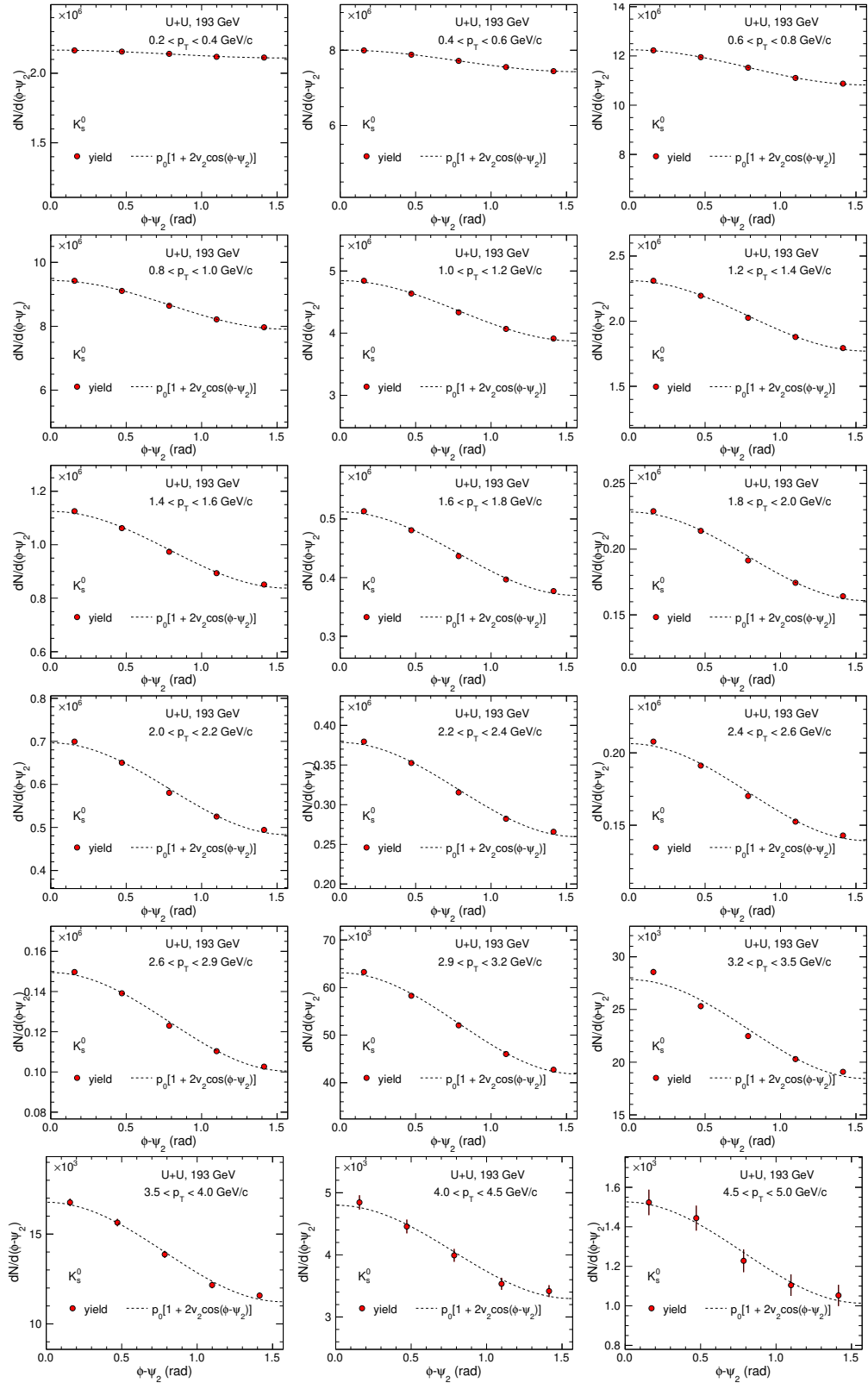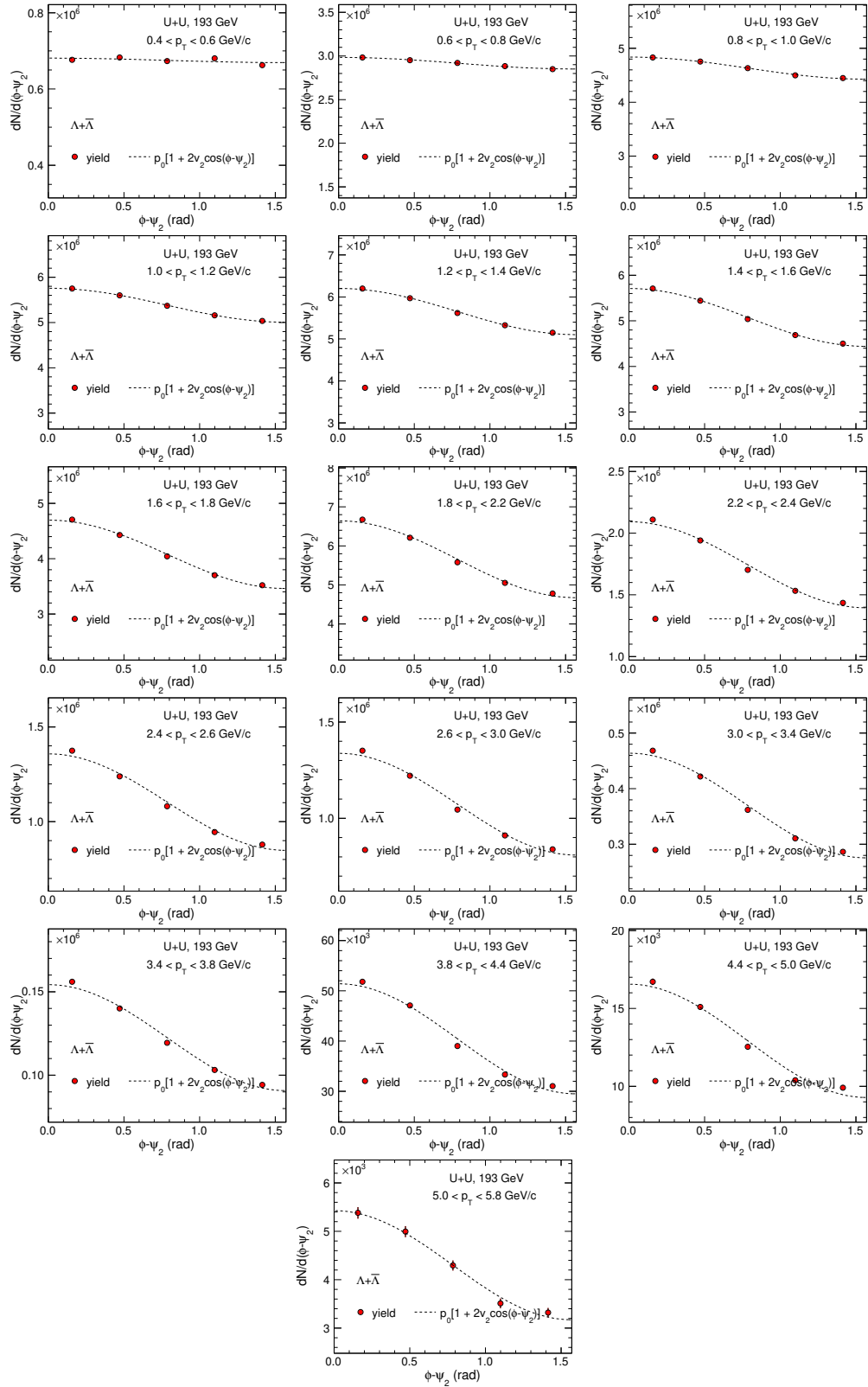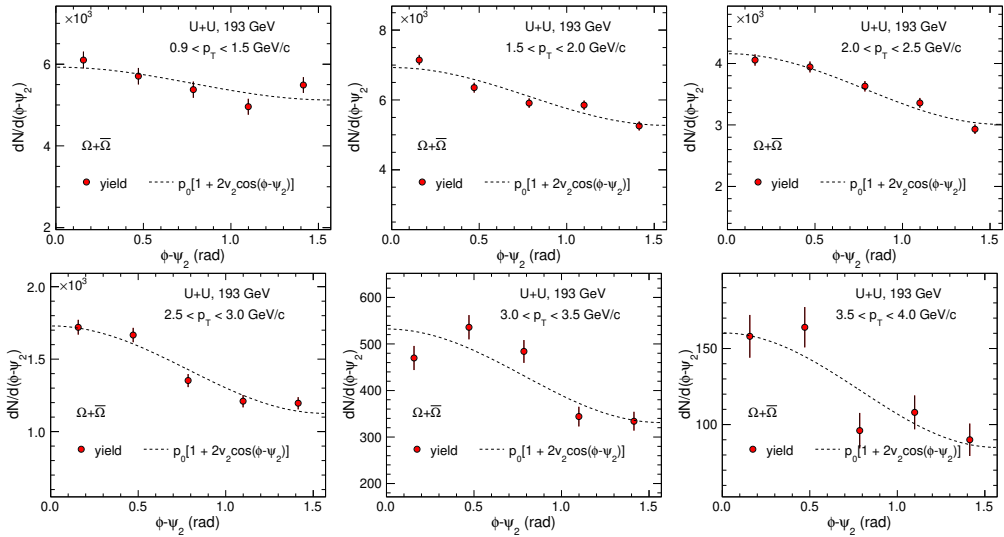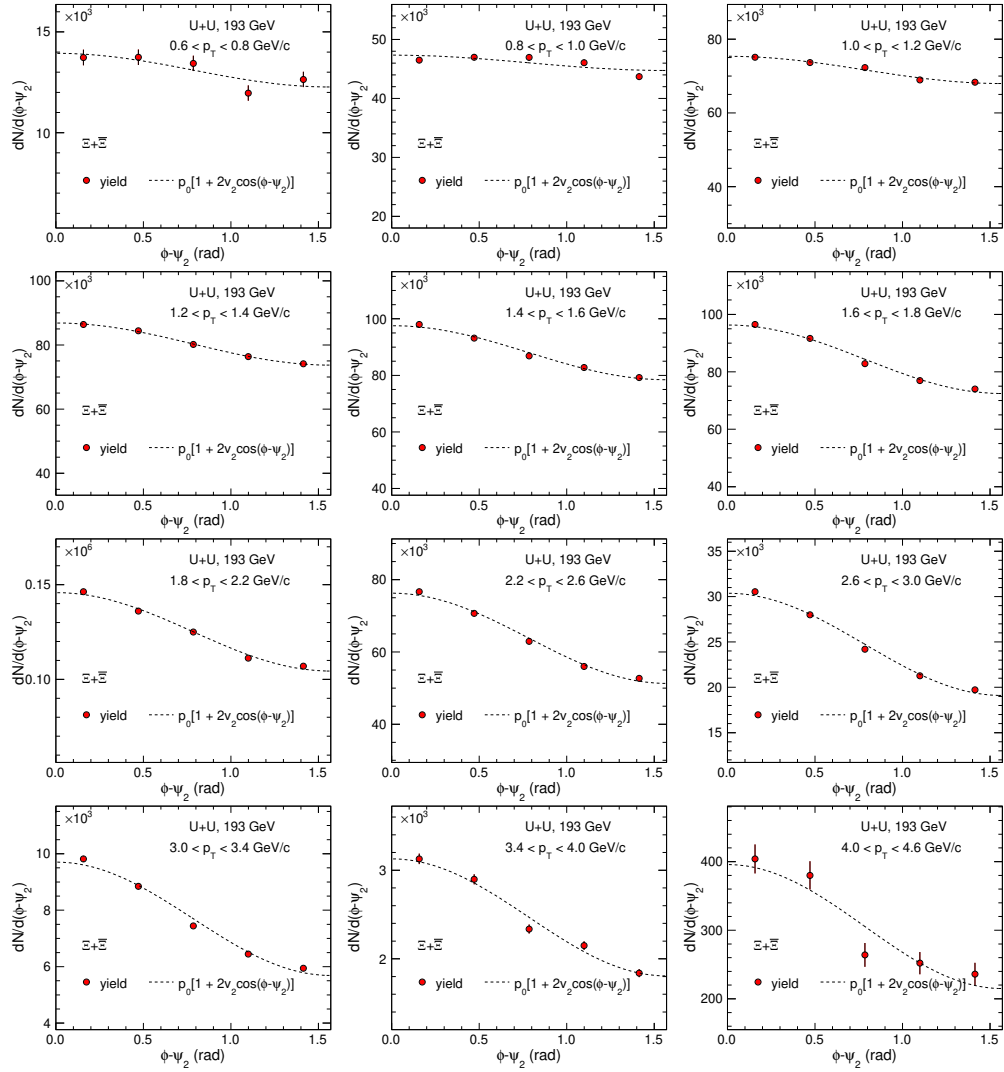
3.10.10 v_n data points:

Unit of p_T is GeV/c for all tables below.

p_T	v_2	Stat. Err	Sys. Err
0.30	0.0107	0.0005	0.001
0.50	0.0300	0.0002	0.0004
0.70	0.0499	0.0002	0.0002
0.90	0.0710	0.0002	0.0002
1.10	0.0899	0.0003	0.0003
1.30	0.1067	0.0004	0.0004
1.50	0.1180	0.0006	0.0004
1.70	0.1305	0.0008	0.0005
1.90	0.140	0.001	0.0008
2.10	0.146	0.001	0.002
2.30	0.150	0.001	0.001
2.50	0.156	0.002	0.001
2.75	0.158	0.002	0.001
3.05	0.164	0.004	0.002
3.35	0.164	0.005	0.002
3.75	0.160	0.007	0.004
4.25	0.15	0.01	0.005
4.75	0.16	0.02	0.01

Table: K_s^0 : 0-80% centrality

p_T	v_3	Stat. Err	Sys. Err
0.30	0.000	0.001	0.0009
0.50	0.0042	0.0005	0.0004
0.70	0.0110	0.0004	0.0002
0.90	0.0216	0.0004	0.0003
1.10	0.0318	0.0006	0.0004
1.30	0.0407	0.0008	0.0003
1.50	0.050	0.001	0.0006
1.70	0.056	0.002	0.0006
1.90	0.070	0.003	0.0008
2.20	0.078	0.002	0.001
2.60	0.087	0.003	0.002
3.00	0.087	0.006	0.003
3.45	0.10	0.01	0.004
3.95	0.09	0.02	0.006
4.45	0.08	0.04	0.02
5.10	0.07	0.06	0.02

Table: K_s^0 : 0-80% centrality

p_T	v_4	Stat. Err	Sys. Err
0.30	0.000	0.002	0.0008
0.50	0.000	0.001	0.0004
0.70	0.0038	0.0008	0.0004
0.90	0.0048	0.0009	0.0007
1.10	0.014	0.001	0.0008
1.30	0.016	0.002	0.001
1.50	0.020	0.002	0.002
1.70	0.033	0.004	0.002
2.00	0.042	0.004	0.001
2.40	0.047	0.005	0.002
2.80	0.040	0.009	0.002
3.30	0.03	0.02	0.004
3.90	0.05	0.03	0.02
4.60	0.10	0.07	0.02

Table: K_s^0 : 0-80% centrality

ϕ-meson (0-80%) centrality:

ϕ-meson : 0-80% centrality			
p_T	v_2	Stat. Err	Sys. Err
0.70	0.025	0.003	0.002
0.90	0.035	0.003	0.002
1.10	0.060	0.003	0.002
1.30	0.074	0.003	0.002
1.50	0.096	0.003	0.002
1.80	0.112	0.003	0.002
2.20	0.127	0.004	0.002
2.60	0.136	0.005	0.003
3.00	0.137	0.007	0.004
3.40	0.13	0.01	0.01
3.90	0.14	0.01	0.02
4.50	0.14	0.02	0.04

ϕ-meson : 0-80% centrality			
p_T	v_3	Stat. Err	Sys. Err
0.85	-0.001	0.006	0.002
1.15	0.013	0.006	0.004
1.45	0.042	0.006	0.005
1.75	0.063	0.007	0.007
2.10	0.078	0.008	0.008
2.50	0.089	0.01	0.008
2.90	0.10	0.02	0.01
3.30	0.07	0.02	0.02
3.80	0.08	0.03	0.02
4.45	0.03	0.04	0.03

ϕ-meson : 0-80% centrality			
p_T	v_4	Stat. Err	Sys. Err
0.75	0.00	0.01	0.001
1.05	0.00	0.01	0.003
1.35	0.01	0.01	0.004
1.70	0.01	0.01	0.005
2.10	0.04	0.02	0.005
2.55	0.08	0.02	0.01
3.05	0.07	0.03	0.02
3.55	0.08	0.04	0.06
4.15	0.06	0.06	0.07

$\Lambda + \bar{\Lambda}$ (0-80%) centrality:

$\Lambda + \bar{\Lambda}$: 0-80% centrality			
p_T	v_2	**Stat. Err**	**Sys. Err**
0.50	0.007	0.002	0.002
0.70	0.0183	0.0006	0.0006
0.90	0.0356	0.0004	0.0004
1.10	0.0560	0.0003	0.0004
1.30	0.0782	0.0003	0.0005
1.50	0.1005	0.0003	0.0006
1.70	0.1219	0.0003	0.0004
2.00	0.1400	0.0003	0.0009
2.30	0.1607	0.0007	0.0008
2.50	0.1856	0.0008	0.001
2.80	0.1978	0.0008	0.001
3.20	0.205	0.001	0.002
3.60	0.208	0.002	0.002
4.00	0.218	0.004	0.002
4.40	0.226	0.007	0.005
4.80	0.21	0.01	0.007
5.40	0.19	0.02	0.02

$\Lambda + \bar{\Lambda}$: 0-80% centrality			
p_T	v_3	**Stat. Err**	**Sys. Err**
0.50	0.002	0.004	0.004
0.70	-0.002	0.002	0.0007
0.90	0.007	0.001	0.001
1.10	0.0161	0.0009	0.0008
1.30	0.0289	0.0008	0.0009
1.50	0.0380	0.0008	0.0007
1.70	0.0546	0.0009	0.001
2.00	0.0639	0.0009	0.003
2.40	0.081	0.001	0.001
2.80	0.101	0.002	0.004
3.20	0.123	0.004	0.004
3.60	0.134	0.007	0.004
4.10	0.14	0.01	0.006
4.80	0.12	0.02	0.01
5.60	0.15	0.07	0.05

$\Lambda + \bar{\Lambda}$: 0-80% centrality			
p_T	v_4	**Stat. Err**	**Sys. Err**
0.70	0.015	0.003	0.005
0.90	0.021	0.002	0.004
1.10	0.022	0.002	0.002
1.30	0.025	0.002	0.002
1.50	0.035	0.001	0.002
1.90	0.037	0.001	0.002
2.50	0.063	0.002	0.001
3.00	0.090	0.004	0.004
3.40	0.083	0.008	0.004
3.80	0.11	0.01	0.009
4.30	0.14	0.02	0.01
5.00	0.12	0.05	0.02

$\Xi + \bar{\Xi}$ (0-80%) centrality:

$\Xi + \bar{\Xi}$: 0-80% centrality			
p_T	v_2	Stat. Err	Sys. Err
0.70	0.05	0.02	0.01
0.90	0.023	0.006	0.005
1.10	0.042	0.004	0.002
1.30	0.066	0.003	0.002
1.50	0.088	0.003	0.002
1.70	0.115	0.002	0.001
2.00	0.134	0.002	0.002
2.40	0.159	0.002	0.002
2.80	0.185	0.004	0.003
3.20	0.212	0.006	0.004
3.70	0.22	0.01	0.003
4.30	0.24	0.03	0.01

$\Xi + \bar{\Xi}$: 0-80% centrality			
p_T	v_3	Stat. Err	Sys. Err
0.75	0.00	0.02	0.01
1.05	0.021	0.007	0.005
1.35	0.041	0.005	0.004
1.65	0.034	0.004	0.003
2.00	0.064	0.004	0.002
2.40	0.080	0.005	0.002
2.80	0.094	0.007	0.004
3.20	0.12	0.01	0.01
3.70	0.14	0.02	0.008
4.30	0.08	0.06	0.04

$\Xi + \bar{\Xi}$: 0-80% centrality			
p_T	v_4	Stat. Err	Sys. Err
0.90	0.00	0.02	0.02
1.30	0.008	0.009	0.005
1.65	0.009	0.008	0.006
1.95	0.028	0.008	0.006
2.25	0.06	0.01	0.003
2.60	0.07	0.01	0.005
3.10	0.08	0.02	0.01
3.70	0.12	0.04	0.01
4.40	0.1	0.1	0.06

$\Omega + \bar{\Omega}$ **(0-80%) centrality:**

$\Omega + \bar{\Omega}$: 0-80% centrality			
p_T	v_2	**Stat. Err**	**Sys. Err**
1.20	0.06	0.02	0.01
1.75	0.11	0.01	0.007
2.25	0.13	0.01	0.006
2.75	0.17	0.02	0.005
3.25	0.19	0.03	0.01
3.75	0.25	0.05	0.01

$\Omega + \bar{\Omega}$: 0-80% centrality			
p_T	v_3	**Stat. Err**	**Sys. Err**
1.25	0.06	0.04	0.02
1.75	0.06	0.02	0.009
2.30	0.08	0.02	0.01
2.90	0.13	0.03	0.01
3.60	0.11	0.06	0.02

$\Omega + \bar{\Omega}$: 0-80% centrality			
p_T	v_4	**Stat. Err**	**Sys. Err**
1.3	0.00	0.06	0.06
1.9	0.06	0.04	0.02
2.6	0.09	0.05	0.02
3.4	0.03	0.09	0.05

K_s^0 **(0-10%) centrality:**

K_s^0 : 0-10% centrality			
p_T	v_2	**Stat. Err**	**Sys. Err**
0.30	0.001	0.002	0.001
0.50	0.0113	0.0007	0.0005
0.70	0.0219	0.0005	0.0009
0.90	0.0348	0.0005	0.0008
1.10	0.0472	0.0007	0.0009
1.30	0.056	0.001	0.0008
1.50	0.063	0.001	0.0007
1.70	0.073	0.002	0.0007
1.90	0.080	0.003	0.002
2.10	0.086	0.004	0.002
2.35	0.091	0.005	0.004
2.65	0.101	0.009	0.004
3.00	0.10	0.01	0.009
3.40	0.09	0.02	0.02
3.90	0.07	0.04	0.02
4.50	0.08	0.07	0.04

K_s^0 : 0-10% centrality			
p_T	v_3	**Stat. Err**	**Sys. Err**
0.30	-0.004	0.002	0.002
0.50	0.003	0.001	0.0008
0.70	0.0084	0.0007	0.0002
0.90	0.0180	0.0007	0.0004
1.10	0.025	0.001	0.001
1.30	0.033	0.002	0.001
1.50	0.040	0.002	0.001
1.75	0.046	0.003	0.001
2.05	0.065	0.003	0.002
2.35	0.079	0.004	0.002
2.70	0.078	0.006	0.002
3.10	0.083	0.01	0.005
3.55	0.10	0.02	0.006
4.05	0.08	0.03	0.006
4.55	0.06	0.06	0.02
5.20	0.03	0.09	0.04

K_s^0 : 0-10% centrality			
p_T	v_4	**Stat. Err**	**Sys. Err**
0.3	-0.002	0.004	0.001
0.5	0.003	0.002	0.0008
0.7	0.001	0.001	0.0007
0.9	0.002	0.001	0.001
1.1	0.011	0.002	0.002
1.3	0.020	0.003	0.001
1.5	0.016	0.004	0.002
1.7	0.030	0.006	0.004
2.0	0.033	0.005	0.001
2.4	0.036	0.007	0.003
2.8	0.04	0.01	0.003
3.3	0.02	0.02	0.007
3.9	0.01	0.05	0.01
4.6	0.08	0.09	0.02

ϕ-meson (0-10%) centrality:

ϕ-meson : 0-10% centrality			
p_T	v_2	**Stat. Err**	**Sys. Err**
0.60	0.02	0.01	0.01
0.80	0.014	0.009	0.01
1.00	0.017	0.009	0.01
1.25	0.030	0.007	0.008
1.55	0.047	0.008	0.006
1.85	0.05	0.01	0.006
2.15	0.06	0.01	0.006
2.45	0.07	0.01	0.01
2.75	0.06	0.02	0.01
3.15	0.05	0.02	0.04

ϕ-meson : 0-10% centrality			
p_T	v_3	**Stat. Err**	**Sys. Err**
0.70	0.02	0.02	0.02
0.95	0.00	0.01	0.004
1.25	0.02	0.01	0.007
1.60	0.03	0.01	0.007
2.00	0.07	0.02	0.01
2.40	0.08	0.02	0.01
2.80	0.08	0.03	0.01
3.25	0.10	0.04	0.03

ϕ-meson : 0-10% centrality			
p_T	v_4	**Stat. Err**	**Sys. Err**
0.8	0.00	0.02	0.02
1.2	0.00	0.02	0.02
1.6	0.01	0.02	0.01
2.0	0.02	0.03	0.01
2.4	0.04	0.04	0.02
2.9	0.10	0.05	0.03
3.5	0.11	0.09	0.04
4.2	0.1	0.1	0.2

$\Lambda + \bar{\Lambda}$ (0-10%) centrality:

$\Lambda + \bar{\Lambda}$: 0-10% centrality			
p_T	v_2	**Stat. Err**	**Sys. Err**
0.50	-0.014	0.008	0.004
0.70	-0.004	0.002	0.001
0.90	0.002	0.001	0.002
1.10	0.011	0.001	0.002
1.30	0.0239	0.0008	0.001
1.50	0.0399	0.0008	0.0004
1.70	0.0565	0.0009	0.002
2.00	0.0660	0.0009	0.0008
2.30	0.0781	0.002	0.002
2.50	0.101	0.002	0.002
2.80	0.113	0.002	0.002
3.20	0.110	0.004	0.003
3.60	0.118	0.006	0.005
4.05	0.13	0.01	0.009
4.55	0.14	0.02	0.02
5.10	0.14	0.05	0.05

$\Lambda + \bar{\Lambda}$: 0-10% centrality			
p_T	v_3	**Stat. Err**	**Sys. Err**
0.5	0.00	0.01	0.01
0.7	-0.001	0.004	0.004
0.9	-0.004	0.003	0.0008
1.1	0.001	0.002	0.0008
1.3	0.013	0.002	0.001
1.5	0.016	0.002	0.002
1.7	0.032	0.002	0.002
2.0	0.043	0.002	0.003
2.4	0.057	0.003	0.003
2.8	0.076	0.005	0.006
3.2	0.089	0.009	0.007
3.6	0.12	0.02	0.01
4.1	0.13	0.02	0.02
4.8	0.11	0.06	0.05
5.6	0.0	0.2	0.1

$\Lambda + \bar{\Lambda}$: 0-10% centrality			
p_T	v_4	**Stat. Err**	**Sys. Err**
0.7	0.000	0.008	0.004
0.9	0.013	0.005	0.006
1.1	0.003	0.004	0.002
1.3	0.000	0.003	0.001
1.5	0.010	0.002	0.002
1.9	0.013	0.002	0.003
2.5	0.031	0.003	0.003
3.0	0.055	0.008	0.008
3.4	0.04	0.01	0.009
3.9	0.09	0.02	0.02
4.5	0.1	0.06	0.04
5.1	0.0	0.1	0.1

$\Xi + \bar{\Xi}$ (0-10%) centrality:

$\Xi + \bar{\Xi}$: 0-10% centrality			
p_T	v_2	**Stat. Err**	**Sys. Err**
0.90	0.02	0.02	0.009
1.25	0.01	0.01	0.004
1.55	0.041	0.007	0.008
1.85	0.059	0.006	0.004
2.20	0.075	0.006	0.004
2.60	0.102	0.008	0.004
3.00	0.12	0.01	0.008
3.55	0.13	0.02	0.01
4.15	0.19	0.07	0.04

$\Xi + \bar{\Xi}$: 0-10% centrality			
p_T	v_3	**Stat. Err**	**Sys. Err**
0.95	0.03	0.02	0.02
1.35	0.04	0.01	0.01
1.65	0.03	0.01	0.005
2.00	0.052	0.008	0.005
2.40	0.07	0.01	0.005
2.80	0.10	0.01	0.008
3.20	0.12	0.02	0.02
3.70	0.17	0.04	0.02
4.30	0.15	0.14	0.08

$\Xi + \bar{\Xi}$: 0-10% centrality			
p_T	v_4	**Stat. Err**	**Sys. Err**
0.90	0.04	0.05	0.04
1.30	-0.01	0.03	0.02
1.65	0.00	0.02	0.01
2.00	0.05	0.02	0.01
2.50	0.07	0.02	0.01
3.10	0.10	0.03	0.02
3.80	0.18	0.08	0.04

$\Omega + \bar{\Omega}$ **(0-10%) centrality:**

$\Omega + \bar{\Omega}$: 0-10% centrality			
p_T	v_2	**Stat. Err**	**Sys. Err**
1.25	0.00	0.08	0.08
1.75	-0.02	0.04	0.03
2.25	0.06	0.04	0.01
2.75	0.12	0.05	0.03
3.60	0.13	0.07	0.03

$\Omega + \bar{\Omega}$: 0-10% centrality			
p_T	v_3	**Stat. Err**	**Sys. Err**
1.4	0.04	0.09	0.06
2.2	0.12	0.05	0.03
3.0	0.19	0.08	0.03
3.8	0.0	0.2	0.09

$\Omega + \bar{\Omega}$: 0-10% centrality			
p_T	v_4	**Stat. Err**	**Sys. Err**
1.3	-0.00	0.06	0.06
1.9	0.06	0.04	0.02
2.6	0.09	0.05	0.02
3.4	0.03	0.09	0.05

K_s^0 (10-40%) centrality:

K_s^0 : 10-40% centrality			
p_T	v_2	**Stat. Err**	**Sys. Err**
0.30	0.0154	0.0006	0.0005
0.50	0.0322	0.0003	0.0003
0.70	0.0523	0.0002	0.0005
0.90	0.0758	0.0002	0.0006
1.10	0.0958	0.0003	0.0008
1.30	0.1144	0.0004	0.0007
1.50	0.1264	0.0006	0.0008
1.70	0.1398	0.0009	0.001
1.90	0.148	0.001	0.001
2.10	0.158	0.002	0.001
2.30	0.155	0.002	0.001
2.50	0.160	0.003	0.002
2.75	0.167	0.004	0.001
3.05	0.156	0.006	0.003
3.35	0.157	0.009	0.006
3.75	0.12	0.01	0.007
4.35	0.14	0.03	0.02

K_s^0 : 10-40% centrality			
p_T	v_3	**Stat. Err**	**Sys. Err**
0.30	0.002	0.001	0.0007
0.50	0.0045	0.0006	0.0003
0.70	0.0116	0.0005	0.0003
0.90	0.0218	0.0005	0.0003
1.10	0.0334	0.0007	0.0004
1.30	0.042	0.001	0.0005
1.50	0.052	0.001	0.0007
1.75	0.062	0.002	0.0008
2.05	0.074	0.002	0.001
2.35	0.080	0.003	0.002
2.70	0.091	0.005	0.002
3.10	0.082	0.009	0.004
3.55	0.09	0.02	0.006
4.05	0.08	0.03	0.008
4.65	0.04	0.05	0.01

K_s^0 : 10-40% centrality			
p_T	v_4	**Stat. Err**	**Sys. Err**
0.3	0.002	0.003	0.0008
0.5	-0.003	0.001	0.0007
0.7	0.004	0.001	0.0004
0.9	0.005	0.001	0.0007
1.1	0.013	0.001	0.0008
1.3	0.012	0.002	0.001
1.5	0.020	0.003	0.002
1.7	0.034	0.004	0.003
2.0	0.048	0.005	0.002
2.4	0.051	0.006	0.002
2.8	0.03	0.01	0.004
3.3	0.04	0.02	0.006
4.0	0.08	0.04	0.01

ϕ-meson (10-40%) centrality:

p_T	v_2	Stat. Err	Sys. Err
0.5	0.009	0.007	0.005
0.7	0.031	0.004	0.003
0.9	0.034	0.003	0.002
1.1	0.062	0.003	0.002
1.3	0.082	0.003	0.002
1.5	0.105	0.004	0.004
1.8	0.111	0.003	0.002
2.2	0.129	0.004	0.004
2.6	0.148	0.005	0.004
3.0	0.163	0.007	0.005
3.4	0.14	0.01	0.01
3.9	0.12	0.01	0.02
4.5	0.05	0.02	0.03

ϕ-meson : 10-40% centrality

p_T	v_3	Stat. Err	Sys. Err
0.85	0.000	0.006	0.005
1.15	0.022	0.006	0.006
1.45	0.038	0.007	0.006
1.75	0.046	0.008	0.006
2.10	0.061	0.008	0.006
2.50	0.08	0.01	0.006
2.90	0.09	0.02	0.01
3.30	0.05	0.02	0.02
3.80	0.10	0.03	0.02
4.45	0.02	0.04	0.02

ϕ-meson : 10-40% centrality

p_T	v_4	Stat. Err	Sys. Err
0.75	0.00	0.01	0.0008
1.05	0.00	0.01	0.004
1.35	0.02	0.01	0.005
1.70	0.03	0.01	0.006
2.10	0.04	0.02	0.02
2.55	0.07	0.02	0.02
3.05	0.03	0.03	0.02
3.55	0.03	0.05	0.04
4.15	0.03	0.08	0.07

ϕ-meson : 10-40% centrality

$\Lambda + \bar{\Lambda}$ (10-40%) centrality:

$\Lambda + \bar{\Lambda}$: 10-40% centrality			
p_T	v_2	**Stat. Err**	**Sys. Err**
0.5	0.006	0.002	0.002
0.7	0.0153	0.0006	0.001
0.9	0.0341	0.0004	0.0009
1.1	0.0571	0.0004	0.0009
1.3	0.0818	0.0003	0.0007
1.5	0.1066	0.0003	0.0008
1.7	0.1306	0.0004	0.001
2.0	0.1526	0.0003	0.0008
2.3	0.1760	0.0007	0.0008
2.5	0.1994	0.0009	0.0008
2.8	0.2107	0.0009	0.0009
3.2	0.222	0.001	0.001
3.6	0.221	0.002	0.001
4.0	0.230	0.004	0.003
4.5	0.225	0.007	0.007
5.1	0.19	0.02	0.02
5.7	0.14	0.03	0.03

$\Lambda + \bar{\Lambda}$: 10-40% centrality			
p_T	v_3	**Stat. Err**	**Sys. Err**
0.5	0.000	0.005	0.003
0.7	-0.002	0.002	0.0005
0.9	0.004	0.001	0.0009
1.1	0.013	0.001	0.0008
1.3	0.0261	0.0009	0.0009
1.5	0.0384	0.0009	0.0009
1.7	0.053	0.001	0.0007
2.0	0.062	0.001	0.003
2.4	0.084	0.002	0.001
2.8	0.108	0.003	0.004
3.2	0.127	0.004	0.003
3.6	0.141	0.007	0.003
4.1	0.15	0.01	0.007
4.8	0.12	0.03	0.02
5.6	0.17	0.07	0.04

$\Xi + \bar{\Xi}$ (10-40%) centrality:

$\Xi + \bar{\Xi}$: 10-40% centrality			
p_T	v_2	**Stat. Err**	**Sys. Err**
0.7	0.02	0.01	0.01
0.9	0.020	0.006	0.004
1.1	0.0448	0.004	0.003
1.3	0.067	0.003	0.002
1.5	0.092	0.003	0.0008
1.7	0.116	0.002	0.001
2.0	0.140	0.002	0.001
2.4	0.169	0.002	0.001
2.8	0.191	0.004	0.002
3.2	0.226	0.007	0.004
3.7	0.23	0.01	0.005
4.3	0.23	0.03	0.01

$\Xi + \bar{\Xi}$: 10-40% centrality			
p_T	v_3	**Stat. Err**	**Sys. Err**
0.85	0.01	0.01	0.008
1.20	0.022	0.005	0.004
1.60	0.032	0.004	0.003
2.00	0.069	0.004	0.002
2.40	0.083	0.006	0.002
2.80	0.094	0.009	0.005
3.20	0.111	0.02	0.01
3.70	0.124	0.03	0.01
4.30	0.112	0.07	0.05

$\Xi + \bar{\Xi}$: 10-40% centrality			
p_T	v_4	**Stat. Err**	**Sys. Err**
0.90	0.00	0.02	0.02
1.30	0.006	0.009	0.006
1.65	0.008	0.009	0.005
1.95	0.03	0.01	0.004
2.25	0.06	0.01	0.005
2.60	0.09	0.01	0.006
3.10	0.09	0.02	0.01
3.70	0.10	0.06	0.02

$\Omega + \bar{\Omega}$ **(10-40%) centrality:**

$\Omega + \bar{\Omega}$: 10-40% centrality			
p_T	v_2	**Stat. Err**	**Sys. Err**
1.20	0.07	0.02	0.009
1.75	0.11	0.01	0.008
2.25	0.15	0.01	0.006
2.75	0.18	0.02	0.004
3.25	0.25	0.03	0.02
3.80	0.24	0.06	0.01

$\Omega + \bar{\Omega}$: 10-40% centrality			
p_T	v_3	**Stat. Err**	**Sys. Err**
1.20	0.05	0.04	0.02
1.75	0.03	0.02	0.01
2.30	0.06	0.02	0.01
2.90	0.10	0.04	0.02
3.60	0.11	0.07	0.02

$\Omega + \bar{\Omega}$: 10-40% centrality			
p_T	v_4	**Stat. Err**	**Sys. Err**
1.3	0.05	0.08	0.08
1.9	0.10	0.05	0.02
2.6	0.16	0.06	0.02
3.4	0.15	0.1	0.04

K_s^0 (40-80%) centrality:

K_s^0 : 40-80% centrality			
p_T	v_2	Stat. Err	Sys. Err
0.3	0.023	0.001	0.0007
0.5	0.0485	0.0006	0.0003
0.7	0.0781	0.0005	0.0005
0.9	0.1063	0.0006	0.0005
1.1	0.1301	0.0008	0.0006
1.3	0.152	0.001	0.0005
1.5	0.164	0.002	0.001
1.7	0.177	0.003	0.002
2.0	0.198	0.003	0.002
2.4	0.190	0.004	0.001
2.8	0.184	0.008	0.004
3.2	0.20	0.02	0.007
3.7	0.22	0.02	0.01
4.4	0.22	0.05	0.07

K_s^0 : 40-80% centrality			
p_T	v_3	Stat. Err	Sys. Err
0.30	-0.003	0.004	0.003
0.50	0.008	0.002	0.0007
0.70	0.02	0.001	0.001
0.90	0.030	0.002	0.0009
1.10	0.040	0.002	0.001
1.30	0.055	0.003	0.001
1.50	0.063	0.005	0.001
1.80	0.068	0.006	0.003
2.20	0.076	0.008	0.004
2.65	0.08	0.01	0.004
3.20	0.08	0.03	0.005
3.90	0.09	0.06	0.02

K_s^0 : 40-80% centrality			
p_T	v_4	Stat. Err	Sys. Err
0.3	0.000	0.008	0.0008
0.5	0.007	0.004	0.002
0.7	0.012	0.003	0.002
0.9	0.012	0.003	0.001
1.1	0.025	0.005	0.003
1.3	0.018	0.007	0.002
1.6	0.032	0.008	0.005
2.0	0.02	0.02	0.006
2.4	0.04	0.02	0.01
2.8	0.04	0.04	0.02
3.3	0.07	0.06	0.03
3.9	0.01	0.09	0.06

ϕ-meson (40-80%) centrality:

ϕ-meson : 40-80% centrality			
p_T	v_2	**Stat. Err**	**Sys. Err**
0.7	0.024	0.005	0.009
0.9	0.068	0.004	0.006
1.1	0.089	0.004	0.003
1.3	0.112	0.005	0.004
1.5	0.135	0.006	0.004
1.8	0.171	0.005	0.004
2.2	0.196	0.006	0.004
2.6	0.190	0.008	0.004
3.0	0.20	0.01	0.006
3.4	0.16	0.02	0.008
3.9	0.14	0.02	0.03
4.5	0.15	0.03	0.03

ϕ-meson : 40-80% centrality			
p_T	v_3	**Stat. Err**	**Sys. Err**
0.85	-0.01	0.01	0.001
1.15	0.00	0.01	0.0009
1.45	0.03	0.01	0.007
1.75	0.07	0.02	0.009
2.10	0.05	0.02	0.009
2.55	0.08	0.02	0.01
3.05	0.15	0.04	0.02
3.55	0.14	0.06	0.03
4.10	0.03	0.09	0.04

$\Lambda + \bar{\Lambda}$ (40-80%) centrality:

p_T	v_2	Stat. Err	Sys. Err
$\Lambda + \bar{\Lambda}$: 40-80% centrality
0.5	0.031	0.002	0.002
0.7	0.0546	0.0009	0.0008
0.9	0.0817	0.0007	0.0008
1.1	0.1140	0.0007	0.0007
1.3	0.1491	0.0007	0.0007
1.5	0.1810	0.0008	0.0007
1.7	0.2059	0.0008	0.0009
2.0	0.2244	0.0008	0.0006
2.3	0.243	0.001	0.001
2.5	0.276	0.002	0.001
2.8	0.292	0.002	0.001
3.2	0.292	0.003	0.002
3.6	0.303	0.005	0.003
4.0	0.300	0.009	0.007
4.4	0.31	0.01	0.008
4.9	0.29	0.03	0.03

$\Xi + \bar{\Xi}$ (40-80%) centrality:

$\Xi + \bar{\Xi}$: 40-80% centrality			
p_T	v_2	**Stat. Err**	**Sys. Err**
0.7	0.08	0.01	0.008
0.9	0.051	0.007	0.005
1.1	0.091	0.006	0.002
1.3	0.115	0.005	0.002
1.5	0.135	0.005	0.004
1.7	0.169	0.006	0.002
2.0	0.187	0.005	0.002
2.4	0.216	0.006	0.003
2.8	0.25	0.01	0.002
3.2	0.27	0.02	0.008
3.7	0.25	0.03	0.01
4.3	0.14	0.08	0.03

$\Omega + \bar{\Omega}$ (40-80%) centrality:

$\Omega + \bar{\Omega}$: 40-80% centrality			
p_T	v_2	**Stat. Err**	**Sys. Err**
1.15	0.03	0.03	0.01
1.65	0.18	0.02	0.009
2.20	0.21	0.02	0.006
2.75	0.20	0.04	0.005
3.50	0.20	0.07	0.02

Chapter 4

Elliptic flow of ϕ-meson and inclusive charged hadrons in Au+Au collisions at 14.5 GeV

4.1 Introduction

One of the primary objectives of high energy heavy-ion collision experiments is the exploration of QCD phase-diagram [1–3]. The phase diagram shows the relationship between baryon chemical potential (μ_B) and temperature (T), which can be varied in an experiment by varying the collision beam energy [4]. The two important aspects to understand the QCD phase diagram are the phase boundary [5] and the critical point [6] of QCD phase transition from partonic to hadronic matter.

To explore the phase boundary and critical point of the QCD phase diagram, first phase of the Beam Energy Scan (BES) program [2,3] with Au+Au collision energies at $\sqrt{s_{NN}} = 7.7$, 11.5, 19.6, 27, and 39 GeV was carried out by RHIC in the years 2010 and 2011 [7]. In the year 2014, data at a new Au+Au collision energy at $\sqrt{s_{NN}} =$

14.5 GeV was recorded in BES-I program to fill the gap of 200 MeV in μ_B between the two beam energies 11.5 and 19.6 GeV [8].

In this chapter, we present measurements of ϕ-meson and inclusive charged hadrons elliptic flow v_2 at mid-rapidity ($|\eta|$ <1.0) in Au+Au collisions at $\sqrt{s_{\mathrm{NN}}}$ = 14.5 GeV [9]. A systematic study of v_2 as a function p_T, η and collision centrality is presented. The inclusive charged hadrons v_2 results are obtained using event plane method ($v_2\{EtaSubs\}$) and 2,4-particle cumulant method ($v_2\{2\}$, $v_2\{4\}$). Elliptic flow scaled by the initial coordinate space eccentricity (v_2/ε) is presented to investigate partonic collectivity in Au+Au collisions at $\sqrt{s_{\mathrm{NN}}}$ = 14.5 GeV. The measurements are compared with the published results from Au+Au collisions at other beam energies ($\sqrt{s_{\mathrm{NN}}}$) by the STAR [8,10,11] and in Pb+Pb collisions at $\sqrt{s_{\mathrm{NN}}}$ = 2.76 TeV by ALICE collaboration [12]. Comparison of the results with UrQMD [13] and AMPT [14] transport model calculations are also presented to understand the dominance of partonic versus hadronic phases of the medium created in Au+Au collisions at $\sqrt{s_{\mathrm{NN}}}$ = 14.5 GeV.

4.2   Dataset, Event and Track selection

The results presented in this chapter are obtained from the data collected by the STAR experiment at RHIC in the year 2014 for Au+Au collisions at $\sqrt{s_{\mathrm{NN}}}$ = 14.5 GeV. The data-set, trigger, event and track selection are discussed in the following sub-sections.

4.2.1   Data-set and Trigger

The data selected with minimum biased trigger are used for the analysis. The trigger detectors used are Beam-Beam Counters (BBCs) [15]. The BBCs are scintillator-

based detectors situated on the east and west sides of the beam pipe about 375 cm from the center of the nominal interaction region (IR). The pseudorapidity range is $2.2 < |\eta| < 5.0$ and full azimuthal coverage. They are also used to reconstruct the BBC event plane for the flow analysis. 253 bad runs are removed out of the total 837 runs from the analysis based on the quality assurance (QA) checks of the data. A total $\sim$17.25 million good events are analyzed. The data-set information like trigger setup Ids etc. are shown in the Table 4.1.

Table 4.1: Data-set and trigger information for Au+Au collisions at $\sqrt{s_{NN}} = 14.5$ GeV.

System/Energy	Production Id	Trigger Ids	Trigger setup
Au+Au, 14.5 GeV	P14id	440005, 440015	production_15GeV_2014

4.2.2 Event selection

Analyzed events were required to have a primary vertex position along the longitudinal direction (V_z) within ± 70 cm from the center of the Time Projection Chamber (TPC) [16]. An additional cut on the primary vertex radius (defined as $V_r = \sqrt{V_x^2 + V_y^2}$, where V_x and V_y are the vertex positions along the x and y directions) is required to be less than 1.0 cm from the center of the beam pipe to minimize effects of beam and beam pipe interactions. The center of the beam pipe is taken as (0.0 cm, -0.89 cm) due to shift in the beam along y direction during data taking. The distributions of z-position of vertex and positions along the x and y directions are shown in Fig. 4.1. To remove pileup events, it was required that at least two tracks from the primary vertex were matched to the cells of the Time Of Flight (TOF) detector [17]. A list of event cuts used are given in the Table 4.2 below.

Table 4.2: Event selection cuts for Au+Au collisions at $\sqrt{s_{NN}} = 14.5$ GeV.

System/Energy	V_z (cm)	V_r (cm)	Events
Au+Au, 14.5 GeV	$|V_z| < 70$	$V_r < 1.0$	~17.25 Million
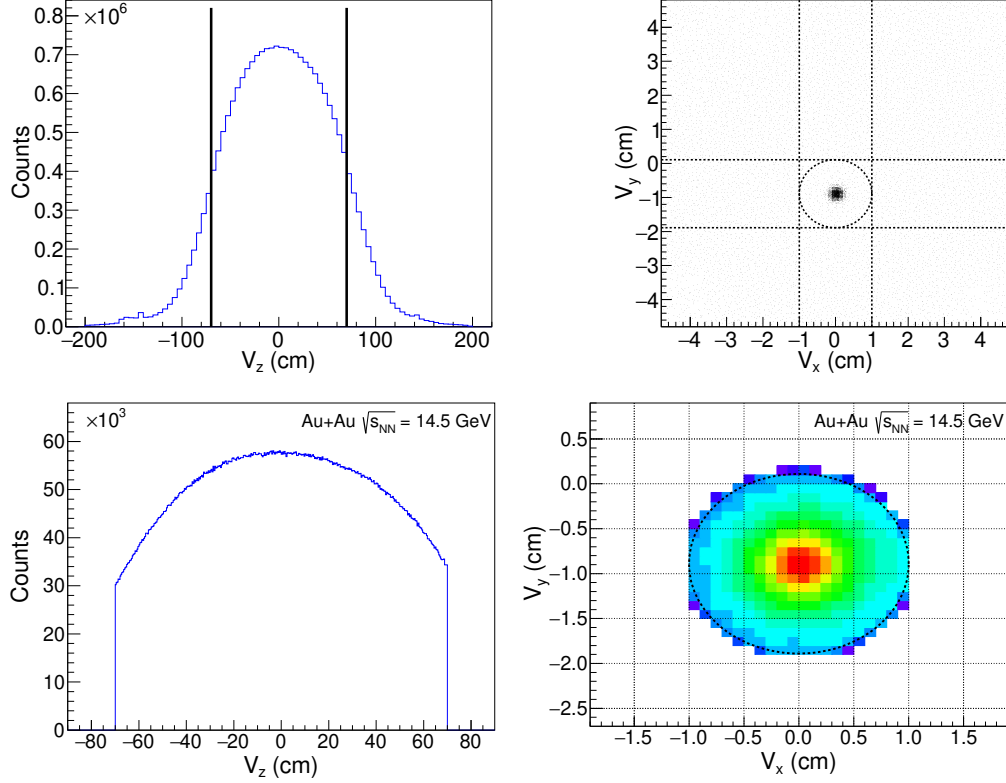
Figure 4.1: Distribution of z-component of primary vertex (left panels) and V_r (right panels) before and after the event cuts in Au+Au collisions at $\sqrt{s_{NN}} = 14.5$ GeV.

4.2.3 Centrality selection

Centrality selection for Au+Au collisions at $\sqrt{s_{NN}} = 14.5$ GeV is based on the reference multiplicity ("refmult") information. The same technique is used as explained in the chapter 3. The number of primary tracks reconstructed by TPC detector over full azimuth and pseudo-rapidity range of $|\eta| < 0.5$ is called the reference multiplicity. The resulted refmult distribution is compared and fitted with a two-component Monte Carlo (MC) Glauber Model [18]. Figure 4.2 shows the measured uncorrected multi-

plicity distribution for charged particles from the TPC (open circles) and for those obtained from MC Glauber model (blue dashed line). The minimum bias events are divided into 9 centrality classes as 0-5%, 5-10%, 10-20%, 20-30%, 30-40%, 40-50%, 50-60%, 60-70%, 70-80%. A documentation of the centrality can be found in the Ref. [19]. A summary of fitting and input parameters of two-component model for Au+Au collisions at $\sqrt{s_{\mathrm{NN}}} = 14.5$ GeV is shown in Table 4.3.
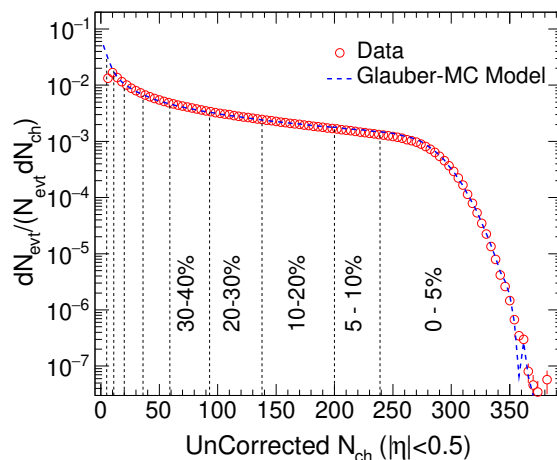
Figure 4.2: Uncorrected charged particle multiplicity distribution (open circles) measured from the TPC detector within $|\eta| < 0.5$ in Au+Au collisions at $\sqrt{s_{\mathrm{NN}}} = 14.5$ GeV. The blue dashed line represents the multiplicity distribution from Monte Carlo Glauber model. The vertical lines represent the centrality selection criteria used in the analysis.

Table 4.3: Summary of fitting and input parameters of two-component model for Au+Au collisions at $\sqrt{s_{\mathrm{NN}}} = 14.5$ GeV.

$\sqrt{s_{\mathrm{NN}}}$ **(GeV)**	n_{pp}	**x**	$\sigma_{NN}^{\mathrm{inel}}$ **(mb)**
14.5	1.15 ±0.05	0.12 ± 0.02	31.5 ± 1.0

The centrality classes are defined by the fractions of geometrical cross section from the simulated multiplicity distributions. For each centrality class, average number of participant nucleons $\langle N_{part} \rangle$, number of binary collisions $\langle N_{coll} \rangle$, reaction plane eccentricity $\langle \epsilon_{RP} \rangle$, participant eccentricity $\langle \epsilon_{part} \rangle$, root-mean-square participant eccentric-

ity $\langle \epsilon_{part}\{2\} \rangle$, and transverse area $\langle S_{part} \rangle$ are calculated. Values of these quantities are listed in the Appendix at the end of the chapter. Eccentricities and transverse area are defined as,

$$\epsilon_{RP} = \frac{\sigma_y^2 - \sigma_x^2}{\sigma_y^2 + \sigma_x^2} \tag{4.1}$$

$$\epsilon_{part} = \frac{\sqrt{\left(\sigma_y^2 - \sigma_x^2\right)^2 + 4\sigma_{xy}^2}}{\sigma_y^2 + \sigma_x^2}, \quad \epsilon_{part}\{2\} = \sqrt{\langle \epsilon_{part}^2 \rangle} \tag{4.2}$$

$$S_{part} = \pi \sqrt{\sigma_x^2 \sigma_y^2 - \sigma_{xy}^2}, \tag{4.3}$$

where,

$$\sigma_x^2 = \{x^2\} - \{x\}^2, \quad \sigma_y^2 = \{y^2\} - \{y\}^2, \quad \sigma_{xy} = \{xy\} - \{x\}\{y\}. \tag{4.4}$$

4.2.4 Track selection

Primary tracks are used in this analysis. Charged particle tracks are identified using TPC and TOF detectors. Several track cuts are applied to ensure quality of the reconstructed tracks. The distance of closest approach (DCA) of the tracks with respect to the primary vertex is required to be less than 3 cm to suppress tracks from secondary vertices. The number of fit points required to be 15 or more out of maximum possible 45 hits in the TPC. The ratio of TPC fit points to the maximum possible hits on a track is required to be greater than 0.52. All tracks within the pseudo-rapidity range of $|\eta| < 1.0$ are selected. A list of the track cuts applied in the analysis is shown in the Table 4.4.

Table 4.4: Track selection cuts for Au+Au collisions at $\sqrt{s_{\mathrm{NN}}} = 14.5$ GeV.

Track parameter	value
Distance of closed approach	$|\mathrm{DCA}| < 3.0$ cm
Number of fit points	nHitsFit ≥ 15
nHitsFit/nHitsPoss	Ratio ≥ 0.52
Transverse Momentum	$p_T \geq 0.2$ (GeV/c)
Pseudorapidity	$|\eta| < 1.0$

4.3 Particle identification

In this section, we discuss identification methods of charged particles using the TPC and TOF detectors.

4.3.1 Particle identification using TPC

Particle identification in the TPC is done by measuring the ionization energy loss (dE/dx) for each of the selected tracks. The measured ionization energy loss (dE/dx) from TPC is shown in the upper panel of Fig. 4.3. The dashed curves represent theoretical values predicted by the Bichsel function [20]. To identify individual charge particles, we define a variable normalized energy loss $(n\sigma)$,

$$n\sigma = \ln \left[\frac{(dE/dx)_{Exp.}}{(dE/dx)_{Bichsel}} \right] / R, \tag{4.5}$$

where the quantity R is the dE/dx resolution of the TPC detector for individual hadrons. For a minimum ionizing particle that produces a single track with the maximum possible number of TPC pad rows (45), the dE/dx resolution is found to be about 6-8% [21]. A cut within $|n\sigma| < 2$ on normalized energy loss along with other basic track selection cuts has been applied to identify pions, kaons and protons.

4.3.2 Particle identification using TOF

The TPC can identify pions, kaons and protons with relatively low momentum, but the separate bands start merging at higher momentum. The TOF detector is able to enhance the particle identification of the tracks with high momentum (> 1.0 GeV/c) where the dE/dx bands of different particles start to merge. The Time-of-Flight (TOF) detector measures the flight time (Δt) of the tracks in full azimuthal coverage and pseudo-rapidity range of $|\eta| < 0.9$ [17]. The flight time is the time taken by a track to traverse the distance L from the primary vertex to the TOF detector i.e. $\Delta t = t - t_0$. The initial start time t_0 is given by the VPD detector. Velocity (β) of the track can be calculated using the time of flight information. Using the velocity and corresponding momentum (p) from the TPC detector kept inside a magnetic field, mass (m) of the particle can be calculated as,

$$m^2 = p^2 \left(\frac{1}{\beta^2} - 1 \right).$$

(4.6)

4.4 Reconstruction of ϕ-meson

In this section, we discuss the method for reconstructing ϕ-mesons at mid-rapidity ($|y| < 1.0$) in Au+Au collisions at $\sqrt{s_{\mathrm{NN}}} = 14.5$ GeV at RHIC [22]. ϕ-mesons are reconstructed through their hadronic decay channel: $\phi \to K^+ K^-$ (branching ratio = $48.9 \pm 0.5\%$) [23]. The invariant mass, m_{inv}, distribution is constructed using all combinations of positively charged kaon candidates with negatively charged kaon candidates in the same event using the following equation,

$$m_{inv} = \sqrt{(E_{K^+} + E_{K^-})^2 - (\vec{p}_{K^+} + \vec{p}_{K^-})^2}.$$

(4.7)
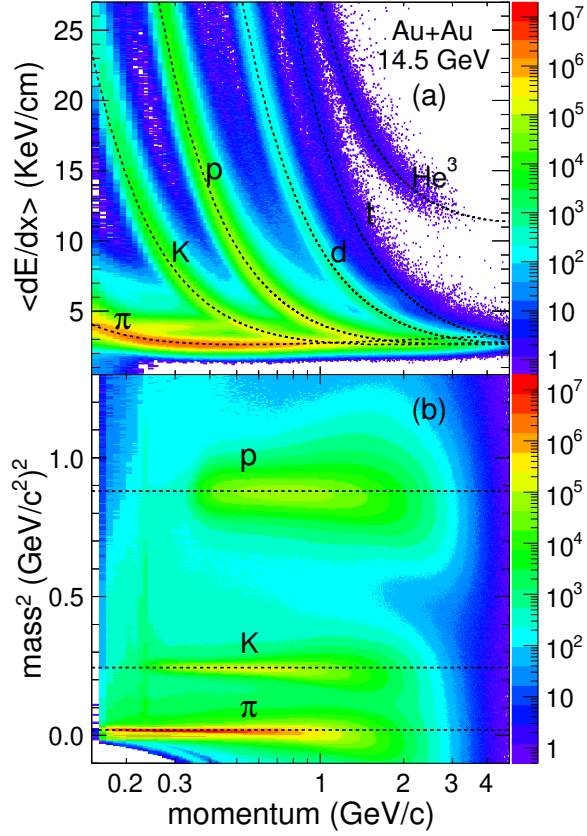
Figure 4.3: (a) The energy loss (dE/dx) distribution of charged particles from TPC as a function of momentum within $|\eta| < 1.0$ for Au+Au collisions at $\sqrt{s_{\mathrm{NN}}} = 14.5$ GeV. The dashed lines corresponds the expected mean value of dE/dx for the corresponding particle from Bichsel function. (b) m^2 as a function of momentum from TOF in Au+Au collisions at $\sqrt{s_{\mathrm{NN}}} = 14.5$ GeV. The dashed lines represent the m^2 values from PDG for the corresponding particle.

A dip-angle cut (> 0.04 radian) is applied in order to exclude conversion electron pairs which may have been misidentified as kaons in the momentum range where the dE/dx bands for kaons and electrons overlap. The dip angle is the angle between the particle momentum (p) and the drift direction (p_z). The dip angle θ between two decay daughter tracks is defined as, $\theta = \cos^{-1}\left(\frac{p_{1T}p_{2T} + p_{1z}p_{2z}}{|p_1||p_2|}\right)$, where p, p_T and p_z are the momentum, transverse momentum and z-component of momentum, respectively. Decay daughter kaon tracks are identified using both the TPC and TOF detector. Kaon m^2 information is used whenever a TOF matched track is available, otherwise

TPC dE/dx information is used to identify kaon tracks. The track selection cuts for ϕ-meson reconstruction in Au+Au collisions at $\sqrt{s_{\mathrm{NN}}} = 14.5$ GeV are listed in the Table 4.5.

Table 4.5: Track selection cuts for ϕ-meson reconstruction.

Number of fit points in TPC	nHitsFit $\geq$ 15
nHitsFit/nHitsPoss	Ratio $\geq$ 0.52
DCA to primary vertex	$|$DCA$|$ < 3.0 cm
Transverse momentum	$p_T \geq 0.2$ (GeV/c)
Pseudo-rapidity	$|\eta|$ < 1.0
$n\sigma_{K^{\pm}}$ dE/dx	$|n\sigma| \leq 2.0$
$m^2_{K^{\pm}}$ from TOF	$0.16 \leq m^2 \leq 0.36$ $(GeV/c^2)^2$

The ϕ-meson signal extracted using Eq. 4.7 sits above a large combinatorial background of uncorrelated pairs of kaons. The combinatorial background from the uncorrelated kaon pairs is estimated using the mixed-event technique. The fact that there are no correlations between the charged tracks from one event to another event and under appropriate condition of mixing of similar kind of event, the mixed event technique reproduces the shape of the background well. Invariant mass distribution constructed using all positively charged kaon candidates from one event mixed with all negatively charged kaon candidates from 'n' other events where n can be set arbitrarily high to minimize effects from statistical fluctuations. For this analysis, n = 5 is used. Effects from multiplicity fluctuations is minimized by dividing events to be mixed into nine centrality classes ($0 - 5\%$, $5 - 10\%$, $10 - 20\%$, $20 - 30\%$, $30 - 40\%$, $40 - 50\%$, $50 - 60\%$, $60 - 70\%$, $70 - 80\%$) and the events are mixed if they fall in the same centrality class. In order to minimize distortions due to acceptance effects, within each centrality class, the events are further sub-divided into 10 bins according to vertex-z position. The background distribution is scaled by the iterative method

as discussed in chapter 3. This procedure is illustrated in the Fig. 4.4. ϕ-meson signal and background distributions for all p_T bins are shown in the Appendix at the end of the chapter.
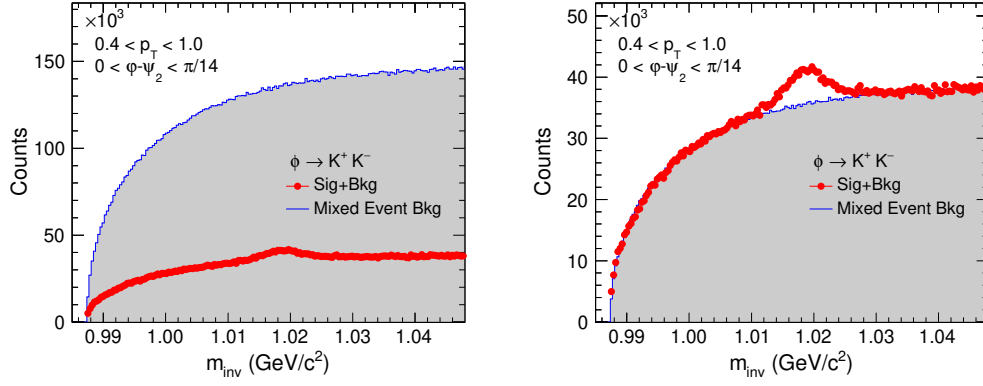
Figure 4.4: Illustration of mixed event background estimation for ϕ-meson in Au+Au collisions at $\sqrt{s_{NN}} = 14.5$ GeV for 0-80% centrality. Left panel shows the signal+background and the mixed event background. Right panel shows the same after background normalization.

4.5   Raw yield of ϕ-meson

Raw yield extraction for ϕ-meson (resonance) is done by Breit-Wigner function fit. An illustration of the raw yield extraction using function fit for ϕ-meson is shown in the Fig. 4.5. The ϕ-meson signal after subtraction of mixed event background is fitted with a Breit-Wigner plus a 2nd order polynomial function for residual background shown by the red line. The invariant mass range chosen for fitting is $0.995 < m_{inv} < 1.05$ (GeV/c^2). The ϕ-meson yield is calculated by integrating the Breit-Wigner function given in Eq. 4.8 below. This procedure is repeated for various p_T ranges and seven $\phi - \psi_2$ bins extend over $[0, \pi/2]$ in each p_T bin. ϕ-meson signal distributions for all p_T and $\phi - \psi_2$ bins are shown in the Appendix at the end of the chapter.

$$BW(m_{inv}) = \frac{1}{2\pi} \frac{A\Gamma}{(m_{inv} - m_0)^2 + (\Gamma/2)^2} + Bm_{inv}^2 + Cm_{inv} + D \qquad (4.8)$$
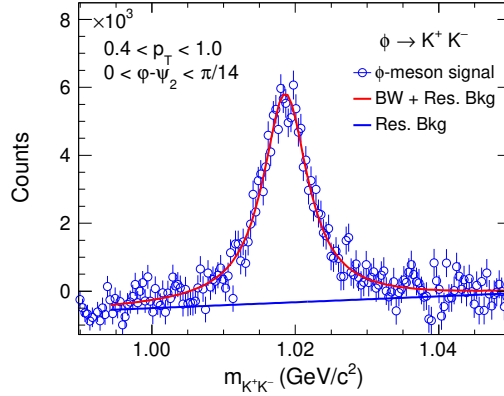
Figure 4.5: ϕ-meson invariant mass distribution for $0.8 < p_T < 1.0$ (GeV/c) for 0-80% centrality in Au+Au collisions at $\sqrt{s_{\mathrm{NN}}} = 14.5$ GeV. The distribution is fitted with a Breit-Wigner plus 2nd order polynomial function (Eq. 4.8) to extract raw-yield.

4.6 ϕ-meson v_2 extraction

The method for ϕ-meson v_2 extraction is discussed in the chapter 3. ϕ-meson v_2 measurement in Au+Au collisions at $\sqrt{s_{\mathrm{NN}}} = 14.5$ GeV is done using the $\phi - \psi$ binning method. The raw yield of ϕ-meson, extracted in the previous section is measured in the bins of angle $(\phi - \psi_2)$, where ϕ is the azimuthal angle of ϕ-meson in the lab-frame and ψ_2 is the 2nd-order event plane angle. The measured distribution $dN/d(\phi - \psi_2)$ is fitted with the functional form of Fourier function to extract v_2.

The raw yields extracted as discussed above for ϕ-meson at mid-rapidity for minimum-bias (0-80%) Au+Au collisions at $\sqrt{s_{\mathrm{NN}}} = 14.5$ GeV are shown in the Fig. 4.6. The obtained raw yields are fitted with the function,

$$\frac{dN}{d(\phi - \psi_2)} = A\left(1 + 2v_2^{obs} \cos n(\phi - \psi_2)\right), \tag{4.9}$$

where A and v_2^{obs} are the fit parameters. The measured v_2^{obs} values obtained from fit are divided by the appropriate event plane resolution to get final v_2 values. The p_T dependence of v_2 is studied by repeating the above procedure for fixed ranges in p_T

176

for various centrality classes in Au+Au collisions at $\sqrt{s_{\mathrm{NN}}} = 14.5$ GeV.
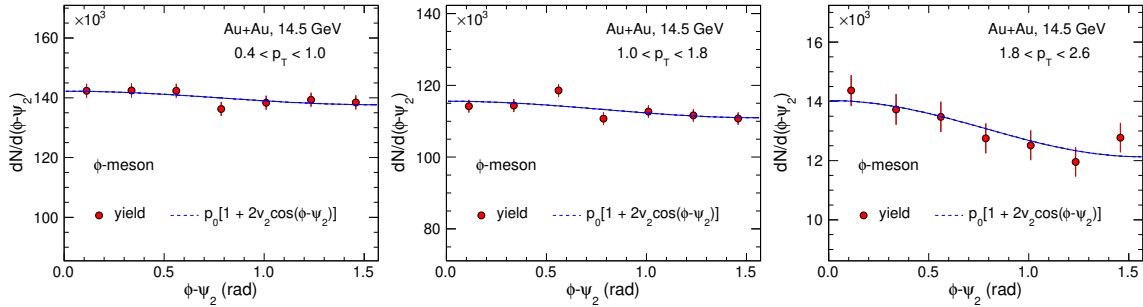
Figure 4.6: $\phi-\psi_2$ distributions for ϕ-meson at mid-rapidity for 0-80% centrality in Au+Au collisions at $\sqrt{s_{\mathrm{NN}}} = 14.5$ GeV. The blue dashed curves represent the fits to the raw-yield as mentioned in Eq. 4.9 to extract v_2.

4.7 Elliptic flow analysis methods

4.7.1 The event-plane method

The azimuthal angle distribution of produced particles with respect to reaction plane angle (ψ_R) can be decomposed in a Fourier series [24]:

$$\frac{dN}{d\phi} \propto 1 + 2\sum_{n=1}^{\infty} v_n \cos(\phi - \psi_R),$$

where ϕ is the azimuthal angle of the produced particles. The coefficients for various order (n) in this expansion are defined as $v_n = \langle \cos[n(\phi - \psi_R)] \rangle$. Here $\langle \ \rangle$ denotes average over all particles in all events. Elliptic flow (v_2) is quantified as the second order Fourier coefficient. Reaction plane is the plane containing the beam axis (z-axis) and the impact parameter vector (perpendicular distance between the center of two colliding nuclei). The angle between x-axis and the reaction plane is called reaction plane angle (ψ_R). As the impact parameter cannot be measured directly in an experiment, therefore the reaction plane angle is unknown. The reaction plane

angle is then estimated using azimuthal angle of produced particles. This estimated reaction plane angle is known as event plane angle, which is defined as [24],

$$\psi_n = \frac{1}{n} \tan^{-1}\left(\frac{Q_{ny}}{Q_{nx}}\right), \tag{4.10}$$

$$Q_n \cos(n\psi_n) = Q_{nx} = \sum_{i=1}^{N} w_i \cos(n\phi_i), \tag{4.11}$$

$$Q_n \sin(n\psi_n) = Q_{ny} = \sum_{i=1}^{N} w_i \sin(n\phi_i), \tag{4.12}$$

where Q_n are event flow vectors and w_i are the weight and N is the total number of particles in an event used for the flow vector calculation. The observed v_2 is calculated with respect to the second order event plane angle ψ_2 as,

$$v_2^{obs} = \langle \cos[2(\phi - \psi_2)]\rangle. \tag{4.13}$$

Tracks used for the v_2 calculation are excluded from the calculation of the flow vector to remove auto-correlation effects. The estimated reaction plane fluctuates owing to finite number of particles. Therefore, one has to correct for this smearing by dividing the observed v_2 by the event plane resolution,

$$v_2 = \frac{v_2^{obs}}{\langle \cos(2(\psi_2 - \psi_R))\rangle}. \tag{4.14}$$

The denominator in Eq. 4.14 could not be calculated directly. Thus, the event plane resolution is calculated by correlating azimuthal angles of the particles from two sub-events, namely A and B as,

$$\langle \cos[2(\psi_2 - \psi_R)]\rangle = C\sqrt{\langle \cos[2(\psi_2^A - \psi_2^B)]\rangle}. \tag{4.15}$$

Here C is a factor calculated from the known multiplicity dependence of the event plane resolution [24].

4.7.1.1 TPC event plane

Event plane calculated from the tracks reconstructed by the TPC detector is known as TPC event plane. Good quality primary tracks have been selected to calculate event plane angle for this analysis. The cuts applied for the track selection are listed in the Table 4.6.

Table 4.6: Track selection cuts for event plane angle.

Number of fit points in TPC	nHitsFit $\geq$ 15
nHitsFit/nHitsPoss	Ratio $\geq$ 0.52
DCA to primary vertex	$|$DCA$|$ < 2.0 cm
Transverse momentum	$0.2 < p_T < 2.0$ (GeV/c)
Pseudo-rapidity	$|\eta| < 1.0$

Collision of two nuclei in the labroatory frame is random, therefore, for an ideal detector acceptance the event plane angle should be isotropic in the laboratory frame. However, in experiments the detectors may have a finite or non-uniform acceptance which makes event plane angle distribution anisotropic in the lab frame. This anisotropy is not related to the true anisotropic flow arising due to pressure gradients developed in the colliding system. Therefore, it is necessary that event plane angle distribution should be uniform in the laboratory frame. Several methods have been introduced to correct the event plane angle distribution [24, 25].

In recenter correction method, the distribution of flow vectors (Q_x, Q_y) is subtracted by the averaged flow vectors over all events,

$$Q_x = Q_x - \langle Q_x \rangle, \qquad Q_y = Q_y - \langle Q_y \rangle. \tag{4.16}$$

The main limitation of this method is that it does not eliminate the higher harmonics from the distribution of ψ_2. To eliminate the higher harmonics the event plane has been further corrected by the shift method. In this method one has to fit the unweighted event plane distribution in the laboratory frame, summed over all events, to a Fourier expansion and devises an event-by-event shifting of the planes needed to make the final distribution isotropic. The equation of shift correction for n^{th}-order event plane angle is,

$$\Delta\psi_n = \frac{1}{n} \sum_i^{i_{max}} \frac{2}{i} [-\langle \sin(in\psi_n) \rangle \cos(in\psi_n) + \langle \cos(in\psi_n) \rangle \sin(in\psi_n)]. \tag{4.17}$$

The minimum value of $i_{max} = 4/n$ where n is the harmonic number of interest. The final corrected event plane angle is,

$$\psi_n' = \psi_n + \Delta\psi_n. \tag{4.18}$$

Figure 4.7 shows the 2nd order event plane angle (ψ_2) distributions for sub events -1.0 < η < -0.075 and 0.075 < η < 1.0 in the laboratory frame.
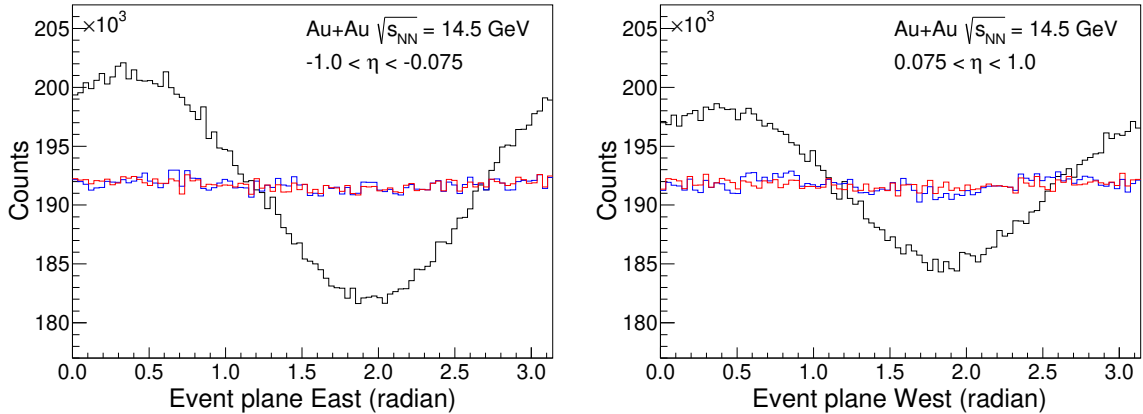
Figure 4.7: Event plane angle distributions for -1.0 < η < -0.075 (left panel) and 0.075 < η < 1.0 (right panel) without corrections (black lines), after recenter correction (blue lines) and after shift correction (red lines) for Au+Au collisions at $\sqrt{s_{NN}}$ = 14.5 GeV.

The 2nd order event plane angle (ψ_2) distributions corrected by re-centering and shift method is fitted by the function $f(x) = p_0[1 + p_1\cos(2x) + p_2\sin(2x)]$ to ensure the flattening as shown in Fig. 4.8. The small values of fit parameters p_1 and p_2 show that the event plane angle are corrected for the detector non-uniformity.
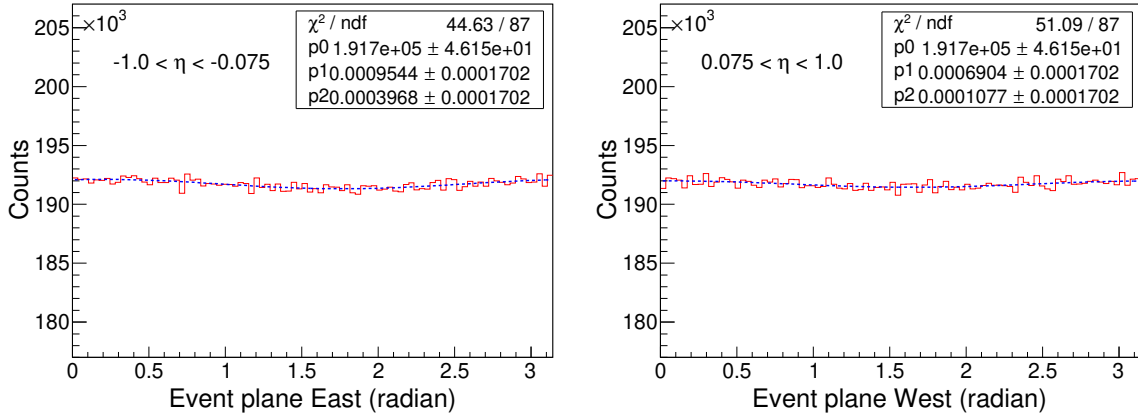
Figure 4.8: Event plane angle distributions for -1.0 < η < -0.075 (left panel) and 0.075 < η < 1.0 (right panel). Solid red lines correspond to the fit to the data by the function $f(x) = p_0[1 + p_1\cos(2x) + p_2\sin(2x)]$ for Au+Au collisions at $\sqrt{s_{NN}} = 14.5$ GeV.

4.7.1.2 BBC event plane

The event plane reconstructed using particle trajectories determined from the hits in the BBC detectors is known as BBC event plane [26]. The first-order event plane angle is calculated using Eqs. 4.10− 4.12. In case of BBC event plane, ϕ_i denotes the fixed azimuthal angle of the center of the ith BBC tile. w_i is the fraction of BBC-observed energy deposition recorded in tile i, which is given by,

$$w_i = \frac{A_i}{\sum_{i=1}^{i=16} A_i}. \tag{4.19}$$

The event plane obtained from one BBC detector is called a subevent. A combination of the subevent-plane from both BBC detectors provides the full event plane,

$$v_2\{BBC\} = \frac{\langle\cos[2(\phi - \psi_1)]\rangle}{C\sqrt{\langle\cos[2(\psi_1^A - \psi_1^B)]\rangle}}, \tag{4.20}$$

where C is the constant in Eq. 4.20. ψ_1^A, ψ_1^B are sub-event plane angles from each BBC detector and ψ_1 is the full event-plane angle from both sub-events combined. The detector acceptance bias is removed by applying the shift method. Equation 4.17 and 4.18 shows the expressions for the shift correction. In this analysis, the correction is done up to the 20th harmonic. The distributions of ψ_1^A and ψ_1^B are separately flattened and then the full-event plane distribution is flattened. Figure 4.9 shows the 1st order event plane angle (ψ_1) distributions for sub events A and B from BBC detector on east and west, respectively.
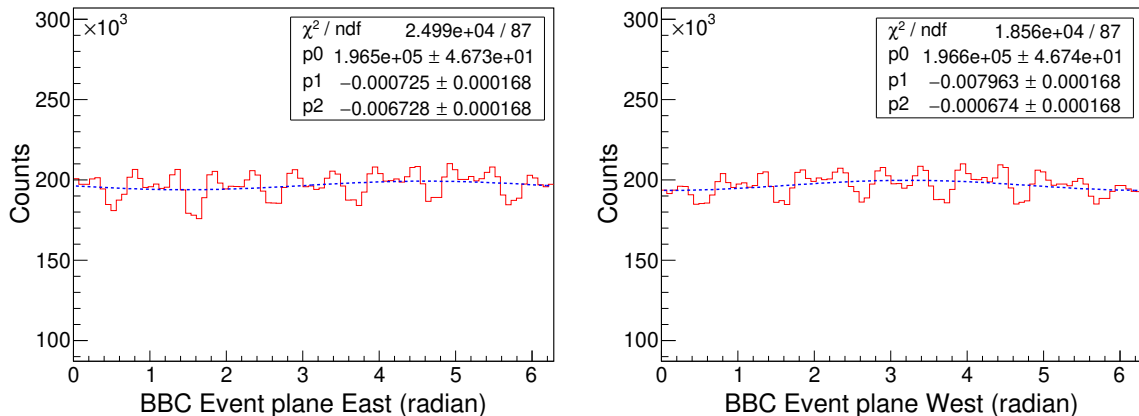
Figure 4.9: 1st order event plane angle (ψ_1) distributions for sub events A and B from BBC detector on east and west in Au+Au collisions $\sqrt{s_{NN}} = 14.5$ GeV. Dashed blue line corresponds to the fit to the data by the function $f(x) = p_0[1 + p_1\cos(x) + p_2\sin(x)]$.

4.7.2 η-sub event plane method

The η-sub event plane method [24] helps to remove the effect of self-correlation and non-flow effects (mainly due to short range correlations) by correlating particles separated in pseudo-rapidity. In this method, each single event is divided into two sub-events in two separate η-windows, namely η_- $(-1.0 < \eta < -0.075)$ and η_+

$(0.075 < \eta < 1.0)$. The flow coefficient v_2 is calculated for each particle based on their measurement in the opposite hemisphere of pseudo-rapidity:

$$v_2(\eta_\pm) = \frac{\langle \cos(2(\phi_\pm - \psi_{2\mp})) \rangle}{\sqrt{\langle \cos(\psi_{2\eta+} - \psi_{2\eta-}) \rangle}}. \tag{4.21}$$

Here $\psi_{2\eta+}$ and $\psi_{2\eta-}$ are the second-order event plane angle defined respectively for particles with positive and negative pseudo-rapidity. An η gap $(\Delta\eta)$ of ± 0.075 between positive and negative pseudo-rapidity sub-events has been introduced to suppress non-flow effects. In above equation, non-flow effects are reduced in both the observed flow (numerator) and the event plane resolution (denominator). Depending on the nature of the remaining non-flow effects, v_2 measured this way may have values that are either lower or higher than those obtained with the standard event plane method [27]. But this method is not sufficient to reduce non-flow effects due to presence of any long-range correlations.

4.7.3   The Q-cumulant method

The Q-cumulant method [28] is a method to calculate cumulants without using nested loops over tracks and without generating functions [29]. The advantage is that it provides fast (one loop over data) and exact (no approximations and no interference between different harmonics) estimates of the correlators. The cumulants are expressed in terms of the moments of the magnitude of the corresponding flow vector Q_n,

$$Q_n \equiv \sum_{i=1}^{M} e^{in\phi_i}. \tag{4.22}$$

The single-event average two and four-particle azimuthal correlations can be then

formulated as

$$\langle 2 \rangle = \frac{|Q_n|^2 - M}{M(M-1)}, \tag{4.23}$$

$$\langle 4 \rangle = \frac{|Q_n|^4 + |Q_{2n}|^2 - 2Re[Q_{2n}Q_n^*Q_n^*]}{M(M-1)(M-2)(M-3)} - 2\frac{2(M-2)|Q_n|^2 - M(M-3)}{M(M-1)(M-2)(M-3)}. \tag{4.24}$$

The average over all events can be performed as

$$\langle\langle 2 \rangle\rangle \equiv \langle\langle e^{in(\phi_1 - \phi_2)} \rangle\rangle \equiv \frac{\sum_{events}(W_{\langle 2 \rangle})_i \langle 2 \rangle_i}{\sum_{events}(W_{\langle 2 \rangle})_i} \tag{4.25}$$

$$\langle\langle 4 \rangle\rangle \equiv \langle\langle e^{in(\phi_1 + \phi_2 - \phi_3 - \phi_4)} \rangle\rangle \equiv \frac{\sum_{events}(W_{\langle 4 \rangle})_i \langle 4 \rangle_i}{\sum_{events}(W_{\langle 4 \rangle})_i} \tag{4.26}$$

where the weights are the number of two and four-particle combinations:

$$W_{\langle 2 \rangle} \equiv M(M-1) \tag{4.27}$$

$$W_{\langle 4 \rangle} \equiv M(M-1)(M-2)(M-3). \tag{4.28}$$

Choosing the multiplicity weights above can make the final multiparticle azimuthal correlations free of multiplicity fluctuations [30]. However, one can also use unit weights treating events with different multiplicity equally. The two and four-particle cumulants without detector bias then can be formulated as

$$c_n\{2\} = \langle\langle 2 \rangle\rangle \tag{4.29}$$

$$c_n\{4\} = \langle\langle 4 \rangle\rangle - 2 \times \langle\langle 2 \rangle\rangle^2. \tag{4.30}$$

The reference flow (e.g., p_T integrated v_n) can be estimated both from two and four-particle cumulants:

$$v_n\{2\} = \sqrt{c_n\{2\}}, \tag{4.31}$$

$$v_n\{4\} = \sqrt[4]{-c_n\{4\}}. \tag{4.32}$$

Once the reference flow is estimated, we proceed to the calculation of differential flow (e.g., as a function of p_T) of the particle of interest (POI), which needs another two vectors p and q. Particles used to estimate reference flow are called reference particles (REPs). For particles labeled as POI,

$$p_n \equiv \sum_{i=1}^{m_p} e^{in\psi_i} \tag{4.33}$$

For particles labeled as both POI and REP,

$$q_n \equiv \sum_{i=1}^{m_q} e^{in\psi_i} \tag{4.34}$$

Then the reduced single-event average two and four-particle correlations are

$$\langle 2' \rangle = \frac{p_n Q_n^* - m_q}{m_p M - m_q} \tag{4.35}$$

$$\langle 4' \rangle = [p_n Q_n Q_n^* Q_n^* - q_{2n} Q_n^* Q_n^* - p_n Q_n Q_{2n}^* - 2M p_n Q_n^*$$
$$-2m_q |Q_n|^2 + 7q_n Q_n^* - Q_n Q_n^* + q_{2n} Q_{2n}^* + 2p_n Q_n^*$$
$$+2m_q M - 6m_q] / \left[(m_q M - 3m_q)(M-1)(M-2)\right]. \tag{4.36}$$

The event average can be obtained as follows:

$$\langle\langle 2' \rangle\rangle = \frac{\sum_{events}(w_{\langle 2' \rangle})_i \langle 2' \rangle_i}{\sum_{events}(w_{\langle 2' \rangle})_i} \tag{4.37}$$

$$\langle\langle 4' \rangle\rangle = \frac{\sum_{events}(w_{\langle 4' \rangle})_i \langle 4' \rangle_i}{\sum_{events}(w_{\langle 4' \rangle})_i} \tag{4.38}$$

Multiplicity weights are

$$w_{\langle 2' \rangle} \equiv m_p M - m_q \tag{4.39}$$

$$w_{\langle 4' \rangle} \equiv (m_p M - 3m_q)(M - 1)(M - 2). \tag{4.40}$$

The two and four-particle differential cumulants without detector bias are given by

$$d_n\{2\} = \langle\langle 2' \rangle\rangle \tag{4.41}$$

$$d_n\{4\} = \langle\langle 4' \rangle\rangle - 2 \times \langle\langle 2' \rangle\rangle\langle\langle 2 \rangle\rangle. \tag{4.42}$$

Equations for the case of detectors without uniform acceptance can be found in Ref. [28]. Estimations of differential flow are expressed as

$$v_n'\{2\} = \frac{d_n\{2\}}{\sqrt{c_n\{2\}}} \tag{4.43}$$

$$v_n'\{4\} = \frac{d_n\{4\}}{\left(-c_n\{4\}\right)^{3/4}} \tag{4.44}$$
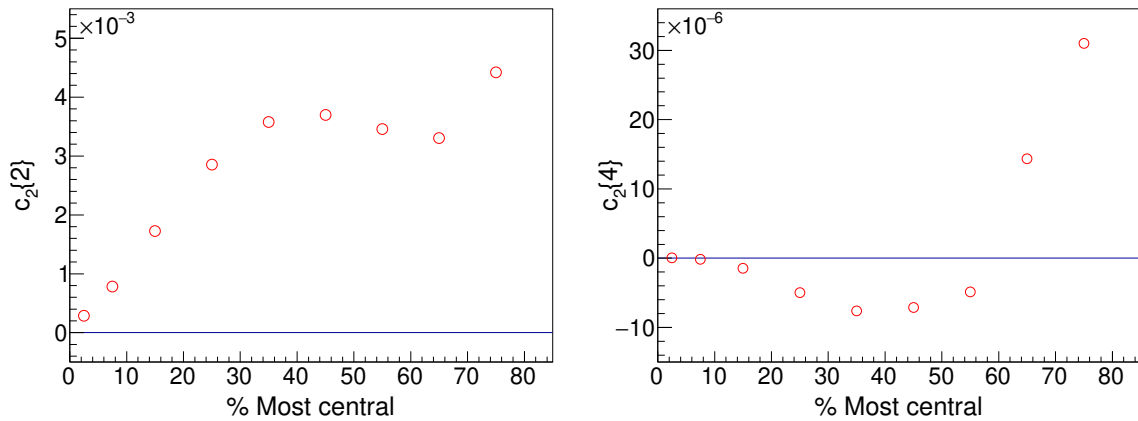
Figure 4.10: p_T integrated reference flow coefficients $c_2\{2\}$(left) and $c_2\{4\}$(right) from two and four-particle cumulants as a function of centrality in Au+Au collisions at $\sqrt{s_{\mathrm{NN}}} = 14.5$ GeV.

4.8   Systematic uncertainties

Systematic uncertainties on v_2 are estimated by varying event and track selection parameters e.g. collision vertex position, the DCA of the primary vertex for the tracks, and the number of fit points used for reconstruction of the tracks etc. Table 4.7 lists all the parameters that were varied for the systematic uncertainties together with the default value.

Table 4.7: Event/Track cut variations for the systematic uncertainties in Au+Au collisions at $\sqrt{s_{\mathrm{NN}}} = 14.5$ GeV.

Parameter	Default value	Variations	No. of variations
$|V_z|$	< 70 cm	< 60 cm, < 65 cm, < 75 cm, < 80 cm	4
$\Delta\eta$	0.075	0.05	1
nHitsFit	≥ 15	$\geq 18, \geq 20,$ $\geq 22, \geq 25$	4
nHitsFit/nHitsPoss	≥ 0.52	$\geq 0.48, \geq 0.50,$ $\geq 0.54, \geq 0.56$	4
$|$DCA$|$	< 3.0 cm	< 2.0 cm, < 2.5 cm	2

Systematic uncertainties are calculated using method suggested in the Ref. [31]. The statistical effect on systematic uncertainties are taken into account using this method. Systematic uncertainties are calculated as follows:

1. First, difference between the v_2 values obtained from the default cut (listed in Table 4.7) and the v_2 values from different variations are calculated, which is denoted as:

$$\Delta v_2 = (v_2)_{i^{th} sys} - (v_2)_{def} \qquad (4.45)$$

2. The quadratic difference between the statistical error on v_2 in default case and

the ith systematic case is calculated as:

$$\Delta\sigma_{stat} = \sqrt{|(\sigma_{stat})^2_{ith} - (\sigma_{stat})^2_{def}|} \tag{4.46}$$

3. After that condition $|\Delta v_2| > \Delta\sigma_{stat}$ is used. If the condition is satisfied then the uncertainty due to the ith systematic cut is included in the calculation, otherwise the uncertainty is taken as 0.

4. The systematic uncertainty due to i^{th} cut is then given by:

$$(\sigma_{sys})_i = \sqrt{|(\Delta v_2)^2 - (\Delta\sigma_{stat})^2|} \tag{4.47}$$

5. The systematic uncertainty due to different type of cuts e.g. track cuts, event cuts and η-gap for event plane are calculated separately as $\sqrt{(\frac{1}{N})\sum_i(\sigma_{sys})^2_i}$, where i $= 1$ to N, N be the number of variation of each type of cuts. Finally, the systematic uncertainty due to each type of cuts is added in quadrature to get the total systematic uncertainties.

A maximum of 2% systematic uncertainty due to event cuts, 1% due to track cuts on v_2 is found for different centrality classes and for different p_T bins in Au+Au collisions at $\sqrt{s_{NN}} = 14.5$ GeV.

4.9 Results and Discussions

In this section, we discussed the systematic measurements of elliptic flow v_2 as a function of transverse momentum (p_T) from Au+Au collisions at $\sqrt{s_{\mathrm{NN}}} = 14.5$ GeV. The results are presented for ϕ-meson and inclusive charged hadrons at mid-rapidity.

4.9.1 Event plane resolution

Due to finite multiplicity of events, the event plane angle ψ_2 may not coincide with the true reaction plane angle ψ_R. Hence a resolution correction is needed to obtain the correct measurement of elliptic flow. For this analysis the event planes are determined from the TPC in the mid-rapidity region, and from the BBC at forward rapidity. Figure 4.11 shows the event-plane resolution from TPC (left panel) and BBC (right panel) as function of centrality in Au+Au collisions at $\sqrt{s_{\mathrm{NN}}} = 14.5$ GeV and compared with different beam energies in Au+Au collisions. The event plane resolution is calculated for nine different centrality (0-5%, 5-10%, 10-20%, 20-30%, 30-40 %, 40- 50%, 50-60%, 60-70% and 70-80%).

The event plane resolution depends on number of particles used for event plane reconstruction, therefore it should increase from peripheral to central collisions. On the other hand, it depends on the anisotropic flow of the event itself, so it should decreases with more central collisions where anisotropy is small. Because of the two competing effects, event-plane resolution first increases from peripheral to mid-central collisions and then decreases. The event-plane resolution from the TPC increases as the collision beam energy increases. The 14.5 GeV resolution values are closer to the 11.5 GeV resolution. This is because of the detector upgrades in the year 2014, additional material is used between the beam pipe and the time projection chamber (TPC), which causes a lower multiplicity giving a slightly lower resolution

than expected. The values of TPC and BBC event plane resolution for Au+Au collisions at $\sqrt{s_{\mathrm{NN}}} = 14.5$ GeV are shown in the Appendix at the end of the chapter.
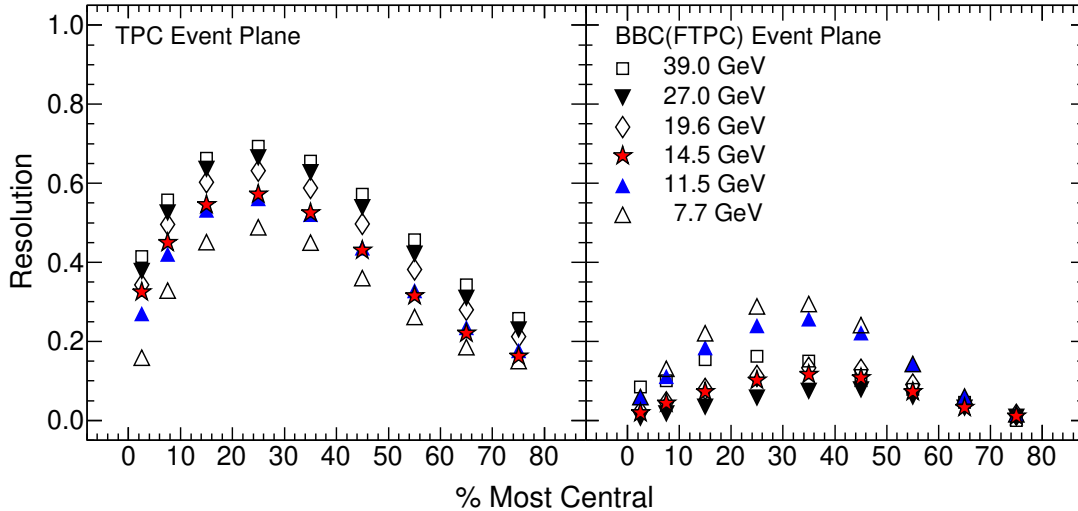
Figure 4.11: The event-plane resolution in Au+Au collisions at $\sqrt{s_{\mathrm{NN}}} = 14.5$ GeV (filled star) as a function of collision centrality compared with other beam energies from 7.7, 11.5, 19.6, 27 and 39 GeV [11]. Left panel shows the resolution of 2nd-harmonic event plane from the TPC ($|\eta| < 1.0$). Right panel shows the resolution for 39 GeV from the FTPCs ($2.5 < |\eta| < 4.0$) and the 2nd-harmonic event-plane resolution using the first-order event plane from the BBCs ($3.8 < |\eta| < 5.2$) [11].

4.9.2 Elliptic flow of identified hadrons

4.9.2.1 Differential $v_2(p_T)$

Figure 4.12 shows the result of v_2 as a function of p_T for identified hadrons at mid-rapidity in minimum bias Au+Au collisions at $\sqrt{s_{\mathrm{NN}}} = 14.5$ GeV. The results are presented for positively charged particles, negatively charged particles and neutral particles separately. $v_2(p_T)$ for positively charged particles (π^+, K^+, p) and negatively charged particles (π^-, K^-, $\bar{p}$) follows a mass ordering at low p_T (< 2 GeV/c), i.e. v_2 of lighter particles are more compared to the heavier particles [32]. The mass ordering of v_2 for charged hadrons at $\sqrt{s_{\mathrm{NN}}} = 14.5$ GeV is similar to what was observed earlier for top RHIC energy [10,27]. Neutral particles (ϕ-meson, Λ) deviate from this general

190

trend of mass ordering at the lower energies ($\sqrt{s_{\text{NN}}} < 19.6$ GeV). As observed from panel (c) of Fig. 4.12, v_2 values of ϕ-mesons are slightly smaller compared to $\bar{\Lambda}$. This indicates that the partonic interactions become gradually smaller at lower beam energies [9].
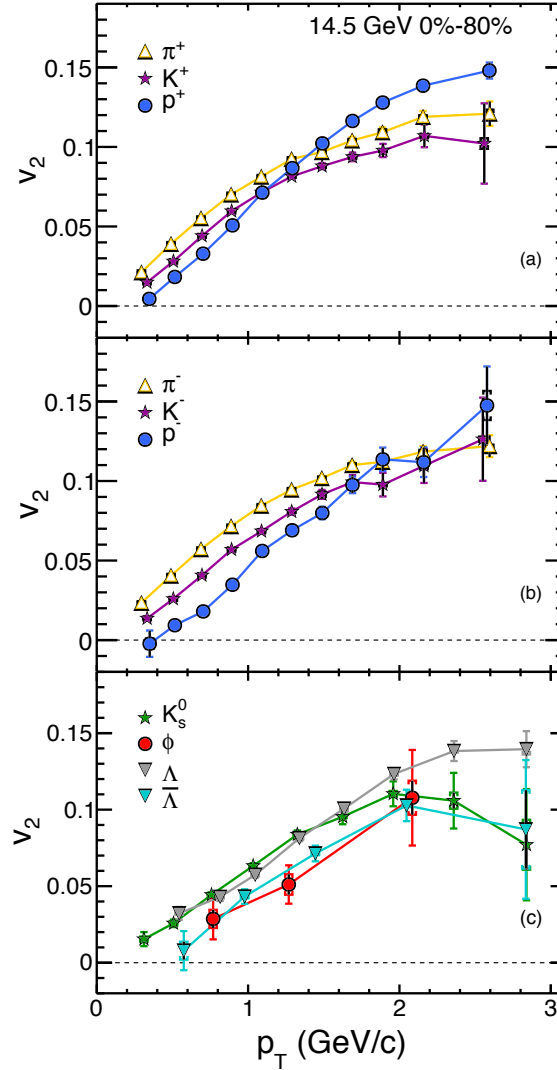
Figure 4.12: Elliptic flow v_2 as a function of p_T at mid-rapidity for minimum bias (0-80% centrality) Au+Au collisions at $\sqrt{s_{\text{NN}}} = 14.5$ GeV for identified particles [9]. (a) Positively charged particles. (b) Negatively charged particles. (c) Neutral particles. The statistical and systematic errors are shown by the vertical lines and short error bars with caps, respectively.

4.9.2.2   Energy dependence of ϕ-meson $v_2(p_T)$

ϕ-meson ($s\bar{s}$) has much smaller hadronic interaction cross section compared to other hadrons [34]. This would result in a smaller $v_2(p_T)$, if hadronic interactions dominate in the evolution of the medium. However, if the interactions are partonic dominated, then ϕ-meson v_2 will reflect the partonic collectivity. The measurements of ϕ-meson $v_2(p_T)$ at different beam energies can be used to understand the effect of partonic and hadronic interactions of the medium.

Figure 4.13 shows the measurements of ϕ-meson v_2 as a function of p_T at mid-rapidity ($|y| < 1.0$) in minimum bias Au+Au collisions at $\sqrt{s_{\mathrm{NN}}} = 7.7$ - 39 GeV. The results for Au+Au collisions at $\sqrt{s_{\mathrm{NN}}} = 14.5$ GeV are new, while the results from other beam energies are from the Ref. [9]. The values of v_2 at highest measured p_T bin for Au+Au collisions at 7.7 and 11.5 GeV are close to zero, which shows the dominance of hadronic interactions. Finite ϕ-meson v_2 at beam energies $\sqrt{s_{\mathrm{NN}}} \geq 14.5$ GeV indicates the formation of partonic phase of the medium in heavy-ion collisions.

4.9.3   Inclusive charged hadrons elliptic flow

4.9.3.1   Transverse momentum and pseudo-rapidity dependence of v_2

Figure 4.14 (left panel) shows inclusive charged hadron v_2 as a function of p_T for various collision centrality classes in Au+Au collisions at $\sqrt{s_{\mathrm{NN}}} = 14.5$ GeV. The results are obtained using η-sub event plane method at mid-rapidity ($|\eta| < 1.0$). The $v_2(p_T)$ shows monotonic increasing trend with increasing p_T for Au+Au collisions at $\sqrt{s_{\mathrm{NN}}} = 14.5$ GeV. The right panel of Fig. 4.14 presents the p_T-intigrated v_2 as a function of η for various centrality classes. The $v_2(\eta)$ has a weak dependence on η. Also, there is a clear centrality dependence observed for both $v_2(p_T)$ and $v_2(\eta)$. These dependence is similar to other beam energies for BES [11].
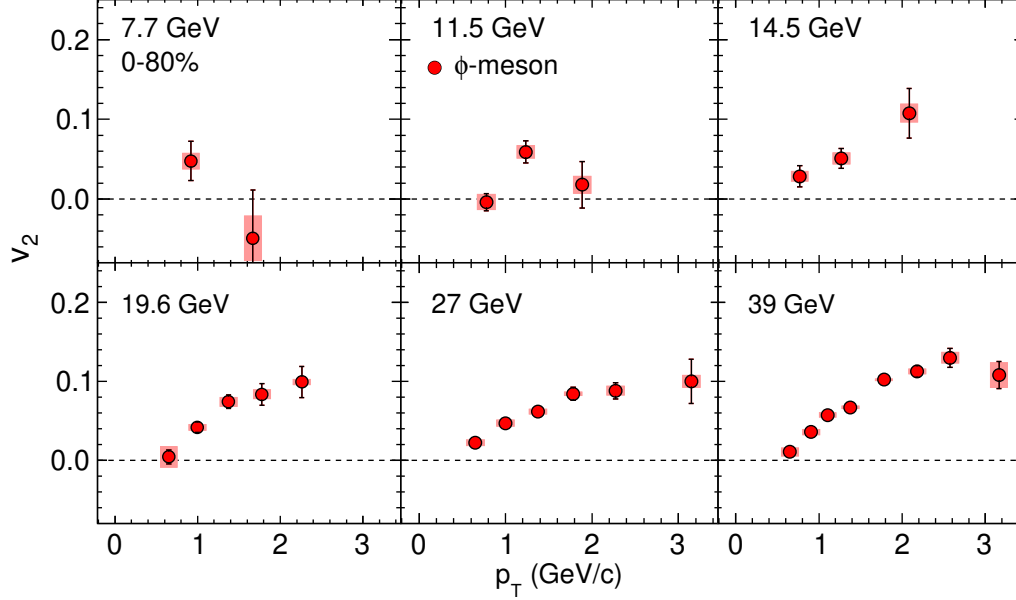
Figure 4.13: $v_2(p_T)$ for ϕ-meson at mid-rapidity ($|y| < 1.0$) in minimum bias (0-80% centrality) Au+Au collisions at $\sqrt{s_{NN}} = 7.7-39$ GeV. The systematic uncertainties are shown by the bands and the vertical lines are statistical uncertainties.
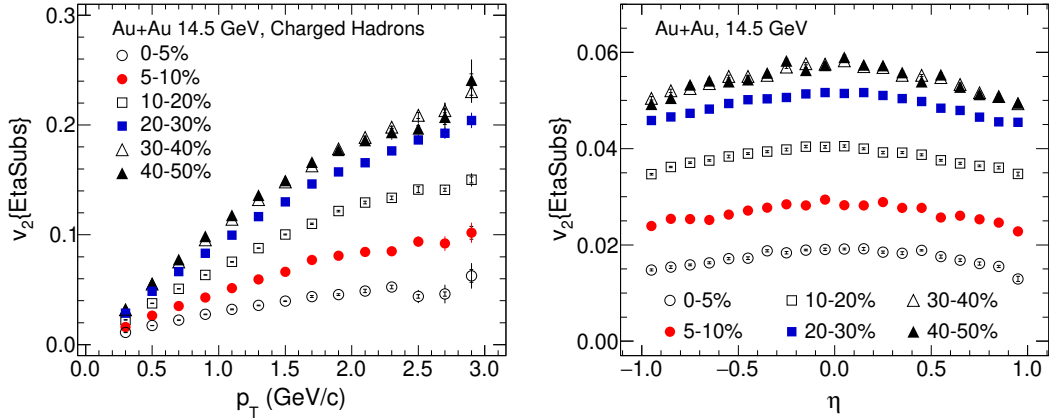
Figure 4.14: Inclusive charged hadrons v_2 as a function of p_T and η in Au+Au collisions at $\sqrt{s_{NN}} = 14.5$ GeV using η-sub event plane method. The results are shown for various centrality classes. Statistical uncertainties are shown by the vertical lines. Systematic uncertainties are within marker size shown by the perpendicular lines at edges. These results are STAR preliminary.

4.9.3.2 v_2 methods comparison: non-flow effects

Figure 4.15 shows inclusive charged hadrons $v_2(p_T)$ measured using various methods in Au+Au collisions at $\sqrt{s_{NN}} = 14.5$ GeV. The different methods have different sensi-

tivity to non-flow effects and fluctuations to v_2. For a clear observation, v_2 from other methods are divided by the v_2 from two-particle cumulant method, shown in the lower panels of the Fig. 4.15. The difference of $v_2\{2\}$ from $v_2\{EtaSubs\}$, $v_2\{BBC\}$ and $v_2\{4\}$ depends on the p_T range. A larger difference is observed in the low-p_T region ($p_T < 1$ GeV/c). The difference between $v_2\{BBC\}$ and $v_2\{4\}$ is relatively small and less dependent on p_T. It suggests that the non-flow contributions to $v_2\{BBC\}$ and $v_2\{4\}$ are less compared to the η-sub event plane using TPC and two-particle cumulant methods. It also shows that the use of first-order event plane from BBC detector (forward rapidity) to study the second harmonic reduces non-flow effects which are not correlated among different harmonics.
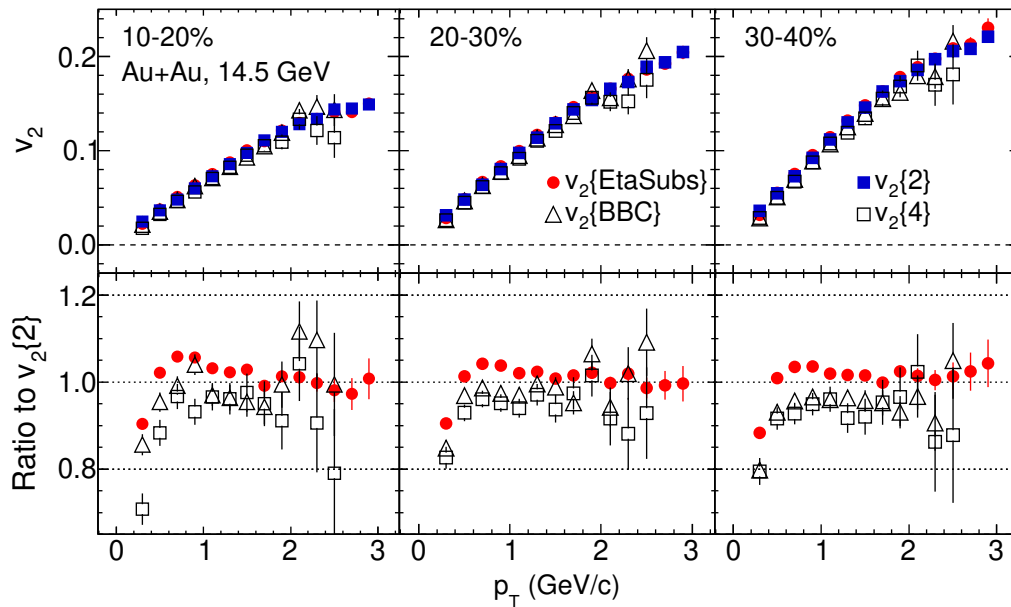
Figure 4.15: Inclusive charged hadron v_2 as a function of p_T for 10-20% (left), 20-30% (middle) and 30-40% (right) central at mid-rapidity in Au+Au collisions at $\sqrt{s_{NN}} = 14.5$ GeV. The results are shown for η-sub event plane (circle), BBC-EP (open triangle), 2-particle (filled square) and 4-particle cumulant (open square) methods. Only statistical uncertainties are shown by the vertical lines. The bottom panels show the ratio of v_2 measured using various methods with respect to the $v_2\{2\}$.

4.9.3.3 Centrality dependence of v_2

Co-ordinate space eccentricity is a measure of the collision centrality. Eccentricity of central collisions is smaller and peripheral collisions is larger. Elliptic flow v_2 depends on the centrality of collision. The larger magnitude of v_2 in peripheral collisions can be attributed to the larger initial eccentricity in peripheral collisions. The root-mean-square participant eccentricity $\varepsilon_{part}\{2\}$ of participant nucleons is calculated using Eq. 4.2 from a MC Glauber model [18].

Figure 4.16 shows the centrality dependence of v_2 over eccentricity ($\varepsilon_{part}\{2\}$) as a function of p_T in Au+Au collisions at $\sqrt{s_{NN}} = 14.5$ GeV for centrality classes 10-20%, 30-40% and 50-60%. Central collisions have higher values of $v_2/\varepsilon_{part}\{2\}$ than peripheral collisions, which suggests stronger collective interactions in collisions with a larger number of participants. The observed centrality dependence of $v_2/\varepsilon_{part}\{2\}$ is found similar as reported in previous measurements at STAR at beam energies $\sqrt{s_{NN}}$ = 7.7 - 62.4 GeV and 200 GeV [8, 10, 11].
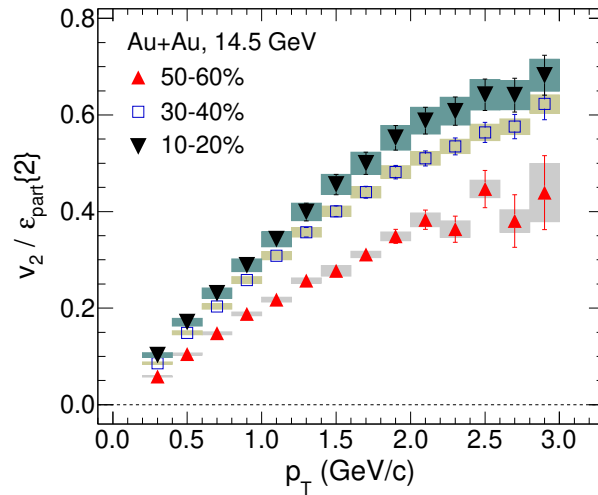
Figure 4.16: The v_2/ε_2 (Glauber) as a function of p_T at mid-rapidity for various collision centrality (10-20%, 30-40% and 50-60%) in Au+Au collisions at $\sqrt{s_{NN}} = 14.5$ GeV. The v_2 values are from η-sub event plane method. The vertical lines and shaded boxes represent the statistical and systematic uncertainties, respectively. These results are STAR preliminary.

4.9.3.4 Beam energy dependence of v_2

The significant v_2 at top RHIC energy [35] is one of the most important experimental observation at RHIC. It is more than 50% larger than at SPS energy [36]. This could be interpreted as the observation of higher degree of thermalization than at lower collision energies. The Beam Energy Scan data of Au+Au collisions from STAR experiment offers an opportunity to study the beam energy dependence of v_2 at midrapidity.
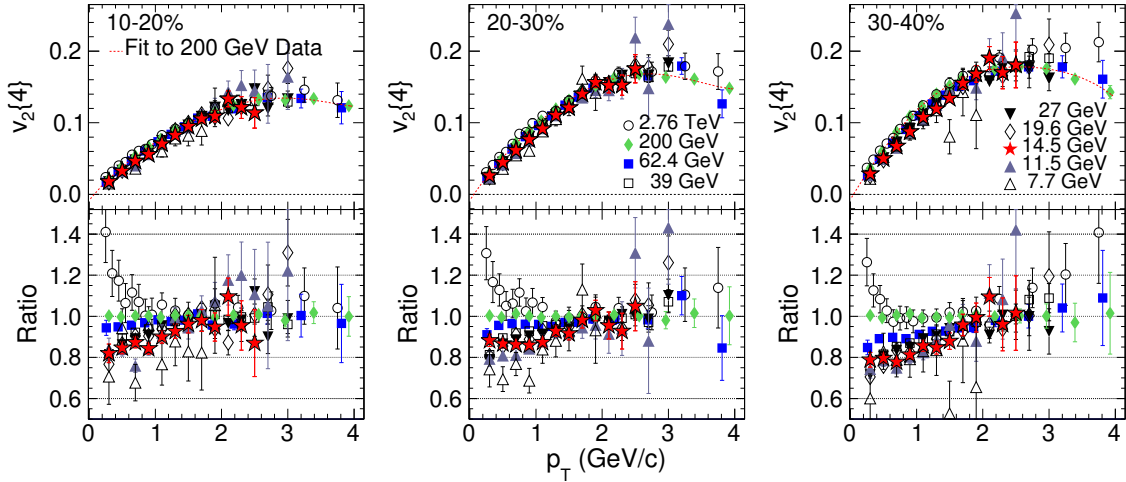
Figure 4.17: $v_2\{4\}$ versus p_T at three centralities: 10-20%, 20-30% and 30-40% for various collision energies ($\sqrt{s_{NN}}$ = 7.7 GeV to 2.76 TeV). The present results at 14.5 GeV and other energies from 7.7 to 200 GeV are for $|\eta| < 1.0$. The measurement of v_2 at 2.76 TeV was done at $|\eta| < 0.8$. Furthermore, all results for $\sqrt{s_{NN}}$ = 7.7 to 200 GeV are for Au+Au collisions and those for 2.76 TeV are for Pb+Pb collisions. The dashed red curves show 5th-order polynomial function fit to the results from Au+Au collisions at $\sqrt{s_{NN}}$ = 200 GeV. The lower panels show the ratio of $v_2\{4\}$ for all energies with respect to the fit curve. Error bars shown are statistical uncertainties only. These results are STAR preliminary.

Figure 4.17 shows the comparison of inclusive charged chadrons $v_2(p_T)$ at midrapidity for Au+Au collisions at $\sqrt{s_{NN}}$ = 14.5 GeV in 10-20%, 20-30%, and 30-40% centrality with other published results from STAR [8, 10, 11] and ALICE [12] collaboration. The v_2 results are from the 4-particle cumulant method $v_2\{4\}$. The reasons to select the results of $v_2\{4\}$ for comparison are the following: (1) to keep

the method for v_2 measurements consistent with the published results; (2) $v_2\{4\}$ is less sensitive to non-flow correlations. The 200-GeV data are empirically fit by a fifth-order polynomial function. For comparison, v_2 from other energies are divided by the fit function and shown in the lower panels of Fig. 4.17. We choose 200-GeV data as a reference because of the smallest statistical errors on v_2. The v_2 values increase with increasing collision energy for p_T below 2 GeV/c. Above $p_T \sim 2$ GeV/c the v_2 values are comparable within statistical errors. The increase of $v_2(p_T)$ as a function of energy can be attributed to the change of chemical composition from low to high energies [8] and/or larger collectivity at the higher collision energies. The baryon chemical potential varies a lot (20-400 MeV) from 200 to 7.7 GeV [8].
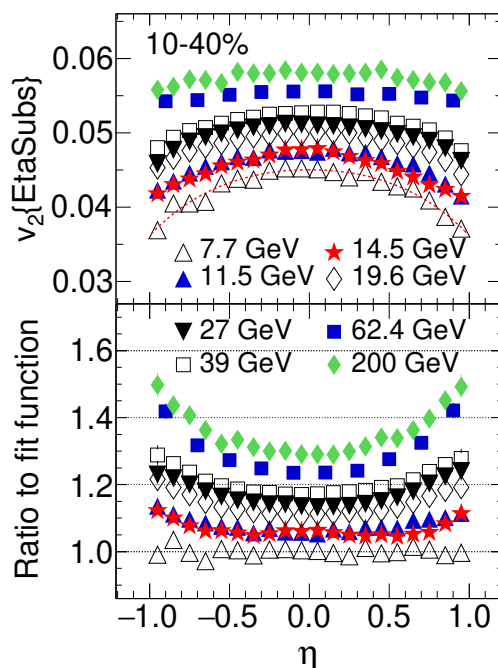
Figure 4.18: Inclusive charged hadron $v_2(\eta)$ for 10-40% centrality in Au+Au collisions at $\sqrt{s_{\mathrm{NN}}} = 14.5$ GeV. The v_2 results are from η-sub event plane method. The results are compared with various beam energies from 7.7 to 200 GeV. The dashed red curve shows the empirical fit to the result from Au+Au collisions at $\sqrt{s_{\mathrm{NN}}} = 7.7$ GeV. The bottom panel shows the ratio of $v_2(\eta)$ for all $\sqrt{s_{\mathrm{NN}}}$ with respect to the fit curve. Error bars shown are statistical uncertainties only.

Figure 4.18 shows v_2 as a function of pseudorapidity for mid-central (10-40%) Au+Au collisions at $\sqrt{s_{\mathrm{NN}}} = 14.5$ GeV compared with other published results from STAR. The data for $\sqrt{s_{\mathrm{NN}}} = 62.4$ and 200 GeV are from the Refs. [27, 37]. The 7.7 GeV data are empirically fit by the following function:

$$v_2\left(\eta\right) = p_0 + p_1\eta^2 + p_2\eta^4, \tag{4.48}$$

The fit parameters are $p_0 = 0.045\pm0.00020$, $p_1 = $ -0.0064$\pm$0.0014, $p_2 = $ -0.0025$\pm$0.0016. Bottom panel of Fig. 4.18 shows the ratio of $v_2(\eta)$ with respect to the fit function.

4.9.3.5 Model comparisons

Measurements from STAR experiment suggest that at energies 11.5 GeV and below, particle production may be dominated by the hadronic processes, whereas at energies 19.6 GeV and above, partonic degrees of freedom might be more important [10,38–40]. The $\sqrt{s_{\mathrm{NN}}} = 14.5$ GeV is in between the two regions. To investigate the partonic and hadronic contribution to v_2 from Au+Au collisions at $\sqrt{s_{\mathrm{NN}}} = 14.5$ GeV, transport model calculations from AMPT (version 2.25t7d) [14], and UrQMD (version 3.3p1) [13] has been done. The v_2 results from Au+Au collisions at $\sqrt{s_{\mathrm{NN}}} = 14.5$ GeV are compared with the corresponding results from models. The initial parameter settings for the models follow the recommendation in the cited papers. The UrQMD model only take the hadronic interactions into consideration, whereas the AMPT model with string-melting (SM) version incorporates both partonic and hadronic interactions, while the default version of AMPT only has hadronic interactions. We have generated $\sim 2\times10^6$ events of UrQMD and AMPT-SM with two possible partonic cross-sections (1.5mb and 10mb). The larger the parton cross section, the later the hadron cascade starts.

198

Figure 4.19 shows v_2 as function of p_T for centrality classes 10-20%, 20-30% and 30-40% from Au+Au collisions at $\sqrt{s_{\mathrm{NN}}} = 14.5$ GeV compared with UrQMD, AMPT 1.5mb and AMPT 10mb. The bottom panels show the ratio of experimental data to the each model calculation. UrQMD calculations is consistently lower for the p_T range studied, while the AMPT-SM with 10mb parton cross section is higher compared to the experimental data. The AMPT-SM with a lower parton cross-section of 1.5mb shows good agreement with the data. Figure 4.20 presents a similar comparison of v_2 as a function of pseudo-rapidity.
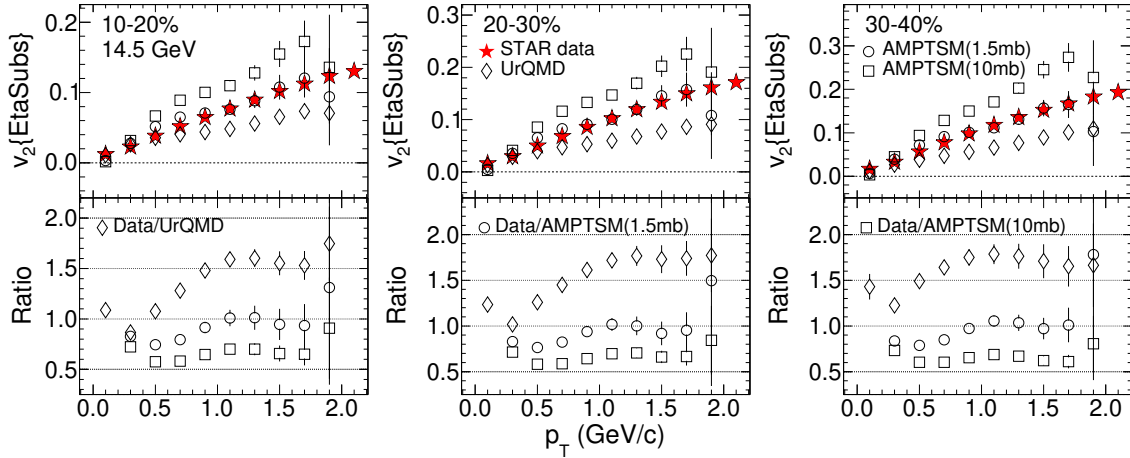
Figure 4.19: p_T dependence of $v_2\{EtaSubs\}$ from Au+Au collisions at $\sqrt{s_{\mathrm{NN}}} = 14.5$ GeV for 10-20%, 20-30% and 30-40% centralities, as measured in STAR data (solid markers). Calculations from UrQMD, AMPT 1.5mb, and AMPT 10mb are also plotted (open markers). (lower panels) Ratios of the experimental data to each model calculation. The vertical lines represent the statistical uncertainties.
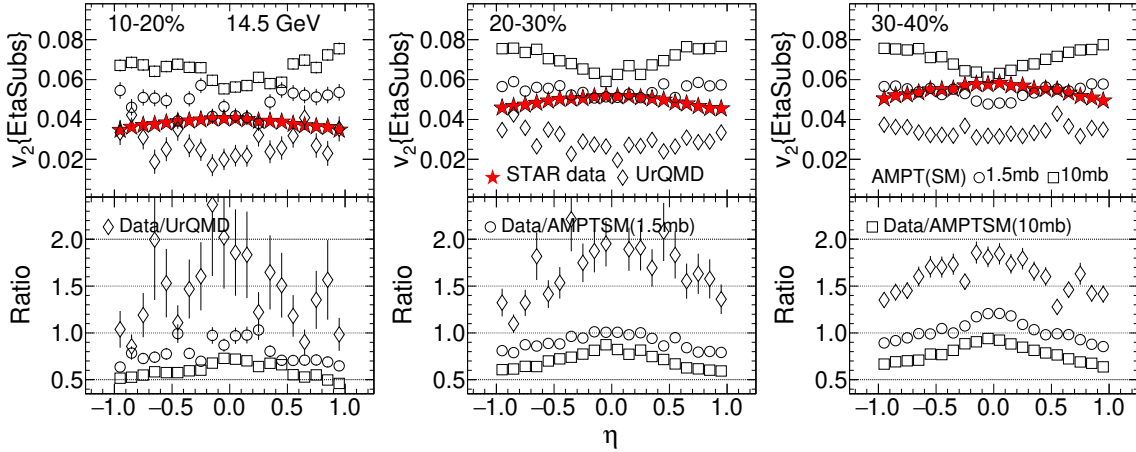
Figure 4.20: η dependence of $v_2\{EtaSubs\}$ from Au+Au collisions at $\sqrt{s_{NN}} = 14.5$ GeV for 10-20%, 20-30% and 30-40% centralities, as measured in STAR data (solid markers). Calculations from UrQMD, AMPT 1.5mb, and AMPT 10mb are also plotted (open markers). (lower panels) Ratios of the experimental data to each model calculation. The vertical lines represent the statistical uncertainties.

4.10   Summary

In this chapter, we have presented the measurements of transverse momentum (p_T), pseudo-rapidity (η) and centrality dependence of elliptic flow (v_2) for inclusive charged hadrons at mid-rapidity in Au+Au collisions at $\sqrt{s_{NN}} = 14.5$ GeV data collected by the STAR detector at RHIC in the year 2014. We have shown calculation of v_2 from various flow methods such as η-sub event plane, two-particle and four-particle cumulant method. The η-sub event plane is measured using TPC and BBC detectors. The results are compared with the other published results from STAR in Au+Au collisions for beam energies 7.7-200 GeV and from ALICE in Pb+Pb collisions at 2.76 TeV. A detail comparison of the results with UrQMD and AMPT models are done in Au+Au collisions at $\sqrt{s_{NN}} = 14.5$ GeV.

We found that v_2 increases monotonically with increasing p_T. A weak η dependence is observed for v_2. A clear centrality dependence for elliptic flow v_2 is observed in Au+Au collisions at $\sqrt{s_{NN}} = 14.5$ GeV. $v_2/\varepsilon_{part}\{2\}$ is found higher for central

200

collisions compared to peripheral collisions, which suggests stronger collective interactions in collisions with a larger number of participants. The v_2 values increase with increasing collision energy for p_T below 2 GeV/c. The increase of $v_2(p_T)$ as a function of energy also suggests larger collectivity at the higher collision energies. Inclusive charged hadrons v_2 values calculated from the UrQMD model are lower than the v_2 values in Au+Au collisions at $\sqrt{s_{\mathrm{NN}}} = 14.5$ GeV data. The AMPT model with parton-parton cross-section of 10mb over-predicts the data, whereas the AMPT string melting with 1.5mb cross-section is in good agreement with the data. This suggests the formation of partonic medium in Au+Au collisions at $\sqrt{s_{\mathrm{NN}}} = 14.5$ GeV.

We also presented transverse momentum dependence of ϕ-meson v_2 in minimum bias Au+Au collisions at $\sqrt{s_{\mathrm{NN}}} = 14.5$ GeV. The results are compared with the identified charged particles. ϕ-meson seems to deviate from usual mass ordering of v_2 in Au+Au collisions at $\sqrt{s_{\mathrm{NN}}} = 14.5$ GeV. We compared the v_2 results with other beam energies from STAR at $\sqrt{s_{\mathrm{NN}}} = 7.7$-39 GeV. We observed finite ϕ-meson v_2 at highest measured p_T, which indicates the formation of partonic phase of the medium at beam energy 14.5 GeV in Au+Au collisions.

Bibliography

[1] "Quark Gluon Plasma an Color Glass Condensate at RHIC? The perspective from the BRAHMS experiment", I. Arsene *et al.* (BRAHMS Collaboration), *Nucl. Phys. A*, **2005**, *757*, 1-27;

"The PHOBOS Perspective on Discoveries at RHIC", B. B. Back *et al.* (PHOBOS Collaboration), *Nucl. Phys. A*, **2005**, *757*, 28-101;

"Experimental and Theoretical Challenges in the Search for the Quark Gluon Plasma: The STAR Collaboration's Critical Assessment of the Evidence from RHIC Collisions", J. Adams *et al.* (STAR Collaboration), *Nucl. Phys. A*, **2005**, *757*, 102-183;

"Formation of dense partonic matter in relativistic nucleus-nucleus collisions at RHIC: Experimental evaluation by the PHENIX collaboration", K. Adcox *et al.* (PHENIX Collaboration), *Nucl. Phys. A*, **2005**, *757*, 184-283.

[2] "Identified particle production, azimuthal anisotropy, and interferometry measurements in Au+Au collisions at $\sqrt{s_{NN}} = 9.2$ GeV", B. I. Abelev *et al.* (STAR Collaboration), *Phys. Rev. C*, **2010**, *81*, 024911;

[3] "Experimental study of the QCD phase diagram & search for the critical point: selected arguments for the Run-10 Beam Energy Scan"

(https://drupal.star.bnl.gov/STAR/starnotes/public/sn0493);

"Studying the phase diagram of QCD matter at RHIC", BES-II whitepaper (STAR Collaboration),

(http://drupal.star.bnl.gov/STAR/starnotes/public/sn0598).

[4] "Chemical and thermal freeze-out parameters from 1A to 200A GeV", J. Cleymans and K. Redlich, *Phys. Rev. C*, **1999**, *60*, 054908;

"Energy and system size dependence of chemical freeze-out in relativistic nuclear collisions", F. Becattini, J. Manninen, and M. Gazdzicki, *Phys. Rev. C*, **2006**, *73*, 044905;

"Hadron production in central nucleus-nucleus collisions at chemical freeze-out", A. Andronic, P. Braun-Munzinger, and J. Stachel, *Nucl. Phys. A*, **2006**, *772*, 167-199.

[5] "Chiral restoration at finite density and temperature", M. Asakawa and K. Yazaki, *Nucl. Phys. A*, **1989**, *504*, 668-684;

"QCD Phase Diagram and the Critical Point", M. A. Stephanov, *Prog. Theor. Phys. Suppl.*, **2004**, *153*, 139-156;

"Canonical partition function and finite density phase transition in lattice QCD", S. Ejiri, *Phys. Rev. D*, **2008**, *78*, 074507.

[6] "Critical point of QCD at finite T and μ, lattice results for physical quark masses", Z. Fodor and S. Katz, *JHEP*, **2004**, *2004*, 050;

"QCD at finite chemical potential with six time slices", R. Gavai and S. Gupta, *Phys. Rev. D*, **2008**, *78*, 114503.

[7] "QCD Phase Diagram: Phase Transition, Critical Point and Fluctuations", B. Mohanty, *Nucl. Phys. A*, **2009**, *830*, 899c-907c;

"An Experimental Exploration of the QCD Phase Diagram: The Search for the Critical Point and the Onset of De-confinement", M. Aggarwal *et al.* (STAR Collaboration), *arXiv:*1007.2613, **2010**.

[8] "Bulk properties of the medium produced in relativistic heavy-ion collisions from the beam energy scan program", L. Adamczyk *et al.* (STAR Collaboration), *Phys. Rev. C*, **2017**, *96*, 044904.

[9] "Centrality dependence of identified particle elliptic flow in relativistic heavy ion collisions at $\sqrt{s_{\mathrm{NN}}}$ = 7.7-62.4 GeV", L. Adamczyk *et al.* (STAR Collaboration), *Phys. Rev. C*, **2016**, *93*, 014907.

[10] "Measurements of ϕ meson production in relativistic heavy-ion collisions at the BNL Relativistic Heavy Ion Collider (RHIC)",B. I. Abelev *et al.* (STAR Collaboration), *Phys. Rev. C*, **2009**, *79*, 064903;

"Centrality and Transverse Momentum Dependence of Elliptic Flow of Multistrange Hadrons and ϕ Meson in Au+Au Collisions at $\sqrt{s_{\mathrm{NN}}}$ = 200 GeV", L. Adamczyk *et al.* (STAR Collaboration), *Phys. Rev. Lett.*, **2016**, *116*, 62301.

[11] "Inclusive charged hadron elliptic flow in Au+Au collisions at $\sqrt{s_{\mathrm{NN}}}$ = 7.7-39 GeV", L. Adamczyk *et al.* (STAR Collaboration), *Phys. Rev. C*, **2012**, *86*, 054908.

[12] "Elliptic Flow of Charged Particles in Pb-Pb Collisions at $\sqrt{s_{\mathrm{NN}}}$ = 2.76 TeV", K. Aamodt *et al.* (ALICE Collaboration), *Phys. Rev. Lett.*, **2010**, *105*, 252302.

[13] "Microscopic Models for Ultrarelativistic Heavy Ion Collisions", S. A. Bass *et al.*, *Prog. Part. Nucl. Phys.*, **1998**, *41*, 255-369;

"Relativistic hadron-hadron collisions in the ultra-relativistic quantum molecular dynamics model", M. Bleicher *et al.*, *J. Phys. G*, **1999**, *25*, 1859.

[14] "Multiphase transport model for relativistic heavy ion collisions", Z. W. Lin *et al. Phys. Rev. C*, **2005**, *72*, 064901.

[15] "The STAR trigger", F. Bieser *et al.*, *Nucl. Inst. Meth. A*, **2003**, *499*, 766-777.

[16] "The STAR Time Projection Chamber: A Unique Tool for Studying High Multiplicity Events at RHIC", M. Anderson *et al.*, *Nucl. Inst. Meth. A*, **2003**, *499*, 659-678.

[17] "The large-area time-of-flight upgrade for STAR", W. Llope, *Nucl. Inst. Meth. B*, **2005**, *241*, 306-310.

[18] "Hadron production in nuclear collisions at RHIC and high density QCD", D. Kharzeev and M. Nardi, *Phys. Lett. B*, **2001**, *507*, 121-128;

"Glauber Modeling in High Energy Nuclear Collisions", M. L. Miller *et al.*, *Annu. Rev. Nucl. Part. Sci.*, **2007** ,*57*, 205-243.

[19] http://www.star.bnl.gov/protected/common/common2010/centrality/index.html.

[20] "A method to improve tracking and particle identi

cation in TPCs and silicon detectors", H. Bichsel, *Nucl. Inst. Meth. A*, **2006**, *562*, 154-197.

[21] "The STAR Time Projection Chamber: A Unique Tool for Studying High Multiplicity Events at RHIC", M. Anderson *et al.*, *Nucl. Inst. Meth. A*, **2003**, *499*, 659-678.

[22] "ϕ meson production in Au+Au and p+p collisions at $\sqrt{s_{\mathrm{NN}}} = 200$ GeV", J. Adams *et al.* (STAR Collaboration), *Phys. Lett. B*, **2005**, *612*, 181-189.

[23] "Review of Particle Physics", M. Tanabashi *et al.* (Particle Data Group), *Phys. Rev. D*, **2018**, *98*, 030001.

[24] "Flow Study in Relativistic Nuclear Collisions by Fourier Expansion of Azimuthal Particle Distributions", S. A. Voloshin, Y. Zhang, *Z. Phys. C*, **1996**, *70*, 665-672.

"Methods for analyzing anisotropic flow in relativistic nuclear collisions", A. M. Poskanzer and S. A. Voloshin, *Phys. Rev. C*, **1998**, *58*, 1671.

[25] "Collective motion in nucleus-nucleus collisions at 800 MeV/nucleon", P. Danielewicz *et al.*, *Phys. Rev. C*, **1998**, *38*, 120;

"Energy and charged particle flow in 10.8 GeV/c Au+Au collisions", J. Barrette *et al.*, *Phys. Rev. Lett.*, **1997**, *55*, 1420;

"Proton and pion production relative to the reaction plane in Au + Au collisions at 11A GeV/c", J. Barrette *et al.*, *Phys. Rev. C*, **1997**, *56*, 3254.

[26] "Directed and elliptic flow of charged particles in Cu+Cu collisions at $\sqrt{s_{\text{NN}}} = 22.4$ GeV", G. Agakishiev *et al.* (STAR Collaboration), *Phys. Rev. C*, **2012**, *85*, 014901.

[27] "Centrality dependence of charged hadron and strange hadron elliptic flow from $\sqrt{s_{\text{NN}}} = 200$ GeV Au+Au collisions", B. I. Abelev *et al.* (STAR Collaboration), *Phys. Rev. C*, **2008**, *77*, 054901.

[28] "Flow analysis with cumulants: Direct calculations", A. Bilandzic, R. Snellings, and S. Voloshin, *Phys. Rev. C*, **2011**, *83*, 044913.

[29] "Flow analysis from multiparticle azimuthal correlations", N. Borghini, P. M. Dinh, and J. Y. Ollitrault, *Phys. Rev. C*, **2001**, *64*, 054901.

[30] "Anisotropic Flow Measurements in ALICE at the Large Hadron Collider", A. Bilandzic, *Ph.D. thesis, Nikhef and Utrecht University*, **2012**.

[31] "Systematic Errors: facts and fictions", R. Barlow, *arXiv:*hep-ex/0207026, **2002**.

[32] "Radial and elliptic flow at RHIC: further predictions", P. Huovinen *et al.*, *Phys. Lett. B*, **2001**, *503*, 58-64.

[33] "Elliptic flow of identified hadrons in Au+Au collisions at $\sqrt{s_{\mathrm{NN}}} = 7.7\text{-}62.4$ GeV", L. Adamczyk *et al.* (STAR Collaboration), *Phys. Rev. C*, **2013**, *88*, 014902.

[34] "ϕ-Meson Production as a Probe of the Quark-Gluon Plasma", A. Shor, *Phys. Rev. Lett.*, **1985**, *54*, 1122;

"Evidence of Early Multistrange Hadron Freeze-Out in High Energy Nuclear Collisions", H. van Hecke, H. Sorge and N. Xu, *Phys. Rev. Lett.*, **1998**, *81*, 5764;

"ϕ-meson photoproduction from nuclei", A. Sibirtsev *et al.*, *Eur. Phys. J. A*, **2006**, *29*, 209.

[35] "Elliptic Flow in Au+Au Collisions at $\sqrt{s_{\mathrm{NN}}} = 130$ GeV", K. H. Ackermann *et al.* (STAR Collaboration), *Phys. Rev. Lett.*, **2001**, *86*, 402;

"Azimuthal anisotropy in Au+Au collisions at $\sqrt{s_{\mathrm{NN}}} = 200$ GeV", J. Adams *et al.* (STAR Collaboration), *Phys. Rev. C*, **2005**, *72*, 014904;

"Directed flow in Au+Au collisions at $\sqrt{s_{\mathrm{NN}}} = 62.4$ GeV", J. Adams *et al.* (STAR Collaboration), *Phys. Rev. C*, **2006**, *73*, 034903;

"System-Size Independence of Directed Flow Measured at the BNL Relativistic Heavy-Ion Collider", B. I. Abelev *et al.* (STAR Collaboration), *Phys. Rev. Lett.*, **2008**, *101*, 252301.

[36] "Centrality dependence of directed and elliptic flow at the SPS", A. M. Poskanzer and S. A. Voloshin, *Nucl. Phys. A*, **1999**, *661*, 341-344.

[37] "Mass, quark-number, and $\sqrt{s_{\mathrm{NN}}}$ dependence of the second and fourth flow harmonics in ultrarelativistic nucleus-nucleus collisions", B. I. Abelev *et al.* (STAR Collaboration), *Phys. Rev. C*, **2007**, *75*, 054906.

[38] "Observation of an Energy-Dependent Difference in Elliptic Flow between Particles and Antiparticles in Relativistic Heavy Ion Collisions", L. Adamczyk *et al.* (STAR Collaboration), *Phys. Rev. Lett.*, **2013**, *110*, 142301;

"Elliptic flow of identified hadrons in Au+Au collisions at $\sqrt{s_{\mathrm{NN}}} = 7.7$-$62.4\,\mathrm{GeV}$", L. Adamczyk *et al.* (STAR Collaboration), *Phys. Rev. C*, **2013**, *88*, 014902.

[39] "Probing parton dynamics of QCD matter with Ω and ϕ production", L. Adamczyk *et al.* (STAR Collaboration), Phys. Rev. C **93**, 021903(R) (2016).

[40] "Using ϕ-meson elliptic flow to map the strength of the partonic interaction", Md. Nasim, *Phys. Rev. C*, **2014**, *89*, 034909.

4.11 Appendix

4.11.1 Centrality selection from reference multiplicity

Table 4.8: Centrality selection criteria, RefMult and number of events for Au+Au collisions at $\sqrt{s_{\mathrm{NN}}} = 14.5$ GeV.

Centrality (%)	RefMult	No. of events
0-5	> 239	1.09 M
5-10	> 200	1.06 M
10-20	> 138	2.27 M
20-30	> 93	2.31 M
30-40	> 59	2.41 M
40-50	> 36	2.29 M
50-60	> 20	2.33 M
60-70	> 11	1.95 M
70-80	> 5	1.74 M

4.11.2 Average quantities from MC Glauber simulations

Table 4.9: Summary of N_{part}, N_{coll}, ε_{RP}, ε_{part}, $\varepsilon_{part}\{2\}$ and S_{part} information for Au+Au collisions at $\sqrt{s_{\mathrm{NN}}} = 14.5$ GeV. The $\pm$ are the errors on the quantities.

Centrality (%)	$\langle N_{part} \rangle$	$\langle N_{coll} \rangle$	$\langle \varepsilon_{RP} \rangle$	$\langle \varepsilon_{part} \rangle$	$\varepsilon_{part}\{2\}$	$\langle S_{part} \rangle$ (fm^2)
0-5	338±2	788±30	0.044±0.01	0.103±0.01	0.117±0.01	25.5±0.6
5-10	289±6	634±20	0.11±0.01	0.15±0.01	0.16±0.01	22.9±0.7
10-20	226±8	454±24	0.18±0.01	0.22±0.01	0.24±0.01	19.3±0.8
20-30	159±10	283±24	0.27±0.01	0.30±0.01	0.32±0.01	15.5±0.9
30-40	108±10	168±22	0.32±0.01	0.37±0.01	0.40±0.01	12.4±1.0
40-50	70±8	94±18	0.37±0.01	0.44±0.01	0.47±0.01	9.8±1.1
50-60	44±8	50±12	0.38±0.01	0.51±0.01	0.54±0.01	7.6±1.1
60-70	26±7	25±9	0.40±0.01	0.59±0.01	0.62±0.01	5.6±1.2
70-80	14±5	12±5	0.37±0.01	0.68±0.01	0.72±0.01	3.5±1.2

4.11.3   TPC and BBC event plane resolution

Table 4.10: TPC and BBC event plane resolution for η-sub event method in Au+Au collisions at $\sqrt{s_{\mathrm{NN}}} = 14.5$ GeV.

Centrality	Resolution ($< R >$)	
	TPC	**BBC**
0-5%	0.325 ± 0.002	0.0197 ± 0.0007
5-10%	0.449 ± 0.001	0.0434 ± 0.0006
10-20%	0.5460 ± 0.0007	0.0730 ± 0.0006
20-30%	0.5720 ± 0.0006	0.1020 ± 0.0006
30-40%	0.5260 ± 0.0007	0.1159 ± 0.0006
40-50%	0.4310 ± 0.0009	0.1072 ± 0.0006
50-60%	0.315 ± 0.001	0.0724 ± 0.0006
60-70%	0.221 ± 0.002	0.0324 ± 0.0009
70-80%	0.162 ± 0.003	0.0101 ± 0.0009

4.11.4   Inclusive charged hadron v_2 data points

Table 4.11: $v_2(p_T)$: centrality 0-5%

p_T (GeV/c)	$v_2\{EtaSubs\}$ ($\pm$**Stat.**$\pm$**Syst. Err.**)	$v_2\{BBC\}$ ($\pm$**Stat.**$\pm$**Syst. Err.**)	$v_2\{2\}$ ($\pm$**Stat. Err.**)
0.3	$0.0111\pm0.0002\pm0.0001$	$0.013\pm0.004\pm0.002$	0.0130 ± 0.0002
0.5	$0.0174\pm0.0003\pm0.0001$	$0.009\pm0.006\pm0.002$	0.0140 ± 0.0003
0.7	$0.0224\pm0.0004\pm0.0002$	$0.017\pm0.007\pm0.006$	0.0166 ± 0.0003
0.9	$0.0276\pm0.0005\pm0.0003$	$0.02\pm0.01\pm0.007$	0.0215 ± 0.0004
1.1	$0.0321\pm0.0007\pm0.0004$	$0.01\pm0.01\pm0.006$	0.0260 ± 0.0005
1.3	$0.0357\pm0.0009\pm0.0003$	$0.04\pm0.02\pm0.007$	0.0331 ± 0.0007
1.5	$0.040\pm0.001\pm0.0003$	$0.06\pm0.02\pm0.02$	0.0373 ± 0.0009
1.7	$0.044\pm0.002\pm0.0009$	$0.02\pm0.03\pm0.01$	0.042 ± 0.001
1.9	$0.046\pm0.002\pm0.0008$	$0.04\pm0.04\pm0.02$	0.043 ± 0.002
2.1	$0.049\pm0.003\pm0.002$	$0.03\pm0.06\pm0.04$	0.048 ± 0.002
2.3	$0.052\pm0.004\pm0.002$	$0.03\pm0.08\pm0.03$	0.056 ± 0.003
2.5	$0.044\pm0.006\pm0.002$		0.053 ± 0.004
2.7	$0.046\pm0.008\pm0.002$		0.057 ± 0.006
2.9	$0.06\pm0.01\pm0.006$		0.064 ± 0.007

Table 4.12: $v_2(p_T)$: centrality 5-10%

p_T (GeV/c)	$v_2\{EtaSubs\}$ ($\pm$**Stat.**$\pm$**Syst. Err.**)	$v_2\{BBC\}$ ($\pm$**Stat.**$\pm$**Syst. Err.**)	$v_2\{2\}$ ($\pm$**Stat. Err.**)	$v_2\{4\}$ ($\pm$**Stat. Err.**)
0.3	0.0160±0.0002±0.0002	0.014±0.002±0.0008	0.0178±0.0002	0.001±0.003
0.5	0.0264±0.0002±0.0002	0.029±0.002±0.001	0.0245±0.0002	0.020±0.004
0.7	0.0352±0.0003±0.0003	0.039±0.003±0.001	0.0311±0.0002	0.027±0.005
0.9	0.0430±0.0004±0.0003	0.040±0.004±0.002	0.0392±0.0003	0.049±0.006
1.1	0.0514±0.0005±0.0002	0.047±0.005±0.002	0.0483±0.0004	0.052±0.008
1.3	0.0593±0.0007±0.0003	0.072±0.007±0.003	0.0580±0.0005	0.06±0.01
1.5	0.0664±0.0009±0.0005	0.067±0.009±0.004	0.0687±0.0007	0.08±0.01
1.7	0.077±0.001±0.001	0.08±0.01±0.006	0.074±0.001	0.11±0.02
1.9	0.081±0.002±0.0008	0.09±0.02±0.007	0.083±0.001	0.08±0.03
2.1	0.084±0.002±0.001	0.13±0.02±0.007	0.086±0.002	0.06±0.04
2.3	0.085±0.003±0.002	0.09±0.03±0.01	0.094±0.002	0.10±0.05
2.5	0.094±0.005±0.003	0.07±0.05±0.02	0.100±0.004	-0.06±0.07
2.7	0.092±0.007±0.002		0.094±0.005	
2.9	0.102±0.009±0.006		0.098±0.006	

Table 4.13: $v_2(p_T)$: centrality 10-20%

p_T (GeV/c)	$v_2\{EtaSubs\}$ ($\pm$**Stat.**$\pm$**Syst. Err.**)	$v_2\{BBC\}$ ($\pm$**Stat.**$\pm$**Syst. Err.**)	$v_2\{2\}$ ($\pm$**Stat. Err.**)	$v_2\{4\}$ ($\pm$**Stat. Err.**)
0.3	0.0226±0.0001±0.0002	0.0214±0.0006±0.0005	0.0250±0.0001	0.0177±0.0009
0.5	0.0376±0.0001±0.0002	0.0351±0.0008±0.0009	0.0368±0.0001	0.032±0.001
0.7	0.0508±0.0002±0.0002	0.048±0.001±0.0005	0.0480±0.0002	0.046±0.001
0.9	0.0635±0.0002±0.0002	0.062±0.001±0.0006	0.0601±0.0002	0.056±0.002
1.1	0.0754±0.0003±0.0003	0.071±0.002±0.0008	0.0731±0.0003	0.071±0.002
1.3	0.0878±0.0004±0.0002	0.083±0.002±0.004	0.0859±0.0003	0.083±0.003
1.5	0.1003±0.0006±0.0005	0.093±0.003±0.001	0.0975±0.0005	0.095±0.004
1.7	0.1100±0.0008±0.0006	0.105±0.004±0.002	0.1110±0.0006	0.106±0.006
1.9	0.122±0.001±0.0007	0.119±0.006±0.003	0.1200±0.0009	0.109±0.008
2.1	0.129±0.002±0.001	0.143±0.009±0.002	0.128±0.001	0.13±0.01
2.3	0.134±0.002±0.002	0.15±0.01±0.004	0.134±0.002	0.12±0.02
2.5	0.141±0.003±0.003	0.14±0.02±0.007	0.144±0.002	0.11±0.02
2.7	0.141±0.004±0.002		0.145±0.003	
2.9	0.150±0.006±0.003		0.149±0.004	

Table 4.14: $v_2(p_T)$: centrality 20-30%

p_T (GeV/c)	$v_2\{EtaSubs\}$ ($\pm$Stat.$\pm$Syst. Err.)	$v_2\{BBC\}$ ($\pm$Stat.$\pm$Syst. Err.)	$v_2\{2\}$ ($\pm$Stat. Err.)	$v_2\{4\}$ ($\pm$Stat. Err.)
0.3	0.0286±0.0001±0.0002	0.0268±0.0005±0.0002	0.0316±0.0001	0.0261±0.0008
0.5	0.0486±0.0002±0.0002	0.0465±0.0006±0.0002	0.0480±0.0001	0.0446±0.0009
0.7	0.0665±0.0002±0.0003	0.0629±0.0008±0.0003	0.0638±0.0002	0.061±0.001
0.9	0.0833±0.0003±0.0003	0.078±0.001±0.0005	0.0803±0.0002	0.076±0.002
1.1	0.0996±0.0004±0.0003	0.095±0.002±0.0005	0.0976±0.0003	0.092±0.002
1.3	0.1166±0.0005±0.0002	0.114±0.002±0.0006	0.1140±0.0004	0.111±0.003
1.5	0.1300±0.0007±0.0003	0.128±0.003±0.001	0.1290±0.0005	0.121±0.004
1.7	0.146±0.001±0.001	0.137±0.004±0.002	0.1440±0.0007	0.140±0.005
1.9	0.157±0.001±0.0005	0.164±0.005±0.004	0.154±0.001	0.156±0.007
2.1	0.166±0.002±0.001	0.156±0.007±0.003	0.166±0.001	0.15±0.01
2.3	0.176±0.003±0.001	0.176±0.01±0.004	0.173±0.002	0.15±0.01
2.5	0.186±0.004±0.002	0.206±0.01±0.005	0.189±0.003	0.18±0.02
2.7	0.192±0.005±0.002		0.194±0.004	
2.9	0.204±0.007±0.003		0.205±0.004	

Table 4.15: $v_2(p_T)$: centrality 30-40%

p_T (GeV/c)	$v_2\{EtaSubs\}$ ($\pm$Stat.$\pm$Syst. Err.)	$v_2\{BBC\}$ ($\pm$Stat.$\pm$Syst. Err.)	$v_2\{2\}$ ($\pm$Stat. Err.)	$v_2\{4\}$ ($\pm$Stat. Err.)
0.3	0.0318±0.0002±0.0002	0.0287±0.0006±0.0004	0.0360±0.0001	0.029±0.001
0.5	0.0551±0.0002±0.0002	0.0508±0.0007±0.0003	0.0546±0.0002	0.050±0.001
0.7	0.0752±0.0003±0.0001	0.0695±0.0009±0.0003	0.0727±0.0002	0.067±0.002
0.9	0.0955±0.0004±0.0001	0.089±0.001±0.0005	0.0922±0.0003	0.088±0.002
1.1	0.1142±0.0005±0.0001	0.107±0.002±0.0007	0.1120±0.0004	0.108±0.003
1.3	0.1321±0.0007±0.0002	0.125±0.002±0.0008	0.1300±0.0005	0.119±0.004
1.5	0.148±0.001±0.0003	0.140±0.003±0.001	0.1460±0.0007	0.134±0.006
1.7	0.163±0.001±0.0005	0.155±0.005±0.001	0.163±0.001	0.155±0.008
1.9	0.178±0.002±0.0004	0.162±0.006±0.004	0.174±0.001	0.17±0.01
2.1	0.189±0.003±0.001	0.180±0.009±0.005	0.186±0.002	0.19±0.02
2.3	0.198±0.004±0.0009	0.18±0.01±0.004	0.197±0.003	0.17±0.02
2.5	0.209±0.005±0.003	0.22±0.02±0.01	0.206±0.004	0.18±0.03
2.7	0.213±0.007±0.002		0.208±0.005	
2.9	0.23±0.01±0.003		0.221±0.006	

Table 4.16: $v_2(p_T)$: centrality 40-50%

p_T (GeV/c)	$v_2\{EtaSubs\}$ ($\pm$Stat.$\pm$Syst. Err.)	$v_2\{BBC\}$ ($\pm$Stat.$\pm$Syst. Err.)	$v_2\{2\}$ ($\pm$Stat. Err.)	$v_2\{4\}$ ($\pm$Stat. Err.)
0.3	0.0321±0.0003±0.0002	0.0286±0.0008±0.0003	0.0386±0.0002	0.028±0.002
0.5	0.0560±0.0003±0.0002	0.050±0.001±0.0004	0.0561±0.0002	0.052±0.003
0.7	0.0775±0.0005±0.0003	0.070±0.001±0.0005	0.0748±0.0003	0.068±0.004
0.9	0.0986±0.0006±0.0003	0.087±0.002±0.0009	0.0948±0.0004	0.091±0.006
1.1	0.1179±0.0009±0.0005	0.104±0.003±0.002	0.1140±0.0006	0.09±0.02
1.3	0.136±0.001±0.0006	0.124±0.004±0.002	0.1320±0.0008	0.10±0.01
1.5	0.150±0.002±0.0008	0.140±0.005±0.002	0.149±0.001	0.16±0.01
1.7	0.166±0.002±0.002	0.144±0.007±0.003	0.166±0.002	0.13±0.02
1.9	0.177±0.003±0.001	0.13±0.01±0.004	0.178±0.002	0.21±0.03
2.1	0.186±0.005±0.001	0.20±0.01±0.005	0.188±0.003	0.16±0.04
2.3	0.193±0.007±0.003	0.22±0.02±0.004	0.191±0.005	0.23±0.06
2.5	0.197±0.009±0.003	0.21±0.03±0.01	0.199±0.006	0.10±0.08
2.7	0.21±0.01±0.007		0.200±0.009	
2.9	0.24±0.02±0.006		0.22±0.01	

Table 4.17: $v_2(p_T)$: centrality 50-60%

p_T (GeV/c)	$v_2\{EtaSubs\}$ ($\pm$Stat.$\pm$Syst. Err.)	$v_2\{BBC\}$ ($\pm$Stat.$\pm$Syst. Err.)	$v_2\{2\}$ ($\pm$Stat. Err.)	$v_2\{4\}$ ($\pm$Stat. Err.)
0.3	0.0298±0.0005±0.0003	0.024±0.002±0.0005	0.0407±0.0003	0.0273±0.009
0.5	0.0534±0.0006±0.0003	0.042±0.002±0.0005	0.0538±0.0004	0.06±0.01
0.7	0.0755±0.0008±0.0003	0.061±0.003±0.001	0.0710±0.0006	0.06±0.01
0.9	0.096±0.001±0.0004	0.085±0.004±0.001	0.0900±0.0008	0.07±0.02
1.1	0.111±0.002±0.001	0.095±0.005±0.002	0.108±0.001	0.08±0.03
1.3	0.131±0.002±0.001	0.113±0.007±0.003	0.126±0.002	0.18±0.04
1.5	0.141±0.003±0.005	0.13±0.01±0.003	0.143±0.002	0.07±0.06
1.7	0.159±0.005±0.002	0.12±0.01±0.005	0.153±0.003	0.15±0.08
1.9	0.178±0.006±0.003	0.13±0.02±0.007	0.169±0.004	0.13±0.09
2.1	0.195±0.009±0.006	0.15±0.03±0.007	0.182±0.006	0.2±0.2
2.3	0.185±0.01±0.008	0.18±0.04±0.01	0.185±0.009	0.2±0.2
2.5	0.23±0.02±0.008	0.07±0.06±0.02	0.19±0.01	0.2±0.3
2.7	0.19±0.03±0.01		0.20±0.02	
2.9	0.22±0.04±0.03		0.20±0.02	

Table 4.18: $v_2(p_T)$: centrality 60-70%

p_T (GeV/c)	$v_2\{EtaSubs\}$ ($\pm$**Stat.**$\pm$**Syst. Err.**)	$v_2\{BBC\}$ ($\pm$**Stat.**$\pm$**Syst. Err.**)	$v_2\{2\}$ ($\pm$**Stat. Err.**)
0.3	0.025±0.001±0.0006	0.017±0.004±0.001	0.0422±0.0006
0.5	0.049±0.001±0.0007	0.041±0.005±0.002	0.0503±0.0008
0.7	0.068±0.002±0.002	0.062±0.006±0.002	0.065±0.001
0.9	0.092±0.002±0.002	0.055±0.009±0.004	0.082±0.002
1.1	0.110±0.004±0.002	0.09±0.01±0.006	0.101±0.002
1.3	0.123±0.005±0.003	0.09±0.02±0.007	0.124±0.003
1.5	0.144±0.007±0.003	0.17±0.03±0.01	0.134±0.004
1.7	0.172±0.01±0.008	0.13±0.04±0.01	0.163±0.006
1.9	0.156±0.01±0.007	-0.01±0.05±0.02	0.156±0.009
2.1	0.22±0.02±0.02	0.14±0.08±0.02	0.19±0.01
2.3	0.18±0.03±0.02	0.36±0.09±0.04	0.19±0.02
2.5	0.25±0.04±0.02	0.3±0.2±0.05	0.26±0.03
2.7	0.27±0.06±0.03		0.23±0.04
2.9	0.38±0.09±0.02		0.23±0.05

Table 4.19: $v_2(p_T)$: centrality 70-80%

p_T (GeV/c)	$v_2\{EtaSubs\}$ ($\pm$**Stat.**$\pm$**Syst. Err.**)	$v_2\{BBC\}$ ($\pm$**Stat.**$\pm$**Syst. Err.**)	$v_2\{2\}$ ($\pm$**Stat. Err.**)
0.3	0.020±0.002±0.0008	0.03±0.01±0.004	0.043±0.001
0.5	0.045±0.002±0.002	0.06±0.01±0.005	0.054±0.001
0.7	0.070±0.003±0.001	0.07±0.02±0.008	0.065±0.002
0.9	0.102±0.004±0.002	0.04±0.03±0.03	0.090±0.003
1.1	0.135±0.006±0.007	0.01±0.04±0.02	0.107±0.004
1.3	0.135±0.009±0.004	0.06±0.06±0.02	0.126±0.006
1.5	0.18±0.01±0.007	0.05±0.09±0.03	0.145±0.009
1.7	0.17±0.02±0.01	0.01±0.1±0.06	0.14±0.01
1.9	0.22±0.03±0.03	0.05±0.2±0.07	0.22±0.02
2.1	0.27±0.04±0.03	-0.08±0.3±0.09	0.21±0.03
2.3	0.37±0.06±0.03	0.2±0.4±0.1	0.24±0.04
2.5	0.38±0.09±0.03		0.26±0.06
2.7	0.4±0.1±0.1		0.23±0.09
2.9	0.4±0.2±0.08		0.30±0.1

$v_2(\eta)$: centrality 0-5%			
η	v_2	**Err. Stat.**	**Err. Syst.**
-0.95	0.0148	0.0007	0.0002
-0.85	0.0154	0.0006	0.0003
-0.75	0.0158	0.0006	0.0002
-0.65	0.0163	0.0006	0.0002
-0.55	0.0171	0.0006	0.0002
-0.45	0.0172	0.0006	0.0003
-0.35	0.0188	0.0006	0.0002
-0.25	0.0184	0.0006	0.0003
-0.15	0.0189	0.0006	0.0002
-0.05	0.0191	0.0006	0.0002
0.05	0.0192	0.0006	0.0002
0.15	0.0192	0.0006	0.0003
0.25	0.0185	0.0006	0.0002
0.35	0.0183	0.0006	0.0003
0.45	0.0189	0.0006	0.0001
0.55	0.0176	0.0006	0.0003
0.65	0.0168	0.0006	0.0003
0.75	0.0161	0.0006	0.0003
0.85	0.0155	0.0006	0.0002
0.95	0.0130	0.0007	0.0005

$v_2(\eta)$: centrality 5-10%			
η	v_2	**Err. Stat.**	**Err. Syst.**
-0.95	0.0239	0.0005	0.0002
-0.85	0.0254	0.0005	0.0003
-0.75	0.0254	0.0005	0.0002
-0.65	0.0252	0.0005	0.0003
-0.55	0.0263	0.0005	0.0003
-0.45	0.0271	0.0005	0.0003
-0.35	0.0277	0.0005	0.0002
-0.25	0.0284	0.0005	0.0004
-0.15	0.0282	0.0005	0.0002
-0.05	0.0294	0.0005	0.0003
0.05	0.0283	0.0005	0.0003
0.15	0.0282	0.0005	0.0003
0.25	0.0289	0.0005	0.0002
0.35	0.0277	0.0005	0.0004
0.45	0.0277	0.0005	0.0005
0.55	0.0257	0.0005	0.0003
0.65	0.0261	0.0005	0.0003
0.75	0.0253	0.0005	0.0002
0.85	0.0246	0.0005	0.0003
0.95	0.0228	0.0005	0.0002

$v_2(\eta)$: centrality 10-20%			
η	v_2	**Err. Stat.**	**Err. Syst.**
-0.95	0.0347	0.0003	0.0002
-0.85	0.0362	0.0003	0.0001
-0.75	0.0371	0.0003	0.0002
-0.65	0.0376	0.0003	0.0002
-0.55	0.0384	0.0003	0.0003
-0.45	0.0390	0.0003	0.0002
-0.35	0.0394	0.0003	0.0002
-0.25	0.0400	0.0003	0.0003
-0.15	0.0404	0.0003	0.0003
-0.05	0.0404	0.0003	0.0003
0.05	0.0405	0.0003	0.0003
0.15	0.0400	0.0003	0.0002
0.25	0.0392	0.0003	0.0003
0.35	0.0392	0.0003	0.0002
0.45	0.0387	0.0003	0.0002
0.55	0.0376	0.0003	0.0002
0.65	0.0369	0.0003	0.0002
0.75	0.0364	0.0003	0.0002
0.85	0.0360	0.0003	0.0003
0.95	0.0347	0.0003	0.0004

$v_2(\eta)$: centrality 20-30%			
η	v_2	**Err. Stat.**	**Err. Syst.**
-0.95	0.0458	0.0004	0.0002
-0.85	0.0466	0.0004	0.0002
-0.75	0.0473	0.0003	0.0002
-0.65	0.0482	0.0003	0.0003
-0.55	0.0494	0.0003	0.0003
-0.45	0.0502	0.0003	0.0002
-0.35	0.0503	0.0003	0.0003
-0.25	0.0506	0.0003	0.0002
-0.15	0.0514	0.0003	0.0003
-0.05	0.0516	0.0003	0.0003
0.05	0.0515	0.0003	0.0002
0.15	0.0517	0.0003	0.0002
0.25	0.0510	0.0003	0.0002
0.35	0.0504	0.0003	0.0003
0.45	0.0498	0.0003	0.0002
0.55	0.0484	0.0003	0.0002
0.65	0.0479	0.0003	0.0002
0.75	0.0465	0.0003	0.0002
0.85	0.0456	0.0004	0.0003
0.95	0.0454	0.0004	0.0004

$v_2(\eta)$: centrality 30-40%			
η	v_2	**Err. Stat.**	**Err. Syst.**
-0.95	0.0505	0.0005	0.0003
-0.85	0.0520	0.0005	0.0003
-0.75	0.0525	0.0005	0.0002
-0.65	0.0535	0.0005	0.0002
-0.55	0.0550	0.0005	0.0003
-0.45	0.0550	0.0005	0.0001
-0.35	0.0552	0.0005	0.0003
-0.25	0.0570	0.0005	0.0003
-0.15	0.0576	0.0005	0.0002
-0.05	0.0575	0.0005	0.0003
0.05	0.0582	0.0005	0.0002
0.15	0.0570	0.0005	0.0003
0.25	0.0568	0.0005	0.0003
0.35	0.0552	0.0005	0.0002
0.45	0.0552	0.0005	0.0002
0.55	0.0548	0.0005	0.0003
0.65	0.0533	0.0005	0.0003
0.75	0.0516	0.0005	0.0002
0.85	0.0508	0.0005	0.0005
0.95	0.0493	0.0005	0.0004

$v_2(\eta)$: centrality 40-50%			
η	v_2	**Err. Stat.**	**Err. Syst.**
-0.95	0.0492	0.0008	0.0004
-0.85	0.0505	0.0008	0.0006
-0.75	0.0533	0.0007	0.0004
-0.65	0.0541	0.0007	0.0005
-0.55	0.0539	0.0007	0.0004
-0.45	0.0543	0.0007	0.0003
-0.35	0.0557	0.0007	0.0002
-0.25	0.0583	0.0007	0.0003
-0.15	0.0563	0.0007	0.0005
-0.05	0.0573	0.0007	0.0002
0.05	0.0590	0.0007	0.0005
0.15	0.0574	0.0007	0.0003
0.25	0.0572	0.0007	0.0004
0.35	0.0558	0.0007	0.0003
0.45	0.0539	0.0007	0.0003
0.55	0.0554	0.0007	0.0003
0.65	0.0528	0.0007	0.0004
0.75	0.0513	0.0007	0.0004
0.85	0.0508	0.0008	0.0005
0.95	0.0495	0.0008	0.0004

$v_2(\eta)$: centrality 50-60%			
η	v_2	**Err. Stat.**	**Err. Syst.**
-0.95	0.0449	0.0001	0.0004
-0.85	0.0546	0.0001	0.0008
-0.75	0.0477	0.0001	0.0008
-0.65	0.0494	0.0001	0.0006
-0.55	0.0518	0.0001	0.0004
-0.45	0.0495	0.0001	0.0004
-0.35	0.0522	0.0001	0.0005
-0.25	0.0525	0.0001	0.0003
-0.15	0.0548	0.0001	0.0002
-0.05	0.0577	0.0001	0.0004
0.05	0.0579	0.0001	0.0004
0.15	0.0562	0.0001	0.0003
0.25	0.0525	0.0001	0.0004
0.35	0.0524	0.0001	0.0006
0.45	0.0482	0.0001	0.0006
0.55	0.0513	0.0001	0.0003
0.65	0.0462	0.0001	0.0005
0.75	0.0477	0.0001	0.0004
0.85	0.0448	0.0001	0.0004
0.95	0.0465	0.0001	0.0008

$v_2(\eta)$: centrality 60-70%			
η	v_2	**Err. Stat.**	**Err. Syst.**
-0.95	0.0417	0.0003	0.001
-0.85	0.0377	0.0003	0.001
-0.75	0.0368	0.0003	0.002
-0.65	0.0442	0.0003	0.002
-0.55	0.0410	0.0003	0.0008
-0.45	0.0406	0.0003	0.001
-0.35	0.0448	0.0003	0.001
-0.25	0.0494	0.0003	0.001
-0.15	0.0538	0.0003	0.0008
-0.05	0.0535	0.0003	0.0007
0.05	0.0517	0.0003	0.002
0.15	0.0512	0.0003	0.001
0.25	0.0449	0.0003	0.0008
0.35	0.0463	0.0003	0.001
0.45	0.0443	0.0003	0.002
0.55	0.0457	0.0003	0.001
0.65	0.0429	0.0003	0.0008
0.75	0.0405	0.0003	0.002
0.85	0.0402	0.0003	0.001
0.95	0.0385	0.0003	0.002

$v_2(\eta)$: centrality 70-80%			
η	v_2	**Err. Stat.**	**Err. Syst.**
-0.95	0.0254	0.0005	0.003
-0.85	0.0414	0.0005	0.003
-0.75	0.0445	0.0005	0.003
-0.65	0.0414	0.0005	0.002
-0.55	0.0424	0.0005	0.002
-0.45	0.0373	0.0005	0.001
-0.35	0.0523	0.0005	0.002
-0.25	0.0368	0.0005	0.004
-0.15	0.0566	0.0005	0.002
-0.05	0.0481	0.0005	0.003
0.05	0.0550	0.0005	0.002
0.15	0.0501	0.0005	0.001
0.25	0.0450	0.0005	0.002
0.35	0.0318	0.0005	0.004
0.45	0.0401	0.0005	0.001
0.55	0.0459	0.0005	0.003
0.65	0.0412	0.0005	0.002
0.75	0.0322	0.0005	0.002
0.85	0.0413	0.0005	0.002
0.95	0.0340	0.0005	0.004

4.11.5 ϕ-meson v_2 data points

$v_2(p_T)$: centrality 0-80%

p_T **(GeV/c)**	v_2	**Error Stat.**	**Error Syst.**
0.77	0.03	0.01	0.006
1.27	0.05	0.01	0.007
2.08	0.11	0.03	0.01

4.11.6 ϕ-meson signal+background (0-80%)
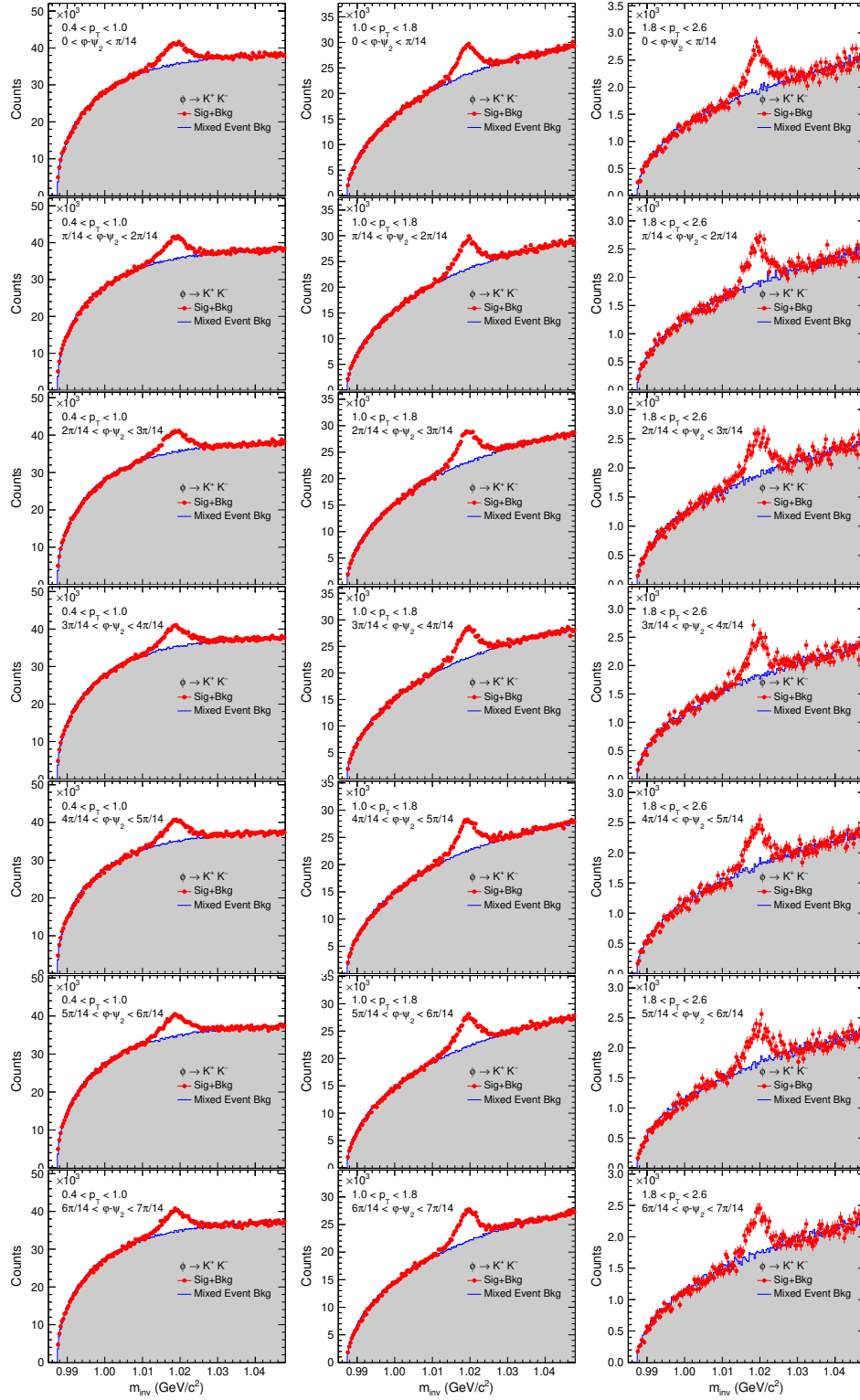
4.11.7 ϕ-meson raw yield extraction (0-80%)
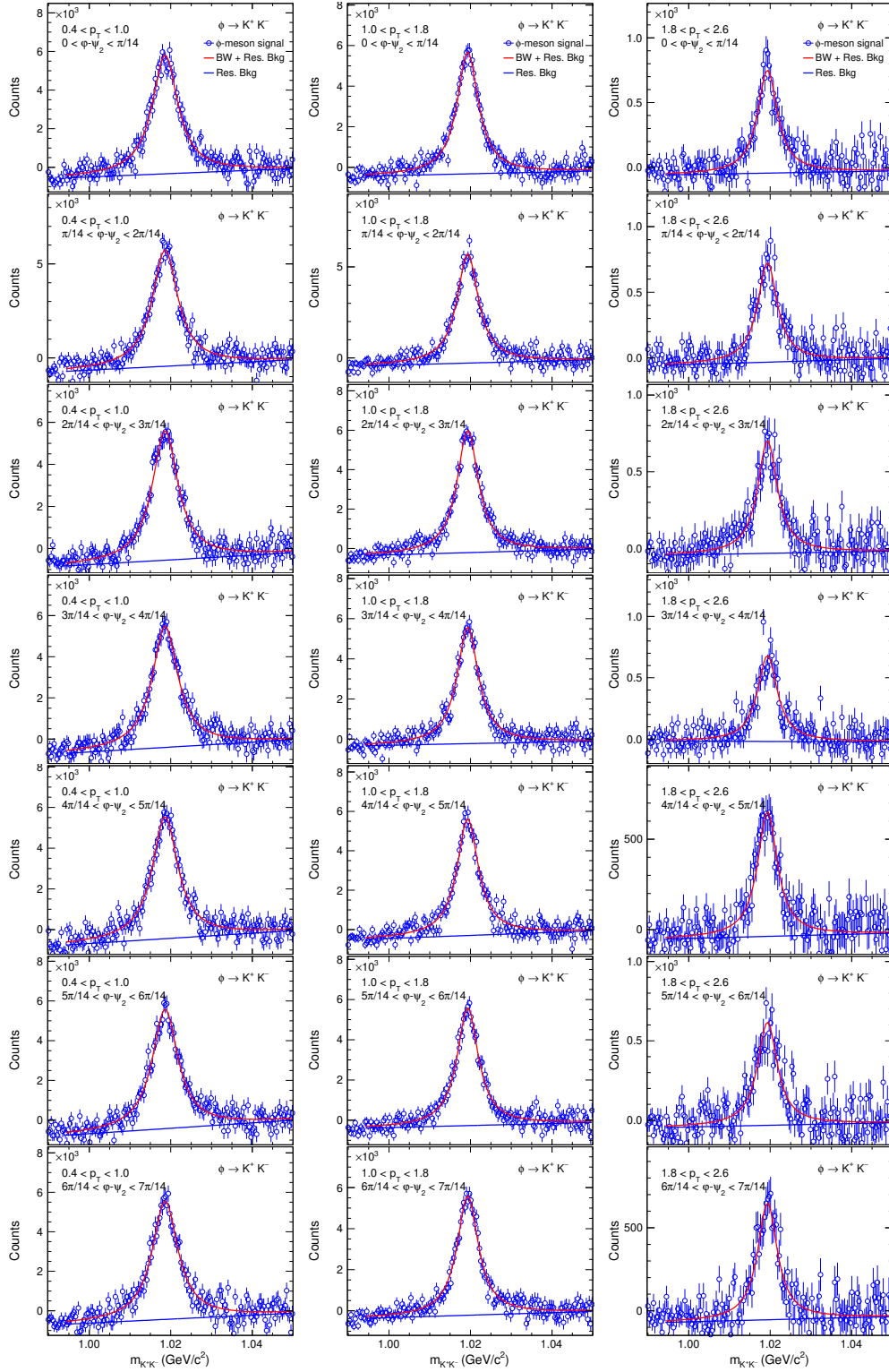
Chapter 5

Study of event selection in U+U collisions using AMPT model

5.1 Introduction

The initial overlap region in central heavy-ion collisions with spherical nuclei such as Gold (Au) or Lead (Pb) is always circular. However, in U+U collisions, the initial overlap region can acquire different configurations owing to the deformed shape of the Uranium nuclei [1]. The elliptic flow (v_2) has been studied in Ref. [1] and it is found to be strongly correlated with the different configurations of the initial overlap region. Moreover, in heavy-ion collisions, the energetic spectator protons can produce a strong magnetic field reaching $eB_y \sim m_\pi^2$ [2]. Such a strong magnetic field can give rise to chiral magnetic effect (CME) and chiral separation effect (CSE) [2, 3]. Azimuthal anisotropy acts as a background to these processes [4]. Therefore, it is necessary to minimise the azimuthal anisotropy to observe these phenomena in experimental data. The heavy-ion collision events which have low azimuthal anisotropy (v_2) and very high magnetic field are the perfect candidates for the CME and CSE. In a central Au+Au

or Pb+Pb collisions, the azimuthal anisotropy is very low, but the magnetic field is also low due to less number of spectator protons. In a non-central Au+Au or Pb+Pb collisions, although the magnetic field is comparatively high, the azimuthal anisotropy (v_2) also starts increasing and therefore, increasing the background to CME and CSE.
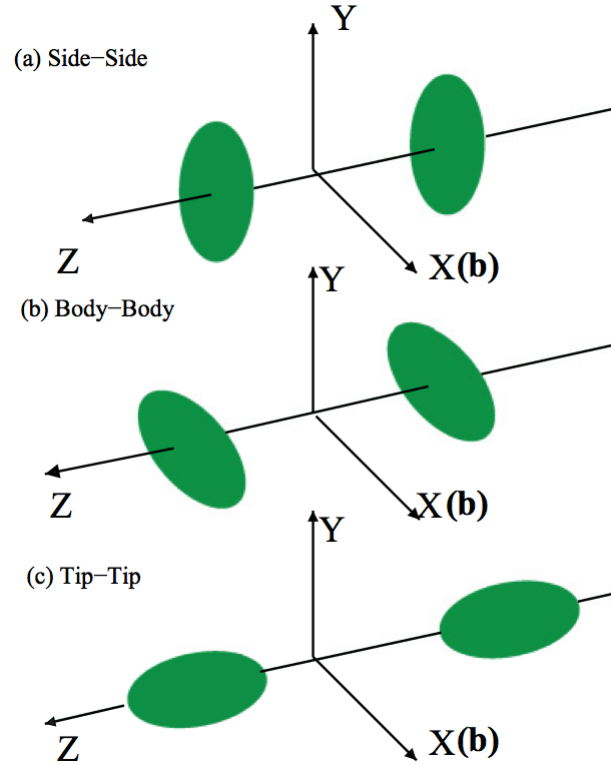
Figure 5.1: Various initial collision configurations for central ($b = 0$) U+U collisions [1]; (a) side-side (b) body-body (c) tip-tip. The impact parameter is along the X-axis.

The Uranium nuclei, due to its deformed shape, can have different initial collision configurations as shown in the Fig. 5.1. However, there is a unique orientation in which the magnetic field is very high in central collisions and as well as the azimuthal anisotropy is also very low. Therefore, U+U collisions may provide an unique opportunity to study these exotic effects in relativistic heavy-ion collisions. However, it has not been experimentally possible so far to unambiguously select specific configurations in U+U collisions.
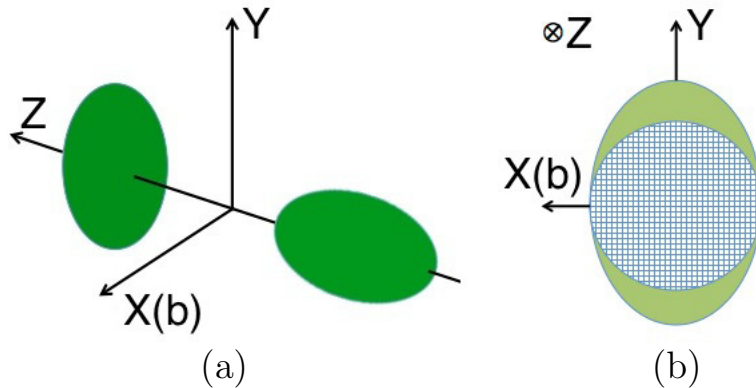
Figure 5.2: (a) Body-tip configuration in the laboratory frame of reference. The impact parameter is along the X-axis. (b) The cross sectional view of the overlap region (shown by mesh) for a central ($b = 0$) body-tip collision.

In this chapter, we present a method to select body-tip configuration from un-biased events in U+U collisions using AMPT model. A schematic diagram of the body-tip configuration is shown in Figure 5.2(a), where the impact parameter (b) is along X-axis and the beam direction is along Z-axis. In this configuration, the (right going) Uranium nuclei whose major axis is perpendicular to beam direction is called body and other one (left going) whose major axis is along the beam direction is called tip [5]. As seen in Figure 5.2(b), the overlap region in such a body-tip collision is circular (shown by the mesh). The nucleons which lies in the overlap are called participants and those which do not take part in the collisions and lies outside the overlap region are called spectators. Figure 5.2(b) shows that one Uranium nucleus get completely occluded into the other, leaving almost no spectators, where as the other one will always have some spectator from the non-overlapping regions. This gives rise to asymmetry in the spectator counts in the two opposite directions. This particular feature of body-tip configuration can be use to separate it out from rest of all the other random configurations possible in deformed Uranium nuclei.

5.2 The AMPT model

A Multi-Phase Transport model (AMPT) is a hybrid transport model for the simulation of high energy heavy-ion collisions. It has four main stages: the initial conditions, partonic interactions, the conversion from the partonic to the hadronic matter, and a final hadronic interactions stage [6]. The initial conditions used in AMPT model is same as in HIJING model [7]. Scattering among partons are modelled by Zhang's parton cascade [8], which calculates two-body parton scatterings using cross sections from pQCD with screening masses. There are two versions of AMPT model. In the default AMPT model, partons are recombined with their parent strings and when they stop interacting, the resulting strings fragment into hadrons according to the Lund string fragmentation model [9]. However in the string melting (SM) scenario, these strings are converted to soft partons and a quark coalescence model is used to combine parton into hadrons. The evolution dynamics of the hadronic matter is described by A Relativistic Transport (ART) model [10].

We have used string melting (SM) mode of AMPT version 2.25t7, with parton-parton cross section of 10mb which will give rise to substantial amount of v_2. A total of 0.6 million 0-5% central U+U collision events are generated using this model for the analysis. The details of input parameters used for the event generation is given in the Appendix at the end of this chapter. We have studied azimuthal anisotropy of charged particles in U+U collisions at $\sqrt{s_{\mathrm{NN}}} = 193$ GeV using the AMPT model. The deformation of Uranium nuclei is implemented in the AMPT model as described in the following subsection.

5.2.1 Implementing deformed shape of Uranium nucleus in AMPT

The Uranium nucleus has prolate shape. The shape of Uranium nucleus and its collision configurations are implemented in the AMPT model by modifying the Woods-Saxon density distribution [11] as,

$$\rho(r) = \frac{\rho_0}{1 + exp([r - R']/a)} \tag{5.1}$$

$$R' = R[1 + \beta_2 Y_2^0(\theta) + \beta_4 Y_4^0(\theta)] \tag{5.2}$$

where ρ_0 is the normal nuclear density, R is the radius of the nucleus, and a denotes the surface diffuseness parameter. $Y_l^m(\theta)$ are spherical harmonics and θ is the polar angle with respect to the symmetry axis of the nucleus. The values of $R = 6.81$ fm, $a = 0.55$ fm, $\beta_2 = 0.28$ and $\beta_4 = 0.093$ are used from Ref. [1]. The presence of deformation parameters $\beta_2 > 0$ (Quadrupole) and β_4 (Hexadecapole) give prolate shape to the Uranium nucleus. The positions of nucleons are sampled by the expression $4\pi r^2 \sin\theta \rho(r) d\theta d\phi$. Both the projectile and target nuclei are randomly rotated along the θ and ϕ directions event by event with probability distribution $\sin\theta$ and uniform distribution for ϕ and θ, respectively. The $\sin\theta$ weight is needed to simulate unpolarized nucleus-nucleus collisions [12].

In this analysis, we have generated specific configuration body-tip (Figure 5.2) and unbiased (without any specific choice of orientation of U nucleus) U+U collisions. We have shown a new method for the selection of body-tip configuration from the unbiased U+U collisions using the AMPT model in context of experiment. This method, in particular uses asymmetry in the spectator neutron numbers in the two opposite directions of U+U collisions, can be use in the experimental data.

5.3 Experimental significance and observables

In the experiments it is possible to get the measure of spectators using Zero Degree Calorimeter (ZDC) detector which lies very close to the beam pipe in the forward (and backward) direction [13]. The ZDC detector gives a electrical signal which is proportional to the number of spectator neutrons. The charged spectator protons do not reach at ZDC because of the magnetic field in the experiment. Therefore, we used only neutrons from the spectators for this analysis. Figure 5.3(a) shows the spectator neutron correlation for both body and tip oriented Uranium nuclei in body-tip collisions. As seen from the figure, the spectator neutron counts are not symmetric for body-tip collisions. In a real experiment, these spectator neutrons are detected by Zero Degree Calorimeters (ZDC). Therefore, it is worthwhile to convert this spectator neutrons counts into experimentally measurable ZDC signal. We use the ZDC response of the STAR experiment at RHIC from Ref. [13] to convert neutrons number into corresponding ZDC signal. Figure 6 of Ref. [13] shows that the resolution of a single neutron ZDC response is 18%. Therefore, we smear the energy deposited by each individual spectator neutron by a Gaussian distribution with the width of 18% of the mean value to imitate the response in the ZDC detector. The mean value of energy deposited by a single neutron for this study is 96.5 GeV. The energy deposited by the spectator neutrons in the ZDC, event by event, is shown in Figure 5.3(b).

We can select the body-tip events from all the other configurations using this correlation shown in Figure 5.3(b). One such selection procedure is shown by the dotted line, with slope = 0.25 and intercept = -180. We select all the events which lies below this line, therefore selecting the events with asymmetric spectator neutrons. The ZDC response for all possible configurations in U+U collisions is shown in Figure 5.3(c). Since both left going and right going nuclei can be in either body or

in tip orientation, therefore, we select these events along both (left and right) axis. The two dotted lines show the selection ranges for the possible body-tip events from all possible configurations in central U+U collisions. Figure 5.3(d) shows the ZDC response of the selected events.
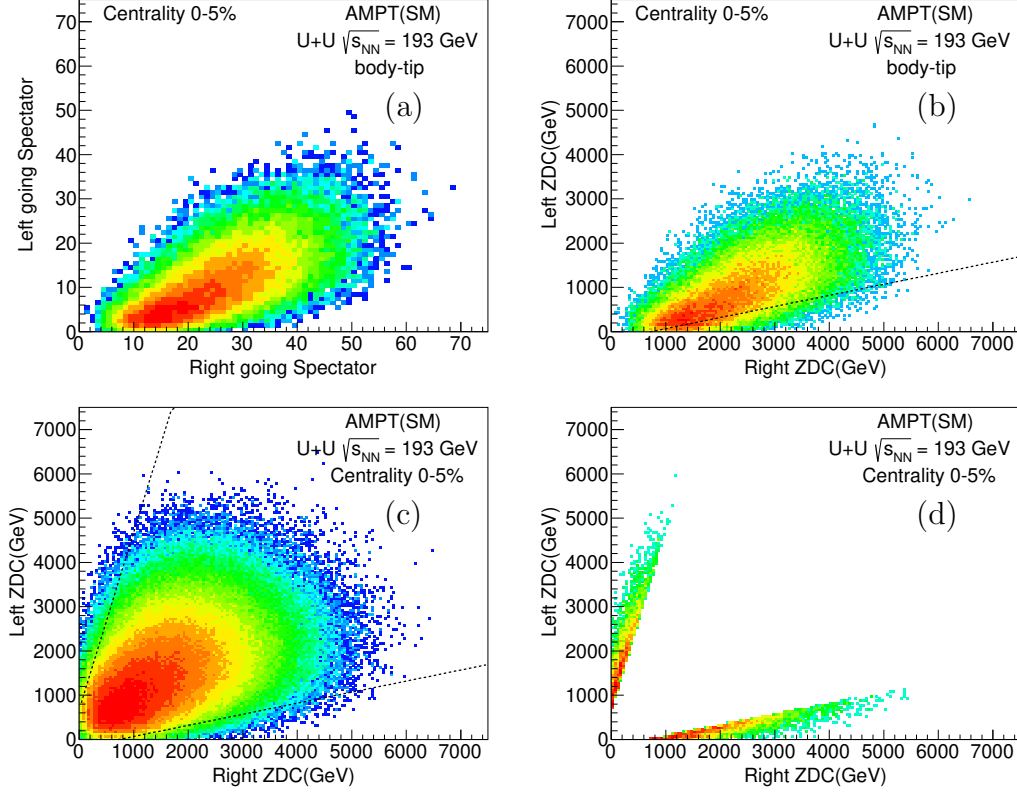
Figure 5.3: (a) Spectator neutron distribution for 0-5% central events in body-tip configuration of U+U collisions at $\sqrt{s_{NN}} = 193$ GeV. (b) Energy deposited by spectator neutrons in ZDC for the same events of body-tip configuration as in (a). (c) Energy deposited by spectator neutrons in ZDC for all configurations in U+U collisions. The dotted lines show the selection range for body-tip events. (d) The spectator neutron energy in ZDC after selecting events using the dotted lines in (c).

One way to differentiate between the minimum bias (all possible configurations) and the body-tip configurations is to look at the variable S_η which is defined as,

$$S_\eta = \frac{\eta(dN/d\eta)}{N_{tot}} \tag{5.3}$$

228

where, N_{tot} is the number of particles within $-1.0 < \eta < 1.0$. Figure 5.4 shows the variable S_η as a function of N_{tot} for minimum bias, selected body-tip events from the minimum bias, and pure body-tip events. As can be seen from Fig. 5.4, the S_η for minimum bias configurations lies close to zero, suggesting symmetry in particle production. The particle production in body-tip events are asymmetric in η as shown by solid squares in the Fig. 5.4. However, when selecting body-tip events from minimum bias configurations, both the projectile and the target can either be in body or in tip configuration. Therefore we have two set of S_η (when projectile is body, target is tip and vice-versa) for selected events. The difference observed in S_η of selected events and minimum bias configurations enhances the possibility of our method to select the body-tip events in real experiments.
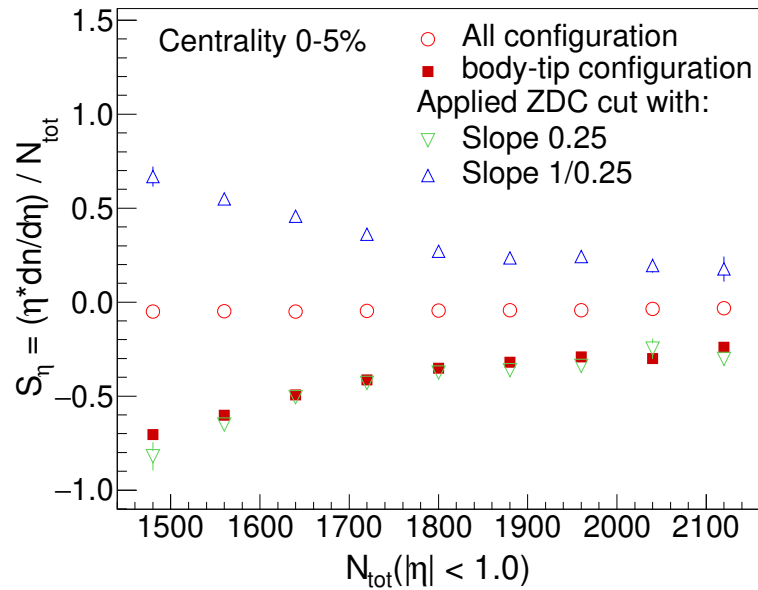
Figure 5.4: S_η (from Eq. 5.3) as a function of N_{tot} for minimum bias, selected body-tip events from minimum bias, and pure body-tip events in 0-5% central U+U collisions.

5.4 v_2 measurement method

The elliptic flow is usually quantified with a Fourier decomposition of the azimuthal distribution of produced particles with respect to the reaction plane (ψ_{RP}). The reaction plane angle is estimated using particles to determine event plane angle (ψ_{EP}). The observable related to elliptic flow is the second order Fourier coefficient with respect to the event plane angle $(v_2\{EP\})$ [14]. In such calculations elliptic flow v_2 is assumed to be aligned with the orientation of the reaction plane. Due to fluctuation in the positions of nucleons of initial collision geometry, the reaction plane does not always coincides with the direction of nucleon-nucleon interaction points. Therefore, elliptic flow v_2 is calculated with respect to the participant plane angle (ψ_{2pp}). The participant plane angle is defined as,

$$\psi_{2pp} = \frac{arctan\left(\langle r^2 \sin(2\phi_{part})\rangle, \langle r^2 \cos(2\phi_{part})\rangle\right) + \pi}{2},\tag{5.4}$$

where r and ϕ_{part} are the positions of participant nucleons (nucleons which take part in the collisions) in the polar coordinates. Then the elliptic flow v_2 is calculated with respect to ψ_{2pp} as,

$$v_2 = \langle\cos(2(\phi - \psi_{2pp}))\rangle,\tag{5.5}$$

where the average $\langle\ \rangle$ is over all particles and events. The detailed method of calculating ψ_{2pp} using the position co-ordinates of participants using Monte-Carlo Glauber model is given in the Ref. [15]. In the following section, we have shown results for the observable v_2 with respect to both the event plane angle (ψ_{2EP}) and participant plane angle (ψ_{2pp}) using AMPT model in U+U collisions at $\sqrt{s_{\mathrm{NN}}} = 193$ GeV.

5.5 Results and discussion

In this section, we show the results for v_2 of the selected events after the selection of body-tip events from all possible configurations in U+U collisions at $\sqrt{s_{\mathrm{NN}}} = 193$ GeV. As the overlap region in a central body-tip collision is circular (Fig. 5.2(b)), therefore we expect that magnitude of v_2 for selected events should be less compared to a set of events without selection of any specific configuration in U+U collisions. Figure 5.5 shows the v_2 of charged particles at mid-rapidity ($|\eta| < 1.0$), measured with respect to participant plane angle (ψ_{2pp}) for 0-5% central events in U+U collisions at $\sqrt{s_{\mathrm{NN}}}$ = 193 GeV. Figure 5.5(a) shows that the v_2 in body-tip events is lower compared to minimum bias configurations in U+U collisions. The selected body-tip events might also contain some small amount of other possible configurations of U+U collisions. Therefore, we have varied the slope of the dotted line shown in Figure 5.3(c) to make the selection more strict or relaxed. The corresponding change in the v_2 is also shown in the Figure 5.5(a).
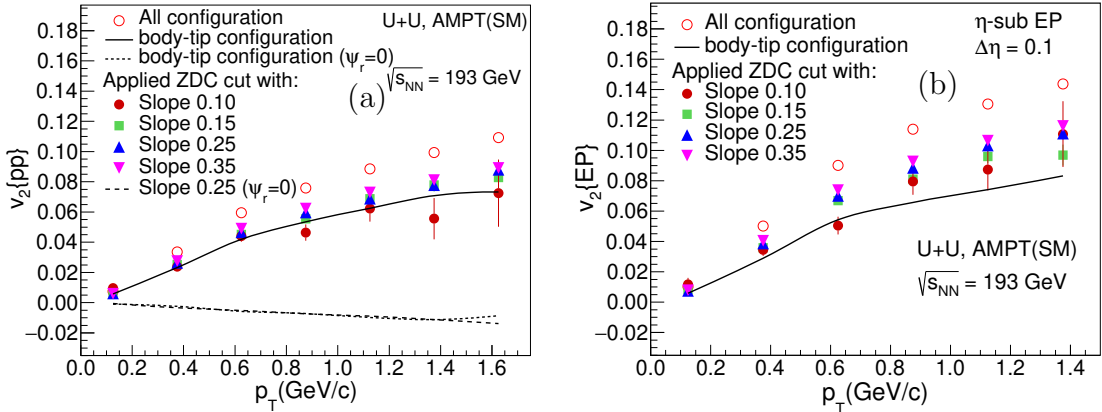
Figure 5.5: (a) $v_2\{pp\}$ for 0-5% central U+U collisions at $\sqrt{s_{\mathrm{NN}}} = 193$ GeV without ZDC cut (open markers) and with ZDC cut (solid markers). (b) $v_2\{EP\}$ for the same events without ZDC cut (open markers) and with ZDC cut (solid markers). Solid line in (a) and (b) corresponds to $v_2\{pp\}$ and $v_2\{EP\}$ for pure body-tip events. Dashed lines in (a) corresponds to $v_2\{pp\}$ with respect to $\psi_r = 0$.

The magnitude of charged particle $v_2(p_T)$ in the selected body-tip events are systematically 25% lower than that in all configurations. The $v_2(p_T)$ for purely body-tip events (i.e. orientation of Uranium nuclei are fixed according to body and tip orientation) in AMPT is also shown as solid curve in Figure 5.5(a). The dotted and dashed lines in Figure 5.5(a) corresponds to the v_2 measured with respect to reaction plane angle (ψ_r) in body-tip and selected body-tip events from all configurations respectively. The difference in the $v_2\{\psi_r\}$ and $v_2\{pp\}$ shown in Figure 5.5(a) arises due the fluctuations in the initial participants distribution. ψ_r is the reaction plane angle. Reaction plane is the plane subtended by the impact parameter and the beam direction. The angle made by reaction plane with X-axis is the reaction plane angle (ψ_r) and is a known quantity in the AMPT model. In experiments, however, the position of the participant nucleons are unknown. In this scenario, the event plane is calculated using the anisotropic distribution of the produced particles [14]. We followed η sub-event plane method to calculate v_2 of charged particles. In this method, each event is divided into two uncorrelated sub-events in two different η windows. Then 2nd order event plane (ψ_2) is calculated separately in both of these sub-events. Each particle is then correlated with the event plane of opposite η so as to remove the self-correlation effect [14]. The v_2 result obtained in this method is then corrected for the η sub-event plane resolution [14]. We have followed event-by-event resolution correction [16] for our analysis. The details of the procedure of event plane calculation and resolution correction can be found in [17]. The $v_2\{EP\}$ results for 0-5% central U+U collisions, calculated with event plane method, are shown in Figure 5.5(b). The $v_2\{EP\}$ for all configuration is shown by open markers in Figure 5.5(b). The $v_2\{EP\}$ for different ZDC cuts are shown by solid markers. As seen in Figure 5.5(b), $v_2\{EP\}$ is also systematically 25% lower for selected body-tip events compared to $v_2\{EP\}$ of all configurations. The $v_2\{EP\}$ for purely body-tip events is shown by solid curve

in Figure 5.5(b). As we see in Figure 5.5(b), with decreasing slope parameter (i.e. selecting events with higher spectator neutron asymmetry), $v_2\{EP\}$ of selected events systematically decreases compared to that of all configurations. Therefore, using lower slope value (higher spectator asymmetry), we can enhance the selection of body-tip events from all configurations in U+U collisions.
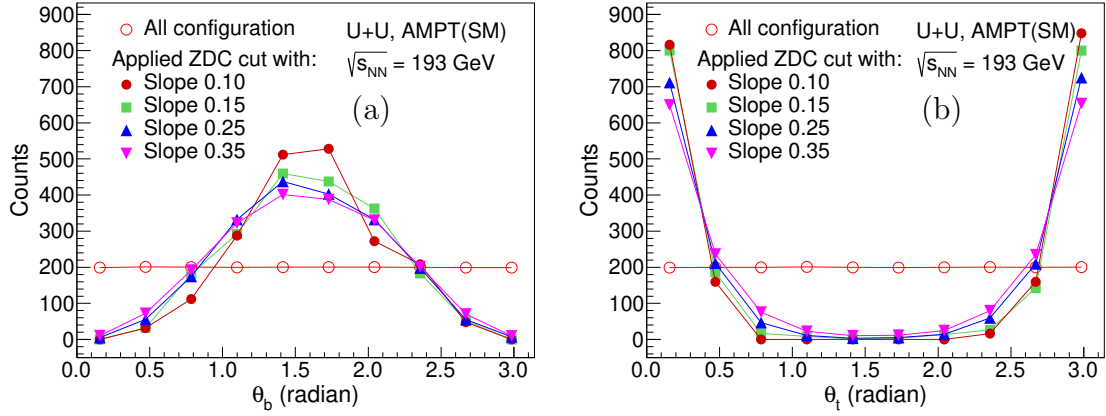
Figure 5.6: (a) Distribution of the angle of the major axis with the beam axis for body (θ_b) and for (b) tip (θ_t) oriented Uranium nuclei for different slope parameters. For pure body-tip events, $(\pi/2 - 0.005) < \theta_b < (\pi/2 + 0.005)$ and $0 < \theta_t < 0.05$ (radian).

Figure 5.6(a) and Figure 5.6(b) shows the distribution of the angle of the major axis of the Uranium with the beam axis for body (θ_b) and tip (θ_t) orientation for slope = 0.25. θ_b and θ_t for two different slope values and for all configuration in U+U collisions are also shown for comparison. Although lower slope values enhance the selection of body-tip events from all configuration, it also results in reduced event statistics. The selected events may possibly contain some other configurations. Therefore, we have calculated the purity of the selected events. By purity we infer that how much of the selected events can be specified as body-tip type events. We defined purity as,

$$purity(\%) = \frac{\text{No. of selected events with } \theta_t, \theta_p \text{ within the relaxation limits } \theta_R}{\text{total number of events satisfying the ZDC cut}} \times 100$$

(5.6)

233

Here we call an selected event to be body-tip if $-\theta_R < \theta_t < \theta_R$ and $(\pi/2 - \theta_R) < \theta_b < (\theta_R + \pi/2)$.

Table 5.1: Purity (%) of selected events for different slope parameter and angular relaxation.

Angular relaxation (θ_R) / slope parameter	$\pm 10°$	$\pm 20°$	$\pm 30°$
0.10	34%	62%	74%
0.15	28%	52%	70%
0.25	26%	48%	67%
0.35	24%	45%	63%

Since the angular distribution of both of the selected Uranium nuclei has some finite width, therefore, we assume that out of the selected events, the number of events for which θ_b and θ_t lies within $\pm \theta_R$ degree of the corresponding default values in body-tip events ($\theta_b = \pi/2$ and $\theta_t = 0$) is the pure body-tip sample. It is worth mentioning that the purity of the selected events depends on the relaxation on the angular width (θ_R) we set to classify the selected event as body-tip. Hence we have calculated the purity of the selected event sample for different angular relaxation and the results are listed in Table 5.1. As seen from Table 5.1, the purity of selected events increases as we decrease the value of slope parameter or if we increase the angular relaxation. As can be found in Table 5.1, more than 70% purity can be achieved using low slope value (i.e. higher order of spectator neutron asymmetry).

5.6 Summary

We present an experimental procedure to select the body-tip configuration among all possible configuration in 0-5% central U+U collisions at $\sqrt{s_{\mathrm{NN}}} = 193$ GeV. We found that the spectator neutron energy deposited in the Zero Degree Calorimeter (ZDC) is a useful tool to select body-tip oriented events in central U+U collisions. We have used a new variable S_η to differentiate between the body-tip and the minimum bias configurations. We are able to select body-tip configuration with conditions applied on spectator neutron asymmetry simulated with the ZDC. Elliptic flow (v_2) is calculated for the selected events with respect to both participant plane angle (ψ_{pp}) and event plane angle (ψ_2). As expected, v_2 of selected events is found to be systematically lower compared to that in all configurations in U+U collisions. The ZDC selection cut (slope) was varied and it was found that selecting events with higher spectator neutron asymmetry results in lower v_2 values which tends to match with v_2 of pure body-tip events. Finally we calculated the purity of the selected events from all configurations in the U+U collisions. We observed that purity increases for decreasing slope parameter. In other words, if we apply cut selecting higher order of left-right spectator neutron asymmetry, then the purity of the selected events increases.

Bibliography

[1] "Multiplicity, average transverse momentum, and azimuthal anisotropy in U + U collisions at $\sqrt{s_{NN}} = 200$ GeV using a multiphase transport model", Md. R. Haque, Z. W. Lin and B. Mohanty, *Phys. Rev. C*, **2012**, *85*, 034905.

[2] "The effects of topological charge change in heavy ion collisions: "Event by event P and CP violation"", D. Kharzeev *et al.*, *Nucl. Phys. A*, **2008**, *803*, 227-253.

[3] "Parity violation in hot QCD: why it can happen, and how to look for it", D. Kharzeev, *Phys. Lett. B*, **2006**, *633*, 260-264;

"Charge separation induced by P-odd bubbles in QCD matter", D. Kharzeev and A. Zhitnitsky, *Nucl. Phys. A*, **2007**, *797*, 67-79.

[4] "Beam-Energy Dependence of Charge Separation along the Magnetic Field in Au+Au Collisions at RHIC", L. Adamczyk *et al.*, *Phys. Rev. Lett.*, **2014**, *113*, 052302.

[5] "Separation of flow from the chiral magnetic effect in U + U collisions using spectator asymmetry", S. Chatterjee and P. Tribedy, *Phys. Rev. C*, **2015**, *92*, 011902.

[6] "Partonic effects on the elliptic flow at relativistic heavy ion collisions", Z. W. Lin and C. M. Ko, *Phys. Rev. C*, **2002**, *65*, 034904;

"Multiphase transport model for relativistic heavy ion collisions", Z. W. Lin *et al.*, *Phys. Rev. C*, **2005**, *72*, 064901;

"Pseudorapidity dependence of anisotropic flows in relativistic heavy-ion collisions", L. W. Chen *et al.*, *Phys. Lett. B*, **2005**, *605*, 95.

[7] "hijing: A Monte Carlo model for multiple jet production in pp, pA, and AA collisions", X. N. Wang and M. Gyulassy, *Phys. Rev. D*, **1991**, *44*, 3501.

[8] "ZPC 1.0.1: a parton cascade for ultrarelativistic heavy ion collisions", B. Zhang, *Comput. Phys. Commun.*, **2008**, *109*, 193-206.

[9] "Parton fragmentation and string dynamics", B. Andersson *et al.*, *Phys. Rep.*, **1983**, *97*, 31-145.

[10] "Formation of superdense hadronic matter in high energy heavy-ion collisions", B. A. Li and C. M. Ko, *Phys. Rev. C*, **1995**, *52*, 2037;

[11] "Deformation parameter for diffuse density", K. Hagino, N. W. Lwin, and M. Yamagami, *Phys. Rev. C*, **2006**, *74*, 017310.

[12] "Predictions of Elliptic flow and nuclear modification factor from 200 GeV U+U collisions at RHIC", H. Masui, B. Mohanty, and N. Xu, *Phys. Lett. B*, **2009**, *679*, 440-444.

[13] "The RHIC Zero Degree Calorimeter", C. Adler *et al.*, *Nucl. Inst. and Meth. A*, **2001**, *470*, 488-499.

[14] "Methods for analyzing anisotropic flow in relativistic nuclear collisions", A. Poskanzer and S. Voloshin, *Phys. Rev. C*, **1998**, *58*, 1671;

"Collective phenomena in non-central nuclear collisions", S. Voloshin, A. Poskanzer, R. Snellings, *arXiv*:0809.2949v2, **2008**.

[15] "Importance of correlations and fluctuations on the initial source eccentricity in high-energy nucleus-nucleus collisions", B. Alver *et al.*, *Phys. Rev. C*, **2008**, *77*, 014906;

"Collision-geometry fluctuations and triangular flow in heavy-ion collisions", B. Alver and G. Roland, *Phys. Rev. C*, **2010**, *81*, 054905.

[16] "Event plane resolution correction for azimuthal anisotropy in wide centrality bins", H. Masui and A. Schmah, A. Poskanzer, *Nucl. Inst. and Meth. A*, **2016**, *833*, 181-185.

[17] "Elliptic flow of identified hadrons in Au+Au collisions at $\sqrt{s_{\mathrm{NN}}} = 7.7$-$62.4\,\mathrm{GeV}$", L. Adamczyk *et al.* (STAR Collaboration), *Phys. Rev. C*, **2013**, *88*, 014902.

5.7 Appendix

5.7.1 Input parameter for AMPT model

Value	Parameter
193	EFRM ($\sqrt{s_{\mathrm{NN}}}$ in GeV if FRAME is CMS)
CMS	FRAME
A	PROJ
A	TARG
238	IAP (projectile A number)
92	IZP (projectile Z number)
238	IAT (target A number)
92	IZT (target Z number)
1000	NEVNT (total number of events)
0.	BMIN (minimum impact parameter in fm)
15.	BMAX (maximum impact parameter in fm)
4	ISOFT (D=1): select Default AMPT or String Melting(4)
150	NTMAX: number of timesteps (D=150)
0.2	DT: time step in fm (hadron cascade time= DT*NTMAX) (D=0.2)
2.2	PARJ(41): parameter a in Lund symmetric splitting function
0.5	PARJ(42): parameter b in Lund symmetric splitting function
1	(D=1,yes;0,no) flag for popcorn mechanism(net baryon stopping)
1.0	PARJ(5) to control BMBbar vs BBbar in popcorn (D=1.0)
1	shadowing flag (Default=1,yes; 0,no)
0	quenching flag (D=0,no; 1,yes)
2.0	quenching parameter -dE/dx (GeV/fm) in case quenching flag=1
2.0	p0 cutoff in HIJING for minijet productions (D=2.0)
1.8d0	parton screening mass in fm^{-1} (D=3.2264d0)
0	IZPC: (D=0 forward-angle parton scatterings; 100,isotropic)
0.47d0	alpha in parton cascade
1d6	dpcoal in GeV
1d6	drcoal in fm
11	ihjsed: take HIJING seed from below (D=0) or at run time(11)
53153511	random seed for HIJING
8	random seed for parton cascade

0	flag for K_s^0 weak decays (D=0,no; 1,yes)
1	flag for ϕ decays at end of hadron cascade (D=1,yes; 0,no)
1	flag for π^0 decays at end of hadron cascade (D=0,no; 1,yes)
0	optional OSCAR output (D=0,no; 1,yes; 2 and 3,more parton info)
0	flag for perturbative deuteron calculation (D=0,no; 1 or 2,yes)
1	integer factor for perturbative deuterons(≥ 1 and ≤ 10000)
1	choice of cross section assumptions for deuteron reactions
-7.	Pt in GeV: generate events with ≥ 1 minijet above this value
1000	maxmiss (D=1000): maximum no. of tries to repeat a HIJING event
3	flag to turn off initial and final state radiation (D=3)
1	flag to turn off Kt kick (D=1)
0	flag to turn on quark pair embedding (D=0,no; 1,yes)
7., 0.	Initial Px and Py values (GeV) of the embedded quark (u or d)
0., 0.	Initial x and y values (fm) of the embedded back-to-back q/qbar
1, 5., 0.	nsembd(D=0), psembd (in GeV),tmaxembd (in radian).
0	Flag to enable users to modify shadowing (D=0,no; 1,yes)
1.d0	Factor used to modify nuclear shadowing
0	Flag for random orientation of reaction plane (D=0,no; 1,yes)

5.7.2 Event plane resolution from AMPT model

Table 5.2: Event plane resolution for η-sub event method in U+U collisions at $\sqrt{s_{\mathrm{NN}}} = 193$ GeV.

Centrality	Resolution ($< R >$)
0-5%	0.6093 ± 0.0007
5-10%	0.6442 ± 0.0007
10-20%	0.7059 ± 0.0009
20-30%	0.7236 ± 0.0009
30-40%	0.6808 ± 0.0010
40-50%	0.5691 ± 0.0012
50-60%	0.4026 ± 0.0014
60-70%	0.2149 ± 0.0015
70-80%	0.0792 ± 0.0015

Chapter 6

Study of initial conditions in heavy-ion collisions

6.1 Introduction

Initial state is one of the least understood topic in the field of heavy-ion collisions. A precise knowledge of initial state is required in order to extract the properties of the medium created in relativistic heavy-ion collisions like values of transport coefficients. Also, it is required to preform sensitive test of the theoretical framework, e.g. relativistic viscous hydrodynamics, which correctly describes the evolution of the strongly interacting QGP matter produced in heavy-ion collisions experiments. In the Refs. [1–4], it has been shown that depending on the choice of initial conditions used to evolve relativistic hydrodynamics equations, the value of extracted shear viscosity to entropy density (η/s) in Au+Au collisions at 200 GeV at RHIC can vary by a factor of 2.

Unlike p+p collisions, the nuclei used in heavy-ion collisions experiments are extended objects. This results in event-by-event quantum fluctuations in positions of

the nucleons (in nuclear distribution function) in addition to the geometric fluctuations. The geometry of the nuclei in heavy-ion collisions have various characteristics of the initial state, e.g. number of participant nucleons N_{part}, number of binary collisions N_{coll}, shape of the overlap region (eccentricity ε_2) etc. All of these quantities are correlated with the impact parameter (b). However, in experiments impact parameter is unknown, therefore none of the above initial state quantities are directly observed.

The standard technique of characterising heavy-ion collision events into different centrality classes are obtained from the final state charged particle multiplicity (as shown in Chapter 3 and 4) correspond to different initial states. This averages out the various initial configurations and restricts the study to only a limited range of initial conditions. The event-by-event geometric and quantum fluctuations in the initial conditions result in appreciable variation of b, N_{part}, N_{coll} and ε_2, even within a same centrality class. Thus, a lack of proper knowledge of initial state makes the job of precise comparisons between theory and experiments very challenging.

In this analysis, we propose a new method for binning heavy-ion collision events in terms of total spectator neutrons along with the centrality bins. This will help us to probe events with broader range of initial conditions and provide us opportunity to analyse events with rare initial conditions which otherwise get masked when analysed by centrality binning alone. The significant role played by the spectator asymmetry in the various experimental observables and the possibility of selecting specific initial configurations in heavy-ion collisions using deformed Uranium nuclei has been shown in the Refs. [5,6]. In these refs., using Monte Carlo Glauber [7] and AMPT model [8], it has been suggested that spectator asymmetry can be used to select specific collision configurations called Body-Tip with sufficient magnetic field and much lower anisotropic flow which can lead to the disentanglement of chiral magnetic effect from its dominant background anisotropic flow in U+U collisions (details in Chapter 5).

In this chapter, we focused on probing heavy-ion collisions with non-deformed nuclei using spectators. We analysed $\sim 2 \times 10^6$ events of Pb+Pb collisions at $\sqrt{s_{\text{NN}}}$ = 2.76 TeV generated using heavy-ion collisions model AMPT in the default version. We constructed an initial state observable, the total spectator neutron $(L+R)$, which is the sum of the left going (L) and right going (R) spectator neutrons that can be detected by the Zero Degree Calorimeters (ZDCs) in the experiment. Here, we have proposed an additional binning in terms of the $L+R$ along with the standard centrality bins in Pb+Pb collisions at $\sqrt{s_{\text{NN}}} = 2.76$ TeV using AMPT model and obtained results with this new binning procedure. We show that by performing a further binning over $L+R$ in addition to the standard centrality binning, it is possible to probe the medium with novel initial state conditions as compared to the centrality binning alone. In the following section, we discuss the details of our proposed method of binning events in AMPT model.

6.2   Event selection method

The standard technique to categorise heavy-ion collision events into different centrality classes is according to charged particle multiplicity. Figure 6.1(a), shows the standard centrality binning, in which different centrality classes (0-5%, 5-10% etc.) are shown as alternate white and grey bands. In our method, we have proposed a second round of binning with the total spectator neutron number $L + R$ within each centrality class. An illustration of $L + R$ binning in one centrality class (10-15%) is shown in the Fig. 6.1(b). The distribution of $L + R$ in the figure shows a prominent peak around $85 - 95$ and then falls off rapidly on either side. The number of events drops by a factor of 5 as $L + R$ shifts by ~ 20. This shows that when the analysis is performed with centrality binning alone, we mainly study properties of the events

with $L + R$ around $85 - 95$. Introduction of the new $L + R$ binning gives us opportunity to study properties of the rare events with both fewer and higher values of $L + R$ compared to the mean value in centrality binning. This is the justification to introduce the additional $L + R$ binning on top of the centrality to study the new initial conditions in heavy-ion collisions.
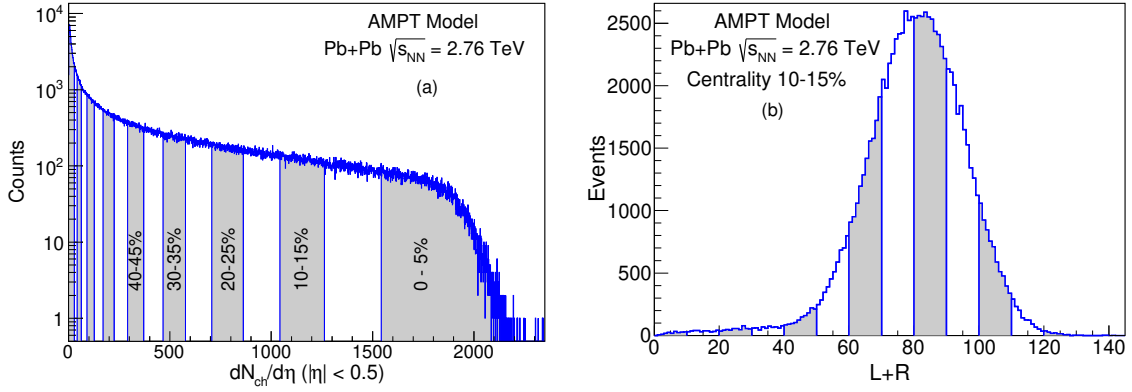
Figure 6.1: Left panel: The multiplicity distribution for minimum bias Pb+Pb collisions at $\sqrt{s_{\mathrm{NN}}} = 2.76$ TeV. Different centrality bins are shown by the alternate white and grey bands. Right panel: The total spectator neutron number $L + R$ distribution in a given centrality class (10-15% centrality). The different $L + R$ bins are also shown by the alternate white and grey bands.
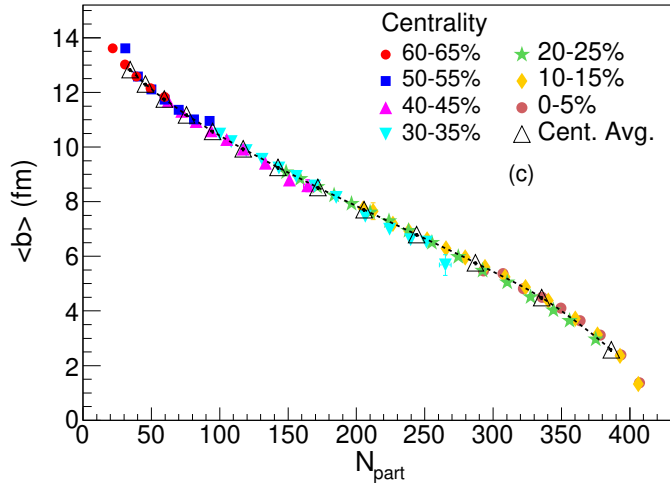
Figure 6.2: The impact parameter b as a function of N_{part} for different centrality classes (open triangle) and $L + R$ bins (color markers) in Pb+Pb collisions at $\sqrt{s_{\mathrm{NN}}} = 2.76$ TeV from AMPT model.

Figure 6.2 shows the variation of impact parameter (b) with N_{part}. We found that the centrality and $L + R$ bins follow the same trend, which shows that the observable $L + R$ is equally good for the study of initial and final state effects. In the next sections we have shown various other initial state attributes of heavy-ion collisions with the new $L + R$ binning and the results of translation of these initial states into different final state observables.

6.3 Initial state geometry

We defined a plane called collision plane which is the plane transverse to the collision axis. The distribution of participant nucleons in the collision plane gives the idea of the initial size of the fireball created at the time of the collision. Due to the event-by event fluctuations in the positions of participant nucleons the principal axis of inertia of participants (P) is shifted as well as rotated with respect to the nucleus-nucleus (N) system [9]. Hence, we first perform the necessary translation as,

$$x' = x_N - \langle x_N \rangle$$

$$y' = y_N - \langle y_N \rangle, \tag{6.1}$$

where $(x_N,\, y_N)$ denote the co-ordinates of nucleons in the N system and $\langle x_N \rangle$, $\langle y_N \rangle$ are the event averaged values. After the shifting, we further rotate the primed co-ordinate system by the second order participant plane angle (ψ_2^{pp}) so as to coincide the N system with the P system. The ψ_2^{pp} is defined as,

$$\varepsilon_n e^{i\psi_n^{pp}} = \frac{\sum_i r_i'^n e^{in\phi_i'}}{\sum_i r_i'^n}, \tag{6.2}$$

where (r'_i, ϕ'_i) is the shifted co-ordinates of the ith participant in the polar co-ordinate system and $n = 2$ for ψ_2^{pp}. The initial overlap geometry is encoded in the eccentricities ε_n defined the in Eq. 6.2.
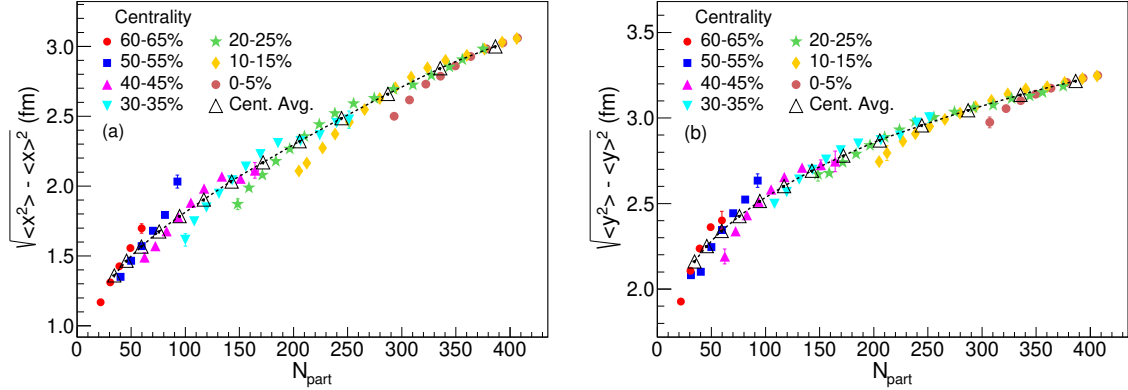
Figure 6.3: Standard deviations σ_x, σ_y of participant positions as a function of N_{part} with centrality and $L + R$ bins in Pb+Pb collisions at $\sqrt{s_{\mathrm{NN}}} = 2.76$ TeV using AMPT model. Error bars shown are the statistical uncertainties.

Figure 6.3(a) and (b), shows the average of standard deviations in the x_P and y_P co-ordinates of the participants measured with respect to the P co-ordinate system. where standard deviations σ_x and σ_y are defined as,

$$\sigma_x = \sqrt{\langle x_P^2 \rangle - \langle x_P \rangle^2}$$
$$\sigma_y = \sqrt{\langle y_P^2 \rangle - \langle y_P \rangle^2}. \tag{6.3}$$

The results from centrality binning alone are shown by the open triangles joined by a dotted line. Here we propose to further bin each centrality into different $L + R$ spectator bins as well, which are shown by the colored symbols, each color corresponds to a definite centrality bin. In the Fig. 6.3, σ_x and σ_y vs. N_{part} show different correlations along centrality and $L + R$ bins. They both decrease more rapidly along $L + R$ bins than the centrality bins. σ_x and σ_y gives us an idea of the initial size of the fireball on the collision plane at the time of collision.

246
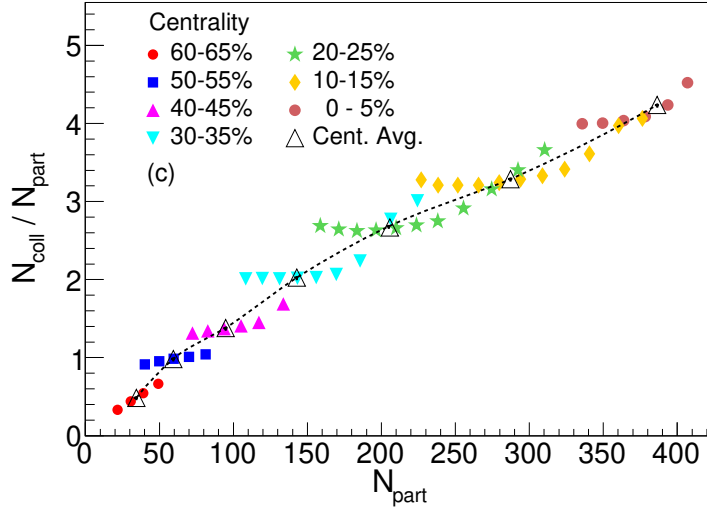
Figure 6.4: Number of binary collisions scaled by N_{part} (N_{coll}/N_{part}) as a function of N_{part} with centrality and $L + R$ bins in Pb+Pb collisions at $\sqrt{s_{NN}} = 2.76$ TeV using AMPT model. Error bars shown are the statistical uncertainties (within marker size).

In a two component Glauber model, initial conditions and particle production are based on the geometry of heavy-ion collisions. The observables N_{part} and N_{coll} are the two essential ingredients that determine the initial states and final state multiplicity [7]. A collision between two nucleons (one from each nucleus) with co-ordinates (x_A, y_A) and (x_B, y_B) is modeled by the following simple geometrical criteria,

$$(x_A - x_B)^2 + (y_A - y_B)^2 \leq \frac{\sigma_{NN}}{\pi}, \tag{6.4}$$

where σ_{NN} is the nucleon-nucleon cross-section. N_{part} is the sum of all the nucleons that satisfy the Eq. 6.4. Where as N_{coll} is the sum of all such possible binary collisions between the participant nucleons. The distribution of participants on the collision plane determine the initial state eccentricities given by the Eq. 6.2. In Fig. 6.4, N_{coll} normalised to N_{part} is shown with centrality and $L+R$ binning. The values of N_{coll} are larger for $L + R$ bins of higher centrality compared to a lower centrality, which is the effect of σ_x and σ_y values from Fig. 6.3. As seen from Fig. 6.3 (a) and (b), bins with

247

same N_{part} but higher centrality occupy a smaller area on the collision plane implied by the smaller values of σ_x and σ_y. This suggests that the participating nucleons are more aligned along the beam direction than perpendicular to it. Therefore, the values of N_{coll} are higher for $L + R$ bins with smaller σ_x and σ_y.
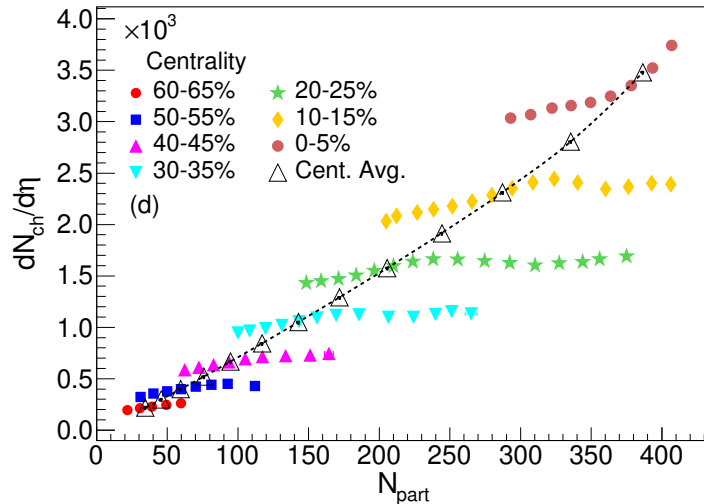
Figure 6.5: Charged particle multiplicity $dN_{\text{ch}}/d\eta$ as a function of N_{part} with centrality and $L + R$ bins in Pb+Pb collisions at $\sqrt{s_{\text{NN}}} = 2.76$ TeV using AMPT model.

Figure 6.5 shows $dN_{\text{ch}}/d\eta$ vs. N_{part} with centrality and $L + R$ bins in Pb+Pb collisions at $\sqrt{s_{\text{NN}}} = 2.76$ TeV using AMPT model. The correlation between $dN_{\text{ch}}/d\eta$ and N_{part} along centrality bins is very different than along $L + R$ bins. For a given centrality bin N_{part} decreases as $L + R$ increases, however $dN_{\text{ch}}/d\eta$ almost remains constant which implies that the initial energy deposition is same even though N_{part} decreases. This suggests that the energy deposition pattern changes from lower to higher $L + R$ bins in a given centrality. We expect larger energy gradients as the same energy is deposited over a smaller transverse area by lesser N_{part}. This would result in very different viscous effects as we analyse bins with varying $L + R$ at a given centrality in relativistic heavy-ion collisions. Such a viscosity driven effect of initial states can be best observed by the final state observable like azimuthal anisotropic flow.

6.4 Effects of initial state on final state observables

The collective hydrodynamic response converts the initial spatial anisotropy of the fireball as reflected by ε_n into the final state azimuthal anisotropy of the produced particles in momentum space. The azimuthal anisotropy is characterised by the Fourier coefficients (v_n) with respect to the event plane angle (ψ_n^{EP}). The flow observables (v_n, ψ_n^{EP}) are measured as,

$$
\begin{aligned}
\frac{dN}{d\phi} &\propto 1 + 2\sum_{n=1}^{\infty} v_n \cos\left(n\left(\phi - \psi_n^{EP}\right)\right) \\
&= 1 + 2\sum_{n=1}^{\infty}\left(v_{nx}\cos(n\phi) + v_{ny}\sin(n\phi)\right)
\end{aligned}
\tag{6.5}
$$

$$
Q_{nx} = \sum_{i=1}^{M} w_i \cos(n\phi_i), \quad Q_{ny} = \sum_{i=1}^{M} w_i \sin(n\phi_i)
\tag{6.6}
$$

$$
v_{nx} = \frac{Q_{nx}}{M}, \quad v_{ny} = \frac{Q_{ny}}{M}, \quad v_n = \sqrt{v_{nx}^2 + v_{ny}^2},
\tag{6.7}
$$

where ϕ_i is the azimuthal angle of the ith particle, M is the total number of particles. ψ_n^{EP} is the event plane angle, measured using the produced particles [10]. w_i are the weights, which we have taken as unity.

The effects of initial event shape on the fireball dynamics and various final state observables in heavy-ion collisions have been studied previously in the Refs. [11, 12]. Here in this analysis, we have focused our attention on the event shape, how to tune initial state geometry using control parameter spectators $L + R$ binning.

Figure 6.6 shows the variation of initial state observables $(\varepsilon_2, \varepsilon_3)$ and corresponding final state observables (v_2, v_3) with N_{part} in Pb+Pb collisions at $\sqrt{s_{\text{NN}}} = 2.76$ GeV using AMPT model. From Figs. 6.6 (a) and (c) it is clear that the ε_2 and ε_3 can
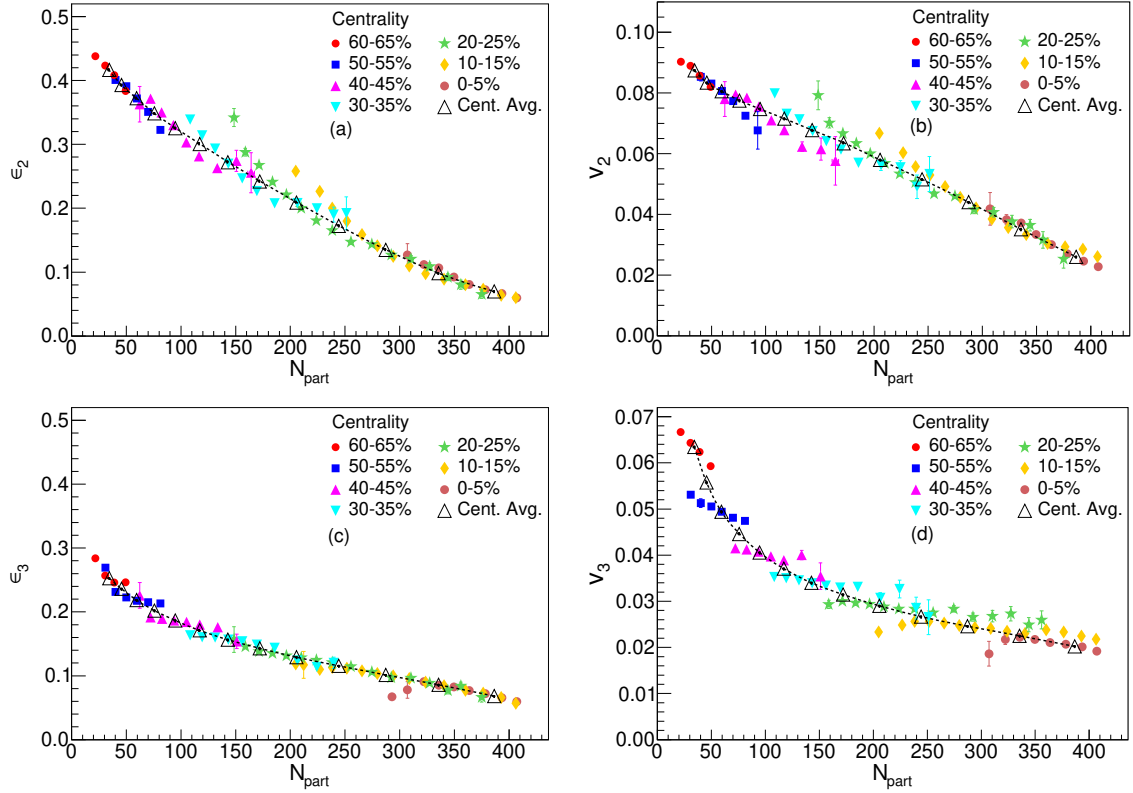
Figure 6.6: Dependence of various quantities ε_2, ε_3, v_2 and v_3 with centrality and $L + R$ bins in Pb+Pb collisions at $\sqrt{s_{\text{NN}}} = 2.76$ TeV using AMPT model. Error bars shown are the statistical uncertainties.

be tuned by different $L + R$ bins within a particular centrality bin. This shows that binning spectators allow us a direct access to the event shape in heavy-ion collisions. For central events, ε_2 and ε_3 show almost similar variation along centrality and $L + R$ bins. Starting from 20-25% centrality bin, for mid-central to peripheral events, the correlation between ε_2 and N_{part} along spectator bins is sightly steeper compared to the centrality bins. On the other hand, ε_3 correlation with N_{part} is gentler along spectator bins. This difference in variation of ε_2 and ε_3 along $L + R$ bins compared to centrality bin alone is more clearly visible in the final state flow observables.

In Figs. 6.6 (b) and (d), variation of v_2 and v_3 with N_{part} is shown. It can be seen from the figure that the $L + R$ bins preserve the usual linear relation between (ε_2, ε_3) and (v_2, v_3). This study of effects of initial event shape using $L + R$ bins on various

final state observables is similar to what is done using q_2 bins in the Refs. [11, 12], where q_2 is obtained from the second order flow vector Q_2 [10, 11],

$$Q_2 = \sqrt{Q_{2x}^2 + Q_{2y}^2}, \quad q_2 = \frac{Q_2}{\sqrt{M}}. \tag{6.8}$$

Here it is important to note that the Q_{2x} and Q_{2y} are computed using particles produced in the final state. Therefore, unlike the q_2 binning procedure, in our method of studying initial state through $L + R$ bins the linear relationship between $(\varepsilon_2, \varepsilon_3)$ and (v_2, v_3) is not essential as the spectators, being initial state observables, provide a direct access to the initial state geometry.
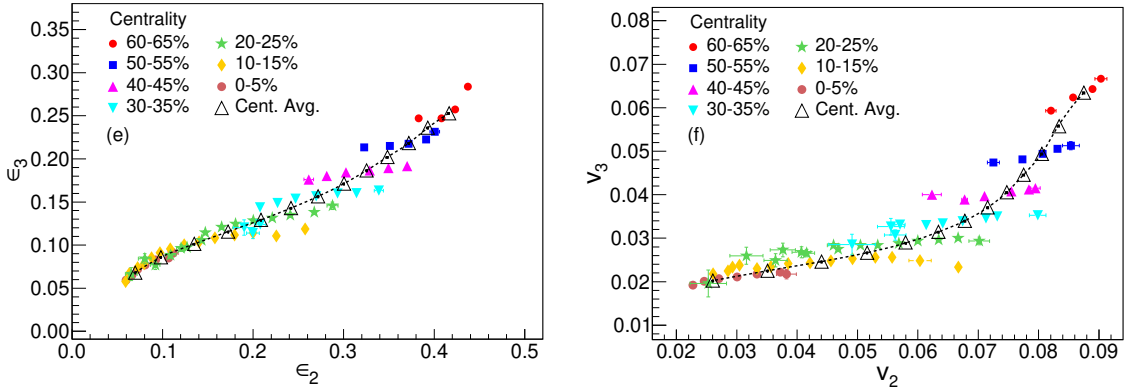
Figure 6.7: Correlation between ε_2 and ε_3 (Left panel), between v_2 and v_3 (Right panel) with centrality and $L + R$ bins in Pb+Pb collisions at $\sqrt{s_{\mathrm{NN}}} = 2.76$ TeV using AMPT model.

Figure 6.7 shows the correlations $\varepsilon_2 - \varepsilon_3$ and $v_2 - v_3$ with centrality and $L + R$ bins. The new $L + R$ binning allow us to access novel geometries in terms of $(\varepsilon_2, \varepsilon_3)$ pairs, which cannot be accessible in centrality binning alone. Since the correlations along spectator bins are quite different than the centrality average bins, they cannot be accessed even if one tries to perform a narrower centrality binning alone. For 20-25% and more peripheral bins the correlation is much smaller along $L + R$ bins compared to that centrality bins. For example, while the value of v_3 changes by only

10% for different $L+R$ bins, v_2 varies by $\sim$130%. This will allow us to disentangle the effects of v_2 from v_3 on other observables like the non-linear mode couplings during the hydrodynamic expansion that result in correlations $v_2 - v_4$ and $v_2, v_3 - v_5$ [13, 14]. Thus, it will be interesting to look at correlation plots of (v_2, v_4), (v_2, v_5) and (v_3, v_5) in experimental data with combined binning in $dN_{ch}/d\eta$ and $L + R$ bins.

In this regards, we have discussed two cases, (a) N_{part} and N_{coll} and their contribution towards final state $dN_{ch}/d\eta$ and (b) ε_2 and ε_3 and their contribution towards v_2 and v_3 respectively. In Fig. 6.8 we show the correlation between $N_{\mathrm{coll}}/N_{\mathrm{part}}$ with ε_2 and ε_3. Thus we can now study the evolution of similar initial geometry (ε_2, ε_3) but with different mechanism of energy deposition ($N_{\mathrm{coll}}/N_{\mathrm{part}}$) by the introduction of $L + R$ bins.
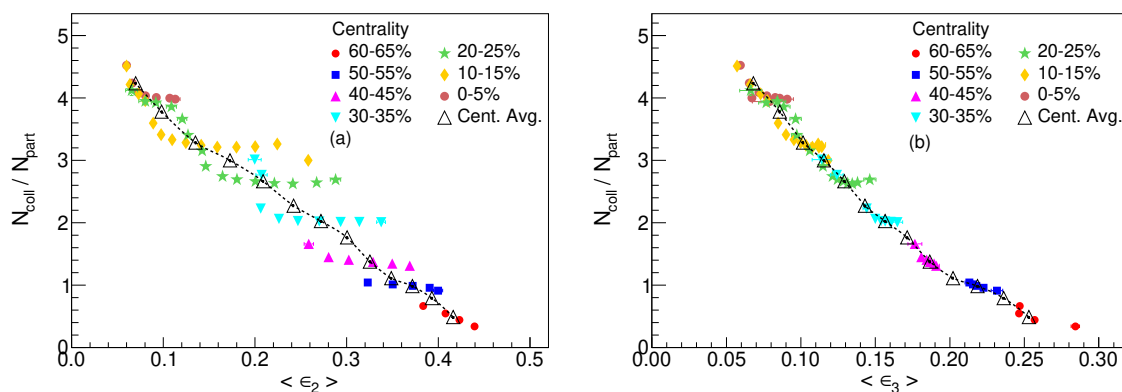
Figure 6.8: Correlation between $\varepsilon_2 - N_{\mathrm{coll}}/N_{\mathrm{part}}$ (Left panel) and $\varepsilon_3 - N_{\mathrm{coll}}/N_{\mathrm{part}}$ (Right panel) with centrality and $L+R$ bins in Pb+Pb collisions at $\sqrt{s_{\mathrm{NN}}} = 2.76$ TeV using AMPT model. Error bars shown are the statistical uncertainties.

6.5 Results and Discussions

6.5.1 Eccentricity scaling of v_2

Ideal fluid hydrodynamics is scale invariant. As a result the ratio of v_2/ε_2 is independent of the system size [15]. Viscous corrections in a non-ideal fluid arising due to the incomplete thermalization introduce system size dependence and tend to reduce the v_2/ε_2 ratio. The ratio of the microscopic mean free path λ to the macroscopic system size Λ, λ/Λ is known as the *Knudsen number K*. Inverse of K (K^{-1}) is expected to be a good measure of the thermalization achieved in relativistic heavy-ion collisions [1, 15].

The azimuthal anisotropy develops during the rapid expansion of the fireball but it is not exactly clear what should be the value of λ and Λ to be used to determine the degree of thermalization. In preivous studies, it has been pointed out that v_2 dominantly develops in the early stages of the fireball evolution. Therefore K^{-1} estimated at time $\tau \sim \Lambda_T/c_S$ at the onset of transverse expansion of the fireball, should be used as a measure of thermailzation [1, 15]. Where Λ_T is the transverse size of the fireball on the collision plane and c_s is the speed of sound. It has also been suggested that K^{-1} at time Λ_T/c_S approximately scales with the $(1/S)dN_{ch}/d\eta$, where S is the initial transverse area on the collision plane. Similar scaling relation between v_2/ε_2 and $(1/S)dN_{ch}/d\eta$ is also expected in the low density regime [16–18].

Previous analysis of experimental data with centrality binning have indeed found very good scaling relation between v_2/ε_2 and $(1/S)dN_{ch}/d\eta$ for different systems like Cu+Cu and Au+Au [1–3]. The detailed mechanism of energy deposition in the initial stages of heavy-ion collisions which ultimately leads to particle production is yet to be understood completely. It is difficult to discriminate between predictions from

models with different mechanisms of particle production with centrality as the only tuning parameter to separate different initial conditions. Now, with the introduction of $L + R$ bins, we are able to pin down the initial conditions more precisely.
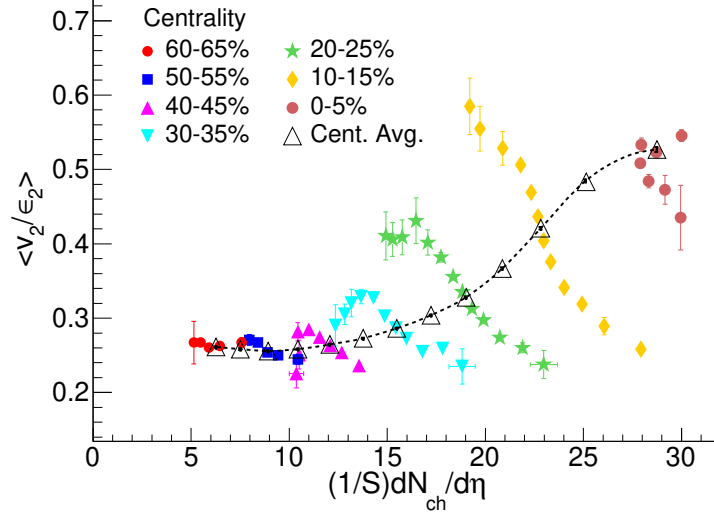
Figure 6.9: v_2/ε_2 vs. $(1/S)dN_{ch}/d\eta$ for different centrality and $L + R$ bins in Pb+Pb collisions at $\sqrt{s_{\mathrm{NN}}} = 2.76$ TeV using AMPT model. The $L + R$ bins break the scaling relation between v_2/ε_2 and $(1/S)dN_{ch}/d\eta$ that is exhibited by centrality bins.

Figure 6.9 shows the ratio v_2/ε_2 as a function of $(1/S)dN_{ch}/d\eta$ for different centrality and $L + R$ bins. The centrality averaged points (open triangles) exhibit the usual trend of an initial fast rise and final saturation of the ratio v_2/ε_2 with $(1/S)dN_{ch}/d\eta$. However, the $L+R$ bins (filled color markers) in each centrality show the opposite behaviour and breaks the usual scaling relation. For a given centrality, with increase in $L + R$, the transverse overlap area S falls sharply while $dN_{ch}/d\eta$ remains almost constant. Thus $(1/S)dN_{ch}/d\eta$ which is a proxy for K^{-1} increases with $L + R$ although the hydrodynamic response v_2/ε_2 falls sharply. This suggests more (less) hot spots and gradients in the initial energy profile of events with larger (smaller) $L+R$, which leads to more (less) viscous correction. The breaking of scaling also suggests the inefficient conversion of the initial ε_n to the final v_n in the events with larger $L + R$ as compared to events with smaller $L + R$ bin.

6.5.2 Acoustic scaling of v_2

The ratio of v_n/ε_n is expected to exhibit acoustic scaling and receives viscous corrections that grow exponentially as n^2 and $1/\Lambda_T$ [19–22]

$$\ln\left(\frac{v_n}{\varepsilon_n}\right) \propto -\frac{4}{3}\frac{n^2\eta}{\Lambda_T T s}, \tag{6.9}$$

where the initial transverse size of the system Λ_T is given by $1/\Lambda_T = \sqrt{1/\sigma_x^2 + 1/\sigma_y^2}$. The acoustic scaling was found in experimental data across a wide range of beam energies and the shear viscosity to entropy density ratio η/s was extracted from the slope of the plot, $\ln\left(\frac{v_2}{\varepsilon_2}\right)$ vs. $1/\Lambda_T$ [20–22]. In all these refs., the scaling is studied with centrality binning alone. In this analysis, we studied this scaling using simulation data by including $L + R$ bins in every centrality bin.
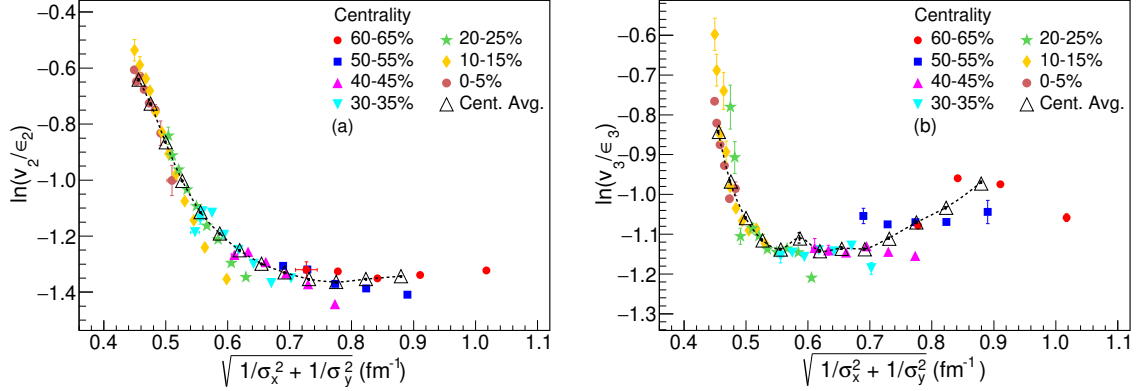
Figure 6.10: Acoustic scaling of the hydrodynamic response $\ln(v_n/\varepsilon_n)$ vs. $1/\Lambda_T$ with $n = 2$ (Left panel) and $n = 3$ (Right panel) for different centrality and $L + R$ bins in Pb+Pb collisions at $\sqrt{s_{NN}} = 2.76$ TeV using AMPT model. Error bars shown are the statistical uncertainties.

Figure 6.10 shows the scaling $\ln(v_2/\varepsilon_2)$ and $\ln(v_3/\varepsilon_3)$ vs. $1/\Lambda_T$ for Pb+Pb collisions at $\sqrt{s_{NN}} = 2.76$ TeV using AMPT model data. We found that the scaling law from Eq. 6.9 approximately holds for (0-40%) centrality as well as their corresponding $L + R$ bins. On a careful observation, it seems that the slope parameter for bins

of different $L + R$ of a particular centrality is different from the slope of different centrality resulting in a mild breaking of the acoustic scaling. Thus, the introduction of the $L + R$ bins enable a more refined extraction of η/s from data.

6.5.3 Reverse binning procedure for consistency

In the previous sections, we have discussed results for events first binned by the charged particle multiplicity ($dN_{\mathrm{ch}}/d\eta$) followed by spectators ($L + R$). If collision geometry (i.e. impact parameter b) was the only event-by-event fluctuating quantity, then b, $dN_{\mathrm{ch}}/d\eta$ and $L+R$ would have a one to one correspondence and hence the final results would be independent of the order of binning procedure. However, as discussed above, in heavy-ion collisions there are additional event-by-event fluctuations apart from the geometrical fluctuation in impact parameter. This means the final results are sensitive to the order of the binning procedure. In order to illustrate this point, we have also analysed the events in the reverse binning procedure: first we bin by $L + R$ followed by $dN_{\mathrm{ch}}/d\eta$.
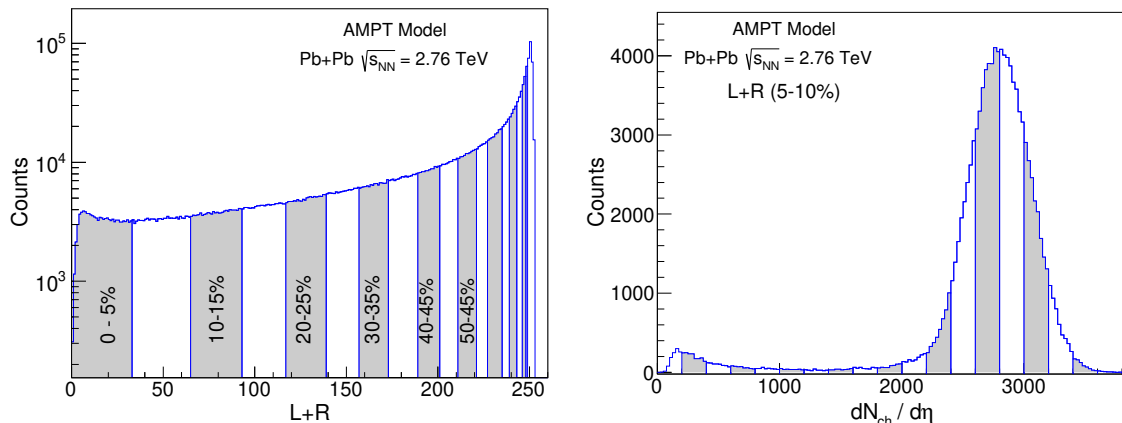
Figure 6.11: Left panel: The total spectator neutron number $L + R$ distribution for minimum bias Pb+Pb collisions at $\sqrt{s_{\mathrm{NN}}} = 2.76$ TeV. Different $L + R$ bins are shown by the alternate white and grey bands. Right panel: The multiplicity distribution in a given $L + R$ bin (5-10%). The different multiplicity bins are also shown by the alternate white and grey bands.

256
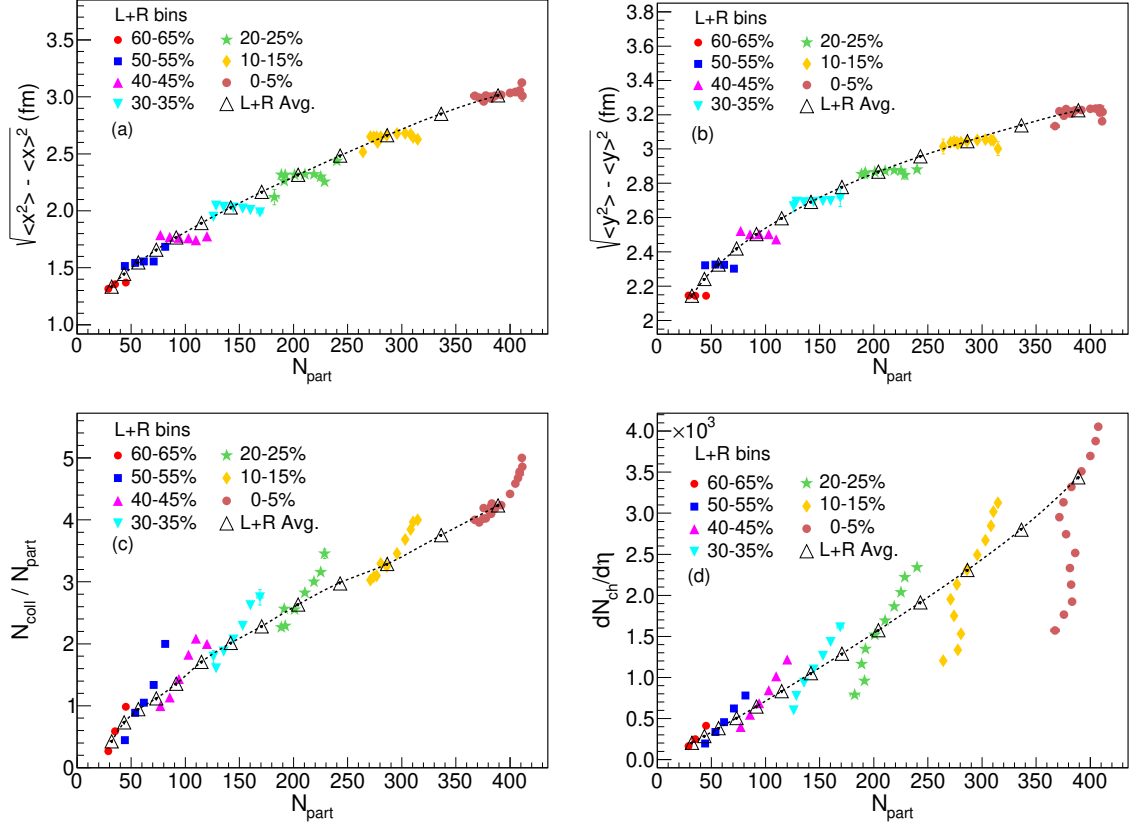
Figure 6.12: Standard deviations σ_x, σ_y, N_{coll}/N_{part} and $dN_{ch}/d\eta$ as a function of N_{part} with reverse binning procedure in Pb+Pb collisions at $\sqrt{s_{NN}} = 2.76$ TeV using AMPT model.

Figure 6.12 (a) and (b) show the standard deviations σ_x, σ_y of participant positions as a function of N_{part} with reverse binning procedure in Pb+Pb collisions at $\sqrt{s_{NN}} = 2.76$ TeV using AMPT model. σ_x and σ_y which are the measures of initial system size, almost remain constant in a particular $L + R$ bin while N_{part} changes. This results in the strong variation of N_{coll}/N_{part} within a $L + R$ bin as shown in Fig. 6.12 (c). The variation of N_{coll}/N_{part} finally translates into a stronger variation in $dN_{ch}/d\eta$ within a $L + R$ bin with N_{part} compared to different $L + R$ bins.

Figure 6.13 (a) shows the result of eccentricity scaled v_2 (v_2/ε_2) as a function of $(1/S)dN_{ch}/d\eta$ with the reverse binning procedure in Pb+Pb collisions at $\sqrt{s_{NN}} = 2.76$ TeV using AMPT model. Within a particular $L + R$ bin, the bins with higher
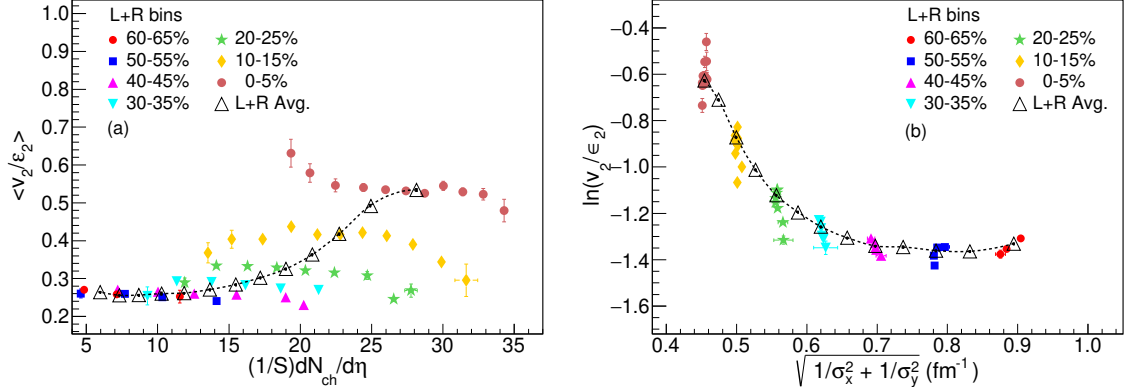
Figure 6.13: v_2/ε_2 vs. $(1/S)dN_{\mathrm{ch}}/d\eta$ and $1/\Lambda_T$ with the reverse binning procedure (first binned by $L+R$ followed by $dN_{\mathrm{ch}}/d\eta$) in Pb+Pb collisions at $\sqrt{s_{\mathrm{NN}}} = 2.76$ TeV using AMPT model. Error bars shown are the statistical uncertainties.

$(1/S)dN_{\mathrm{ch}}/d\eta$ have higher $N_{\mathrm{coll}}/N_{\mathrm{part}}$ ratio than the average resulting in smaller v_2/ε_2 compared to the $L+R$ averaged trend. This trend of breaking of eccentricity scaling is similar to the earlier binning procedure. In Fig. 6.13 (b), the acoustic scaling relation given in Eq. 6.9 does not hold anymore as the slope along different $dN_{\mathrm{ch}}/d\eta$ bins in a given $L+R$ bin is quite different than the average $L+R$. Thus the breaking of acoustic scaling relation which was mild in the earlier binning procedure becomes much more stronger in the reverse binning procedure.

6.5.4   Calculations with HIJING model

So far we have shown results from the AMPT model for the combined binning procedure with $dN_{\mathrm{ch}}/d\eta$ followed by $L+R$ bin. In this section, we show the results for the combined binning from HIJING model [23] in Pb+Pb collisions at $\sqrt{s_{\mathrm{NN}}} = 2.76$ TeV. AMPT model takes into account later stage interactions in the partonic as well as hadronic phases while in HIJING model such interactions are absent.

In Fig. 6.14 we show the results for impact parameter b and charged particle multiplicity $dN_{\mathrm{ch}}/d\eta$ as a function of N_{part} with our new binning procedure. We
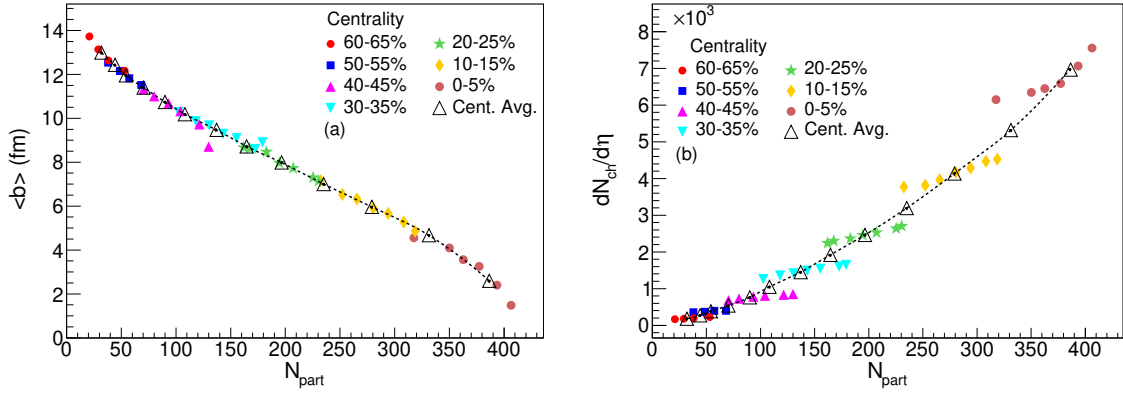
Figure 6.14: Impact parameter b and charged particle multiplicity $dN_{ch}/d\eta$ variation with N_{part} with combined binning procedure as obtained from HIJING model in Pb+Pb collisions at $\sqrt{s_{NN}} = 2.76$ TeV. Error bars shown are the statistical uncertainties.

found that the variation of b and $dN_{ch}/d\eta$ are very similar to what we obtained in the case of AMPT model in Fig. 6.2 and Fig. 6.5.
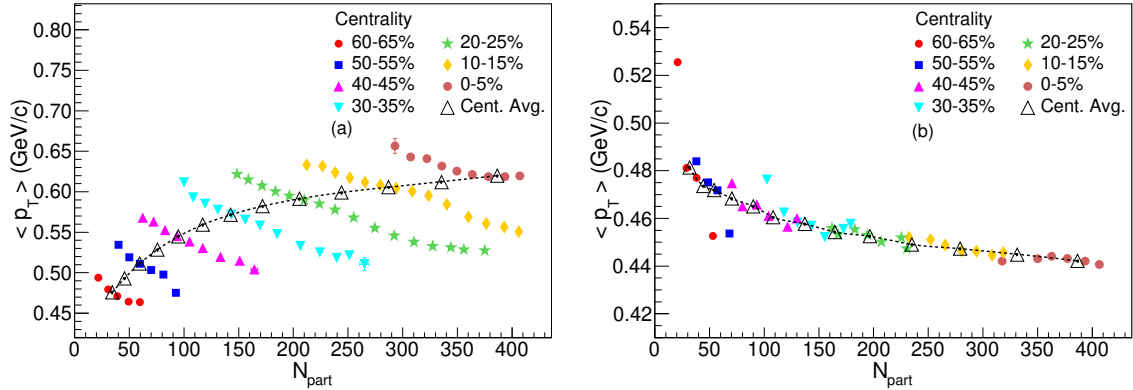
Figure 6.15: Mean p_T as a function of N_{part} with combined binning procedure as obtained from AMPT (a) and HIJING (b) model in Pb+Pb collisions at $\sqrt{s_{NN}} = 2.76$ TeV. Error bars shown are the statistical uncertainties.

Figure 6.15 shows the results for $\langle p_T \rangle$ with N_{part} from AMPT model in Pb+Pb collisions at $\sqrt{s_{NN}} = 2.76$ TeV compared to HIJING model. $\langle p_T \rangle$ variation with N_{part} along $L + R$ bins is very different to that of the average trend along the different centrality bins. For a given centrality bin, the variation of $\langle p_T \rangle$ is about 10-15% for different $L + R$ bins. On the other hand, in HIJING model the $\langle p_T \rangle$ does not depend

on the binning procedure. The trend of $\langle p_T \rangle$ values along $L + R$ bins is similar to centrality average values. We conclude that this different in $\langle p_T \rangle$ from two cases should be stemming from the fact that medium effects which are taken into account into AMPT are missing in HIJING model. In different $L + R$ bins there is different degree of medium interactions and collectivity resulting in different values of the final $\langle p_T \rangle$. The observation of different values of v_2/ε_2 along different $L + R$ bins support the above conclusion as well. Thus the measurement of $\langle p_T \rangle$ with such a combined binning procedure can also be used to measure degree of collectivity achieved in relativistic heavy-ion collisions.

6.6   Summary

In this chapter, we demonstrated the important role played by the spectators to determine the initial condition in relativistic heavy-ion collisions using the data generated by the AMPT model. The standard technique to analyse events of heavy-ion collisions involves binning by their final state charged particle multiplicity. This procedure treats events with varying initial conditions as same if they produce similar multiplicity. In this analysis, we showed that by binning events according to the total number of spectator neutrons along with the multiplicity, it is possible to separate events with different initial conditions which were earlier clubbed together in the centrality binning only. This new method provides us an opportunity to study events with rare initial conditions.

We showed that it is possible to vary ε_2 and ε_3 independently of each other and hence enables one to extract the contribution due to non-linear mode coupling between v_2 and v_3, v_4 and v_5. Here it is important to note that for this purpose it is not essential to know $L + R$ very accurately. We found that the variation of

$dN_{\mathrm{ch}}/d\eta$ with N_{part} to be quite different for $L+R$ bins compared to usual centrality bins thus allowing us to study different energy deposition mechanism within the same centrality. In a given centrality bin, larger $L+R$ bins have higher energy gradients and more number of energy hot spots as compared to smaller $L+R$ bins which result in strong inhomogeneities in the initial conditions. This indicates larger viscosity driven effects and hence smaller v_2/ε_2 for bins with higher $L+R$. We also found the breaking of usual scaling relation between v_2/ε_2 and $1/SdN_{\mathrm{ch}}/d\eta$ with $L+R$ bins. A comparatively small breaking of the acoustic scaling relation between $\ln(v_n/\varepsilon_n)$ and initial system size $1/\Lambda_T$ is observed for both centrality as well as $L+R$ bins.

In summary, the results from this study suggest that one might be able to extract more accurate value of medium properties like η/s ratio with the introduction of spectator bins. We also observe that $\langle p_T \rangle$ in combined bins of $dN_{\mathrm{ch}}/d\eta$ and $L+R$ is a good way to measure the degree of medium interaction without a precise measurement of $L+R$. Finally, this new binning procedure can be used to analyse initial conditions with the current performance of ZDC detectors in high energy heavy-ion collision experiments.

Bibliography

[1] "Centrality dependence of elliptic flow, the hydrodynamic limit, and the viscosity of hot QCD", H. J. Drescher *et al.*, *Phys. Rev. C*, **2007**, *76*, 024905.

[2] "Viscosity Information from Relativistic Nuclear Collisions: How Perfect is the Fluid Observed at RHIC?", P. Romatschke, U. Romatschke, *Phys. Rev. Lett.*, **2007**, *99*, 172301;

"Conformal relativistic viscous hydrodynamics: Applications to RHIC results at $\sqrt{s_{\mathrm{NN}}} = 200$ GeV", M. Luzum, P. Romatschke, *Phys. Rev. C*, **2008**, *78*, 034915; "Erratum", M. Luzum, P. Romatschke, *Phys. Rev. C*, **2009**, *79*, 033903.

[3] "200A GeV Au+Au Collisions Serve a Nearly Perfect Quark-Gluon Liquid", H. Song *et al.*, *Phys. Rev. Lett.*, **2011**, *106*, 192301; "Erratum", H. Song, *et al.*, *Phys. Rev. Lett.*, **2012**, *109*, 139904.

[4] "Comparison of results from a (2+1)-D relativistic viscous hydrodynamic model to elliptic and hexadecapole flow of charged hadrons measured in Au-Au collisions at $\sqrt{s_{\mathrm{NN}}} = 200$ GeV", V. Roy, A. K. Chaudhuri, B. Mohanty, *Phys. Rev. C*, **2012**, *86*, 014902;

"Elliptic and Hexadecapole flow of charged hadron in viscous hydrodynamics with Glauber and Color Glass Condensate initial conditions for Pb-Pb collision

at $\sqrt{s_{\mathrm{NN}}} = 2.76$ TeV", V. Roy, B. Mohanty, A. K. Chaudhuri, *J. Phys. G*, **2013**, *40*, 065103.

[5] "Separation of flow from the chiral magnetic effect in U + U collisions using spectator asymmetry", S. Chatterjee and P. Tribedy, *Phys. Rev. C*, **2015**, *92*, 011902.

[6] "Selecting specific initial configurations using spectator neutrons in U + U collisions", V. Bairathi, M. R. Haque, B. Mohanty, *Phys. Rev. C*, **2015**, *91*, 054903.

[7] "Multiplicity Distributions in Nucleus-Nucleus Collisions at High-Energies", A. Bialas, M. Bleszynski, W. Czyz, *Nucl. Phys. B*, **1976**, *111*, 461-476;

"Energy and Centrality Dependence of Rapidity Densities at RHIC Energies", X. N. Wang, M. Gyulassy, *Phys. Rev. Lett.*, **2001**, *86*, 3496;

"Hadron production in nuclear collisions at RHIC and high density QCD", D. Kharzeev, M. Nardi, *Phys. Lett. B*, **2001**, *507*, 121-128.

[8] "Partonic effects on the elliptic flow at relativistic heavy ion collisions", Z. W. Lin and C. M. Ko, *Phys. Rev. C*, **2002**, *65*, 034904;

"Multiphase transport model for relativistic heavy ion collisions", Z. W. Lin *et al.*, *Phys. Rev. C*, **2005**, *72*, 064901;

"Pseudorapidity dependence of anisotropic flows in relativistic heavy-ion collisions", L. W. Chen *et al.*, *Phys. Lett. B*, **2005**, *605*, 95.

[9] "Eccentricity fluctuations and elliptic flow at RHIC", R. Bhalerao, J. Y. Ollitrault, *Phys. Lett. B*, **2006**, *641*, 260-264.

[10] "Methods for analyzing anisotropic flow in relativistic nuclear collisions", A. Poskanzer, S. Voloshin, *Phys. Rev. C*, **1998**, *58*, 1671.

[11] "Ultra-relativistic nuclear collisions: Event shape engineering", J. Schukraft, A. Timmins, S. Voloshin, *Phys. Lett. B*, **2013**, *719*, 394-398.

[12] "Elucidating the event-by-event flow fluctuations in heavy-ion collisions via the event-shape selection technique", P. Huo, J. Jia, S. Mohapatra, *Phys. Rev. C*, **2014**, *90*, 024910.

[13] "Mapping the hydrodynamic response to the initial geometry in heavy-ion collisions", F. G. Gardim *et al.*, *Phys. Rev. C*, **2012**, *85*, 024908;

"Nonlinearities in the harmonic spectrum of heavy ion collisions with ideal and viscous hydrodynamics", D. Teaney, L. Yan, *Phys. Rev. C*, **2012**, *86*, 044908.

[14] "Event-by-event shape and flow fluctuations of relativistic heavy-ion collision fireballs", Z. Qiu, U. Heinz, *Phys. Rev. C*, **2011**, *84*, 024911;

"Mode-coupling effects in anisotropic flow in heavy-ion collisions", J. Qian, U. Heinz, J. Liu, *Phys. Rev. C*, **2016**, *93*, 064901.

[15] "Elliptic flow and incomplete equilibration at RHIC", R. Bhalerao, J. Blaizot, N. Borghini, J. Ollitrault, *Phys. Lett. B*, **2005**, *627*, 49-54.

[16] "Elliptic flow and Hanbury-Brown–Twiss correlations in noncentral nuclear collisions", H. Heiselberg, A. M. Levy, *Phys. Rev. C*, **1999**, *59*, 2716.

[17] "The physics of the centrality dependence of elliptic flow", S. Voloshin, A. Poskanzer, *Phys. Lett. B*, **2000**, *474*, 27-32.

[18] "Elliptic flow at SPS and RHIC: from kinetic transport to hydrodynamics", P. Kolb, P. Huovinen, U. Heinz, H. Heiselberg, *Phys. Lett. B*, **2001**, *500*, 232-240.

[19] "Fate of the initial state perturbations in heavy ion collisions. II. Glauber fluctuations and sounds", P. Staig, E. Shuryak, *Phys. Rev. C*, **2011**, *84*, 034908.

[20] "Scaling of the higher-order flow harmonics: implications for initial-eccentricity models and the "viscous horizon"", R. Lacey, A. Taranenko, N. Ajitanand, J. Alexander, *arXiv:*1105.3782, **2011**.

[21] "Is anisotropic flow really acoustic?", R. Lacey *et al.*, *arXiv:*1301.0165, **2013**.

[22] "Beam Energy Dependence of the Viscous Damping of Anisotropic Flow in Relativistic Heavy Ion Collisions", R. Lacey *et al.*, *Phys. Rev. Lett.*, **2014**, *112*, 082302.

[23] "hijing: A Monte Carlo model for multiple jet production in pp, pA, and AA collisions", X. N. Wang and M. Gyulassy, *Phys. Rev. D*, **1991**, *44*, 3501.

Chapter 7

Summary and Conclusions

In this thesis work, we have analyzed the data collected with the STAR detector at RHIC for U+U collisions at $\sqrt{s_{\mathrm{NN}}} = 193$ GeV during the year 2012 and Au+Au collisions at $\sqrt{s_{\mathrm{NN}}} = 14.5$ GeV during the year 2014 as a part of Beam Energy Scan program (Phase-I). The deformed shape (prolate) of Uranium nucleus gives rise to various initial collision configurations in U+U collisions compared to more spherical Gold (Au) nucleus. The value of final state observables v_n can be larger or smaller depending on the collision configuration in U+U collisions. Therefore it is necessary to compare the results of v_n coefficients in deformed shape Uranium collisions with Au+Au collisions. In this thesis, we have compared our results with the published results of identified hadrons v_2 in Au+Au collisions at $\sqrt{s_{\mathrm{NN}}} = 200$ GeV from STAR experiment at RHIC.

We have presented results on azimuthal anisotropy of strange and multi-strange hadrons in U+U collisions at $\sqrt{s_{\mathrm{NN}}} = 193$ GeV. We applied extensive topological cuts and studied various backgrounds to reconstruct strange and multi-strange hadrons K_{s}^0, ϕ, $\Lambda(\bar{\Lambda})$, $\Xi(\bar{\Xi})$ and $\Omega(\bar{\Omega})$ using invariant mass technique. Transverse momentum (p_T) dependence of flow coefficients v_2, v_3 and v_4 of identified particles at mid-rapidity

for different centrality classes (0-10%, 10-40% and 40-80%) are presented in U+U collisions at $\sqrt{s_{NN}} = 193$ GeV. The magnitude of elliptic flow $v_2(\psi_2)$ is found to be greater than that of the higher order flow coefficients $v_3(\psi_3)$ and $v_4(\psi_4)$. The shape of differential $v_2(p_T)$ in U+U collisions at $\sqrt{s_{NN}} = 193$ GeV is observed to be similar to the published results of $v_2(p_T)$ in Au+Au collisions at $\sqrt{s_{NN}} = 200$ GeV. The magnitude of $v_2(p_T)$ is also similar to Au+Au collisions at $\sqrt{s_{NN}} = 200$ GeV, which shows the development of partonic collectivity of the medium created in U+U collisions at $\sqrt{s_{NN}} = 193$ GeV at RHIC.

Strange and multi-strange hadrons $v_n(p_T)$ is measured for three combined centrality classes: central (0-10%), mid-central (10-40%) and peripheral (40-80%). A strong centrality dependence of $v_2(p_T)$ is observed in U+U collisions at $\sqrt{s_{NN}} = 193$ GeV. The v_2 values for peripheral collisions are higher than central collisions reflecting the effect of initial spatial anisotropy (eccentricity of overlap region) on final state momentum space azimuthal anisotropy. Higher order flow coefficients does not show a centrality dependence, this is expected because the origin of higher order flow coefficients is event-by-event fluctuations in the initial density profile of participating nucleons rather than the initial overlap geometry.

The particle mass dependence of elliptic flow v_2 is predicted by the hydrodynamic models of heavy-ion collisions and it has been extensively studied in Au+Au collisions at RHIC. In this thesis work, we have studied mass-ordering of v_n coefficients at mid-rapidity in U+U collisions at $\sqrt{s_{NN}} = 193$ GeV. We observed mass-ordering of v_2 at low p_T (< 2 GeV/c). For low p_T lighter mass particles have higher values of v_2 than the heavier mass particles. Although at higher p_T (> 2 GeV/c) v_2 seems to follow particle type (baryon/meson) dependence rather than mass. The v_2 of all particles are grouped according to their baryon-meson type. The v_2 of baryons (Λ, Ξ and Ω) are higher than the mesons (K_s^0 and ϕ). Higher order flow coefficients v_3 and v_4 show the

267

similar particle mass dependence as v_2 but it is difficult to conclude precisely due to large statistical uncertainties. The observation of mass dependence of v_n coefficients at low p_T and particle type dependence at higher p_T leads us to the NCQ scaling of v_n coefficients.

Quark coalescence and recombination models for heavy-ion collisions predicted that if particles are made up of quarks then the elliptic flow v_2 will scale with their number of constituent quarks. This NCQ scaling of flow coefficients indicates that the collective flow has been developed at the partonic phase of the medium created in the heavy-ion collisions . In this work, we have tested the NCQ scaling of v_2 and higher order flow coefficients at mid-rapidity in U+U collisions at $\sqrt{s_{NN}} = 193$ GeV. We have plotted $v_n(p_T)$ as a function of transverse kinetic energy $(m_T - m_0)$ and scaled both the axis with number of constituent quarks (n_q). We observed NCQ scaling of $v_2(p_T)$ for identified hadrons at mid-rapidity in U+U collisions at $\sqrt{s_{NN}} = 193$ GeV for minimum bias and different centrality classes. Thus, the NCQ scaling provides evidence for the partonic degrees of freedom of the medium created in heavy-ion collisions. Although, NCQ scaling works well for v_2 at RHIC, but for higher order flow coefficients there are hints from the deviation of the universal NCQ scaling. Hence, the coefficients v_3 and v_4 are plotted with the scale factor $n_q^{n/2}$ instead of n_q. Modified NCQ scaling is observed for v_3 and v_4 in U+U collisions at $\sqrt{s_{NN}} = 193$ GeV within statistical and systematic uncertainties.

The results of strange and multi-strange v_2 are compared with the light hadrons $(\pi^{\pm}, K(\bar{K})$ and $p(\bar{p}))$ v_2 at mid-rapidity in U+U collisions at $\sqrt{s_{NN}} = 193$ GeV. We observed a similar mass-ordered hierarchy of v_2 at low p_T and baryon/meson type dependence at higher p_T.

Further the measurements of azimuthal anisotropy of strange and multi-strange hadrons are compared with the heavy-ion collision model calculations. We have used a multi-phase transport (AMPT) model and hydrodynamics based model for the comparison. AMPT string melting version with a parton-parton interaction cross-section of 3 mb is used. Ideal-hydrodynamical model with LQCD equation of state without viscosity is used. We observed that the AMPT model explains the results of strange and multi-strange v_n coefficients at low p_T and under-estimates the results at higher p_T. The hydrodynamics model also over-predicts the data, which shows the need of viscous corrections to the model.

We have calculated two ratios of v_n coefficients v_3/v_2 and $v_4/2v_2^2$ for strange and multi-strange hadrons at mid-rapidity in minimum bias U+U collisions at $\sqrt{s_{\mathrm{NN}}} = 193$ GeV. The ratio v_3/v_2 increases at low p_T (< 2.0 GeV/c), which shows that the relative strength of v_3 increases with the transverse momentum compared to v_2. This observation suggests that the v_3 is more sensitive to viscosity than v_2 as predicted by the viscous hydrodynamics models. We have also observed the ratio v_3/v_2 at $p_T > 2.0$ GeV/c becomes flat and does not depends on the mass of the particles. This mass independence of the ratio v_3/v_2 is also predicted by the viscous hydrodynamics for fast particles (i.e high p_T particles). The ratio $v_4/2v_2^2$ shows a weak p_T dependence and its values approaches to 1.0 for $p_T > 2.0$ GeV/c. The values of the ratio $v_4/2v_2^2$ larger than 0.5 indicate deviations from ideal fluid behavior predicted by the hydrodynamical models. The ratio v_4/v_2^2 for identified hadrons is related to v_4/v_2^2 of quarks in simple coalescence models for heavy-ion collisions. The large $v_4/2v_2^2$ ratio might also be a indication of large quark v_4 values. We have also compared the ratios calculated using AMPT and ideal-hydro model with the data. Results from hydro-model show the similar p_T dependence but over-estimates the values of v_n ratios. AMPT string melting model results agree well with the data within statistical uncertainties.

This thesis work also includes azimuthal anisotropy studies in Au+Au collisions at center of mass energy of 14.5 GeV. The data at $\sqrt{s_{\mathrm{NN}}}$ = 14.5 GeV, recorded in the year 2014, was taken to fill the gap of 200 MeV in baryon chemical potential between the two beam energies 11.5 and 19.6 GeV in BES-I program. Therefore, it is necessary to measure v_2 to understand the dominance of partonic on hadronic phases of the medium created in the Au+Au collisions at $\sqrt{s_{\mathrm{NN}}}$ = 14.5 GeV. In this thesis work, we have presented the measurements of elliptic flow v_2 of ϕ-meson and inclusive charged hadrons at mid-rapidity ($|\eta| < 1.0$) in Au+Au collisions at $\sqrt{s_{\mathrm{NN}}}$ = 14.5 GeV. A systematic study of v_2 as a function of p_T, η and collision centrality is presented. The inclusive charged hadrons v_2 results are obtained using event plane method ($v_2\{EtaSubs\}$) and 2,4-particle cumulant method ($v_2\{2\}$, $v_2\{4\}$).

The ϕ-meson v_2 measurements are done using event plane method at mid-rapidity in Au+Au collisions at $\sqrt{s_{\mathrm{NN}}}$ = 14.5 GeV. The results are compared with the v_2 of identified hadrons. The v_2 of negatively charged particles (π^-, K^-, $\bar{p}$) and positively charged particles (π^+, K^+, p) follows a mass ordering at low p_T (< 2.0 GeV/c). The mass ordering of v_2 of these charged hadrons in Au+Au collisions at $\sqrt{s_{\mathrm{NN}}}$ = 14.5 GeV is found similar to what is observed at top RHIC energy. Neutral particles (ϕ-meson, $\Lambda(\bar{\Lambda})$) seems to deviate from this general trend of mass ordering at the low energies ($\sqrt{s_{\mathrm{NN}}} < 19.6$ GeV). This indicates that the partonic interactions are gradually becoming smaller at the lower beam energies. We also compared the ϕ-meson v_2 as a function of p_T at mid-rapidity in minimum bias Au+Au collisions at $\sqrt{s_{\mathrm{NN}}}$ = 14.5 GeV with other beam energies from 7.7 to 39 GeV. The ϕ-meson v_2 values at highest measured p_T bin for Au+Au collisions at 7.7 and 11.6 GeV are close to zero, which shows the dominance of hadronic interactions. We found finite value of ϕ-meson v_2 at highest measured p_T bin in Au+Au collisions at 14.5 GeV. This indicates the formation of partonic phase of the medium at beam energies $\sqrt{s_{\mathrm{NN}}} \geq$

14.5 GeV in heavy-ion collisions.

Inclusive charged hadrons v_2 is presented as a function of transverse momentum (p_T) and pseudo-rapidity (η) for various collision centrality classes in Au+Au collisions at $\sqrt{s_{\mathrm{NN}}} = 14.5$ GeV. The $v_2(p_T)$ shows monotonic increasing trend with increasing p_T. The p_T-integrated $v_2(\eta)$ shows a weak dependence on η. Also, we found a clear centrality dependence for both $v_2(p_T)$ and $v_2(\eta)$. The dependence of v_2 on p_T and η is consistent with the published results at other beam energies from BES-I.

The different methods of v_2 measurement have different sensitivity to non-flow effects and fluctuations. Therefore, we have measured v_2 using various methods $v_2\{EtaSubs\}$, $v_2\{BBC\}$, $v_2\{2\}$ and $v_2\{4\}$. On comparison, we found that the difference of $v_2\{2\}$ from other methods depends on the p_T range. A larger difference is observed for low p_T (< 1 GeV/c) region. The difference between $v_2\{4\}$ and $v_2\{BBC\}$ is relatively small and less dependent on p_T. It suggests the non-flow contribution to $v_2\{4\}$ and $v_2\{BBC\}$ are less compared to the event plane and two-particle cumulant methods. It also shows that the use of first-order event plane from BBC detector (forward rapidity) to study the second harmonic reduces non-flow effects which are not correlated among different harmonics.

We measured inclusive charged hadron v_2 in nine different centrality classes from central to peripheral collisions. We found that the elliptic flow v_2 depends on the collision centrality and strongly correlated with the initial co-ordinate space eccentricity. We calculated the root-mean-square participant eccentricity $\varepsilon_{part}\{2\}$ using a Monte Carlo Glauber model. We have plotted v_2 scaled by the $\varepsilon_{part}\{2\}$ as a function of p_T to remove the effect of initial state overlap geometry. After scaling, we found higher values of $v_2/\varepsilon_{part}\{2\}$ in central collisions compared to peripheral collisions, which suggests stronger collective interactions in events with larger number of participants. The observed centrality dependence of $v_2/\varepsilon_{part}\{2\}$ is found similar as reported in the

271

published results from STAR experiment in Au+Au collisions at beam energies $\sqrt{s_{\mathrm{NN}}}$ = 7.7−62.4 GeV and 200 GeV.

The observation of significant v_2 at higher beam energies at RHIC could be interpreted as higher degree of thermalization than at lower beam energies. Therefore, we compared our results of inclusive charged hadrons v_2 from 4-particle cumulant method in Au+Au collisions at $\sqrt{s_{\mathrm{NN}}} = 14.5$ GeV with other published results from STAR and ALICE collaboration at various beam energies. We found a beam energy dependence of inclusive charged hadrons v_2 as a function of p_T. The v_2 increases with increasing beam energy below p_T 2 GeV/c. Above $p_T \sim 2$ GeV/c the values for all energies are comparable within statistical uncertainties. The increase of $v_2(p_T)$ with beam energy can be attributed to the change of baryon chemical potential from lower to higher energies and/or larger collectivity at higher collision energies.

The results are compared with the transport model calculations from AMPT and UrQMD to understand the particle production mechanism and partonic versus hadronic contribution to v_2 in Au+Au collisions at $\sqrt{s_{\mathrm{NN}}} = 14.5$ GeV. The UrQMD model only takes hadronic interaction into consideration, where as the AMPT model with string melting version incorporates both partonic and hadronic interactions and the default AMPT model also has only hadronic interactions. The UrQMD results is consistently lower than the data for the p_T range studied, which shows that only hadronic interactions are not sufficient to explain the experimental data. The AMPT-SM with a parton-parton cross-section of 1.5mb shows a good agreement with the data. This suggests the formation of partonic medium in Au+Au collisions at $\sqrt{s_{\mathrm{NN}}}$ = 14.5 GeV. A larger parton cross-section of 10mb over-estimates the data, which could be used to interpret hadronic versus partonic contribution to the v_2 because a larger parton cross-section means late start of hadron cascade.

Keeping in mind the analysis of U+U data in this thesis, we have attempted to give a method to separate unique collision configurations in U+U collisions. The physics motivation for this is the following. In relativistic heavy-ion collisions, the energetic spectator protons can produce a strong magnetic field, which give rise to the exotic effects like chiral magnetic effect (CME) and chiral separation effect (CSE). Azimuthal anisotropy acts as a background for these processes. Therefore, it is necessary to minimise the azimuthal anisotropy to observe these phenomena in experimental data. The events which have low azimuthal anisotropy and very high magnetic field are the perfect candidates for the observation of CME and CSE. The Uranium nuclei have a deformed prolate shape. Due to its deformed shape, the U+U collisions can have various initial collision configurations. Therefore, U+U collisions provide an unique opportunity to study these exotic effects in relativistic heavy-ion collisions. It has not been experimentally possible so far to unambiguously select specific configurations in U+U collisions.

In this thesis, we present a new method to select body-tip configuration from unbiased events in central U+U collisions using AMPT model in context of experiments. We have used asymmetry in the total spectator neutron number in the two opposite directions of the beam in central U+U collisions. First of all, we have implemented deformed shape of Uranium nuclei in AMPT model using modified Woods-Saxon nucleon density distribution function. We have generated both the specific body-tip and unbiased U+U collisions events for the analysis. We have converted the spectator neutron number into corresponding experimentally measurable ZDC signal. We used response of ZDC detectors from the STAR experiment at RHIC. The resolution of a single neutron ZDC response is 18%. We have smeared the energy deposited by each individual neutron for event-by-event by a Gaussian distribution of width 18% about the mean value (96.5 GeV). We have plotted the converted ZDC signal for left

going spectator neutrons versus right going spectator neutrons in unbiased (without any specific orientation of Uranium nuclei) U+U collisions at $\sqrt{s_{NN}} = 193$ GeV. We select all those events which lie below the straight line with slope = 0.25 and intercept = -180, therefore potentially selecting the events with asymmetric spectator neutrons.

We also devised a new variable S_η to differentiate between the body-tip and the minimum bias events in central U+U collisions. Particle production in minimum bias configurations is symmetric in η, therefore the variable S_η lies close to zero. But in case of body-tip configurations particle production is asymmetric thereby giving non-zero values of S_η. The observed difference in S_η between the body-tip and minimum bias events enhances the possibility of our method to select the body-tip events in real experiments.

We have calculated elliptic flow v_2 of charged particles at mid-rapidity after the selection of specific configuration body-tip from all possible configurations in U+U collisions at $\sqrt{s_{NN}} = 193$ GeV. The v_2 results are shown with respect to both the event plane angle and the participant plane angle. As expected, we found that the magnitude of v_2 for selected events is systematically 25% lower compared to all con-figurations. The selected body-tip events from minimum bias may possibly contain some other configurations. Therefore, we present the purity of the selected events i.e. how much of the selected events can be specified as body-tip events. We have changed the slope parameter and angular relaxation for different values. We observed that the purity of selected events increase as we decrease the value of slope parameter or if we increase the angular relaxation. More than 70% purity can be achieved by using a lower slope value i.e. higher order of left-right spectator neutron asymmetry.

The above results motivated us to use the method developed to access unique initial conditions even for collision of spherical nuclei like Au or Pb. A precise knowledge of initial conditions is very essential for a complete understanding of the medium

created in relativistic heavy-ion collisions. It is also required to test theoretical framework of the models, which correctly describes the evolution of the strongly interacting QGP matter produced in relativistic heavy-ion collisions. There are event-by-event geometrical and quantum fluctuations in the initial states of heavy-ion collisions. The standard technique of characterising heavy-ion collisions into different centrality classes are obtained from the final state charged particle multiplicity corresponds to different initial states. This averages out various initial configurations and restrict the study to only a limited range of initial conditions. Thus, a precise knowledge of initial state is required in order to do a proper comparison between theory and experimental results.

In this thesis, we proposed a new method for binning the heavy-ion collisions events in terms of total spectator neutrons $(L + R)$ along with the centrality bins. This will help us to probe events with rare initial states which otherwise get masked when analysed by the centrality binning alone. The advantage of using total spectator neutrons to probe initial state is that it is an experimentally observable quantity. Also it is not required to know total spectator neutron number very precisely. Here we presented an additional binning in $L + R$ on top of the standard centrality binning in Pb+Pb collisions at $\sqrt{s_{\text{NN}}} = 2.76$ TeV using AMPT model and obtained results with new binning procedure.

We found that the centrality and $L+R$ bins shows the same variation of impact parameter (b) with N_{part}, which shows that the observable $L+R$ is equally good for the study of initial states and their effect on final states. We found that the variation of $dN_{\text{ch}}/d\eta$ with N_{part} is quite different for $L+R$ bins compared to usual centrality bins, which can be used to study different energy deposition mechanism within the same centrality. In a given centrality bin, larger $L + R$ bins have higher energy gradients compared to smaller $L + R$ bins which results in strong inhomogeneities in the initial

conditions. We also showed that it is possible to vary ε_2 and ε_3 independently of each other. This will enable us to extract the contribution due to non-linear mode coupling between v_2 and higher order flow coefficients v_3, v_4 and v_5. We found that the breaking of usual scaling relation between v_2/ε_3 and $1/SdN_{\mathrm{ch}}/d\eta$ when using $L + R$ binning. A mild breaking of the acoustic scaling relation between $\ln(v_n/\varepsilon_n)$ and initial system size $(1/\Lambda_T)$ is also observed with both $L+R$ and centrality binning.

The results from this study suggest that one might be able to extract values of medium properties like η/s ratio more accurately with the introduction of $L + R$ bins. We also observed that $< p_T >$ in combined bins of $dN_{\mathrm{ch}}/d\eta$ and $L+R$ is a good way to measure the degree of medium interaction without a precise measurement of $L + R$. Finally, the proposed new binning procedure can be use to analyze initial conditions with the current performance of ZDC detectors in heavy-ion collisions experiments to understand the QGP medium created in relativistic heavy-ion collisions more accurately.